



Norwegian University of
Science and Technology

Experimental study and CFD simulation of water coning phenomenon in perforated geometry

Kristian Stautland
Halvor Weberg

Master of Energy and Environmental Engineering

Submission date: June 2016

Supervisor: Zhilin Yang, EPT

Co-supervisor: Ole Jørgen Nydal, EPT

Norwegian University of Science and Technology
Department of Energy and Process Engineering

EPT-M-2016-128

EPT-M-2016-153

MASTEROPPGAVE

for

Kristian Stautland &
Halvor Weberg

Våren 2016

Experimental study and CFD simulation of water coning phenomenon in perforated geometry*Eksperimentell studie og CFD simuleringer av vannkoning fenomen i perforerte geometri***Bakgrunn og målsetting**

Long horizontal wells require Inflow Control Devices (ICD) to optimize production and to maximize recovery. Water or gas coning have previously led to major losses, so ICDs are always installed in these types of wells.

The ICDs in current use consists of restrictions to create pressure drop and to reduce flow rate locally. However, the flow rate depends on the pressure drop. With depletion the pressure profile will therefore change, and may still cause coning at late production times.

The main target of ICD is to deal with the potential coning phenomenon in the reservoir. Once the water has broken through over the whole area of the well, the coning behavior may happen in the well geometry, the potential of coning formation is larger for more viscous oil field. It is therefore , important to understand the mechanism of coning formation in well geometry, and provide important input to improve the design of ICD.

The experimental study and CFD simulations will be conducted to investigate the critical condition of the coning phenomenon with different physical parameters, such as initial water depth, oil viscosity. After the water breakthrough, the water cut variation with the flowrate will also be investigated.

Oppgaven bearbeides ut fra følgende punkter:

1. Modify the existing facility
2. Conduct the experiment with different geometry, fluid and initial condition
3. Data analysis
4. Comparison with existing physical model on critical coming condition
5. A commercial CFD code will be used to simulate the flow process of the experiments. It is expected that the experimental observation is reproduced by the CFD, and the parametric study is conducted on the effect of oil viscosity, density difference, the depth of the water layers, etc. A three-dimensional approach may have to be used.

Senest 14 dager etter utlevering av oppgaven skal kandidaten levere/sende instituttet en detaljert fremdrift- og eventuelt forsøksplan for oppgaven til evaluering og eventuelt diskusjon med faglig ansvarlig/veiledere. Detaljer ved eventuell utførelse av dataprogrammer skal avtales nærmere i samråd med faglig ansvarlig.

Besvarelsen redigeres mest mulig som en forskningsrapport med et sammendrag både på norsk og engelsk, konklusjon, litteraturliste, innholdsfortegnelse etc. Ved utarbeidelsen av teksten skal kandidaten legge vekt på å gjøre teksten oversiktlig og velskrevet. Med henblikk på lesning av besvarelsen er det viktig at de nødvendige henvisninger for korresponderende steder i tekst, tabeller og figurer anføres på begge steder. Ved bedømmelsen legges det stor vekt på at resultatene er grundig bearbeidet, at de oppstilles tabellarisk og/eller grafisk på en oversiktlig måte, og at de er diskutert utførlig.

Alle benyttede kilder, også muntlige opplysninger, skal oppgis på fullstendig måte. For tidsskrifter og bøker oppgis forfatter, tittel, årgang, sidetall og eventuelt figurnummer.

Det forutsettes at kandidaten tar initiativ til og holder nødvendig kontakt med faglærer og veileder(e). Kandidaten skal rette seg etter de reglementer og retningslinjer som gjelder ved alle (andre) fagmiljøer som kandidaten har kontakt med gjennom sin utførelse av oppgaven, samt etter eventuelle pålegg fra Institutt for energi- og prosesssteknikk.

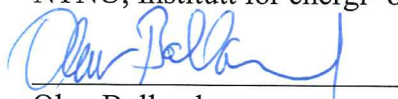
Risikovurdering av kandidatens arbeid skal gjennomføres i henhold til instituttets prosedyrer. Risikovurderingen skal dokumenteres og inngå som del av besvarelsen. Hendelser relatert til kandidatens arbeid med uheldig innvirkning på helse, miljø eller sikkerhet, skal dokumenteres og inngå som en del av besvarelsen. Hvis dokumentasjonen på risikovurderingen utgjør veldig mange sider, leveres den fulle versjonen elektronisk til veileder og et utdrag inkluderes i besvarelsen.

I henhold til ”Utfyllende regler til studieforskriften for teknologistudiet/sivilingeniørstudiet” ved NTNU § 20, forbeholder instituttet seg retten til å benytte alle resultater og data til undervisnings- og forskningsformål, samt til fremtidige publikasjoner.

Besvarelsen leveres digitalt i DAIM. Et faglig sammendrag med oppgavens tittel, kandidatens navn, veileders navn, årstall, institutt navn, og NTNUs logo og navn, leveres til instituttet som en separat pdf-fil. Etter avtale leveres besvarelse og evt. annet materiale til veileder i digitalt format.

- Arbeid i laboratorium (vannkraftlaboratoriet, strømningsmeknikk, varmeteknikk)
 Feltarbeid

NTNU, Institutt for energi- og prosesssteknikk, 02. Juni 2016



Olav Bolland
Instituttleder



Zhilin Yang
Faglig ansvarlig/veileder

Medveileder(e): Ole Jørgen Nydal

Preface

This master thesis has been written as a part of the Master's program at the Norwegian University of Science and Technology (NTNU), at the Department of Energy and Process Engineering in the spring of 2016. The work done in this thesis has been a part of a collaboration between NTNU and Statoil ASA, and is a continuation of the work done by Egor Shevchenko in the spring of 2013. Shevchenko's old setup has been reconstructed and modified to fit the scope of this project. The majority of the workload has been to get this setup functional and run experiments in the laboratory as well as to develop computational fluid dynamics (CFD) models which could replicate the experiments.

We would like to thank our supervisor Zhilin Yang for his expertise and guidance throughout this work. We would also like to thank co-supervisor professor Ole Jørgen Nydal for invaluable answers to our many questions.

This study was made possible through support from NTNU and the Department of Energy and Process Engineering, and especially staff engineers Martin Brustadmo and Lars Sørensen who provided technical help when needed. Last but not least we would thank Nicholas La Forgia for his helpful assistance in the laboratory, and Martin Aasved Holst for his insight into the CFX commercial package.

Trondheim, June 10, 2016.



Kristian Stautland



Halvor Weberg

Abstract

The focus of this thesis is to further examine the water coning phenomenon in annular geometry in a horizontal well completion. This phenomenon is of particular interest to the oil & gas industry, as it may restrict production rates, and lead to reduced production effectiveness due to water carry-over. An overview of industry experience and a review of academic research conducted on the topic of water coning phenomenon is provided. The study has been carried out by conducting experiments of flow inside annular geometry of a horizontal well in a laboratory setup and by utilizing CFD simulations. The experimental findings provided valuable inputs for the CFD simulations, and the CFD simulations may in turn become a useful tool for testing ICD designs. Furthermore, this study provides a detailed analysis and comparison of analytical methods that can be utilized to predict critical flow rates.

The experiments were conducted using a simple, yet effective, setup with a symmetric inflow of the liquids. It was based on a 2D-principle giving good visualization of the experiments. The main emphasis was placed on the single orifice geometry, but geometries with two orifices were also used during the experiments. Two different oils were used: Nexbase 3080 due to its similarity to the North Sea oil regarding viscosity, and Marcol 52 to have an oil with a viscosity between those of water and Nexbase.

A total 766 experimental runs were conducted. From these experiments the effect of water coning was studied in regard to the size of the annulus gap δ , the flow rate, the type of oil, different plate geometries with one and two outlet orifices, and the distance between the water level and the orifice.

The results indicated that water coning features are highly dependent on and all of the parameters mentioned above. High flow rates and a short distance between the initial water level and the orifice, both give a high tendency of water coning and large water cuts. However, large annulus gaps lower the tendency of water coning. Nexbase oil with its high viscosity demonstrated a larger tendency to induce water coning than the less viscous Marcol oil. Low flow rates, large annulus gaps and large distances between the water level and the orifice will minimize the effect

of water coning.

A powerful and versatile CFD package that is well equipped to simulate coning phenomenon, ANSYS-CFX commercial code was utilized for running simulations. A total of 210 simulations were set up and conducted, both in 2D and 3D.

For this research study, it was important to conduct a large number of simulations in order to correctly observe trends when changing the input variables. The simulations were all planned to ensure that an acceptable step size in variable changes was utilized. In this manner it was possible to stay within a reasonable number of simulations while still being able to uncover trends from flow behaviour.

The CFD-simulations conducted indicated that the two-dimensional modeling approach was effective to study water coning phenomenon, in that the simulations displayed the same underlying trends observed in the experiments, and required a relatively short amount of computational time.

The main focus of the analytical aspect of this study is directed towards a pressure balance analysis. However, dimensional analysis was utilized to forge a correlation for the critical flow rate.

The comparisons of the different analytical methods indicate that the dimensional analysis approach may provide valuable insight to critical flow rates. Comparisons with experimental data suggest that the analytical expression derived from pressure balances leads to a largely varying magnitude of discrepancy depending on the case in question.

Sammendrag

Denne masteroppgaven har handlet om å studere vannkoningsfenomenet i perforerte rør. Dette fenomenet er av spesiell interesse for olje- og gassindustrien ettersom det kan legge begrensninger for produksjonsrater og føre til nedsenket produksjonseffektivitet. En gjennomgang av erfaringer fra industrien og av akademisk forskning har blitt utført på temaet vannkoning. I dette studiet har det blitt gjennomført eksperimenter på innvendig strømming i ringformete rør i horisontale brønner i ett laboratorieoppsett. De eksperimentelle resultatene ga verdifull informasjon som ble brukt i CFD-simuleringer. Disse CFD-simuleringene kan bli et verdifullt verktøy for å teste ICD-design. Videre har det blitt gjennomført en grundig analyse og sammenligning av analytiske metoder som kan brukes til å predikere kritiske volumstrømmer.

Eksperimentene har blitt utført i et enkelt men effektivt oppsett med symmetrisk innstrømming av væsker. Oppsettet var basert på et 2D-prinsipp som ga god visualisering av eksperimentene. Hovedfokuset var rettet mot en geometri som bestod av ett utløpshull, men plater med to utløpshull ble også testet. To ulike oljer ble brukt: Nexbase 3080 på grunn av sin likhet med Nordsjøoljen med tanke på viskositet, og Marcol 52 for å ha en olje med en viskositet mellom viskositetsverdiene til henholdsvis vann og Nexbase.

Totalt ble det utført 766 eksperimentelle forsøk. Fra eksperimentene ble effekten av vannkoning studert med tanke på bredden av annulus δ , volumstrøm, oljetype, forskjellige plategeometrier med ett- og to utløp og avstanden mellom vannivået og utløpet.

Resultatene indikerer at vannkoning er høyst avhengig av alle disse parameterne. Store volumstrømmer og en kort avstand mellom opprinnelig vannivå og utløpshull gir en høy tendens til vannkoning og store vannkutt. Brede annulus gir imidlertid lavere tendenser til vannkoning. Med sin høye viskositet viste Nexbase større tendenser til å indusere vannkoner enn den mindre viskøse Marcol. Små volumstrømmer, store bredder på annulus og store distanser mellom vannivå og utløpshull minker effekten av vannkoning.

For å utføre simuleringer ble ANSYS-CFX brukt. Dette er en allsidig CFD-pakke som er godt utrustet til å simulere vannkoningsfenomenet. Totalt ble 210 simuleringer både i 2D og 3D, satt

opp og gjennomført.

For dette forskningsprosjektet var det viktig å gjennomføre store mengder simuleringer for å kunne observere trender når inndataen ble endret. Alle simuleringer var planlagt slik at en fornuftig intervallstørrelse for endringer av parametere ble brukt. På denne måten var det mulig å avdekke trender fra strømningsatferd innenfor ett rimelig antall simuleringer.

Utførte CFD-simuleringer antyder at en todimensjonell tilnærming var effektiv for å studere vannkoningsfenomenet. Simuleringene med denne tilnærmingen viste de samme grunnleggende trendene som ble observert i eksperimentene, og krevde en relativ kort beregningstid.

Hovedfokuset for den analytiske tilnærmingen var rettet mot analyse av trykbalanser. I tillegg ble dimensjonsanalyse brukt for å utlede en korrelasjon for den kritiske volumstrømmen.

Sammenligningene mellom de forskjellige analytiske metodene indikerer at tilnærmingen med dimensjonsanalyse kan gi verdifull innsikt til utregningen av kritiske volumstrømmer. Sammenligninger med eksperimentell data antyder at det analytiske uttrykket utledet fra trykbalansen, fører til store variasjoner innenfor størrelse på avvik.

Contents

Preface	i
Abstract	iii
Sammendrag	v
Nomenclature	xi
1 Introduction & Objectives	1
1.1 Structure of Thesis	2
2 Background Information	6
2.1 Horizontal Wells	6
2.2 Stable Water Coning	9
2.3 Inlet Control Devices	11
2.4 Water Coning in Annular Geometry	15
2.5 Statoil Input Data	19
3 Experimental Facility	22

3.1	Experimental Setup	22
3.1.1	Experimental rig	22
3.1.2	Geometry of housing plates	25
3.1.3	Oil properties	28
3.2	Preparations	28
3.3	Experimental Procedure	34
4	Experimental Results & Discussions	40
4.1	Flow Rate Correlations	40
4.2	Water Jump Phenomenon	43
4.2.1	Plate 1, single orifice housing plate	44
4.2.2	Plate 2, two orifices at the same height	51
4.2.3	Plate 3, two orifices at different heights	53
4.3	Water Cut Measurements	56
4.3.1	Plate 1, single orifice housing plate	56
4.3.2	Plate 2, two orifices at the same height	61
4.3.3	Plate 3, two orifices at different heights	61
5	CFD Methodology	64
5.1	Case Simplifications	64
5.2	Simulation Cases	65

5.3	Simulation Geometries	67
5.4	Boundary Conditions	69
5.5	Momentum Source	70
5.6	Initial Conditions	76
5.7	Meshing	77
5.7.1	Mesh sensitivity analysis	79
5.8	Solver Settings	86
5.9	Monitors and Key Parameters	88
6	CFD Results and Discussions	90
6.1	Expectations	90
6.2	2D Simulations - Single Outlet Orifice	92
6.2.1	Laminar solver with laminar friction	94
6.2.2	Laminar solver with composite friction	103
6.2.3	Transitional solver with composite friction	105
6.3	2D Simulations - Multiple Outlet Orifices	109
6.4	3D Simulations - Single Outlet Orifice	114
6.5	Parametric Study	118
7	Analytical Methods vs. Experimental Data	125
7.1	Dimensional Analysis, Pi-Theorem	125

7.2 Solving Analytical Models	128
7.3 Tuning The Analytical Models	133
7.4 Tuning The Analytical Data	134
7.5 Comparison of The Analytical Methods	135
8 Conclusions and Further Work	140
8.1 Conclusions	140
8.2 Further Work	142
A Laboratory data	144
A.1 Spreadsheet with every single experimental run	144
A.2 Water jump vs. flow rate for each gap	161
A.3 Water cut vs. flow rate for each gap	165
A.4 Flow rate correlations for each gap	169
B CFD Simulations & Results	171
B.1 Laminar Solver with Composite Friction, Plots	171
C Analytical Methods	173
C.1 Dimensional Analysis	173
C.2 Matlab Scripts	175
C.3 Solving Analytical Models, Plots	179

D Miscellaneous 181

List of Figures 182

List of Tables 196

Bibliography 198

Nomenclature

α	Water fraction (water cut)
β	Advection coefficient
$\Delta\vec{r}$	Directional vector
ΔP_a	Acceleration pressure loss
ΔP_f	Frictional pressure loss
ΔP_g	Hydrostatic pressure difference
ΔP_N	Pressure drop over nozzle
$\Delta P_{laminar}$	Laminar friction loss
$\Delta P_{turbulent}$	Turbulent friction loss
Δt	Time step
δ	Annulus gap width
\dot{m}	Mass flow rate
ϵ	Empirical constant for simplified critical flow rate correlation
ϵ^*	Empirical constant for simplified critical flow rate correlation
η	Density ratio
γ	Shear Strain

κ	Empirical constant describing slope between pi groups
μ	fluid viscosity
ν	Kinematic viscosity
ω	Empirical coefficient for tuning data
ϕ	The potential function
ϕ_{ip}	Scalar quantity at initial point
ϕ_{up}	Scalar quantity at upwind point
ψ	The stream function
ρ_m	Mixture density
ρ_o	Density of oil
ρ_w	Density of water
σ	Surface tension
τ	Shear stress
Θ	Contact angle
φ	Angle between cone and orifice, seen from center of production pipe.
φ_{level}	Angle between interface and orifice, seen from center of production pipe.
$A_{cell-face}$	Area of cell walls perpendicular to flow
A_{wall}	Area of cell walls parallel with flow
C	Courant number
C_u	Nozzle geometry constant
C_v	Nozzle geometry constant

D_h	Hydraulic diameter
f	Friction factor
F_v	Force per volume
g	Gravitational constant
h	Height from the initial water level to the entrance of the orifice
h_t	Height of oil zone
k_h	Horizontal permeability
k_v	Vertical permeability
l	Capillary rise
L_e	Hydrodynamic entrance length
L_{cell}	Length of cell
Q	Volumetric flow rate
Q_c	Critical flow rate
r_d	Dimensionless radius
r_e	Exterior radius
Re	Reynolds number
S	Spacing between parallel plates
T	Distance from orifice to water
T_i	Distance from center of orifice to entrance of orifice (radius)
T_o	Distance from the center of orifice to tip of the water cone
U_b	Bulk velocity

U_∞ Free stream velocity

u_θ Circumferential velocity

u_{ave} Average velocity

u_r Radial velocity

V Volume

Chapter 1

Introduction & Objectives

In this day and age newly spudded wells are often horizontal wells, defined as wells with an inclination greater than 85 degrees[1]. Horizontal wells enhance reservoir performance by placing a long wellbore section within the reservoir.

Horizontal wells offer larger and more efficient drainage patterns, leading to increased overall reserves recovery. The production rate increases because of the greater wellbore length exposed to pay zone. Furthermore, gas and water reservoir coning decreases because of reduced draw-down pressure in the reservoir for a given production rate [2].

However, horizontal wells introduce new production challenges. Reservoir coning may still occur and lead to annular coning phenomenon. Inlet control devices (ICD's) and autonomous inlet control devices (AICD's) are frequently installed to remediate the problem.

The necessity of ICD's makes it important to understand the fluid dynamics governing the coning formation in well geometry as well as in annular geometry. With increased understanding of the problem, better designs of the ICD's can be fabricated, leading to overall more efficient field production.

A powerful tool to tackle this problem and quantify performances of ICD designs is by the use of computational fluid dynamics (CFD). The focus of this master thesis was to conduct experi-

ments to study coning phenomenon in perforated annular channels, and develop CFD models able to capture the flow phenomenons observed in the respective experiments. The following objectives are considered:

- Conduct and analyze experiments regarding the water coning phenomenon with different plate geometries, fluid properties and initial conditions. This implies modifying the already existing rig to fit the desired experiments.
- The ANSYS-CFX code will be used to simulate the flow process of the experiments. It is expected that the experimental observation is reproduced by the CFD simulations. A three-dimensional approach may have to be used.
- A parametric study is to be conducted on the effect of oil viscosity, density difference, the depth of the water layers, etc.
- Exploration and comparison of analytical methods to predict stationary coning heights, and critical flow rates.

1.1 Structure of Thesis

This master thesis is divided into eight separate chapters, each of which are briefly described in this section.

Chapter 1 - Introduction

Chapter 1 presents the main goals associated with the master thesis, and aims to demonstrate the topic's relevance in a broader context within the petroleum sector.

Chapter 2 - Background Information

Chapter 2 presents a literature study surrounding the topic of reservoir coning, and annular coning. In addition relevant case data supplied by Statoil is presented. The main topics presented are:

- Horizontal wells
- Stable water coning
- Inlet control devices
- Water coning in annular geometry

Chapter 3 - Experimental Facility

Chapter 3 contains a detailed description of the experimental setup and the experimental procedures. Choices made regarding the setup and procedures are described. In this manner the experiments can easily be recreated and the work can be resumed in the future.

Chapter 4 - Experimental Results & Discussions

In chapter 4 the experimental results are presented. The results presented are divided into three different topics:

- Flow rate correlations
- Water jump phenomenon
- Water cut measurements

During these sections the results are presented for all three geometries, and the results are linked to the background information and flow theory.

Chapter 5 - CFD Methodology

Chapter 5 presents the setup and underlying theory describing the CFD simulations. Choices that were made while creating the CFD model are accounted for. The chapter discusses the following:

- Case simplifications
- Simulations cases
- Simulations geometries
- Boundary conditions
- Momentum source
- Initial conditions
- Meshing
- Solver settings
- Monitors and key parameters

Chapter 6 - CFD Results and Discussions

In chapter 6 the results from the CFD simulations are presented. The chapter is divided into:

- 2D simulations - Single outlet orifice
- 2D simulations - Multiple outlet orifices
- 3D simulations - Single outlet orifice
- Parametric study

The results are analyzed and discussed regarding trends seen in the simulations, and the results are compared against the experimental data. The different models are also compared against each other.

Chapter 7 - Analytical Methods vs. Experimental Data

In chapter 7 various analytical methods are explored. Detailed comparisons of the methods against the experimental data are presented at the end of the chapter.

Chapter 8 - Conclusions and Further Work

Chapter 8 presents the most important findings done in this thesis. Furthermore, the authors of this thesis give their recommendation for further work which can be done on the topic of water coning in annular geometry.

Chapter 2

Background Information

The abundance of available literature indicates that reservoir coning phenomenon have been extensively researched over the past several decades. A wide range of literature on coning in horizontal,- and vertical wells exists. However little available literature was found on the topic of coning in annular geometry.

2.1 Horizontal Wells

In general, a horizontal well is one that is drilled parallel to a bedding plane, as opposed to a vertical well, which intersects the reservoir-bedding plane at 90 degrees. Horizontal drilling technology achieved commercial viability during the late 80's.

Most oil and gas reservoirs are much more extensive in their horizontal area (areal) dimension than in their vertical (thickness) dimension. By drilling that portion of a well which intersects such a reservoir parallel to its plane of more extensive dimension, as seen in figure 2.2, horizontal drilling's immediate technical objective is achieved. That objective is to expose significantly more reservoir rock to the wellbore surface than would be the case with a conventional vertical well penetrating the reservoir perpendicular to its plane of more extensive dimension, as seen in figure 2.1 [2].

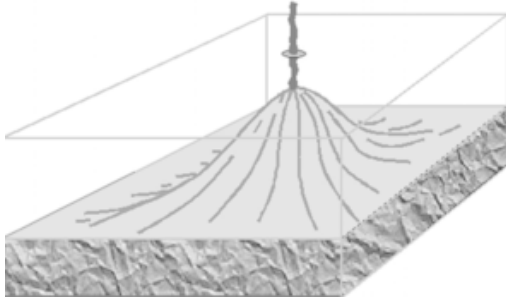


Figure 2.1: Coning in a vertical well[3].

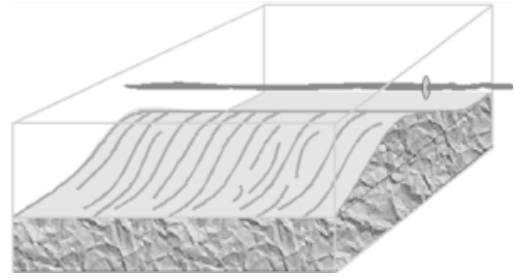


Figure 2.2: Cresting in a horizontal well[3].

In addition, improvements in the critical flow rate of up to a factor of 7 have been reported for horizontal wells in thin oil zones. This improvement is caused by the potential gradients being less severe in the vicinity of a horizontal well than a vertical well [4].

Horizontal wells generally produce more, and more efficiently, than do vertical wells. However, these wells are subject to early water and gas coning toward the heel because of the flow's frictional pressure drop along the horizontal section.

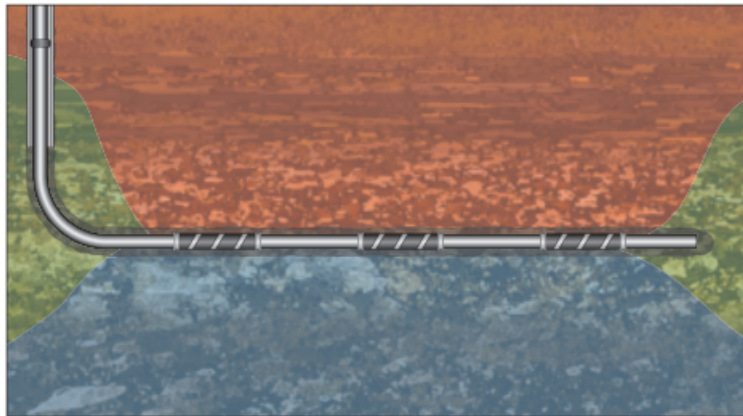


Figure 2.3: Cresting in horizontal well [5].

Cresting is defined as the change in oil-water or gas-oil contact profiles as a result of drawdown pressure during production. Cresting occurs in horizontally or highly deviated wells, as seen in figure 2.3. The phenomenon is affected by both fluid properties and the ratio of horizontal to vertical permeability [6].

In homogenous formations, significant pressure drops occur within the open-hole interval as the fluid flows from the toe towards the heel of the well. The result may be significantly higher

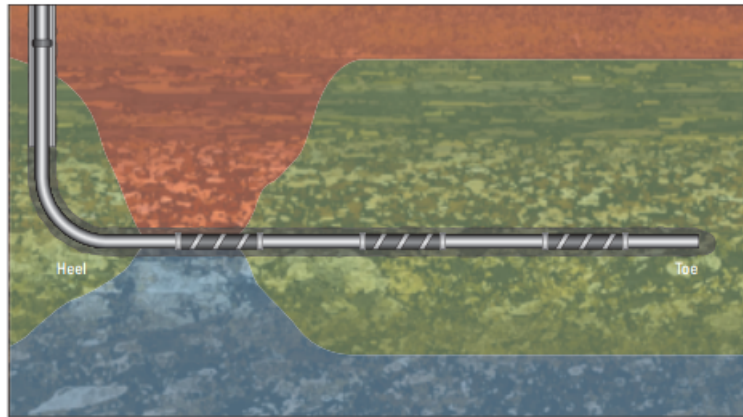


Figure 2.4: Cresting at the heel in a horizontal well [5].

drawdown pressures at the heel of the well. Known as the heel-toe effect, this pressure difference causes unequal inflow along the well path and leads to water or gas coning at the heel, as seen in figure 2.4.

As will always be true in the case for flow systems where actual water coning is possible, the water will be inclined to lie beneath the oil the oil zone, because of its density contrast with respect to the oil. In fact, under usual field conditions when the pay horizon is reasonably homogeneous, the water most frequently enters the well from lower zones. However, even when it enters from intermediate zones it may, in the later life if the well, displace the bottom layers of oil, thus resulting in a system wherein the oil is effectively floating on the water [7].

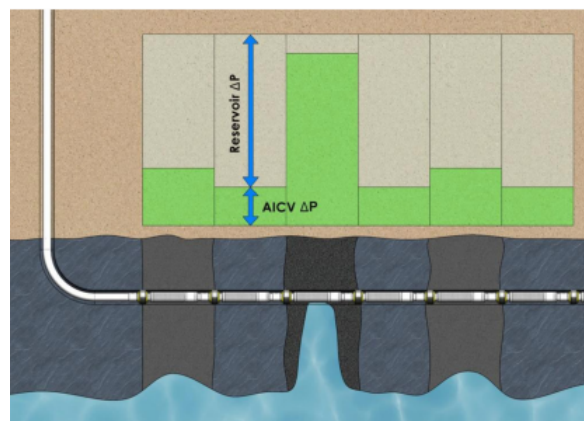


Figure 2.5: Heterogenous reservoir with AICV completion including plot of pressure drops [8].

Oil reservoirs with bottom water drive have the advantage of a high oil recovery due to energy support from the aquifer. However, the encroachment of the water into the producing oil well

caused by the pressure drawdown around the wellbore creates problems over time, see figure 2.5. These problems include water handling and bypass oil [9].

The production of oil and/or gas from a well causes the pressure around the wellbore to drop, inducing a pressure gradient around the wellbore vicinity. A counteracting gravitational force, due to the difference between the oil density and water density, causes the oil-water contact interface to remain stable. However, at a certain critical production rate, the viscous forces due to the pressure gradients around the wellbore become greater than the gravitational forces making the oil-water interface unstable. Consequently, the contact rises up until water breakthrough into the producing well occurs [9].

2.2 Stable Water Coning

For production levels below critical production rates stable stationary water cones may arise. This is seen when the pressure at a given height along the cone interface equals the hydrostatic pressure.

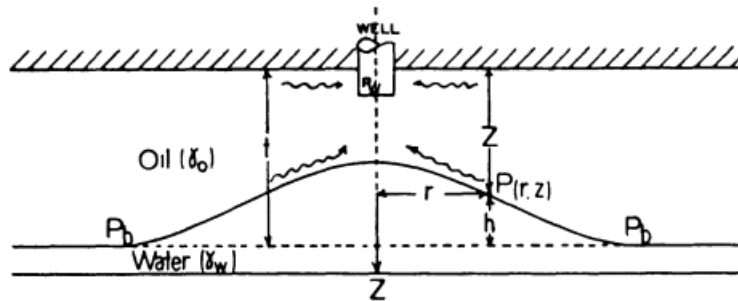


Figure 2.6: Stationary water cone in a vertical well[7, page 144].

Referencing figure 2.6, the following pressure balance can be set up[7]:

$$P_b = h\rho_w g + p(r, z) \quad (2.1)$$

where $p(r, z)$ is defined as the pressure at the oil-water interface on the cone, g is the gravitational constant, and ρ_w is the density of water. Note that ρ_w is expressed as γ_w in figure 2.6.

Equation (2.1) represents a necessary equilibrium condition if the water cone is to be in a static condition.

The critical flow rate can be calculated, however it is complex and dependent on many different factors. This calculation has been carried out for a vertical well by Leif A. Høyland et. al[10]. Høyland's results have since been simulated and plotted by A. Bahadori and A. Nouri in a dimensionless form[11], which can be seen in figure 2.7. The dimensionless radius r_d is given as[11]:

$$r_d = \frac{r_e}{h_t} \sqrt{\frac{k_v}{k_h}} \quad (2.2)$$

where k_v , and k_h is the permeability in the vertical and horizontal direction, h_t is the height of the oil zone and r_e is the exterior radius. It is worth noticing from figure 2.7 that the critical rates have a sudden increase for low values of the non-dimensional radius.

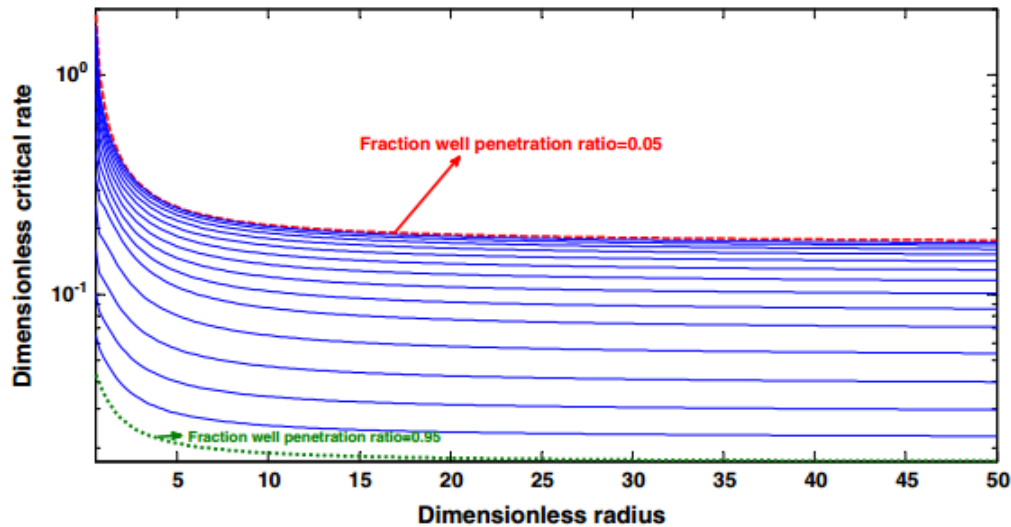


Figure 2.7: Prediction of dimensionless critical rate for high fractional well penetration ratios[11].

Figure 2.8 shows the how the pressure gradients vary in the oil zone (line A), and in the water zone (line B). Line B shows that the only contribution to the pressure gradient in the water zone is the hydrostatic pressure difference, seeing as the cone is in equilibrium. Line A shows that the pressure gradient is very steep near the orifice, due to the velocity gradient and also influenced by the high oil viscosity.

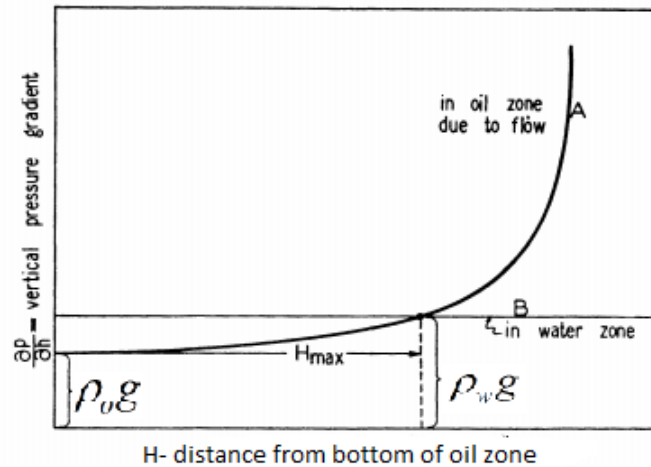


Figure 2.8: Pressure gradient in oil zone vs. water zone [7].

Muskat & Wyckoff describe in detail how there exists a critical height H_{\max} for which the equilibrium coning height becomes unstable, and water rises to the outlet orifice.

The water at the water-oil interface is acted upon by the same pressure gradient acting on the oil, in the immediate adjacent oil zone. Since all flow in the vicinity is directed towards one orifice, the pressure gradients increase quickly near the orifice. In the water zone gravity acts to impose a hydrostatic pressure gradient. Taking into account that the pressure gradients must equal at the oil- water interface, figure 2.8 illustrates the constraint of a maximum H . Any further increase in cone height at this point will cause water to flow into the orifice [7].

2.3 Inlet Control Devices

Inlet control devices are installed in modern wells to mitigate the problem of cresting/coning in the reservoir. ICD's are demonstrated to improve overall oil recovery, and less water production. The ability to optimize results from standard configurations through better reservoir fluid management has been greatly enhanced by the development of remotely operated inflow control valves and chokes. These devices enable engineers to adjust flow from individual zones that are over- or under pressured or from those producing water or gas that may be detrimental to overall well productivity [5].

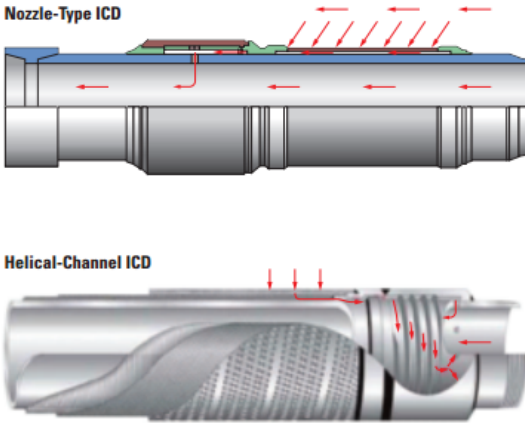


Figure 2.9: ICD designs[5, page 31].

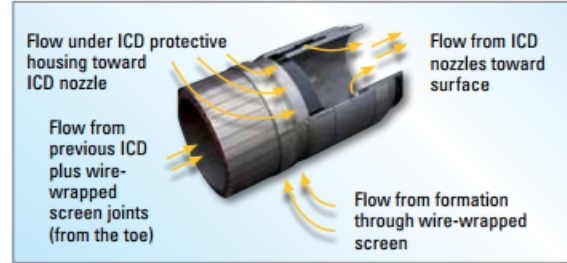


Figure 2.10: Flow schematic in nozzle-type ICD [12].

Figures 2.9, and 2.10 display the two most common ICD designs, the nozzle-type ICD and the helical channel ICD. Fluids from the formation flows through multiple screen layers mounted on an inner jacket, and along the annulus between the solid base pipe and the screens. It then enters through a restriction in the case of nozzle- and orifice-based tools for the nozzle-type ICD, and a tortuous pathway in the case of helical-type ICD [5].

When fluid enters the nozzles, the potential energy is transformed into kinetic energy, which is absorbed in the main flow through the base pipe, thus resulting in a pressure drop between the annulus and the tubing, as described by Bernoulli's equation. The pressure drop over the nozzle is given by [13]:

$$\Delta P_N = C_u \frac{\rho v^2}{2C_v^2} \quad (2.3)$$

The pressure drop through the sand screen is described by Darcy's law[13]:

$$\Delta P_F = \frac{\mu L}{k} \left(\frac{q}{A} \right) \quad (2.4)$$

where ρ is the fluid density, v is the fluid velocity, whilst C_u & C_v are constants determined by the nozzle geometry.

Different nozzle sizes are available, making it possible to design the ICD completion to the required well geometry and flowrate. The ICD nozzle setting can be preset, or alternatively, the nozzle setting may be performed on the pipe deck [9].

The main challenge facing ICD's is the changing conditions of the reservoir with respect to time. The harsh conditions in the well makes electronic devices unwanted. The ICD placement is designed to eliminate the heel-toe effect and obtain a uniform production rate along the well. However, the relationship between the pressure drop and the flow rate for the well is complex and highly non-linear. Reduction in the reservoir pressure changes the relative flow through the different ICD's. Without any control systems the depletion of the reservoir may therefore still cause water coning at later times in the production[14].

To avoid water flowing in the pipe annulus, zone isolation is required in the well completion. This is done by installing packers at specified intervals. One or more ICD's can be placed in each zone depending on the pressure distribution desired at the well. Often several ICD's are put in the zones near the toe of the well, and one or few near the heel. The reason for this is as explained in the previous sections, higher cumulative flowrates at the heel induce a higher local pressure drop. Placing too many ICD's in this zone may be counterproductive, as cresting will occur rapidly.

A modern AICD design is the AICV, as shown in figure 2.11. The autonomous inflow control valve has the feature to distinguish between fluids based on fluid properties as viscosity and density. The design is adapted to the requirements in the relevant field. Several designs are available on the market. They all function by the same key aspect, namely the capability to choke for less viscous fluid after breakthrough [8].

In heterogeneous or fractured heavy oil reservoirs, it is crucial to stop or choke water when breakthrough occurs. Robust inflow control that can choke back and/or close local water producing zones has the potential to increase the oil recovery significantly compared to standard ICD's [8].

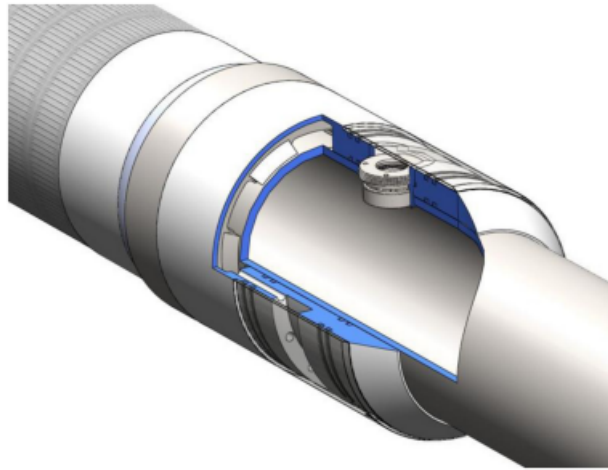


Figure 2.11: AICV design cut open [8].

One such design is the AICV technology, based on the difference in the pressure drop in a laminar flow restrictor compared to a turbulent flow restrictor. From dimensional analysis, pressure-drop relations (2.5), and (2.6) are put forth. U_b , is here designated as a bulk velocity.

$$\Delta P_{laminar} \propto \mu U_b \quad (2.5)$$

$$\Delta P_{turbulent} \propto \rho U_b^2 \quad (2.6)$$

Figure 2.12 demonstrates the implications of the above dimensional analysis. In laminar conditions, the pressure drop is proportional to the viscosity. This implies much greater pressure losses for the viscous oil than for less viscous media such as water or gas. In the turbulent regime, pressure drop is independent of the fluid viscosity, and proportional to the velocity squared, resulting in a much lower pressure drop for heavy oils.

When a low-viscous fluid like water flows through the laminar restrictor the pressure drop will be lower than compared to in oil flow, resulting in a higher pressure at point B. This higher pressure activates a piston that effectively shuts off the flow. It is an autonomous process in that it uses the forces corresponding to the pressure differentials to move the piston. The surface area of either side of the piston is therefore a key design parameter depending on fluid properties and operational flow rates.

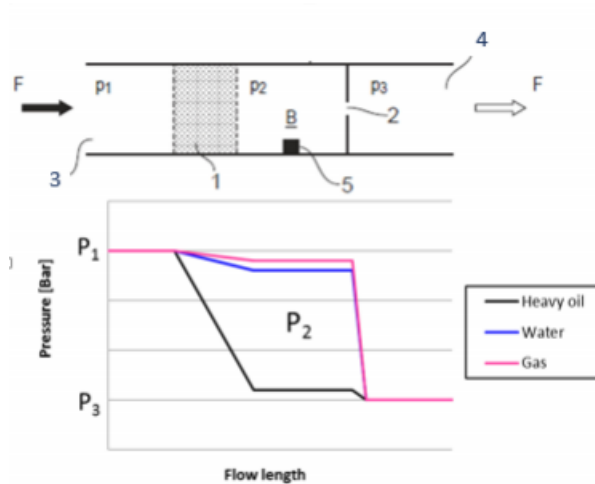


Figure 2.12: Laminar-and turbulent restrictor in series vs. pressure drop [8].

Aakre et al. have run experiments suggesting that the water cut needs to be very high before the piston will plug the flow. For the AICV design tested on, he reported a lower limit of 98% water cut [8].

2.4 Water Coning in Annular Geometry

The velocities into the pipe geometry are relatively small, and thus the flow into the housing is likely to be stratified. Over the joints the valves are arbitrarily oriented as in figure 2.13. This means that valves in the higher regions are exposed to oil while the ones in the lower region may be exposed to water[15].

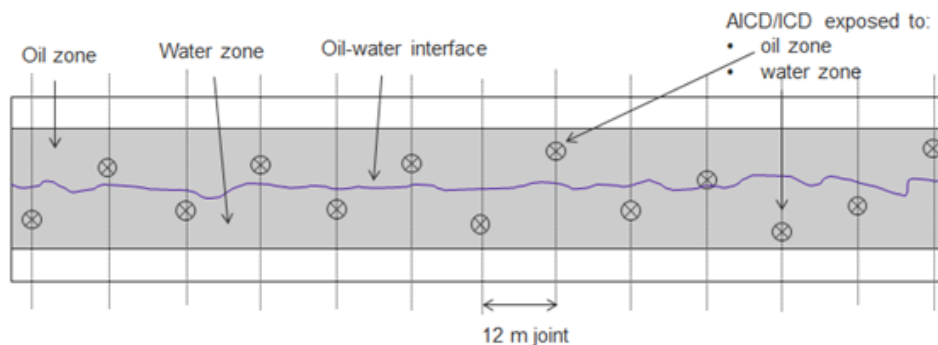


Figure 2.13: The stratified pattern of the fluid mixture with valves arbitrarily oriented along the pipe[15, page 7].

The pressure drop of oil flowing through the ICD/AICD is greater for oil than for water. The difference in pressure drop for water and oil can lead to coning phenomenon also in the piping annulus. If the production is above a certain critical rate water can reach as high as the ICD/AICD, introducing a water cut in the production, and lowering overall production efficiency.

The governing physics is in principle the same as described in section 2.2, however the geometry is slightly more complex, and from a piping axial point of view the ICD/AICD can be placed at different circumferential positions. Moreover, a frictional pressure term will also appear due to the flow through the annulus. Pressure gradient profiles near the orifice of the ICD will necessarily be different for varying circumferential positions, in turn affecting the flow behavior.

The pressure terms in the housing would then be the frictional pressure drop, the acceleration pressure drop, and the gravitational hydrostatic pressure.

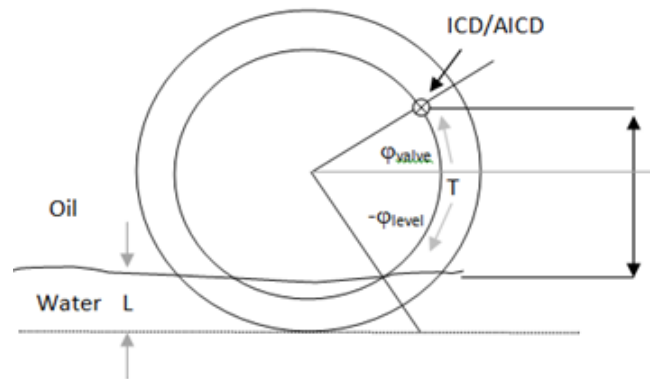


Figure 2.14: Cross-sectional geometry of production piping at valve position[15, page 11].

The ratio between the outer pipe diameter and the annulus gap, D/δ is the order 50-100. Additionally, the velocities are relatively small, the flow is stratified and laminar except in close proximity to the ICD orifice. Thus the velocity profile in the annulus may reasonably be approximated as that of laminar flow between two parallel plates.

The frictional pressure loss is due to the shear stress acting on the annulus walls and can be assessed using the Darcy friction factor formulation:

$$\left(\frac{\partial P}{\partial T}\right)_f = f \frac{1}{2D_h} u_{ave}^2 \rho \quad (2.7)$$

D_h signifies the hydraulic diameter, and u_{ave} the average velocity. The friction factor is set equal to what is defined in equation (2.8). This constitutes the Darcy friction factor valid for flow between parallel plates, following the previous arguments. The hydraulic diameter is thus also set to 2δ , which constitutes the hydraulic diameter between two parallels plates. The friction factor for laminar flow between two parallel plates is given by Frank White as [16] :

$$f = \frac{96}{Re_{D_h}} \quad (2.8)$$

A uniform inflow to the ICD is assumed, and the velocity can be expressed as:

$$u_{ave} = \frac{Q}{2\pi\delta T} \quad (2.9)$$

The variable T , constitutes a given distance from the center of the outlet orifice, as seen in figure 2.14. When equations (2.7), (2.8), and (2.9) are combined the frictional pressure drop is calculated by integrating from the water-oil interface to the entrance of the orifice:

$$\Delta P_f = \frac{6\mu Q}{\pi\delta^3} \ln\left(\frac{T_i}{T_o}\right) \quad (2.10)$$

Here T_i , and T_o signifies the distance from the center of the orifice to the entrance of the orifice, and the distance from the center of the orifice to the tip of the water cone, respectively. The pressure difference due to gravity arises due to the contrast in density between oil and water. Because of the annulus geometry the curvature may be addressed when computing the gravitational pressure term, and is thus computed as:

$$\Delta P_g = g(\rho_w - \rho_o)(\sin\varphi - \sin\varphi_{level}) \frac{D}{2} \quad (2.11)$$

The correct formulation for the pressure drop due to accelerating fluid is easiest seen from the acceleration terms in the Navier-Stokes equation :

$$\left(\frac{\partial P}{\partial T}\right)_a = -\rho u \frac{\partial u}{\partial T} \quad (2.12)$$

When equation (2.9) is differentiated with respect to T , and inserted into equation (2.12), equation (2.13) is obtained after integrating from the tip of the water cone to the entrance of the outlet orifice:

$$\Delta P_a = \frac{\rho}{8} \left(\frac{Q}{\pi \delta}\right)^2 \left(\frac{1}{T_o^2} - \frac{1}{T_i^2}\right) \quad (2.13)$$

As previously discussed the added static pressure of the water cone must balance the pressure loss from friction and acceleration in order to sustain a stagnant water cone:

$$\Delta P_g = \Delta P_{f,o} + \Delta P_{a,o} \quad (2.14)$$

$$0 \leq \frac{\Delta P_{f,o} + \Delta P_{a,o} - \Delta P_g}{\Delta P_g} \quad (2.15)$$

Analogous to a critical reservoir coning height as explained by Wykoff, there exists a critical coning height for any given set of flow conditions for which a stagnant cone can no longer be sustained in the annulus geometry. For flow rates surpassing the critical flow rate the water jumps up to the outlet orifice [7].

2.5 Statoil Input Data

A typical lower completion design is shown in figure 2.15. All of the following data in this section is given from Statoil[15]:

- The total length of the horizontal well: 1271 [m].
- Number of isolated zones: 6, each of around 200 [m] isolated from each other.
- Number of joints: 6 with length of 12 [m]. Each joint includes one or more ICD's/AICD's.

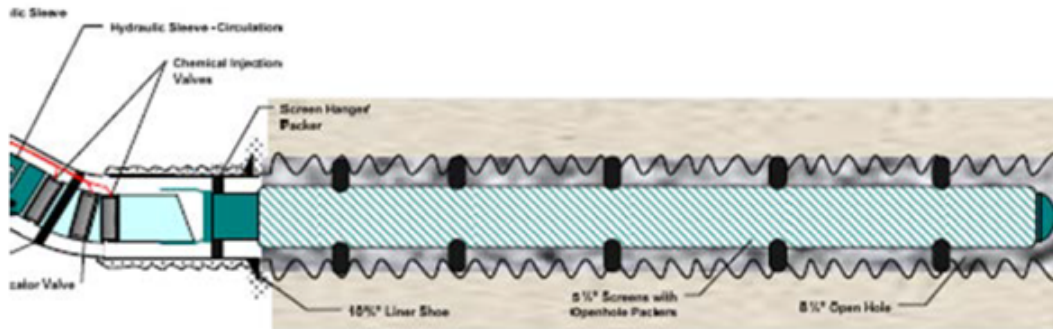


Figure 2.15: Lower completion design for a horizontal well[15, page 14]

Several geometries can be used for the housing of the base pipe and ICD/AICD. Two such geometries are presented in the Statoil document as design 1, figure 2.16, and design 2, figure 2.17[15].

Statoil's AICD have an approximately symmetric inflow into the valve. Both designs have a outer diameter of 5.5" for the base pipe and utilizes two ICD's/AICD's per joint. The annulus gap, and the distance from the screen area to the valve intake is:

- Design 1: $L \sim 180$ [mm], Annular gap $\delta = 7.11$ [mm]
- Design 2: $L \sim 265$ [mm], Annular gap $\delta = 3$ [mm]

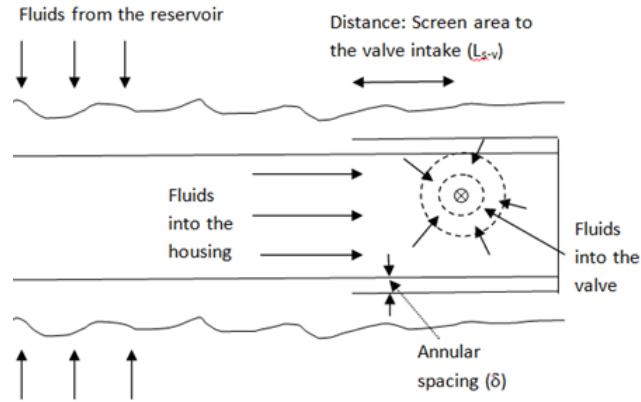


Figure 2.16: Geometry of housing design 1 [15, page 5]

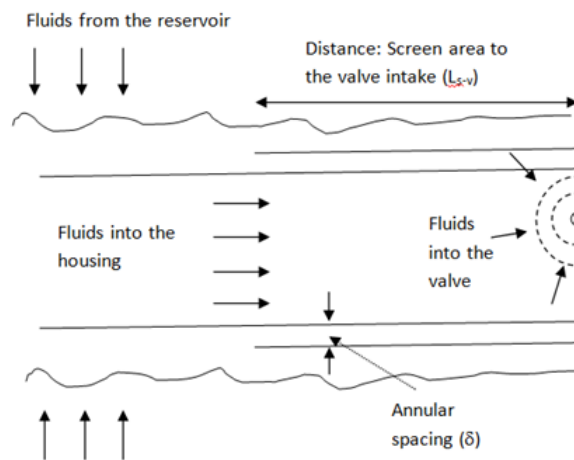


Figure 2.17: Geometry of housing design 2 [15, page 5]

The geometries for the ICD/AICD in the two designs is also different:

- Design 1:
 - Outlet arrangement is not in flush with the inner wall.
 - Flow area out of AICD = $3.3338 \cdot 10^{-4} \text{ [m}^2\text{]}$
- Design 2:
 - Outlet arrangement in flush with the inner pipe wall.
 - Total cross sectional area = $2.2027 \cdot 10^{-4} \text{ [m}^2\text{]}$

The total oil production rate is 3500 [Sm³/d], which corresponds to a rate per joint of 1.52 [Sm³/hr]. The liquid properties are:

- Oil density: 935 [kg/m³]
- Oil viscosity: 67 [cp]
- Water density: 1031 [kg/m³]
- Water viscosity: 0.72 [cp]

Chapter 3

Experimental Facility

This chapter contains a detailed description of the laboratory setup and experimental procedures. In this manner the experiments can easily be recreated and the work resumed in the future.

3.1 Experimental Setup

3.1.1 Experimental rig

The rig was designed by Egor Shevchenko during his project and master thesis. It was built to be a simplified, yet effective, setup based on the input data from Statoil. Some modifications were made on the old setup to adjust the rig to the experiments for this thesis. New base pipe walls were made, and a second flow valve was installed. The rig consisted of:

- Tank filled with oil and water
- Base pipe wall with an orifice
- Flexible tube
- Drainage valve

- Downstream flow valve
- Storage tanks for the oil and water
- Electrical pump for pumping the oil from the storage tank to the experimental tank
- Tray to avoid possible oil spills to the floor

The total rig can be seen in figure 3.1.

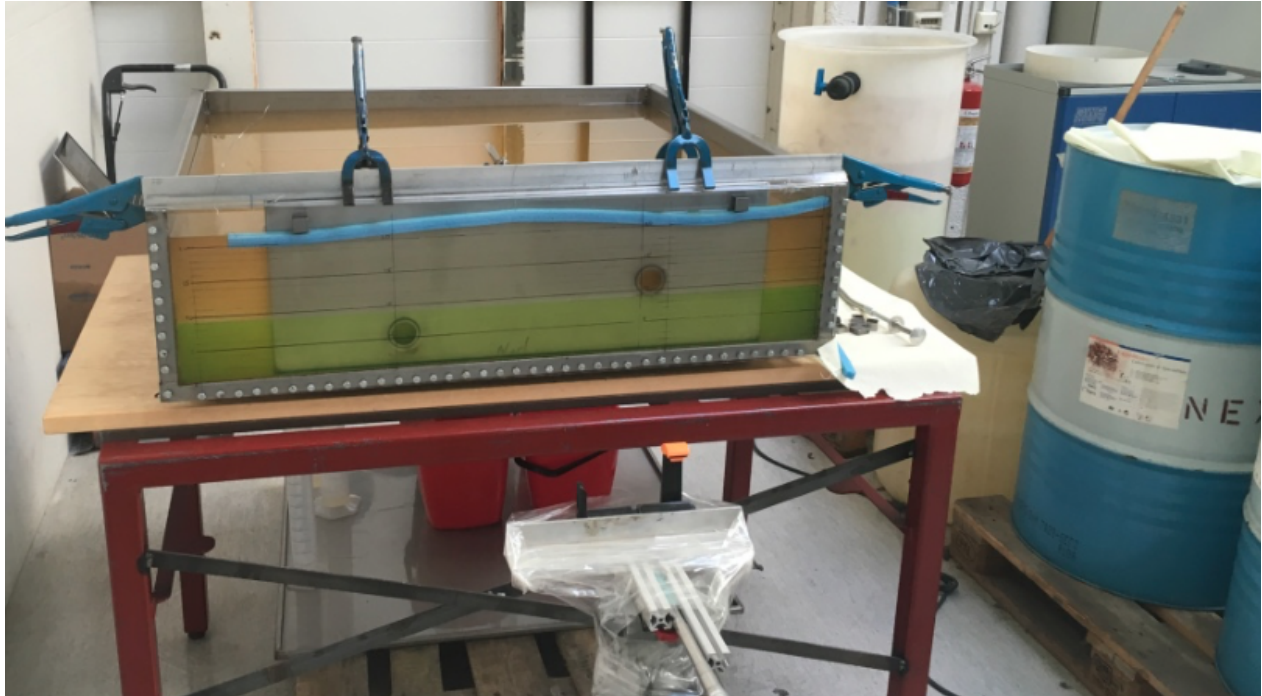


Figure 3.1: The total rig used for the experiments.

The tank was dimensioned to be 1x1 meter with a liquid height of 220 [mm], plus a 30 [mm] safety margin. The liquid height was calculated to match the base half-pipe wall perimeter for a 5.5" pipe by the 2D-principle made by Shevchenko[17]. In essence this principle was to fold out the annular geometry, as seen in figure 3.2. Consequently, this geometry approximation simplified the building of the tank and visualization of the experiments without eliminating any of the possible flow patterns.

To be able to operate with different annulus gaps in the various test, the base pipe wall was made movable. In figure 3.2 the movable plate corresponds to the base pipe wall while the housing wall corresponds to the transparent front wall which was stationary. Some modifications from

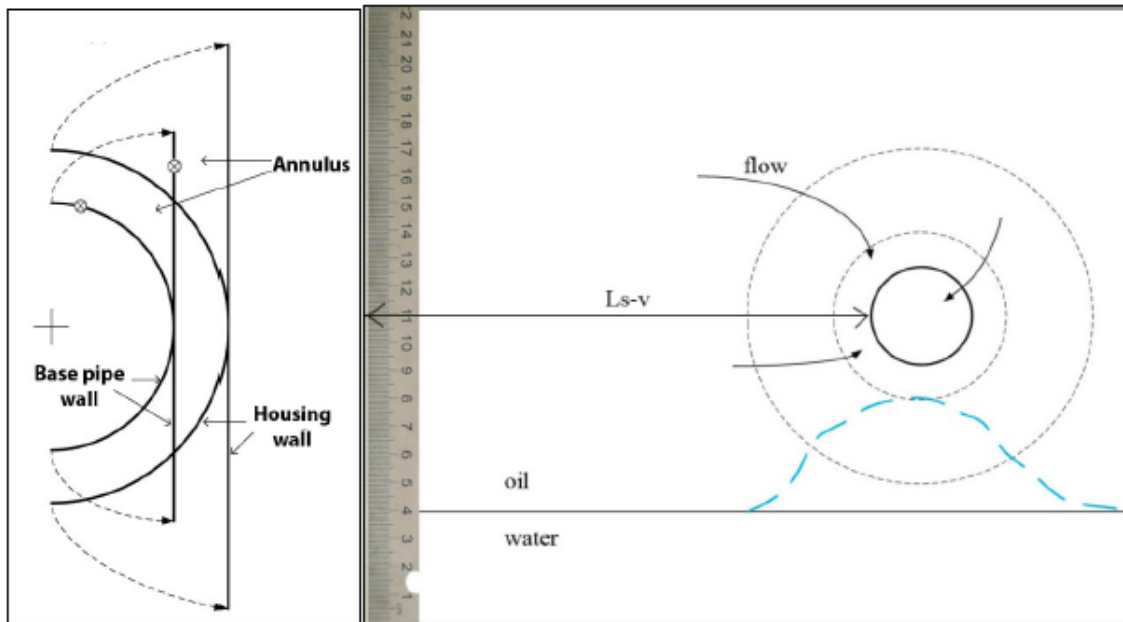


Figure 3.2: The 2D-principle[17, page 22].

the old setup were made. In the new setup all of the experiments were done with a centered plate. In Shevchenko's experiments the plate was placed in one corner with inflow from only one side. To obtain more realistic conditions compared to the ones used by Statoil, a symmetric inflow was desirable. This was made possible by designing a new symmetrical plate, which was a modification of Statoil's design 1 in figure 2.16. The new design required a new solution to keep the plate in the wanted positions during the experiments. A movable beam attached to the top of the tank by clamps was used to solve this problem. A simple figure showing the tank with the most important components can be seen in figure 3.3.

The annulus was set by using metal pieces, as seen in figure 3.5, at the bottom of the tank. As can be seen from figure 3.6, the transparent front wall, which corresponds to the housing wall in 3.2, was bended at the top. To keep a constant distance between the two walls all the way from top to bottom, magnets and custom-made metal pieces, as displayed in figures 3.4 and 3.5, were used to control the distance. Clamps were used to attach the walls together. A roof was also placed at the top attached to the metal pieces to avoid the possibility of air coning. This roof was made of weather stripping of foam and was customized to the different annulus gaps. The whole wall-system can be seen from figure 3.7.

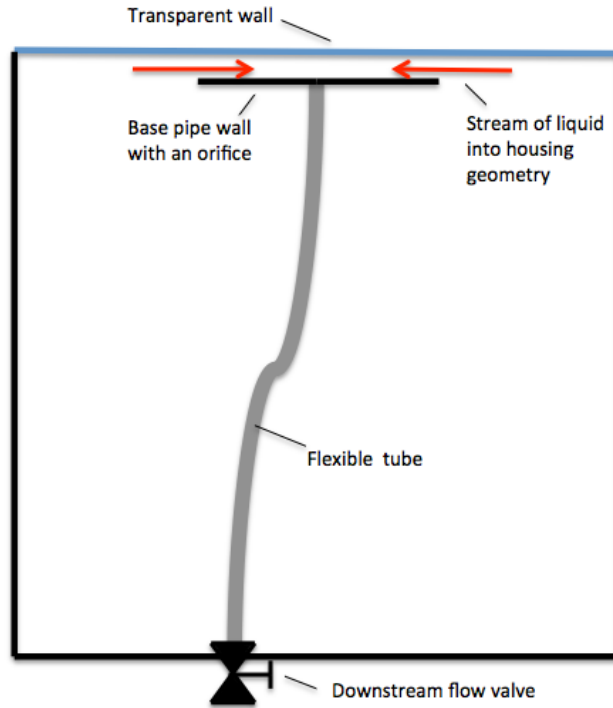


Figure 3.3: A top-side view of the tank with the key components.



Figure 3.4: Custom-made metal pieces at the top of the tank which are attached with magnets to the plate.



Figure 3.5: Custom-made metal pieces at the bottom of the tank.

3.1.2 Geometry of housing plates

Three different plate designs were constructed, and can be seen in figure 3.8, 3.9 and 3.10. All of the plates were made by the same principles and main dimensions. The fluid was flowing through orifices with diameters of 36 [mm] via flexible tubes through perforations in the other end of the tank. The diameter was equal to the one used by both Shevchenko and design 2 from Statoil. From the end of the tank the fluid flowed through downstream flow valves and



Figure 3.6: The bended transparent wall.

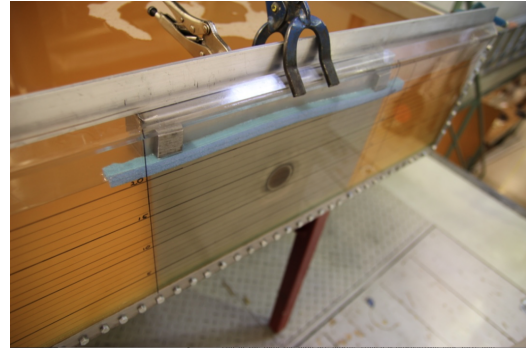


Figure 3.7: The total solution of keeping the wall distance constant with a roof to avoid air coning.

into measuring buckets. The liquid flow was only driven by the liquid head in the tank causing enough pressure difference to obtain the wanted flow rates. These flow rates were controlled by the downstream flow valves which were controlled with valve positions ranging from 1 to 6 as seen in figure 3.11. When changing the experimental conditions by draining out water, the draining valve was used, also shown in figure 3.11.

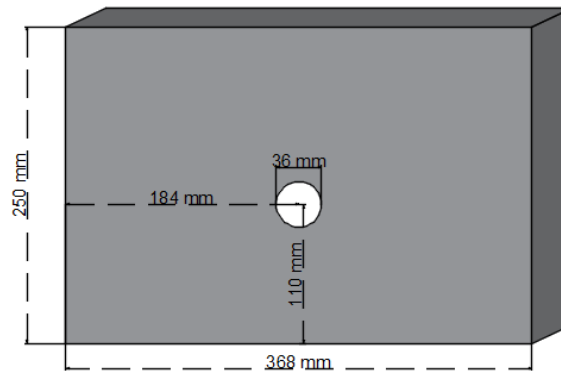


Figure 3.8: Geometry of improved single orifice housing plate.

To avoid any instabilities in the liquid tank causing uneven flow conditions and disturbances there was no refilling of the tank during an experimental run. Even though this would give a variable head causing changes in the flow rate, this was found to be the best and most realistic simulation of a reservoir inflow. To maintain a reasonable constant flow rate the liquid level should not drop more than 1 [cm] during the experimental run corresponding to approximately 10 litres.

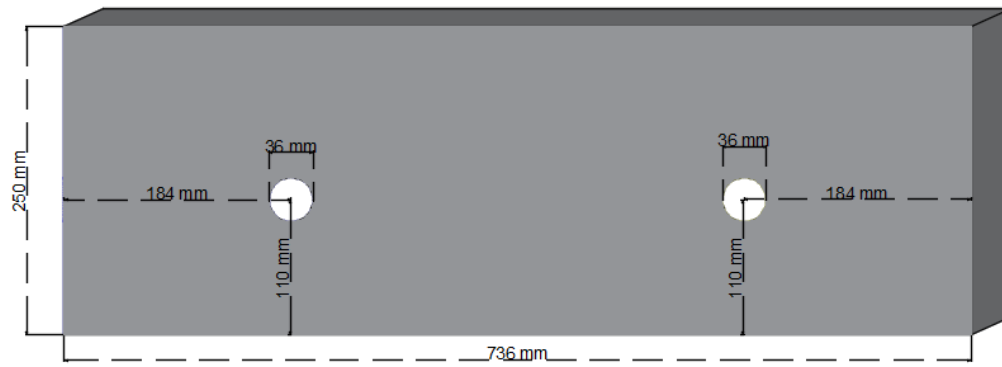


Figure 3.9: Geometry of housing plate with two holes at equal height.

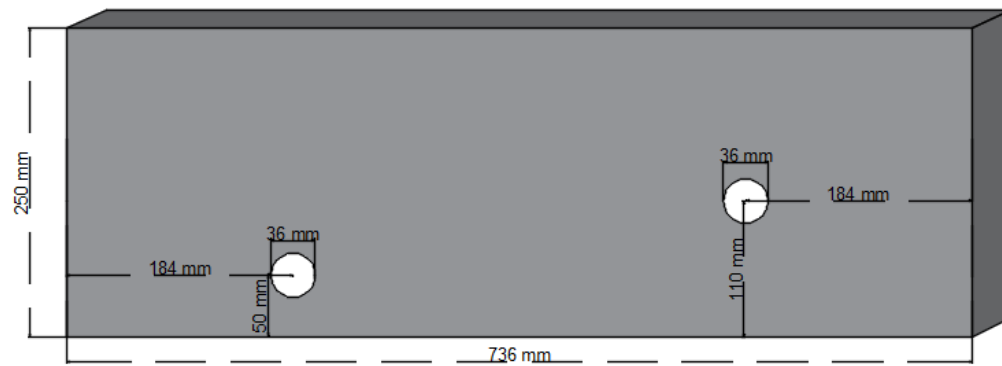


Figure 3.10: Geometry of housing plate with two holes at different height.



Figure 3.11: Draining valve (left) and downstream flow valve (right).

3.1.3 Oil properties

Two different oils were used during the experiments: Nexbase 3080 and Marcol 52. Nexbase was chosen due to its similarity with the oil given by the Statoil data. Marcol 52 was chosen to utilize a less viscous oil, to assess how this would affect the water coning. Both of the oils were tested in a viscometer to check if the given data was correct, as well as to find the viscosity for Nexbase at 20 [°C], which was the temperature in the tank. The properties of the oils can be seen in table 3.1.

Table 3.1: Data of the oils used during the experiments.

Oil	Viscosity at 20°C, [cP]	Density at 15°C, [kg/m ³]
Nexbase 3080	83	845
Marcol 52	12	828

To get a good visual interface between the oil and water, Fluorescein-Natrium (C.I. 45350) was added to the water. This gave the water a green color that helped distinguished the two liquids from one another.

3.2 Preparations

Before the experiments could take place the setup had to be approved. To get the approval the setup had to be in accordance with the safety regulations stated by the department at NTNU. Since the rig has been built and used before, a risk assessment report had already been made by Shevchenko[17]. The report had to be renewed by date before it was approved. All experiments were done within the operation protocols given in the risk assessment report.

When the rig was remounted a leak test was done to control that it remained watertight. The leak test was done by filling the tank with water and no leakages were observed. Water was chosen as test medium because a water spill would be less problematic than an eventual oil spill. Also the drainage valve and downstream flow valve were tested and both functioned properly.

To obtain a general knowledge about the flow rates, two tests were done prior to the experi-

ments:

- Flow rate as function of downstream valve position.
- Flow rate as function of liquid head.

In oil production pipe lines oil is the dominating liquid running through the pipes and therefore both tests were done using oil as the liquid medium.

The flow rate at given valve positions can be seen from table 3.2. In the data from Statoil the production has a flow rate of approximately 6.2 [l/min]. This translates to a valve position between 2 and 2.5 for both oils. This range of flow rates is thus of importance, and it was decided to adding a valve position of 2.25 to the experiments to have a finer step for the flow rate in this range.

Table 3.2: Flow rate versus valve position for Nexbase 3080 and Marcol 52.

Valve position	Flow rate [l/min]	
	Nexbase 3080	Marcol 52
1	0.37	0.62
1.5	2.00	2.51
2	4.66	5.28
2.5	9.04	9.87
3	12.07	13.88
3.5	17.87	20.11
4	23.58	27.46
4.5	27.88	34.91

To maintain identical conditions during the experimental runs it was important to keep the head close to constant. In the preface of the experimental phase, tests were conducted to investigate the flow rate as a function of the liquid head. The tests showed that for both Nexbase 3080 and Marcol 52 the dependence between the head and the flow rate is quite significant. However, as seen in figure 3.12, the concept by Shevchenko of allowing at most a 1 [cm] drop was reasonably good, and it was decided to apply it in this project. This test also displayed a weakness in the setup. Since the downstream flow valve was continuous and not stepwise it was difficult to repeatedly obtain the exact same valve position. This resulted in different flow rates for tests

that should produce the same results. Figure 3.12 indicates discrepancies in flow rates for a given head. It is therefore important to be careful when comparing results as function of the valve position.

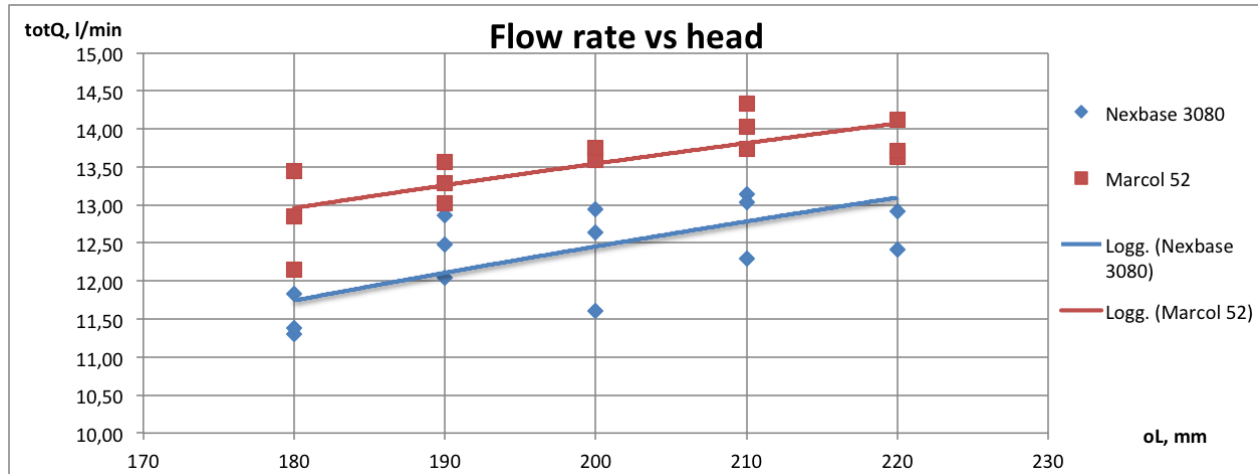


Figure 3.12: Flow rate as a function of the liquid height in the tank.

Before being able to run the experiments in a proper manner three additional tests had to be done:

- Test the influence of the metal pieces at the bottom of the tank during the experiments.
- Test the importance of a roof between the housing wall and the base pipe wall.
- Tests to determine the running time of one experimental run.

Metal pieces were needed to set the annulus gap between the base pipe wall and the transparent wall. Shevchenko kept the metal pieces in place while running the experiments. This was done to make sure that the annulus length was kept constant at all times. The problem with this approach was that the pieces were blocking the inflow of water, especially at low water levels. From figure 3.13 it is clear that the water cut, the percentage of water in the total drained mixture, is significantly lower with the metal pieces in place. Figure 3.14 shows how the water is blocked from flowing into the annulus. These results clearly indicate that the metal pieces affect the inflow. Initial testing indicated no movement for the plates without the metal pieces, hence the experiments could be conducted without them.

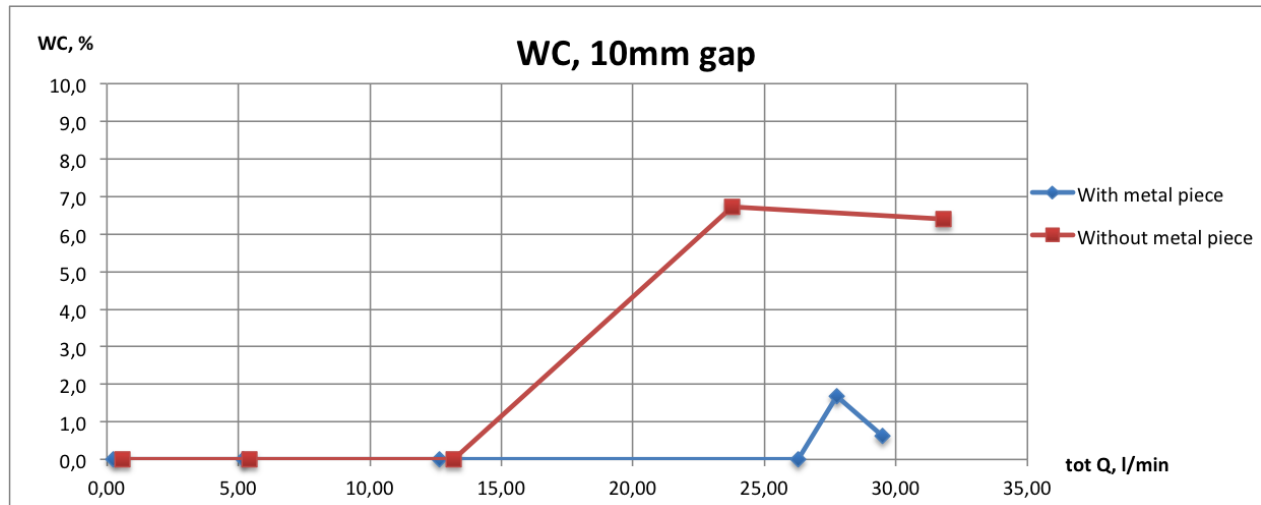


Figure 3.13: Water cut with and without metal pieces at the bottom of the annulus for water level of 10 [mm] and Nexbase 3080.

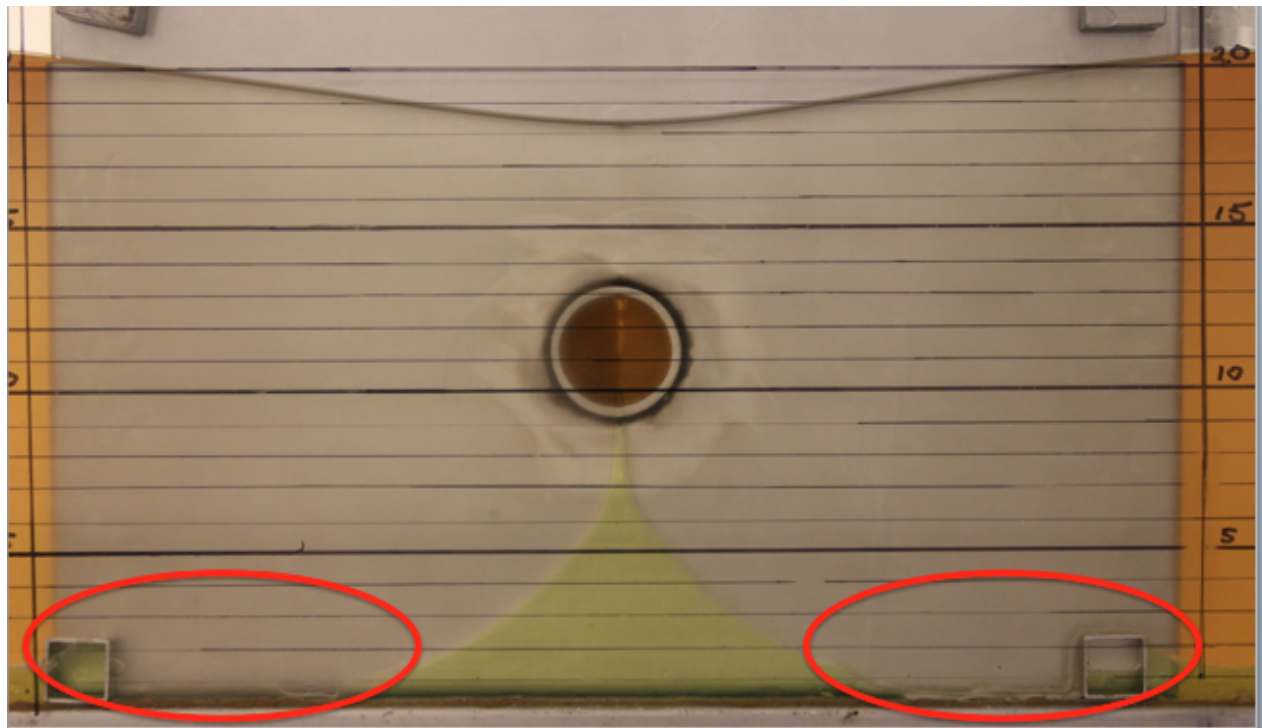


Figure 3.14: Metalpieces blocking the inflow of water.

A simple test was done to check the need of a roof. Employing an annulus gap of 5 [mm] and a water level of 10 [mm] it was clear that the air cone would break into the orifice at high flow rates. Screen shots from the video recordings, figure 3.15 and 3.16, demonstrate the contrast in flow behaviour with a roof and without, respectively. Further investigations with flow rates,

water jump, and water cut did not display any significant difference with or without a roof other than when air intake into the orifice was present. Thus it was decided to run the experiments with a roof to avoid potential air intake.



Figure 3.15: Test with roof at $\delta = 5$ [mm], WL = 10 [mm] and valve position 4.

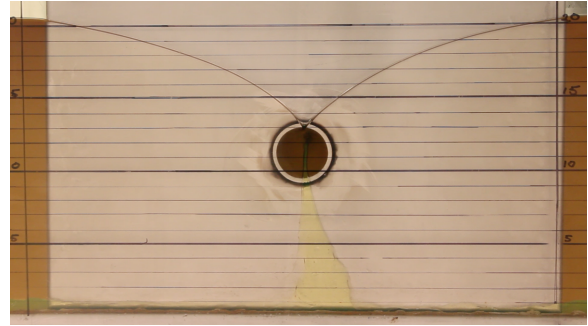


Figure 3.16: Test without roof at $\delta = 5$ [mm], WL = 10 [mm] and valve position 4.

To have the best possible basis for comparison between the experiments it was decided to make guidelines for running time. The main factors deciding the running times were:

- **Do not exceed a maximum drain off of 10 litres.** This was highly important and should not by any means be exceeded. The 10 litres includes the liquid that is measured as well as the liquid that was drained to reach steady state. This was important due to the change in flow rate with shifting liquid head which would compromise the steady state solution.
- **Get as long running time as possible to minimize the error due to manual timing.** It was assumed that every experimental run would have a timing error of ± 0.2 seconds due to unsynchronised start/stop of the timer with start/stop of filling the measuring bucket.
- **Avoid change of measuring cup if possible.** Due to the high viscosity in the oil it sticks to the wall and it was therefore hard to empty the measuring bucket or cup completely. Measurements showed an error of ± 30 [ml] for the 10 [l] measuring bucket and ± 10 [ml] for the 1000 [ml] measuring cup. Also every single reading of volume had a reading error of roughly ± 2.5 [ml]. This error would as well as leading to an uncertainty in the flow rate, lead to an uncertainty in the water cut since oil and not water stuck to the wall.

In the case of one orifice, for the higher flow rates the running times in table 3.3 were restricted

by the 10 litres limit. This means a maximum of 10 litres could be drained out during one experimental run. However, the system was observed to need around 3-4 litres before it reached steady state and the measurements could begin. With adding a safety margin of 1 litre, this left a total of 5 litres of liquid which could be used for measuring the flow rate. The error of the volume measurements would be smallest for a volume of maximum 1 litre because of the avoidance of the 10 litres measuring bucket. If one would exceed this litre the error would decrease with increasing volume having a best possible error of $\pm 1.85\%$ for 5 litres. The timing error would decrease for longer running times as the uncertainty of ± 0.2 seconds would be smaller compared to the total running time.

The best solution to minimize measuring errors, resulted in the running times as presented in table 3.3. Here the valve position 1 and 1.5 were restricted by 1 litres while the rest were restricted to about 5 litres.

Table 3.3: Approximate running time for each valve position for one orifice

Valve position	Running time [s]	
	Nexbase 3080	Marcol 52
1	≈ 150	≈ 90
1.5	≈ 30	≈ 23
2	≈ 60	≈ 55
2.25	≈ 45	≈ 41
2.5	≈ 30	≈ 30
3	≈ 22	≈ 20
3.5	≈ 15	≈ 14
4	≈ 12	≈ 10
4.5	≈ 10	≈ 8

In the case of two orifices it was impossible to keep within the restriction of 10 litres for all flow rates. The two valves had to be manually set and 10 litres would be drained out to only achieve steady state. To partly compensate for this the initial liquid level was set a little higher for the experiments with two outlets. Because of these challenges it was decided to prioritize a short testing period and the running times for two holes can be seen in table 3.4. Valve position 1 was not used as the second downstream flow valve started at a position of 1.5. Valve position 4.5 was omitted because of its high drain out of liquid.

Table 3.4: Approximate running time for each valve position for two orifices

Valve position	Running time [s]	
	Nexbase 3080	Marcol 52
1.5	≈ 25	≈ 20
2	≈ 23	≈ 20
2.25	≈ 17	≈ 15
2.5	≈ 12	≈ 10
3	≈ 8	≈ 7
3.5	≈ 6	≈ 5
4	≈ 5	≈ 4

3.3 Experimental Procedure

To obtain a good study of the water coning phenomenon, a list of variables affecting the flow was prepared. Two considerations were important when deciding the operational principles. First of all it was desired to make the setup as realistic as possible compared to real flow conditions in a well. Secondly, it was of interest to use a setup similar to that of Shevchenko in order to have a sound basis of comparison.

The variables and their control methods during the experiments are shown in table 3.5, and a list of key observables for the experiments can be seen in table 3.6.

Table 3.5: Operational variables.

Variables	Control method	Range
Distance from water interface to the tank bottom, WL	By pumping/draining fluids in/out	Water level from 10 - 110 [mm]
Annulus gap, δ	Moving the base pipe wall	5 - 25 [mm]
Total flow rate, Q	Controlling the downstream flow valve	Valve position: 1-5 Flow rate: 0 - 35 [l/min]
Viscosity, μ	Changing oil	12 and 83 [cP]
Plate geometry	Shift between different plates	One hole, two holes with equal height and two holes with different height

Water cut is the percent-wise fraction of of water in the measured liquid. The water jump is the height the water rises from its initial level.

Table 3.6: Key observables during the experiments.

Observable	Method
Water cut, WC	Volume of water vs. total volume
Water jump, WJ	Video analysis
Water flow rate, WQ	Manual timing and measuring of volume
Oil flow rate, OQ	Manual timing and measuring of volume
Total flow rate, Q	Manual timing and measuring of volume

The experimental procedure can be divided into seven different stages:

1. Getting started from standby mode.
2. Running the experiments.
3. Changing the annulus gap.
4. Changing the water level.
5. Changing the plate geometry.
6. Changing the oil.
7. Packing the setup back to standby mode.

1. Getting started from standby mode.

Getting started

- Post the "Experiment in progress sign"
- Remove the cover from the tank and the measuring buckets
- Set up the film camera

Because of the few risks related to the oil, it was decided for reasons of simplicity not to empty the tank after every experimental day. To keep the oil as clean as possible, a cover was placed over the tank in stand-by mode as well as over the oil drum and measuring buckets. Thus, the oil was shielded from dust and particles. Figure 3.17 shows the rig before and after the "getting started" stage.

2. Running the experiments.

All of the experiments were done in the exactly same manner to get equal conditions for every experimental run. Since the experiments considered the steady state solution of water coning, it was important to define a sufficient standard of measuring liquid and time.

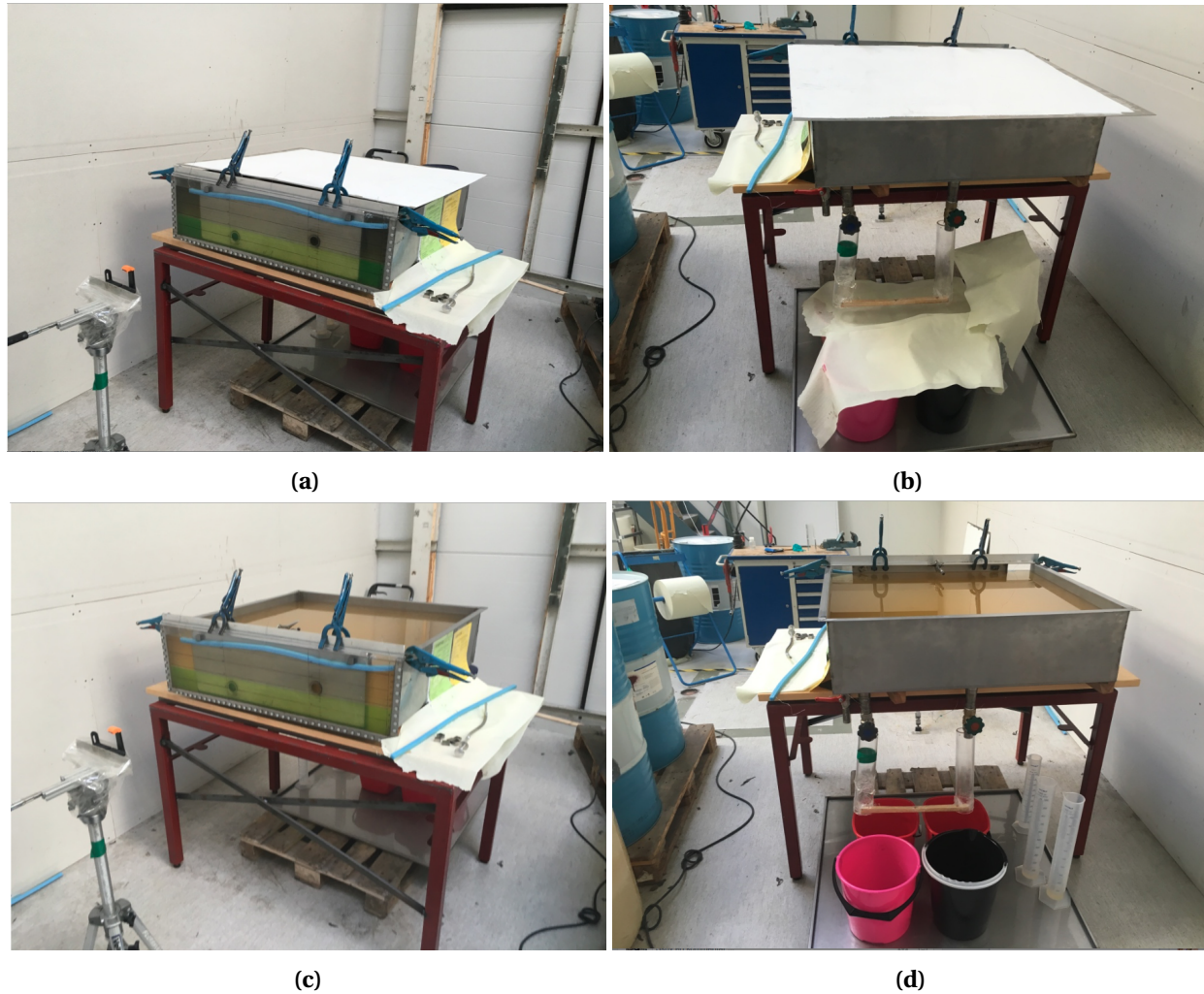


Figure 3.17: Figure (a) and (b) shows the rig in standby mode while (c) and (d) shows the rig in operational mode.

The best solution found was a "two-bucket system". In this system one bucket was placed under the valve as the experiment started. While waiting for steady state to appear all the liquid was drained into this bucket. As steady state was attained the timer was started. Simultaneously a new empty measuring bucket was placed under the valve. When the desired time was reached following table 3.3 or 3.4, the measuring bucket was removed as the timer was stopped and the valve was closed. The same procedure was followed for the setup with two holes. It was made possible by coupling two leading pipes from the valves together by a handle. This arrangement can be seen from figure 3.18. The stopwatch used was a Asaklitt 36-4123.

Before being able to read off the volume measurements it was important to have a completely separated mixture of oil and water. The oil-water mixtures separated within a couple of minutes.

Running the experiments

- Control that the liquid height was equal to the desired height
- Start the recording of the video
- Open the valve to the desired position
- Drain the liquid while timing using the "two-bucket system"
- Shut down the valve and make sure that it was closed
- Stop the recording of the video
- Measure the volume of total liquid and water and log the data
- Fill the liquid gently back into the tank

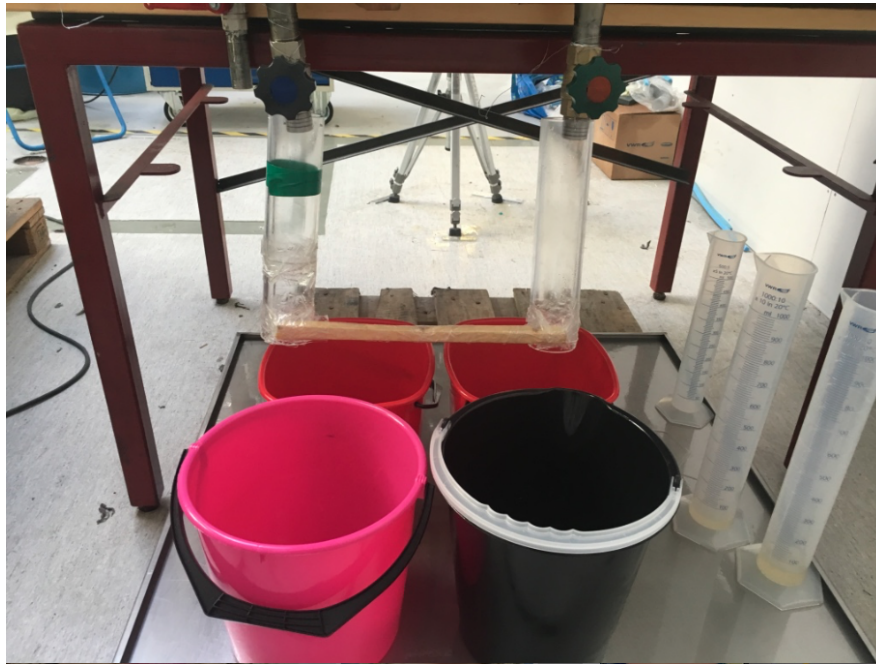


Figure 3.18: The two bucket system.

3. Changing the annulus gap

For every water level, tests were done with four different annulus gaps: 5, 10, 15 and 25 [mm]. A procedure to change between the gaps with minimal mixing of the water and oil was developed:

As the preparations in chapter 3.2 showed, the experiments had to be run without the metal pieces at the bottom. To validate the experimental run it was decided to check if

Changing the annulus gap

- Control that there were no movements of the metal pieces during the last experiments
- Remove all the clamps
- Change the metal pieces and roof with the new sizes
- Fasten the system with clamps
- Remove the metal pieces at the bottom of the tank for testing

there had been any movements during the runs. This was done by inserting the metal pieces back in the annulus gap. If they still fit perfectly, the run had been successful.

4. Changing the water level*Changing the water levels in the tank*

- Drain out as much oil/water as the change calls for
- Refill with the desired liquid to the required level with electrical pump or water hose
- Let the mix stabilize before running experiments

After changing the water level it was important to make sure that the oil-water mixture had separated before starting a new experimental run. The Nexbase oil needed longer time to separate than the Marcol oil. For Marcol the mixture was separated after a couple of hours. However for Nexbase, all water level changes were done at the end of the day. In this way the mixture had at least over night to stabilize. Visual observations showed no difference between waiting over night and over a whole weekend. Therefore waiting over night was deemed sufficient.

5. Changing the plate geometry*Changing the plate geometry*

- Drain out water into a storage bucket until the water level is underneath the orifice
- Drain out around 50 litres of oil into a storage tank
- Drain out more water until $WL = 10$ [mm]
- Remove the old plate from the flexible tube and set in the new one
- Fill the tank with oil until the liquid level reaches 210 [mm]

To change the plates it was necessary to have a liquid level lower than the outlets coupled to the valves at the back end of the tank. Therefore liquid had to be drained out for the

switch to happen. A water level of 10 [mm] was chosen since this would be the starting water level for the next plate. The water contained both colouring and fragments of oil after being used in experiments. Because of this the water was classified as special waste and could not be poured out into the sink. To limit the amount of special waste, the water was stored in a tank and re-used for all experiments for a single oil.

6. Changing the oil

Changing the oil

- Drain out water until the water level is underneath the orifice
- Drain out as much oil as possible without getting any infiltration of water
- Drain out the remaining water
- Clean the hole tank including plates and the flexible tubes
- Fill up the tank with a new oil

For future use it was important that the oil did not contain any water. Low flow rates were therefore necessary to avoid water coning which could infiltrate the oil. After the oil was drained out of the tank it was put back into the oil drum for storage. Since the water would contain fraction of oil it was decided to change the water when changing oil. With this routine the oil would be clean after being used in the experiments and be applicable for re-use at a later occasion.

7. Packing the setup back to standby mode

Packing away

- Clean up eventual oil spills at measuring buckets and around the rig
- Put the cover back on the tank and measuring buckets
- Remove the "Experiments in progress" sign

Chapter 4

Experimental Results & Discussions

During this thesis a total of 766 experimental runs were done including both the preparation stage as well as the actual experiments. In addition, numerous of runs were rejected and had to be redone for various reasons. For every run, data was collected into an excel spreadsheet, which can be seen in appendix A.1. All runs were video recorded and stored in a video library. A couple of screen shots can be seen from figure 4.1. With these recordings the steady state systems were examined with respect to the water jump.

4.1 Flow Rate Correlations

It was of interest to observe how the flow rate was affected by the system and the oils used. Both the liquid head and the outlet pressure were close to constant for every experimental run. Therefore any affect on the flow rate should have been caused by either the valve position or the liquid system. As mentioned in chapter 3.2, comparisons with the valve position as the variable should be done with caution. However, taking all the experimental runs into consideration some observations can still be made.

Figure 4.2 shows all of the flow rates plotted against each other as a function of the valve position for Nexbase 3080 and $\delta = 5$ [mm]. The total flow rate clearly increases moving from left to right.

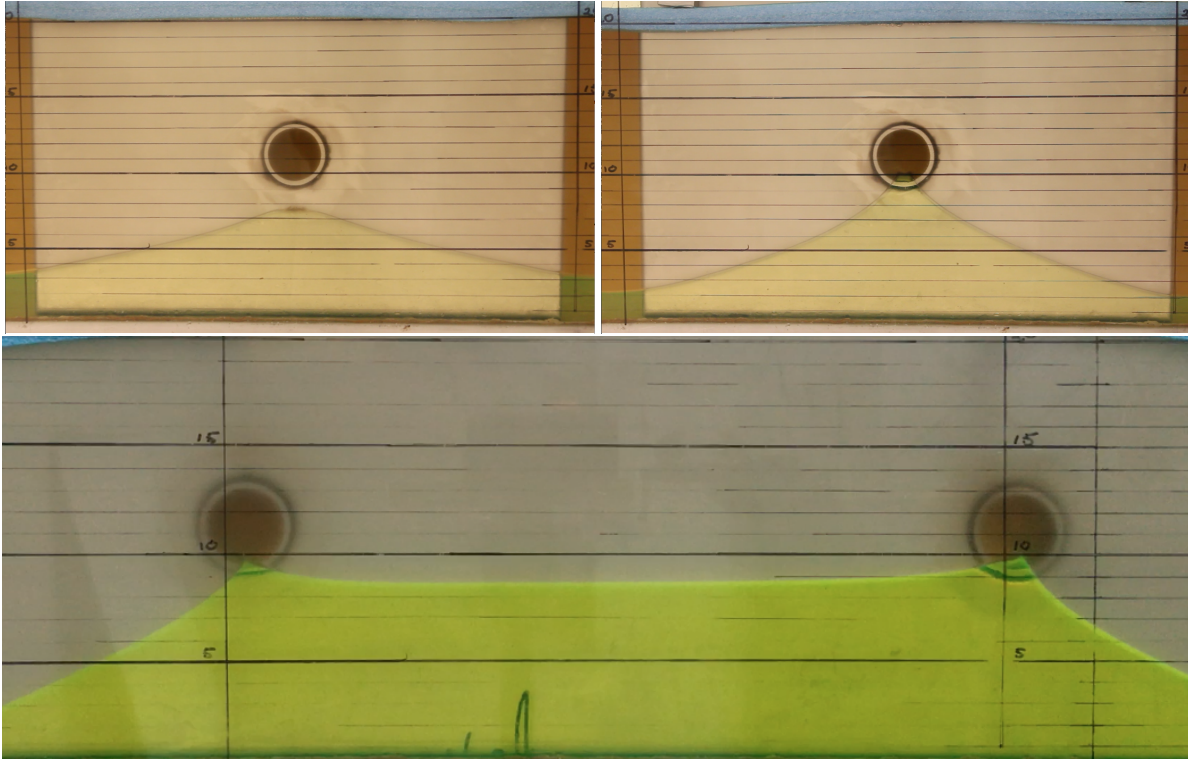


Figure 4.1: Screen shots of different experimental runs illustrating the water coning phenomenon.

It is difficult by only looking at this figure to conclude the reason for the increase, since two factors are changing over the scope. Both the flow rate of water as well as the initial water level is increasing when moving to the right. The liquid head was set by the height of the oil level above the orifice. This level was constant over the scope of these experiments, hence the increase in total flow rate was caused by the increased water cut. This is supported by the plot for an annulus gap of 25 [mm] in figure 4.3. For this gap the water breakthrough first appeared at water level of 70 [mm], and that is when the total flow rate seems to increase. The same trends can be seen from all of the four annulus gap widths, which can be found in appendix A.4. These results were expected due to the low viscosity of water relative to that of the oil. The viscosity is a measure of a fluids resistance to motion[18]. A fluid with low viscosity will therefore flow easier than a fluid with high viscosity. An example showing this is Poiseuille's law, which describes a laminar flow through a horizontal pipe[18]:

$$\dot{V} = \frac{\Delta P \pi D^4}{128 \mu L} \quad (4.1)$$

Here the volume flow is clearly dependent on the viscosity μ . A decrease in μ gives a increase in the volume flow \dot{V} .

With a viscosity of 12 [cP], the Marcol oil flows easier than the Nexbase oil with a viscosity of 83 [cP]. Since regular tap water has a viscosity of approximately 1 [cP], which is much closer to Marcol's viscosity than Nexbase's, the water flow rate should have less influence on the total flow rate when Marcol is used. The experiments showed that when utilizing Marcol oil the total flow rate did not seem to be affected by the increase of water in the system. An example of this is shown in figure 4.4.

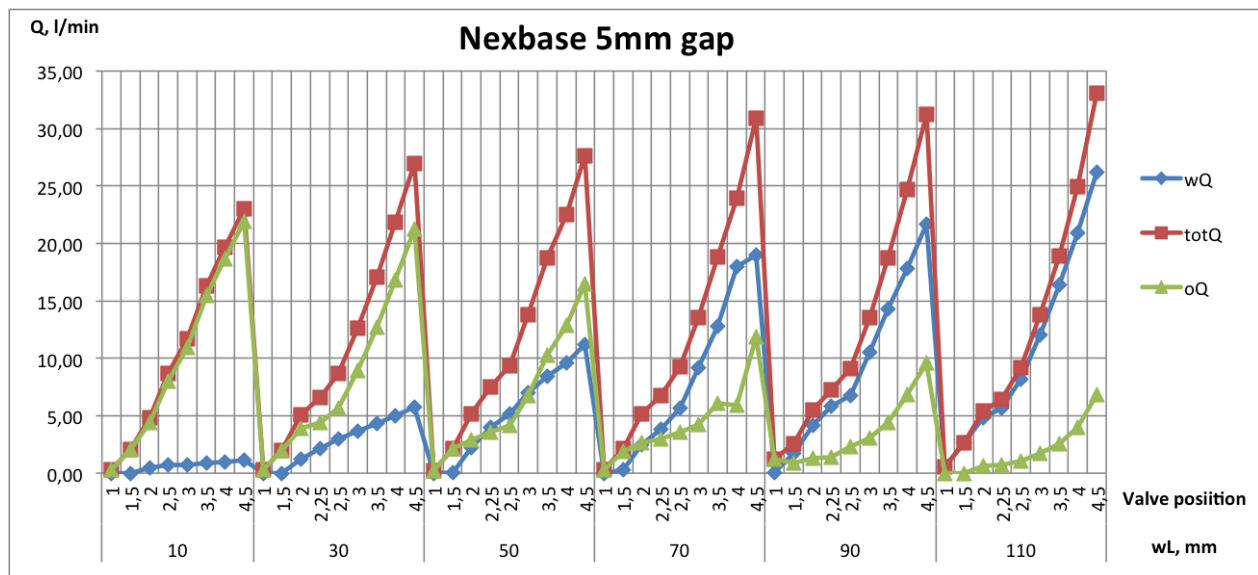


Figure 4.2: The flow rate of oil, water and the total flow rate for Nexbase 3080, $\delta = 5$ mm. Moving from left to right the different sequences are: WL = 10 [mm], WL = 30 [mm], WL = 50 [mm], WL = 70 [mm], WL = 90 [mm] and WL = 110 [mm].

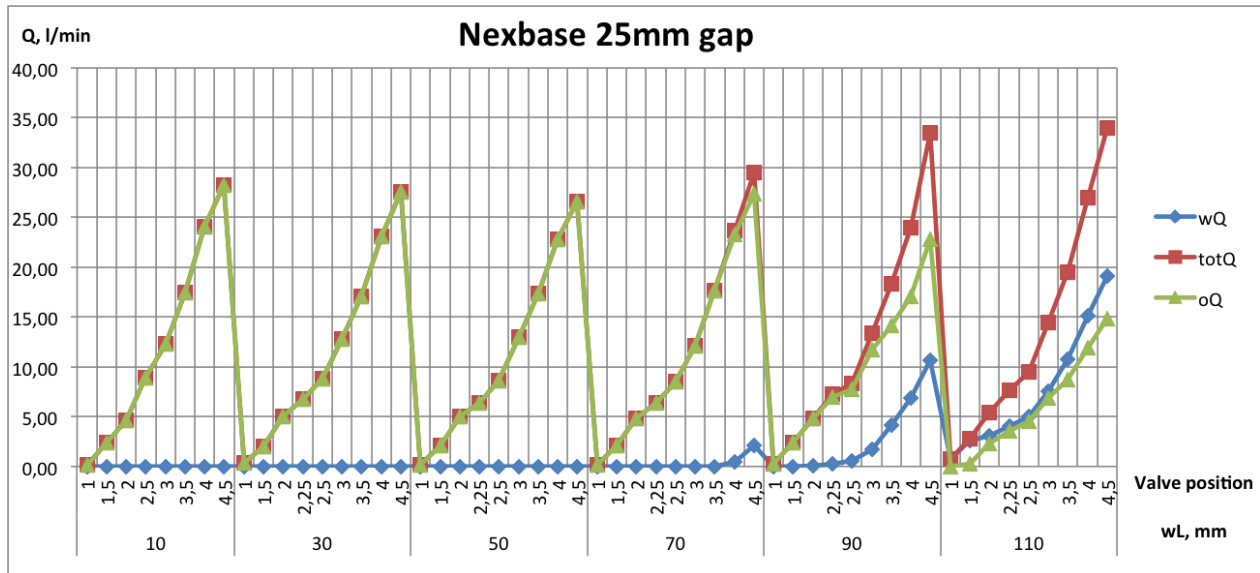


Figure 4.3: The flow rate of oil, water and the total flow rate for Nexbase 3080, $\delta = 25$ mm. Moving from left to right the different sequences are: WL = 10 [mm], WL = 30 [mm], WL = 50 [mm], WL = 70 [mm], WL = 90 [mm] and WL = 110 [mm].

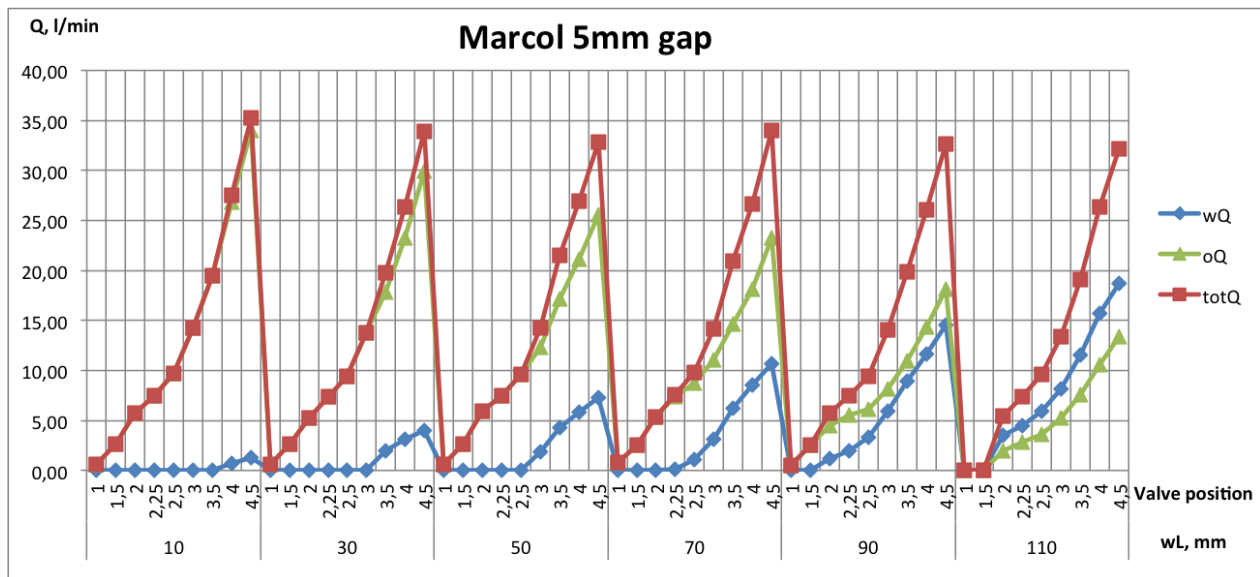


Figure 4.4: The flow rate of oil, water and the total flow rate for Marcol 52, $\delta = 5$ [mm]. Moving from left to right the different sequences are: WL = 10 [mm], WL = 30 [mm], WL = 50 [mm], WL = 70 [mm], WL = 90 [mm] and WL = 110 [mm].

4.2 Water Jump Phenomenon

The water jump together with the water cut are the most important parameters regarding the water coning phenomenon. Since the water breakthrough is a direct consequence of the water

jump it is important to understand what affects the water jump. The water jump was measured by analyzing screen shots from the experiments. The level of uncertainty was approximately ± 2 [mm] due to potential misreadings.

4.2.1 Plate 1, single orifice housing plate

The greater portion of the experiments were done with a single orifice housing plate as seen in figure 3.8. The experiments indicate that the water jump is directly dependent on the flow rate at any water level, annulus gap and for both oils. As the flow rates increased the water jump increased until it reached the orifice. After the water had reached the orifice the jump was rather small as it was drawn into the orifice and water breakthrough occurred. This behaviour can be seen in figure 4.5. In this example for an annulus gap of 10 [mm] with Nexbase 3080, all of the plots flatten out when the flow rates are sufficiently high.

In the experiment with an annulus gap of 15 [mm] for Nexbase 3080, water breakthrough was first observed at an initial water level of 50 [mm]. Figure 4.6 shows how the water jump for WL = 10 [mm] and WL = 30 [mm] continue to increase as the flow rate increases, while the others flatten out. The same behaviour can be seen for Marcol 52 in figure 4.7. Graphs showing the water jump for different annulus gaps and both oils can be found in appendix A.2.

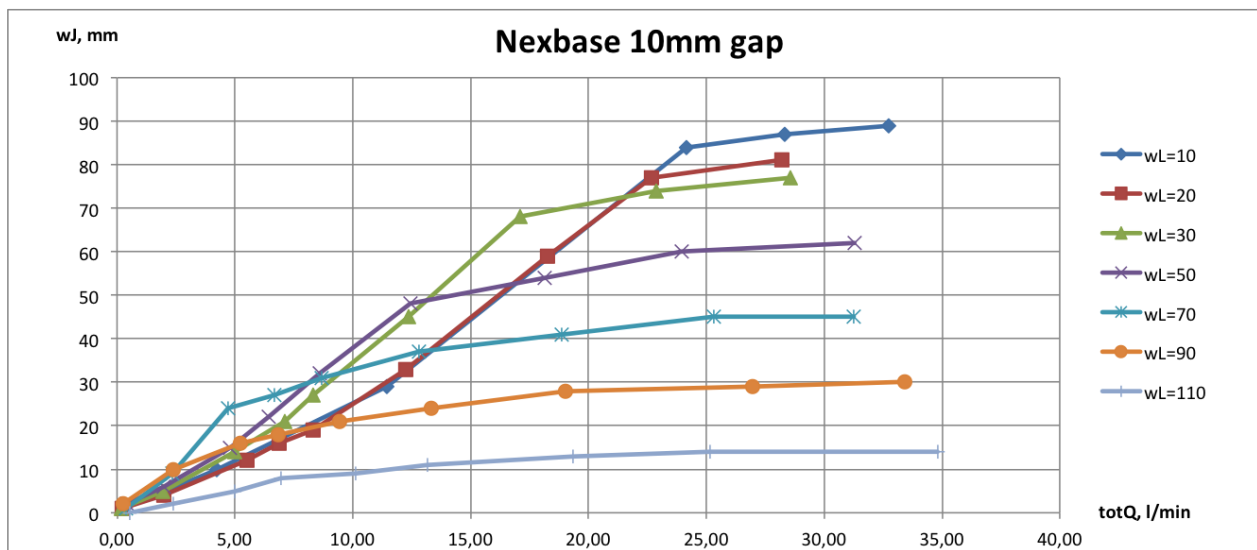


Figure 4.5: Water jump as function of flow rate, $\delta = 10$ [mm], Nexbase 3080.

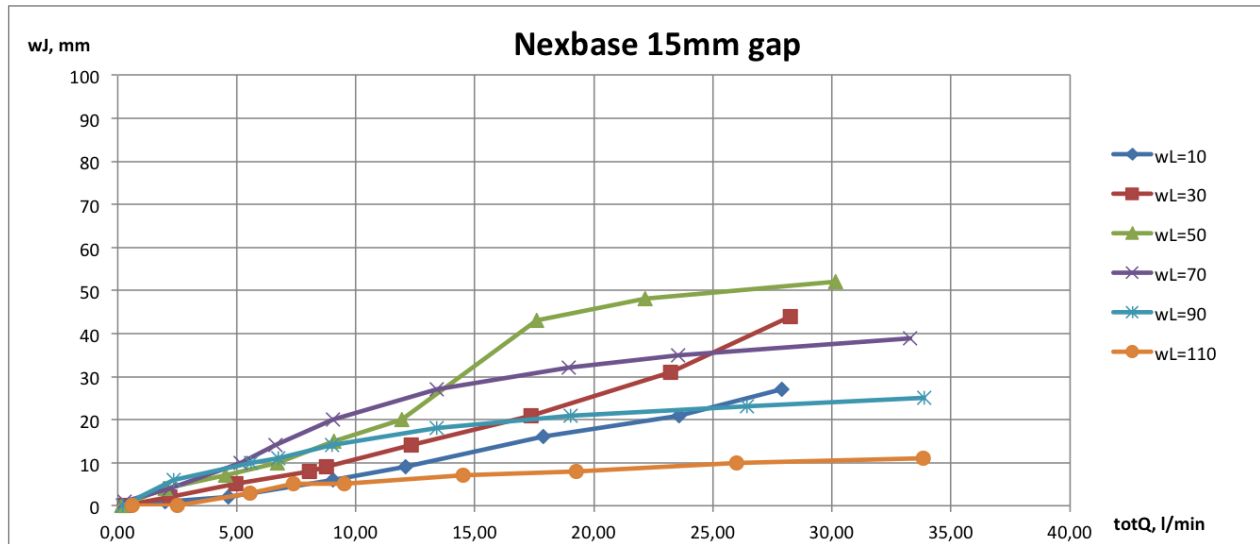


Figure 4.6: Water jump as function of flow rate, $\delta = 15$ [mm], Nexbase 3080.

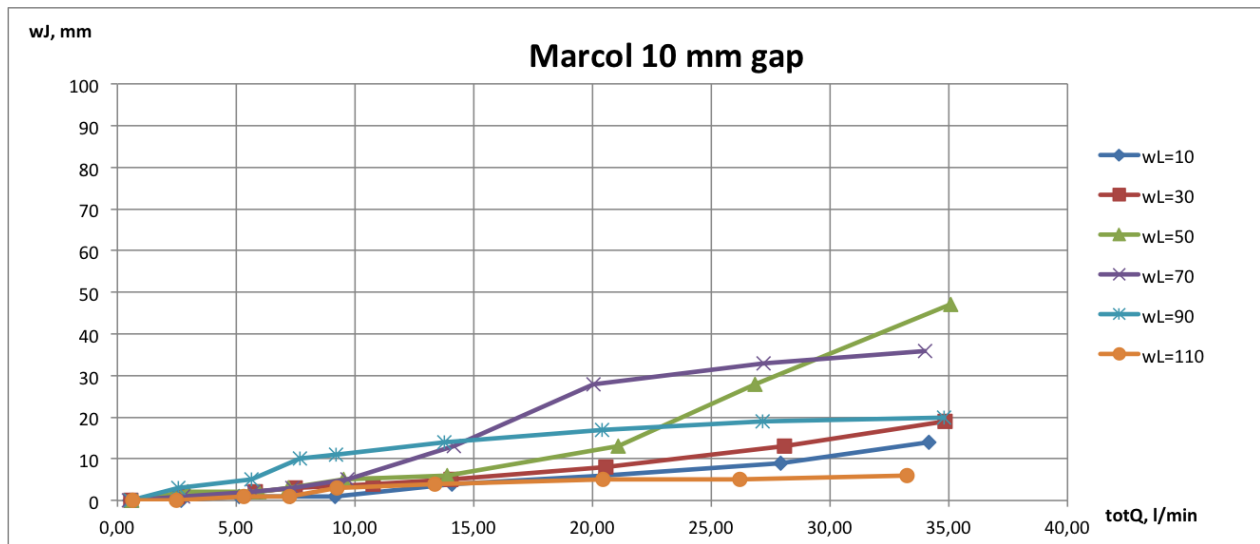


Figure 4.7: Water jump as function of flow rate, $\delta = 10$ [mm], Marcol.

It was observed that the water jump for higher initial liquid levels evolved faster than for lower ones. In figure 4.5 the curve of the water jump for high water levels is steeper at low flow rates, and flattens out quicker. Note that this was not the case for WL = 110 [mm] as the initial water level was above the bottom of the orifice. This trend compares well with fluid dynamics and potential lines. The potential lines can be developed by using the Cauchy-Riemann equations[19]. For a sink using polar coordinates with the assumption of a 2D-flow the set of equations becomes:

$$u_r = \frac{Q}{2\pi r} = \frac{\partial\phi}{\partial r} = \frac{1}{r} \frac{\partial\psi}{\partial\theta} \quad (4.2)$$

$$u_\theta = 0 = \frac{1}{r} \frac{\partial\phi}{\partial\theta} = -\frac{\partial\psi}{\partial r} \quad (4.3)$$

where Q is the flow rate (negative for a sink), r is the radius away from the center, ϕ is the potential function, and ψ is the stream function.

By integrating the velocity the equations can be solved for ψ and ϕ . The potential equation ϕ then becomes:

$$\phi = \frac{Q(f_a, f_f)}{2\pi} \ln r \quad (4.4)$$

As seen from equation (4.4) the flow potential decreases (negative Q) when moving further away from the center. This means that the velocity of the fluid, u_r , increases as the fluid approaches the sink. In other words the suction force gets stronger when moving towards the orifice. In a stable cone this force will be equal to the gravity forces pulling the water down. An increase in the suction force will therefore be compensated with a rise of the cone until the gravity forces balance the pressure again. A higher initial water level moves the interface closer to the orifice and a higher water jump was obtained for equal flow rates as before.

The annulus gap has a significant effect on the water coning. Figure 4.8 shows the dependence between the water jump and the annulus gap for Nexbase 3080. The same dependence can be seen for Marcol 52 in figure 4.9. Even though the flow rates were not necessarily exactly the same for each valve position as mentioned in section 3.2, they were close enough for the

trend to be reliable. The results indicate that tighter annulus gaps give higher water cones. By comparing with equations for pressure drop in chapter 2.4, the results are reasonable. Both the friction pressure drop, equation (2.10), and the acceleration pressure drop, equation (2.13), are dependent on the annulus gap δ . A larger δ makes both the pressure drop due to friction and acceleration decrease. Furthermore, a larger δ will according to the water coning criterion, equation (2.15), result in a lower critical flow rate. This means that higher cones will appear at lower flow rates for tighter annulus gaps which is exactly what is seen in figures 4.8, and 4.9.

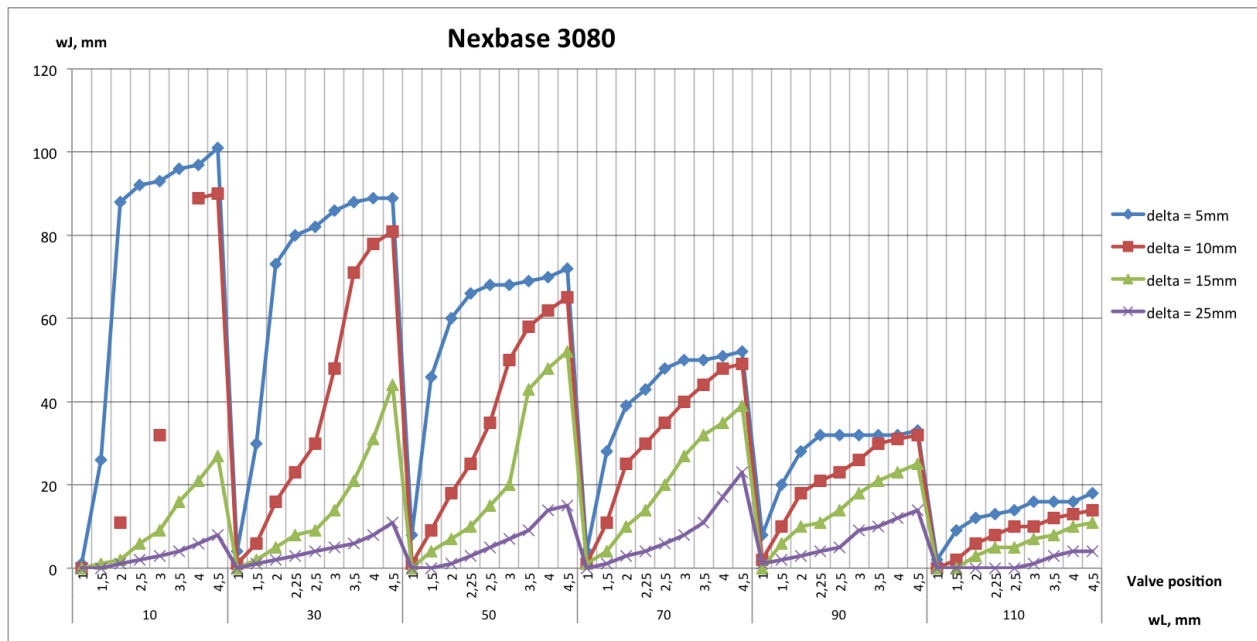


Figure 4.8: Water jump as function of valve position for different annulus gaps for Nexbase 3080. Moving from left to right the different sequences are: WL = 10 [mm], WL = 30 [mm], WL = 50 [mm], WL = 70 [mm], WL = 90 [mm] and WL = 110 [mm].

The two oils which were tested demonstrated large difference regarding water coning. From figure 4.10 and 4.11 it can be seen how the Nexbase 3080 had a much larger tendency to cone. For an annulus gap of $\delta = 10$ [mm] the water jump for the Nexbase is so large that water breakthrough is seen for all initial heights. However for Marcol water breakthrough is first seen at WL = 50 [mm]. The same trend is seen for all results; the water jumps are higher for Nexbase than Marcol and the water breakthrough happens at lower flow rates. The oils differ from each other in both viscosity and density. Nexbase has a density of 845 [kg/m^3] and a viscosity of 83 [cP], whereas Marcol has a density of 828 [kg/m^3] and a viscosity of 12 [cP]. Both Nexbase's higher density and viscosity should by equation (2.14) lead to a higher water cone. Even though the

differences in density are much smaller than the differences in viscosity, it is hard to conclude from the results of the experiments alone which of these factors affects the water jump the most. To explore this further a parametric study was conducted which can be found in section 6.5.

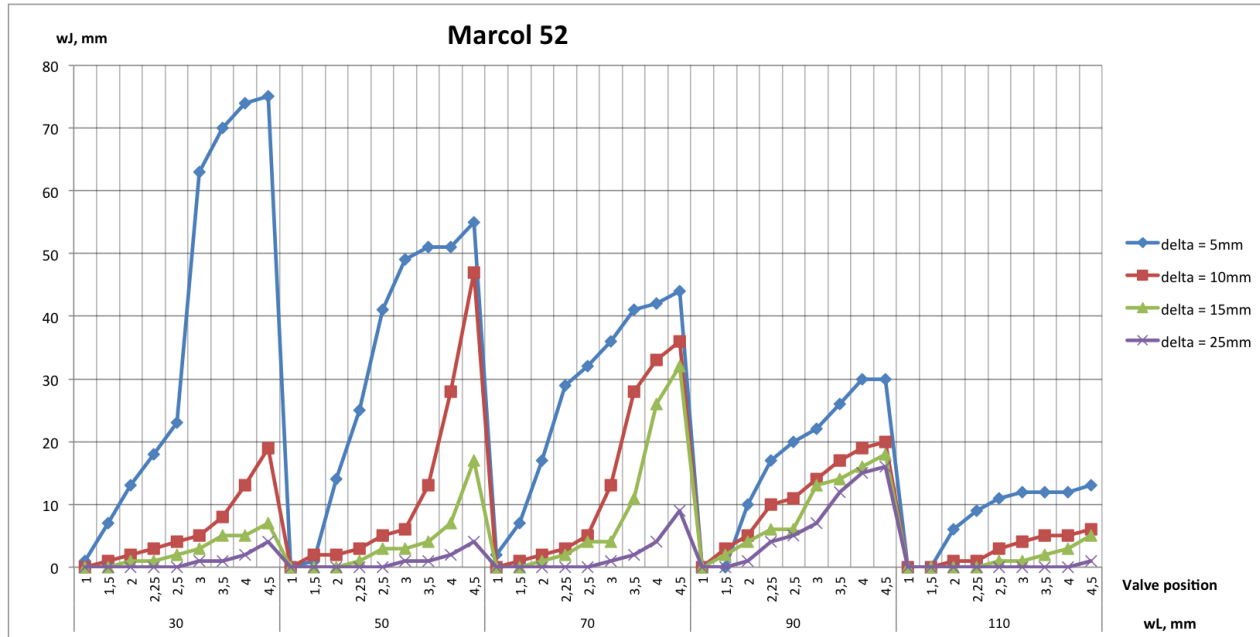


Figure 4.9: Water jump as function of valve position for different annulus gaps for Marcol 52. Moving from left to right the different sequences are: WL = 30 [mm], WL = 50 [mm], WL = 70 [mm], WL = 90 [mm] and WL = 110 [mm].

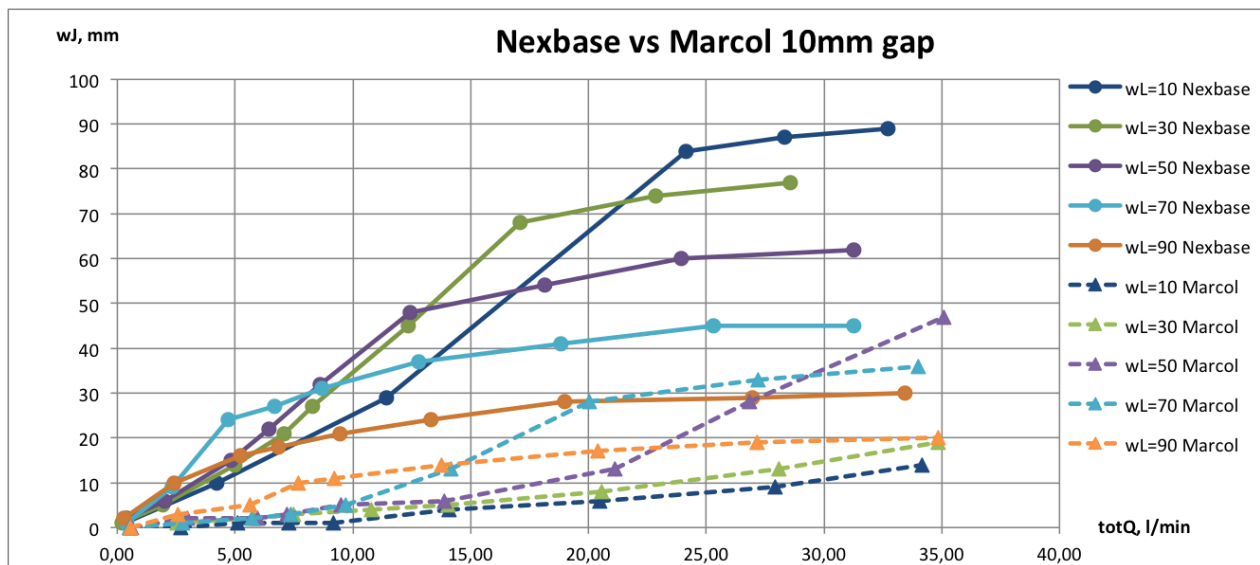


Figure 4.10: Comparison of water jump as function of flow rate for Nexbase 3080 and Marcol 52 for $\delta = 10$ [mm].

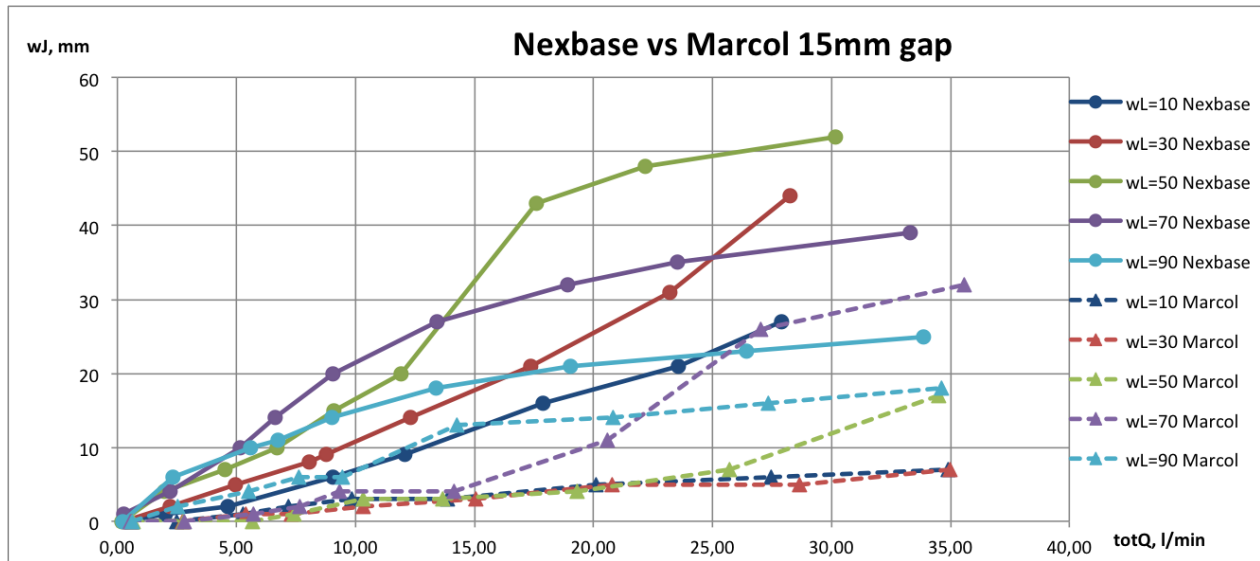


Figure 4.11: Comparison of water jump as function of flow rate for Nexbase 3080 and Marcol 52 for $\delta = 15$ [mm].

In figure 4.12 the results for an annulus gap of 10 [mm] is compared with the results of Schevchenko for asymmetrical inflow[17]. Results from both designs display the same trends. They begin steep and flatten out after a sufficient increase of the flow rate. But it is clear that for the case of one-sided inflow the water breakthrough occurred at lower flow rates than for the two-sided inflow. This is comprehensible with the theory from section 2.4. Equation (2.15) describes the criterion needed for water breakthrough to appear. The main difference between the two cases is the effects caused by the wall instead of having a two-sided inflow. This wall makes the terms for frictional pressure drop, equation (2.10), and acceleration pressure drop, equation (2.13), invalid for this particular case. Locally between the wall and the orifice, the terms increase due to flow along the wall and change in direction of the flow. The increase in both pressure loss terms need to be compensated by higher water jump to maintain a stable water cone. This would eventually lead to an earlier water breakthrough for the asymmetrical case than for the symmetrical inflow, which was seen in the experiments. In fact, the maximum water jump for each water level is also bigger for the asymmetric case. As seen in figure 4.13b the water level actually exceeds the height of the orifice at the wall side. At these flow rates all of the oil was sucked straight into the orifice leaving the water to refill the right hand side. This effect was not seen with a symmetrical inflow as in figure 4.13a, where the water cone was observed to be almost perfectly symmetrical, and not exceeding the orifice.

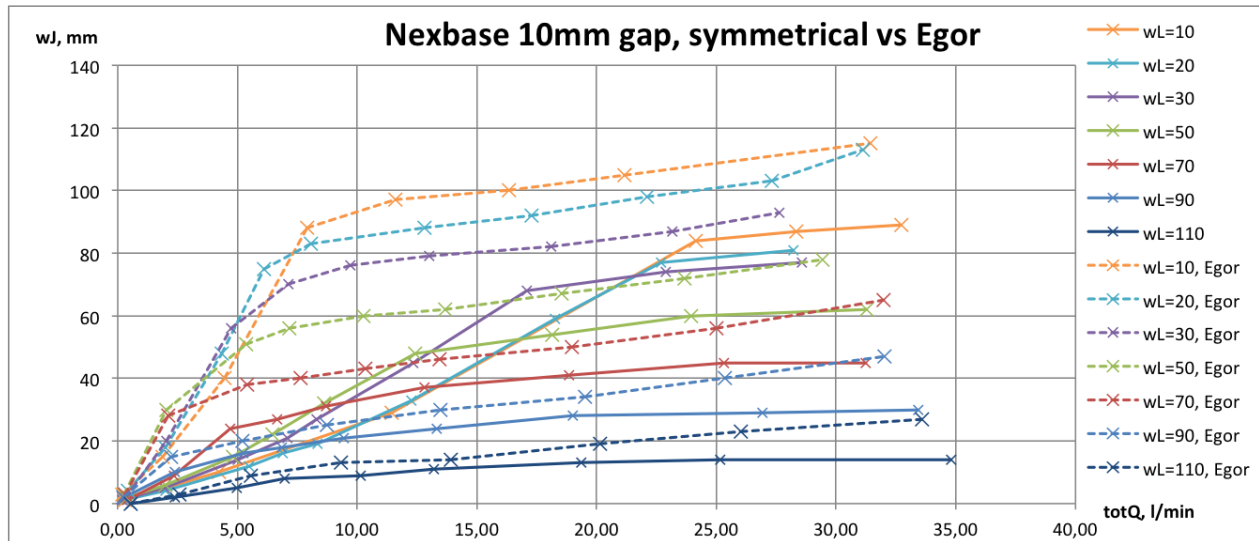


Figure 4.12: Water jump as function of flow rate compared with Egor's for the same system, $\delta = 10$ [mm].



Figure 4.13: Steady state pictures of the water jump for high flow rates and small annulus gaps. Here (a) shows the situation for symmetric inflow, while (b) [17, page 41] shows one-sided inflow.

4.2.2 Plate 2, two orifices at the same height

Figure 3.9 shows the geometry for the plate with two orifices at the same height. The aim for the experiments was to see how adding another orifice would influence the water coning under the same conditions as before. From figure 4.14 it can be observed that instead of being two separate cones, they lift each other upwards, almost as one large cone. In 4.14a the water level in between of the orifices is at almost the same level as in the center of the orifices. This behaviour was observed in all cases for Nexbase. For the case of Marcol, the water cone had a tendency to peak under the orifice at high flow rates as seen in figure 4.14b. However, also for Marcol the water level in between the orifices rose from its initial level.

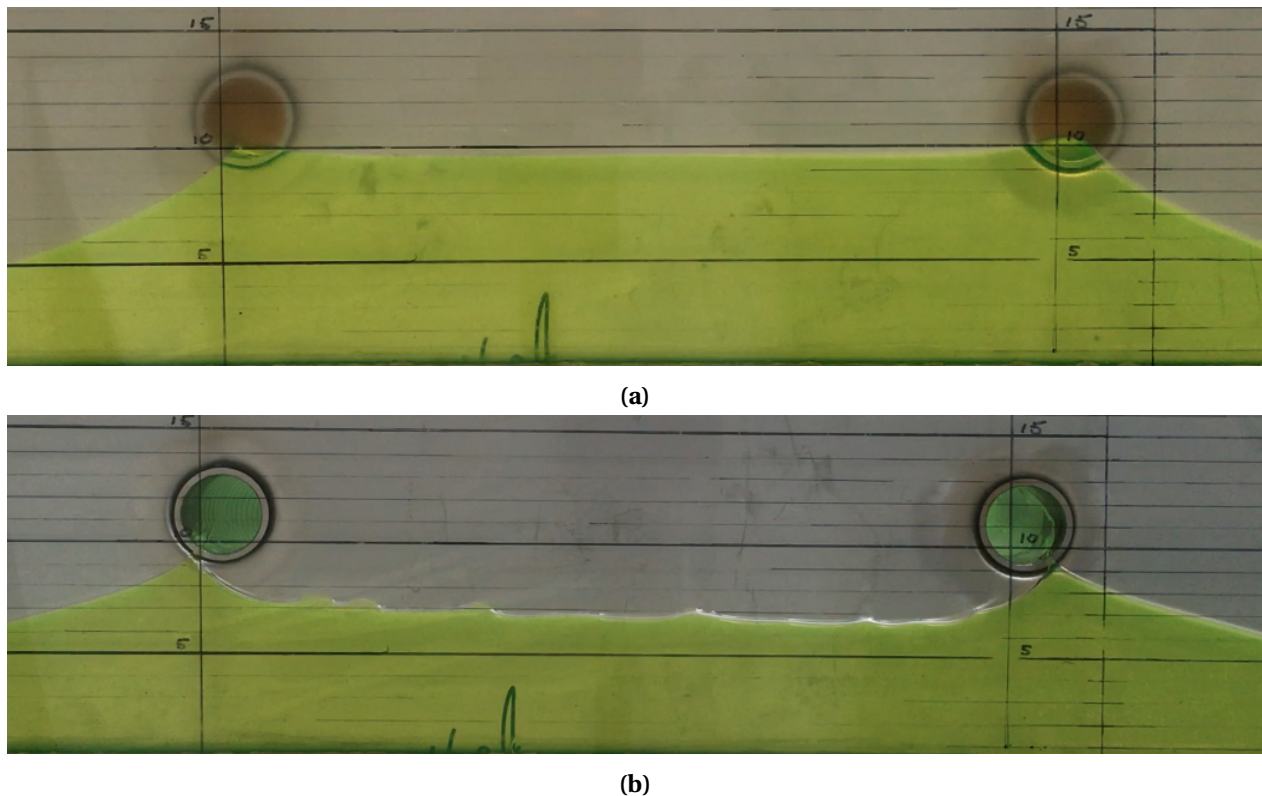


Figure 4.14: Snapshots from the experiments with two orifices at the same height, where (a) is done with Nexbase 3080 and (b) is done with Marcol 52.

When inserting another outlet the system reaches a new level of complexity. Without any literature on the specific system with several holes it was difficult to know what to expect from the results. However, the visual observations clearly indicate that the two outlets influence each other. Together, the drainage of the two holes lifted the water cone higher into the oil zone than

one outlet orifice did. The water jumps were in fact higher for every tested flow rate. Also after water breakthrough the water level was higher into the orifice. From figure 4.15 this behaviour can be seen for Marcol 52 for $\delta = 5$ [mm]. All of the plots follow each other closely, just lifted a little upwards. However, this close correlation was not the case for all situations. In figure 4.16 for Marcol 52, $\delta = 10$ [mm], and figure 4.17 for Nexbase 3080, $\delta = 10$ [mm], the discrepancies are observably larger. The magnitude of the water jump discrepancy differs, but the main trend of a larger water jump is still present.

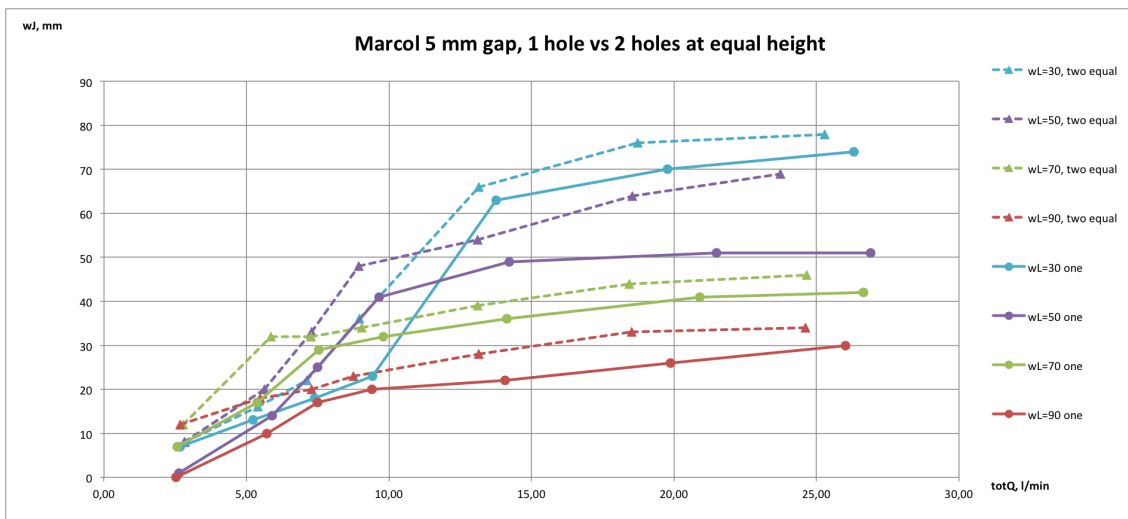


Figure 4.15: Comparison of water jump as function of flow rate for Marcol 52 for $\delta = 5$ [mm] between one single outlet and two outlets at the same height.

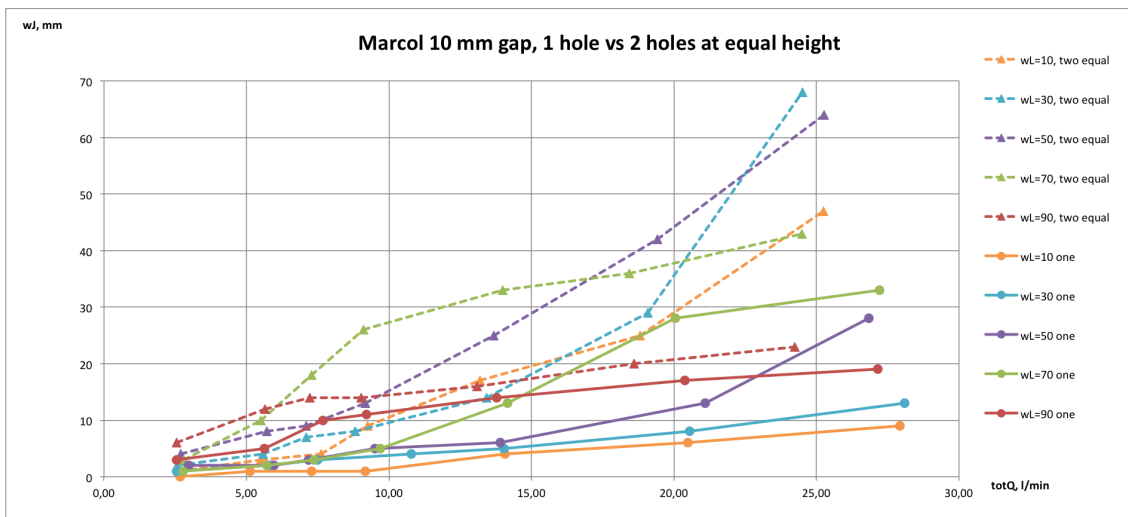


Figure 4.16: Comparison of water jump as function of flow rate for Marcol 52 for $\delta = 10$ [mm] between one single outlet and two outlets at the same height.

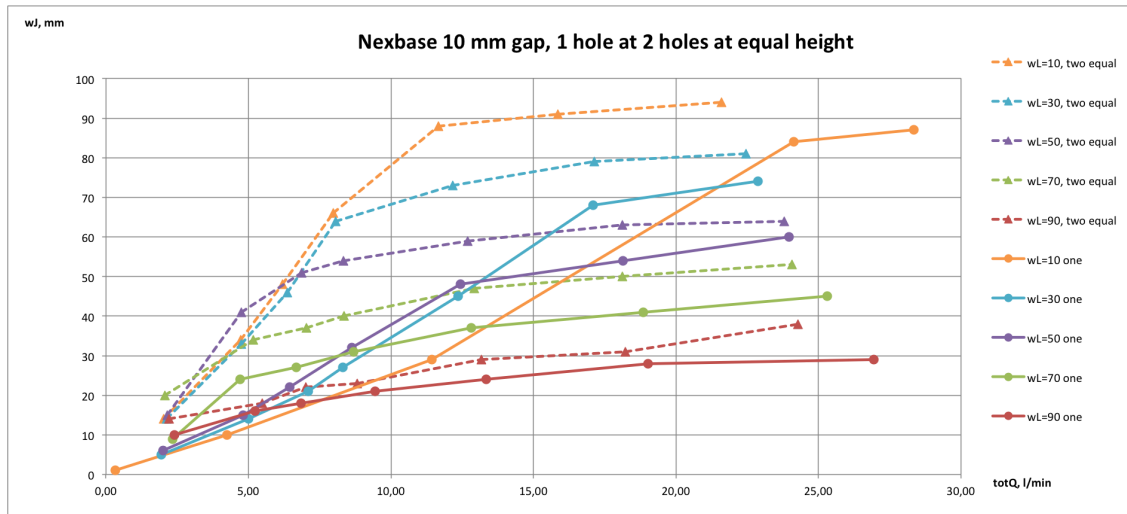


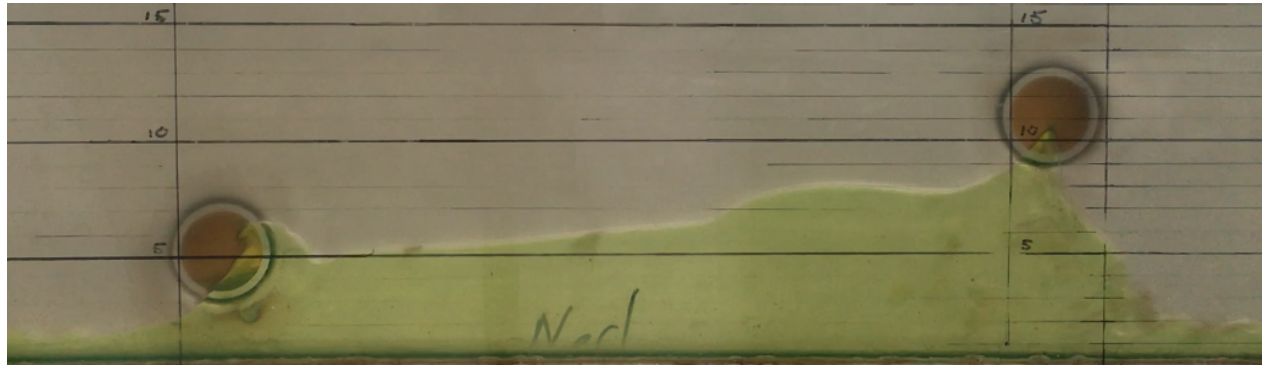
Figure 4.17: Comparison of water jump as function of flow rate for Nexbase for $\delta = 10$ [mm] between one single outlet and two outlets at the same height.

4.2.3 Plate 3, two orifices at different heights

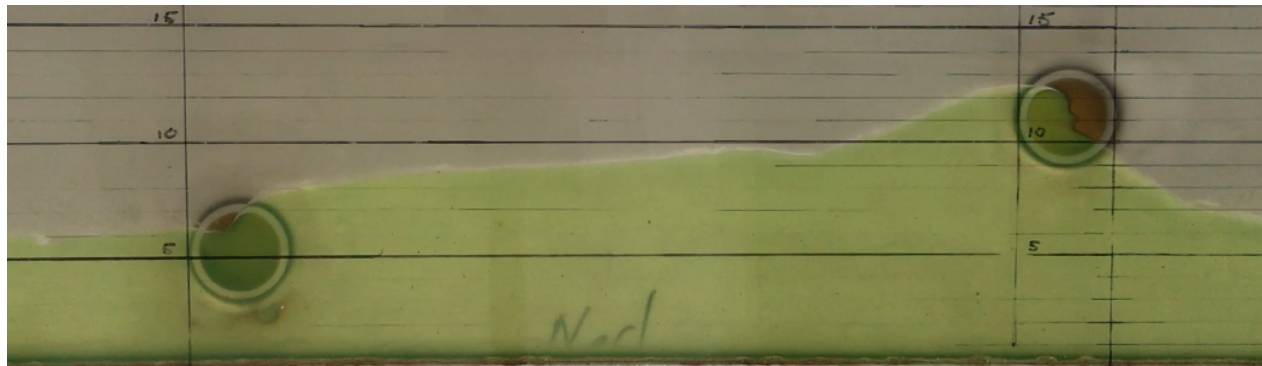
The purpose of the experiments with a plate with two orifices at different heights, figure 3.10, was to see how the water cone was affected when water was drained out from another orifice at the same time. The flow patterns for this case were even more complex than for the case of two orifices at the same height. In figure 4.18 it can be seen how the symmetric flow has vanished. The previously symmetric cone shape has been replaced with an uneven water cone where the height is increasing between the two orifices. Interestingly, as seen figure 4.18b, the water was forming a similar shape as seen during Shevchenko's one sided inflow experiments in figure 4.13b.

For flow rates at lower levels the shapes of the water cones were more stable. Two examples are shown in figure 4.19. The height of the cone increased evenly from the lower orifice to the higher orifice. The entire oil-water interface appeared smooth, and clearly less rough than for the cases employing higher flow rates, showed in figure 4.18.

As for the case with two equal orifices it was difficult to know what to expect for this case. The results were not as clear as for the case with two outlet orifices at the same height. However, the results indicate that two orifices gives a higher water jump than a single outlet. For Marcol



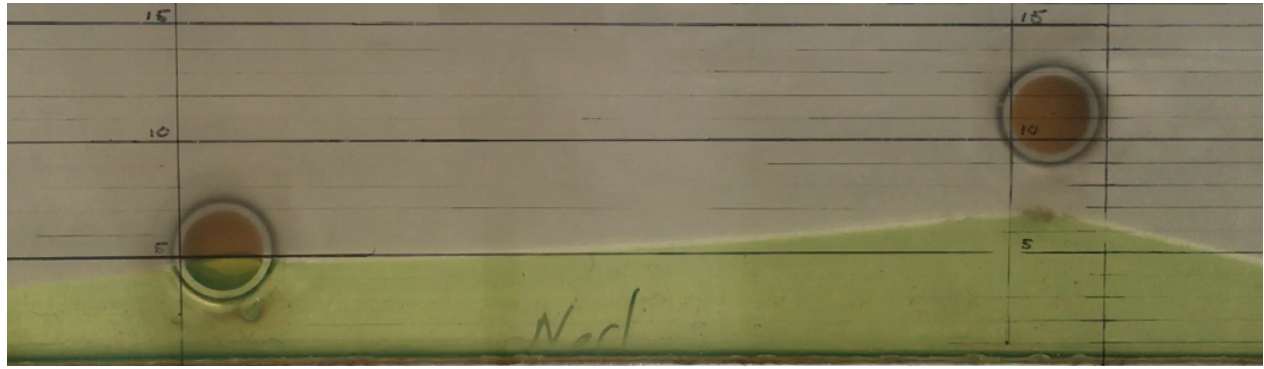
(a)



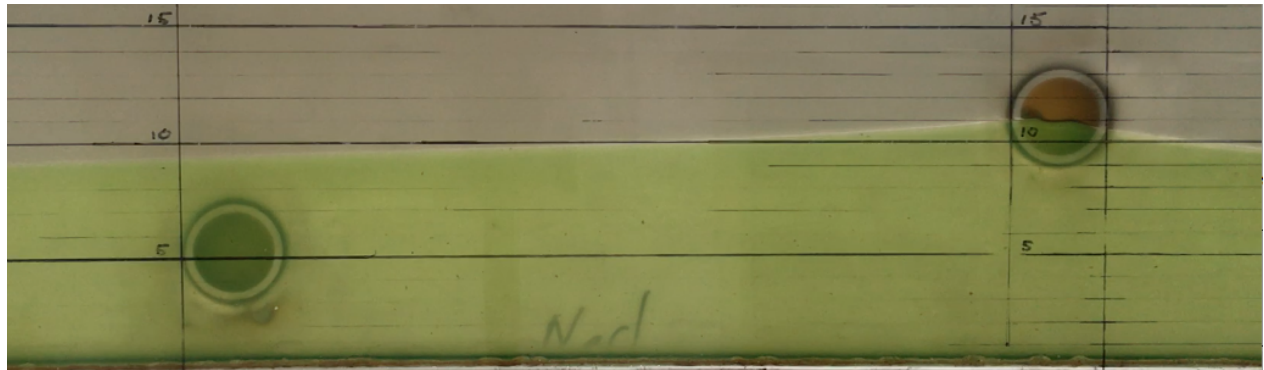
(b)

Figure 4.18: Snapshots from the experiments with two orifices at different height. Both done with Nexbase 3080 with high flow rates between 20 and 30 [l/min].

52 with $\delta = 10$ [mm] in figure 4.20, all plots for two orifices lay above the plots for one orifice. For the case of an annulus gap of 5 [mm], figure 4.21, there were some deviations where the water jumps for one orifice were higher for some values. These deviations might be caused by the uncertainties with the setup. A challenge with this particular plate was to obtain steady state. For the other plates the main challenge was the change in flow rate during the experiments. With one orifice lying under the water level, the water level changed during the experiments as water was drained out. For instance, 5 litres of drained water would reduce the water level in the tank by 5 [mm]. By these means every result for the geometry of plate 3 should be analyzed with caution. However, these uncertainties should give a water jump lower than its real value. Consequently, the conclusion that the two orifices at different heights produce a higher water cone still stands.



(a)



(b)

Figure 4.19: Snapshots from the experiments with two orifices at different height. Both done with Nexbase 3080 with high flow rates between 6 and 7 [l/min].

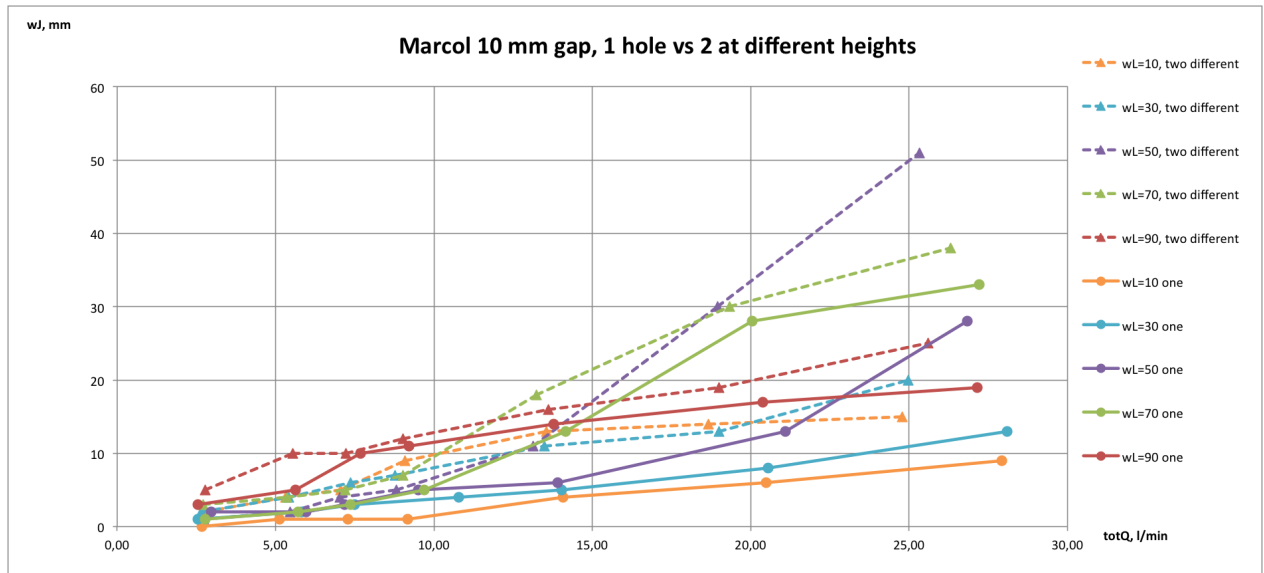


Figure 4.20: Comparison of water jump as function of flow rate for Marcol for $\delta = 10$ [mm] between one single outlet and two outlets at different heights.

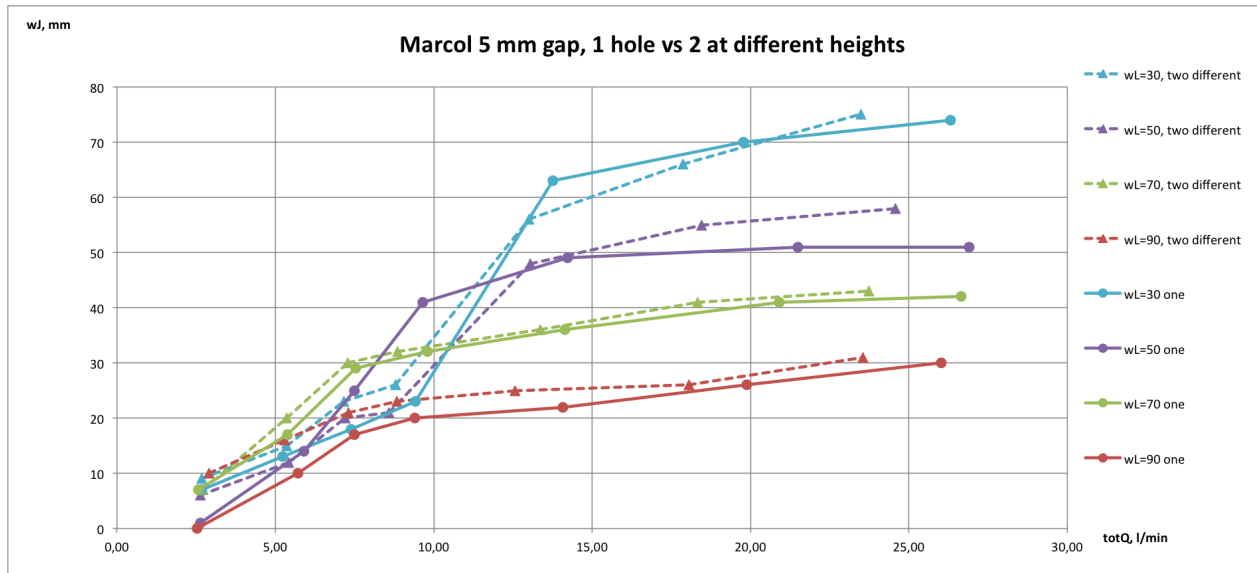


Figure 4.21: Comparison of water jump as function of flow rate for Marcol for $\delta = 5$ [mm] between one single outlet and two outlets at different heights.

4.3 Water Cut Measurements

4.3.1 Plate 1, single orifice housing plate

Similarly as for the water jump, the water cut was also shown to be dependent of the flow rate. An increase in flow rate, or as in an oil well an increase in drawdown pressure, will eventually lead to water breakthrough. Figures 4.22 and 4.23 show the plots of the water cut for Nexbase with an annulus gap of 15 [mm], and for Marcol with an annulus gap of 5 [mm]. Plots for all gap widths and both oils can be found in appendix A.3.

When the conditions exceeded the coning criterion, equation 2.15, water breakthrough appeared at a certain flow rate. After water breakthrough the water cut increased with the flow rate until it reached a maximum value where the water cut stabilized. The stabilizing can be explained from the pressure balance. A higher water cut leads to less oil flowing through the orifice. With less drained oil the pressure loss for the oil drops which again, from equation (2.14), leads to a lower water cone. The lower water cone feeds the system with less water so the water cut again drops and the flow rate of oil increases. In this way it becomes a stable system with a stable water cut. For certain conditions with either a low initial water level, or a large annulus

gap, the maximum value was not reached within the flow rates used in the experiments. This can for instance be seen for WL = 50 [mm] and WL = 70 [mm] in figure 4.22. The water cut is dependent of the initial water level as well as the flow rate. For a certain flow rate the water cut for one initial water level was always higher than for a lower initial water level if water breakthrough had occurred.

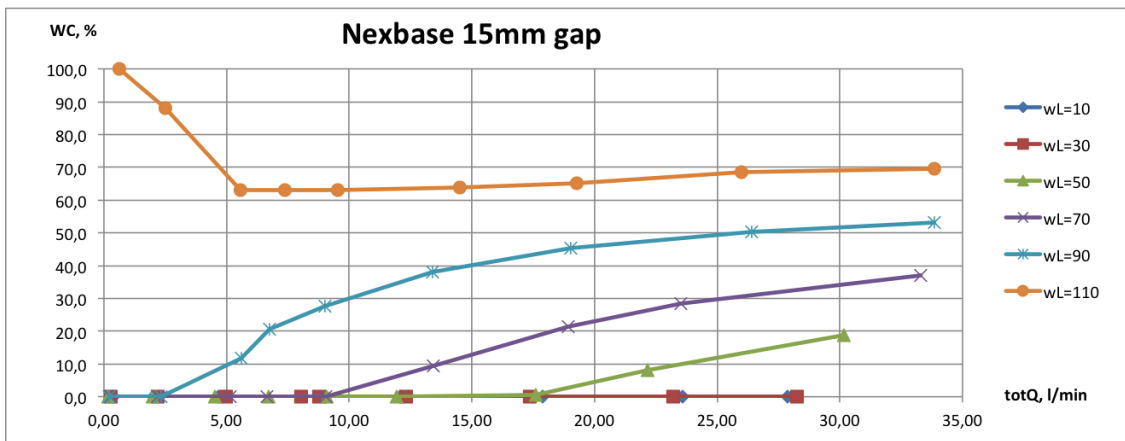


Figure 4.22: Water cut as function of flow rate for Nexbase 3080, $\delta = 15$ [mm].

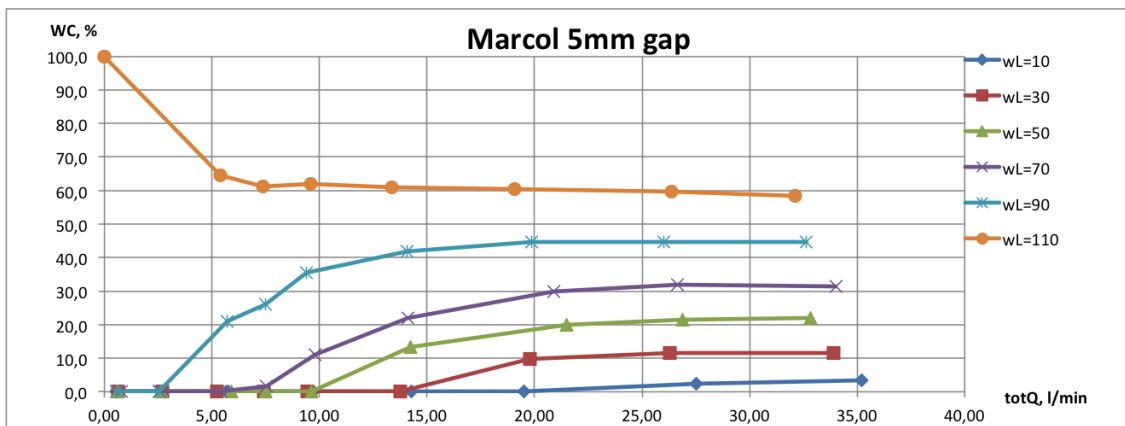


Figure 4.23: Water cut as function of flow rate for Marcol 52, $\delta = 5$ [mm].

It should be noted that the water cut values for WL = 110 [mm] are incorrect up until a certain flow rate. The outlet with the flow valve of the experimental tank was placed lower than the orifice at the housing plate. Because of this, the flexible tube attaching the orifice to the flow valve had a downward inclination. At WL = 110 [mm] the initial water level was above the bottom of the orifice. With its higher density the water filled up the bottom of the pipe close to the flow valve as illustrated in figure 4.24. For the lowest flow rates the refill into the tube could be

sustained by natural flow of water. At a flow rate around 5 [l/min] it seems like the liquid system was flowing as it should and the water cut stabilized.

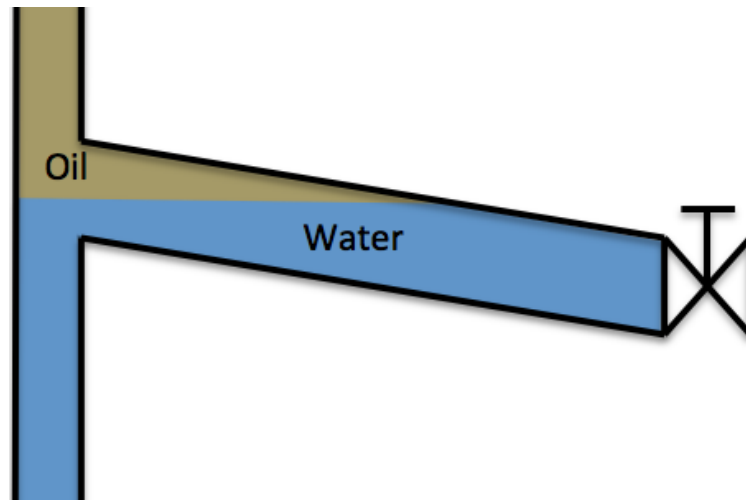


Figure 4.24: Illustration of why the water cut for WL = 110 [mm] is wrong for some flow rates.

The type of oil utilized also had an effect on the water cut. In section 4.2 it was established that Nexbase 3080 had a larger tendency to cone than the Marcol 52 because of its higher density and viscosity. This is also clear from the study of the water cut. Figure 4.25 shows a comparison between Nexbase and Marcol. Here it can be seen that water breakthrough occurred at a lower flow rate for Nexbase than for Marcol, and how the water cut was much higher after water breakthrough when utilizing Nexbase oil as opposed to Marcol. For instance for WL = 70 and 90 [mm] it was as much as approximately 30% higher.

The results for Nexbase with $\delta = 5$ [mm] was a special case which differs from the others, see figure 4.26. Instead of stabilizing after it reached the maximum value, the water cut dropped and stabilized at a lower value. The explanation lies in the flow regimes. Using the switch from valve position 2.25 via 2.5 to 3.0 for WL = 50 [mm] and $\delta = 5$ [mm] the water cut first increases from 52.8% to 55.3% before it decreases to 51.0%. These numbers can be found in appendix A.1. Figure 4.27 shows the transition from an increase to a decrease in the water cut. In figure 4.27a the flow is still stable and laminar. By making a small change in the flow rate, figure 4.27b, a transition in the flow regime begins to evolve for the water phase. The former smooth surface has been replaced by an uneven flow with a dip close to the plate edge. In figure 4.27c an even larger dip and larger fluctuations at the interface is seen. A transition from laminar to turbulent flow

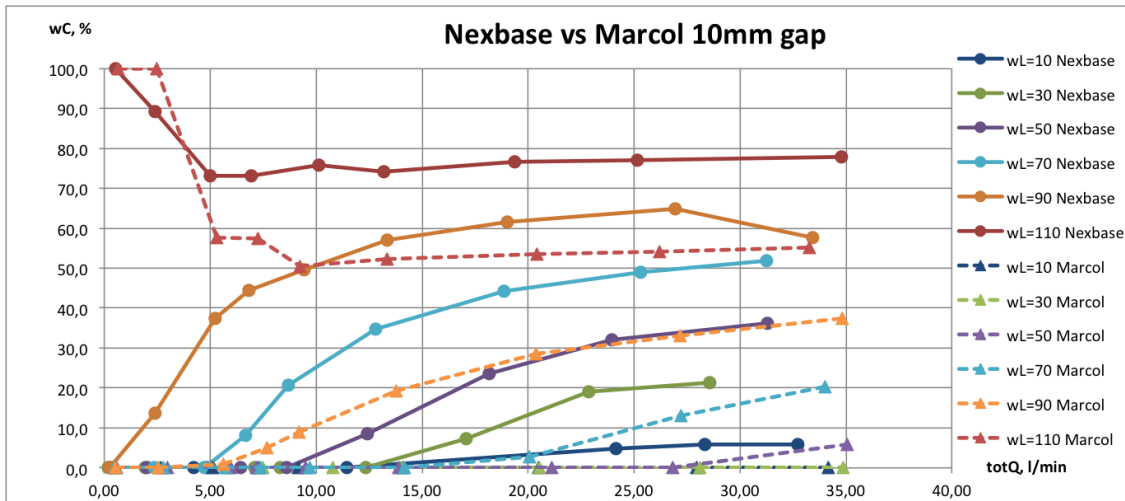


Figure 4.25: Comparison of water cut as function of flow rate for Nexbase 3080 and Marcol 52 for $\delta = 10$ [mm].

would give a higher friction factor[18]. However, the oil would still be in the laminar zone due to its high viscosity, and would therefore not be affected by this transition. The higher friction for the water phase will give a higher resistance along the walls, and would work to impede further increase in water velocity. As the oil was still flowing unaffected of this transition, a drop in the water cut was seen. Videos and data for all of the other experiments were studied looking for a similar flowing behaviour but it was only found for this specific case. The reason why it did not appear for Marcol $\delta = 5$ [mm], may be due to lower flow rates for the water. For the other cases with Nexbase the flow rates for water was lower as well as the velocity of the water decreased due to a larger flow area.

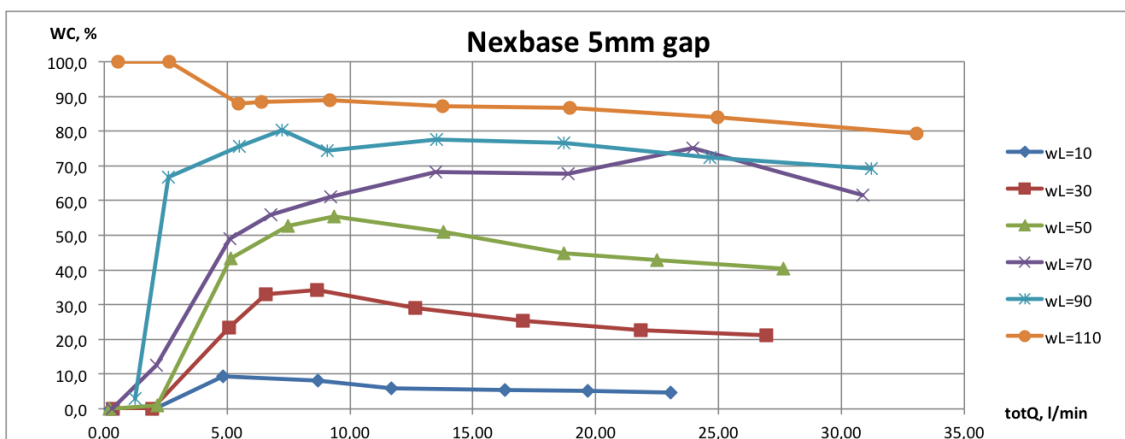


Figure 4.26: Water cut as function of flow rate for Nexbase, $\delta = 5$ [mm].

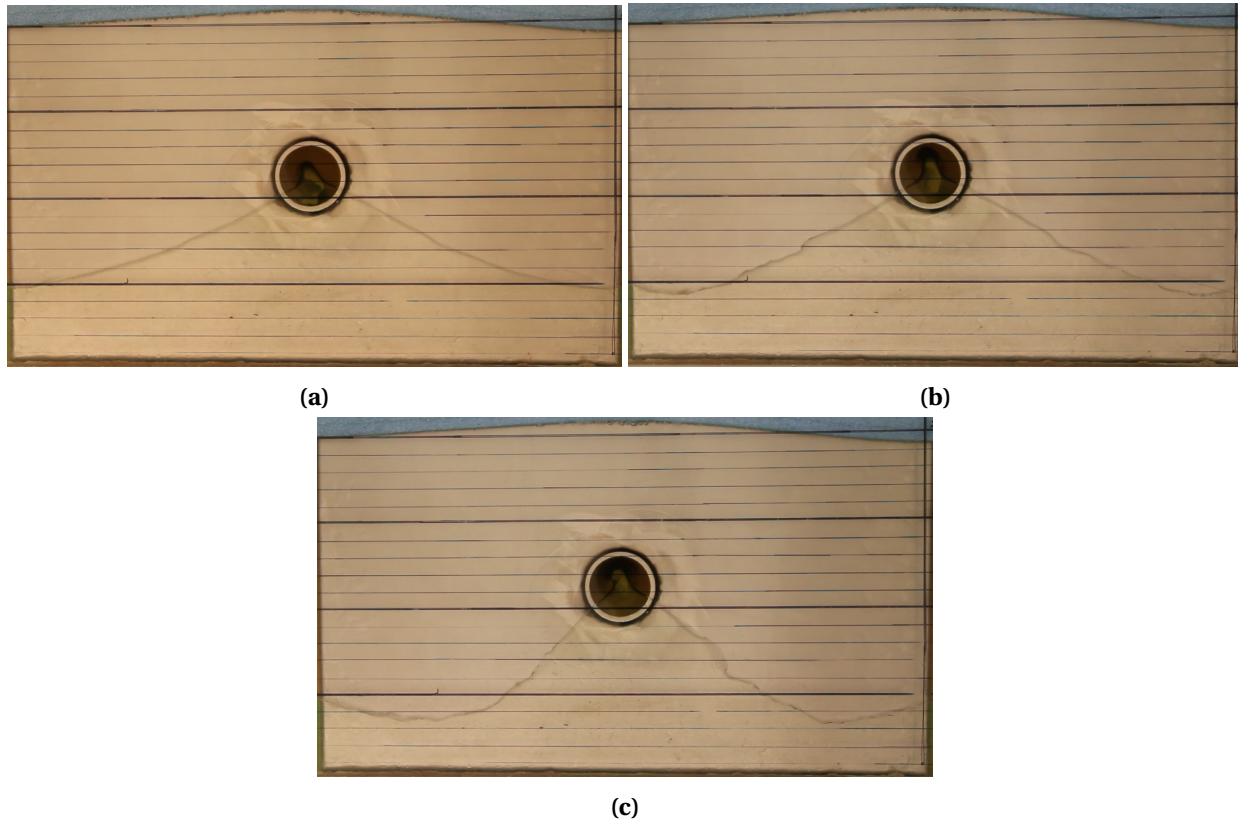


Figure 4.27: Steady state pictures of the flow transition. Figure (a) has valve position= 2.25, (b) = 2.5 and (c) = 3.

The comparison between the symmetric and asymmetric design with one outlet can be seen in figure 4.28. As mentioned in section 4.2 water breakthrough is present at much lower flow rates for the one-sided inflow than the two-sided. The effects on the pressure drop from the wall leads to a higher water cut as well as a higher water jump. This makes the system with a two-sided inflow far superior with respect to the water coning phenomenon. At the lower liquid heights the results in figure 4.28 show that twice the flow rate is needed before water breakthrough is present. It is worth noticing the difference between the symmetric and asymmetric inflow for the two lowest water levels, $WL = 10$ [mm] and $WL = 20$ [mm]. Even though Shevckenko's experiments were run with metal pieces blocking the inflow as mentioned in 3.2, he still obtained a higher water cut. This shows the strength of the two-sided inflow versus the one-sided.

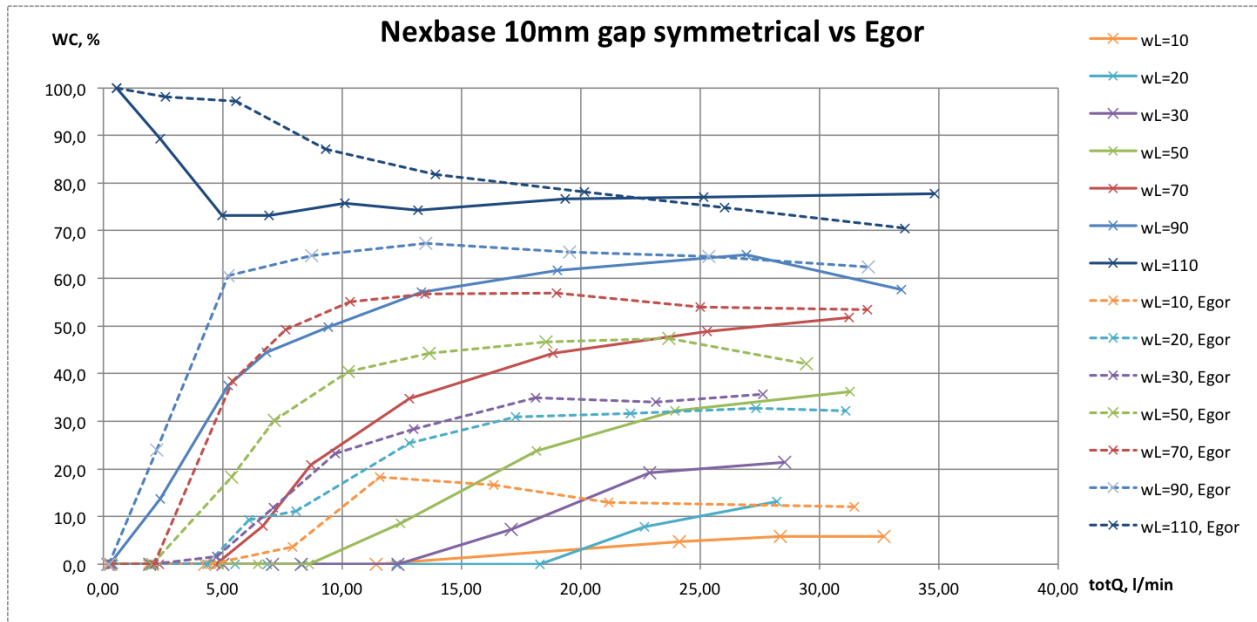


Figure 4.28: Water cut as function of flow rate compared with Egor's for the same system, $\delta = 10$ [mm].

4.3.2 Plate 2, two orifices at the same height

As seen for the water jump, the geometry of plate 2 gave better conditions for water coning. This was supported by the results for the water cut. Figure 4.29 and 4.30 show how the water breakthrough happened at lower flow rates than for the case of one orifice. After water breakthrough the water cut values were higher for all results, thus the case of two orifices at the same height gave more water in the system.

4.3.3 Plate 3, two orifices at different heights

The weakness with the setup for plate 3 seemed to be confirmed by analyzing the water cut trend. From observing figure 4.31 and 4.32 it can be seen how water breakthrough occurs at a lower flow rate for the case of two orifices at different heights. However at a certain point the curves cross, and the water cut for one orifice becomes higher. This may confirm the theory that the falling liquid level during the experiments for plate 3 affects the results. To conclude it can seem like the water cut was bigger for two orifices at different heights than for a single orifice, but further experiments should be conducted with an improved setup for this case.

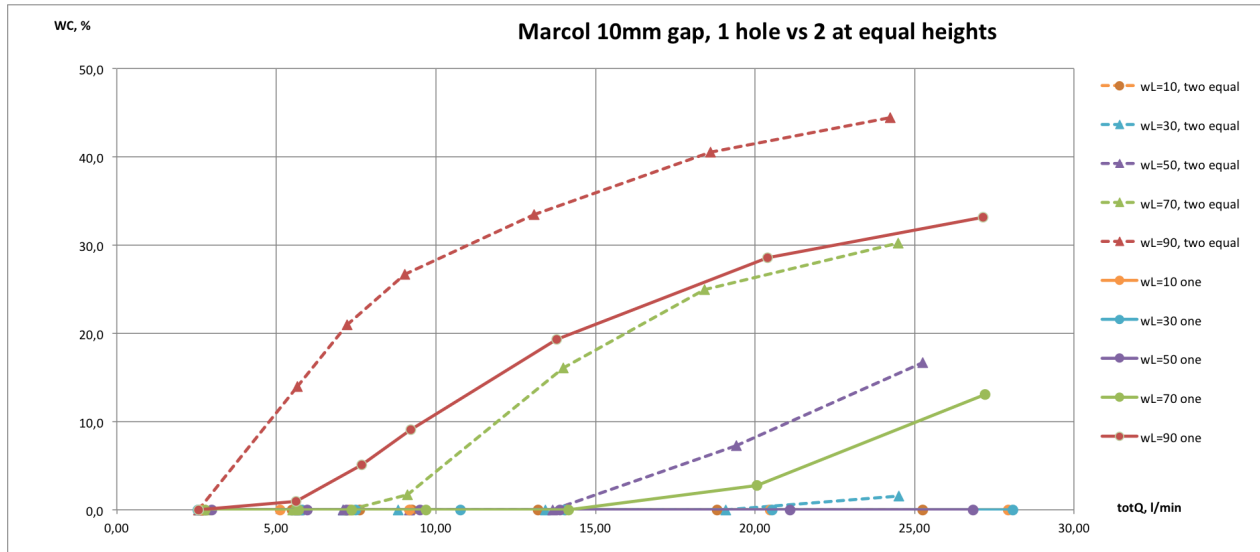


Figure 4.29: Comparison of water cut as function of flow rate for Marcol 52 for $\delta = 10$ [mm] between one single outlet and two outlets at the same height.

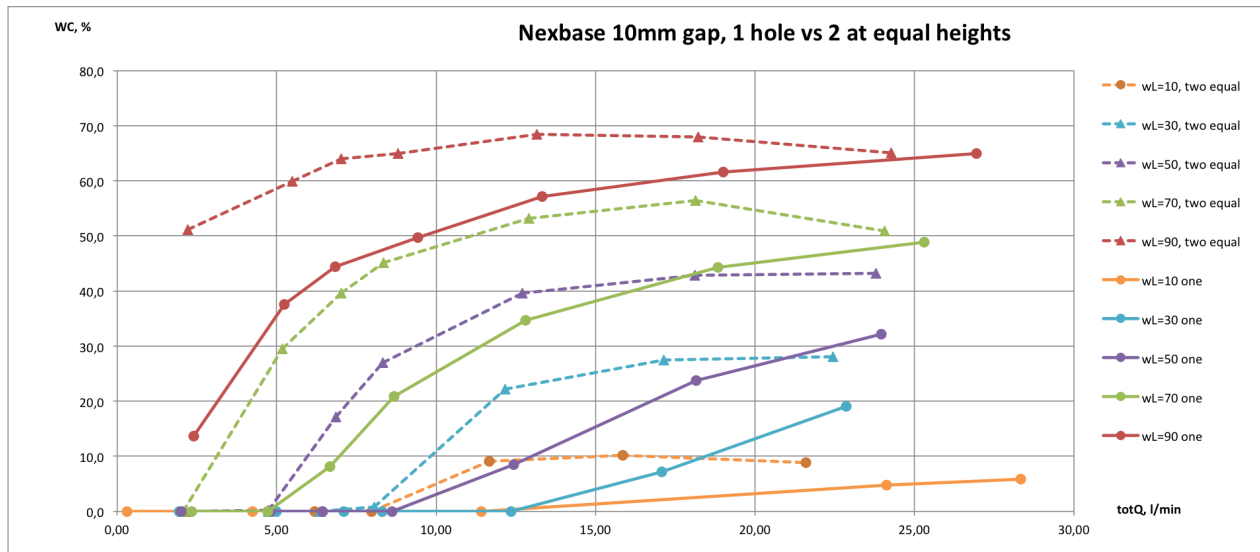


Figure 4.30: Comparison of water cut as function of flow rate for Nexbase for $\delta = 10$ [mm] between one single outlet and two outlets at the same height.

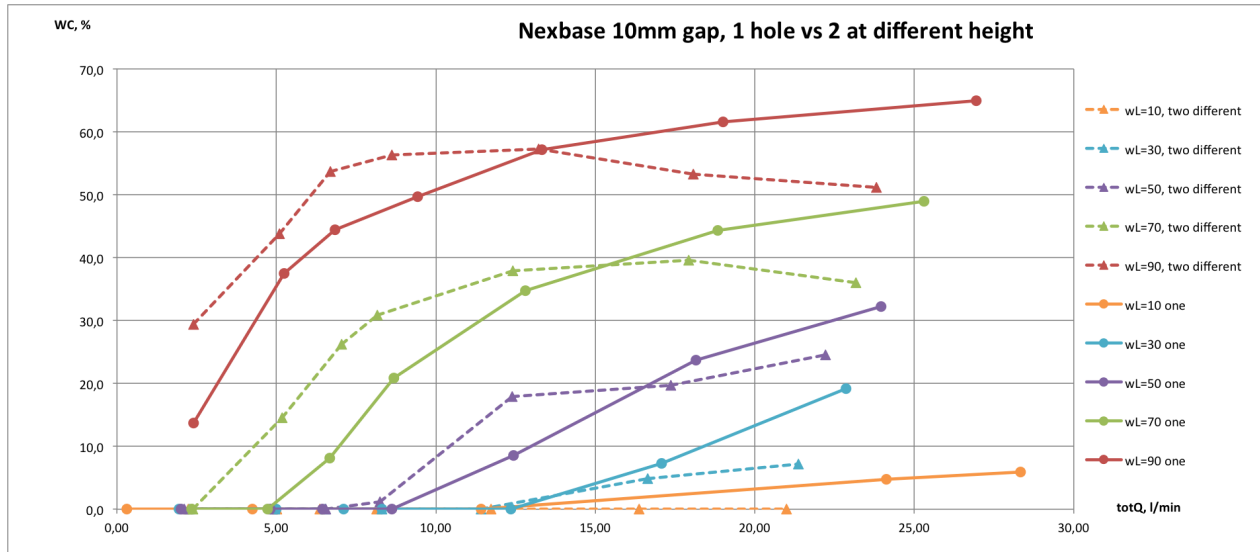


Figure 4.31: Comparison of water cut as function of flow rate for Nexbase for $\delta = 10$ [mm] between one single outlet and two outlets at different height.

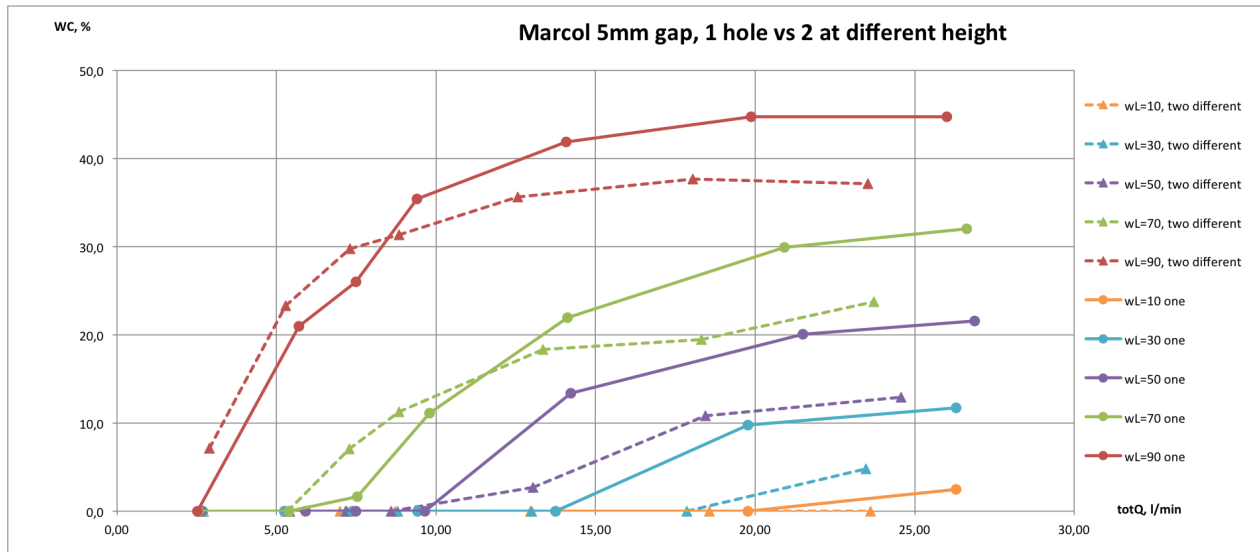


Figure 4.32: Comparison of water cut as function of flow rate for Marcol 52 for $\delta = 5$ [mm] between one single outlet and two outlets at different height.

Chapter 5

CFD Methodology

When creating CFD models there are a lot choices that need to be made. The combination of choices along with the chosen geometry is what defines the model. This chapter aims to describe the important model configurations such as the chosen boundary conditions, meshing technique, among others. Several CFD models were created and utilized for running simulations, thus the differences between the models are also addressed.

5.1 Case Simplifications

For any CFD simulation, understanding the governing physics of the problem is quintessential to simulate the problem at hand. Moreover, since these are transient simulations additional importance is placed on appropriate boundary conditions, and initial conditions. The initial conditions lay the path for all results in transient studies.

The experiments conducted is a multiphase fluid dynamical problem with oil, water and air as working fluids. There is expected to be mixing of the oil and water phases, while the air remains passive in this experiment setup, albeit allowing the height of oil above the orifice to vary. As the pressure gradients increase near the exit orifice, the water interface lifts towards the orifice as the force balance changes. The viscosity of the oil and the density ratio of the fluids play an

important role here.

To properly simulate the experiments, various assumptions and approximations were made in order for the case to be well defined. Most of the simulations conducted were 2D simulations. This simplifies the geometry and total mesh cell count, thus the required computational power is dramatically reduced compared to a full 3D simulation. This simplification implies no 3D flow effects, which are present in the experiments. Moreover, it effectively means there is no annulus width that imposes friction losses.

As opposed to the experiments, air was not included in the CFD model. Instead, the CFD domain consists purely of oil and water. To satisfy continuity, an influx of oil was imposed at an inlet. This simplification ensures there is no varying hydrostatic head. Additionally, the simulation domain was made relatively large to minimize the effect the oil inflow might have on the coning water flow. This approach may cause deviations in fluid behavior compared to what was observed in the experiments.

Furthermore, a no-mixing condition was imposed between the oil and water phase. The fluids are therefore modeled as two stratified fluids. In the experimental case there will always be some mixing or emulsion effects, however this effect was deemed low as the fluids are regarded as immiscible.

In an experimental case with a narrow annulus gap, surface tension may have an effect on the results. For the two-dimensional CFD models, this effect was negligible as there is no annulus width and the other length dimensions in the geometry are relatively large. A contact angle was specified to be 90 degrees between the two fluids to allow for wall wetting effect. The true value of the contact angle between water and the oils used in the experiments was not specified.

5.2 Simulation Cases

In this study several different geometries, meshes, and inherently different modeling approaches were explored. This section provides a general overview, briefly summarizing and explaining the

variations between the three main models.

The three main simulation cases in this study are:

1. 2D simulations with one outlet orifice.

For the 2D simulations two different meshes were tested out, the first consisting of densely packed tetrahedral elements near the outlet orifice, and secondly with hexahedral inflation layers extending radially out from the orifice. Only the latter mesh was used for this simulation case for reasons explained in detail in section 5.7.1, discussing the results of a mesh sensitivity analysis.

Different approaches in the physics modeling was also explored. The friction was added as a force per volume source term in each element. A friction correlation assuming low Reynolds number laminar flow was utilized, as well as a separate set of simulations using three different correlations depending on local Reynolds number. One correlation for laminar conditions, another for transitional conditions, and finally a correlation for fully turbulent conditions. For both the single, and compounded friction modeling approach a laminar solver was utilized in the CFX setup. Further details are found in section 5.5, discussing the added momentum source.

A turbulence model with a gamma-theta transition description was tested as the experiments and consequent local Reynolds number at the orifice indicate that the flow may transition from laminar to turbulent flow. For this solver modelling approach only the compound friction description was utilized. Section 6.2.2 in the results chapter indicate that the difference between the results with each respective friction formulation was small. Thus it was deemed of lesser importance to further compare the two.

2. 2D simulations with two outlet orifices.

Due to the fact that the geometry with one outlet orifice is very similar to the the case of two outlets, the same inflated hexahedral meshing method was employed for this case as well. The compound friction formulation was utilized for these simulations, along with the laminar solver.

3. 3D simulations with one outlet orifice.

The created mesh was similar to that of the 2D cases, albeit extruded to give a third dimension. A drainage pipe was added, and meshed using radial inflation layers. Further details about the meshing technique can be found in section 5.7.

As there can be gradients in all three dimensions, wall boundaries were put in place to ensure a no-slip condition at the annulus walls. This ensures a velocity profile in between the walls, and thus no friction momentum source was needed. A laminar solver was utilized for all 3D simulations.

5.3 Simulation Geometries

The geometries were drawn in ANSYS CAD drawer. In an effort to minimize local effects, and effects from the inlet boundary, the domain surrounding the orifice was made relatively large, as seen in figure 5.1. This enables the flow phenomenon to develop naturally, and to a lesser extent be influenced by the inlet conditions.

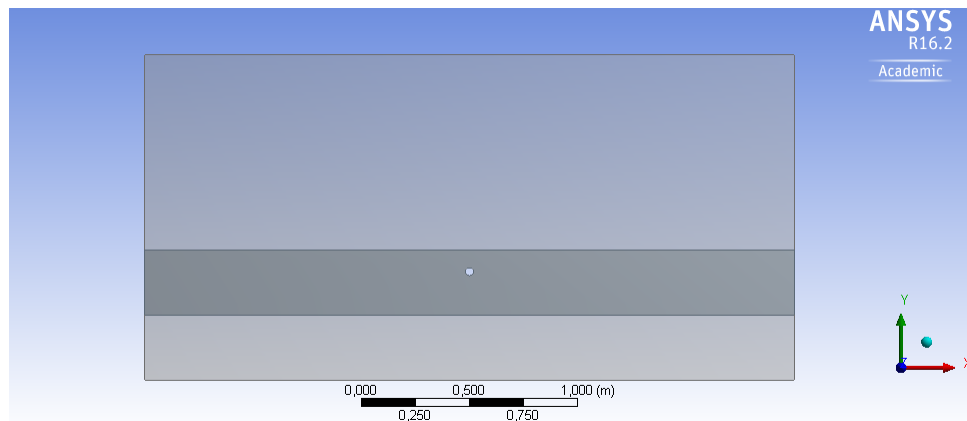


Figure 5.1: 2D simulation geometry, with one outlet orifice.

The geometry for the 2D simulation was drawn as a 3D model, however since the mesh was made with one cell thickness into the z-direction the domain was treated as 2D in the CFX-solver as there would be no gradients in the z-direction. This means that each gap size was achieved

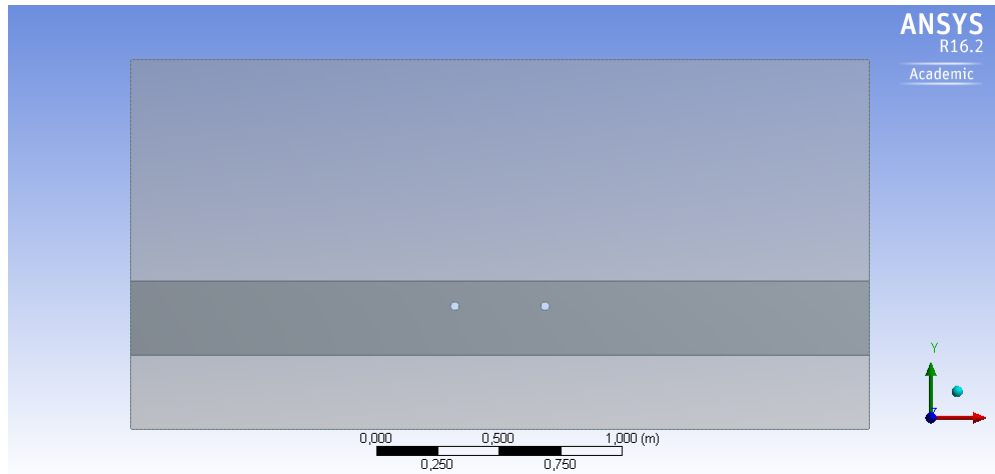


Figure 5.2: 2D simulation geometry, with two outlet orifices.

by extruding the domain one gap width from the sketch plane, in this case the xy -plane as seen in figures 5.1, and 5.2.

The geometry for the simulations with two outlet orifices was nearly identical to the geometry with one outlet orifice, albeit two holes were extruded instead of one.

Creating the 3D simulation geometry was achieved by adding cell layers in the z -direction. Additionally an exit pipe was added at the orifice to recreate the pressure loss of the pipe entrance, and to minimize instabilities of the outlet boundary pressures which can occur when placing the outlet in close proximity to the water cone, see figure 5.3.

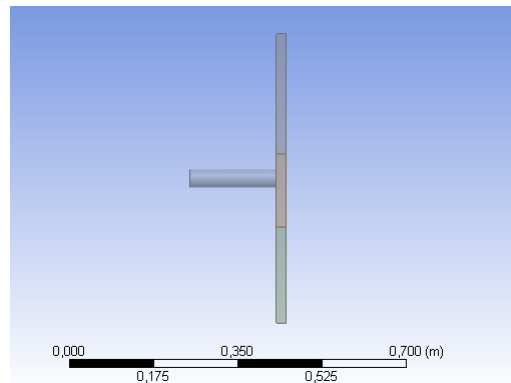


Figure 5.3: 3D simulation geometry, side view.

In order to avoid numerical issues at the inlet to the drain pipe, the edge connecting the annulus to the piping was chamfered to obtain a smoother connection as seen in figure 5.4

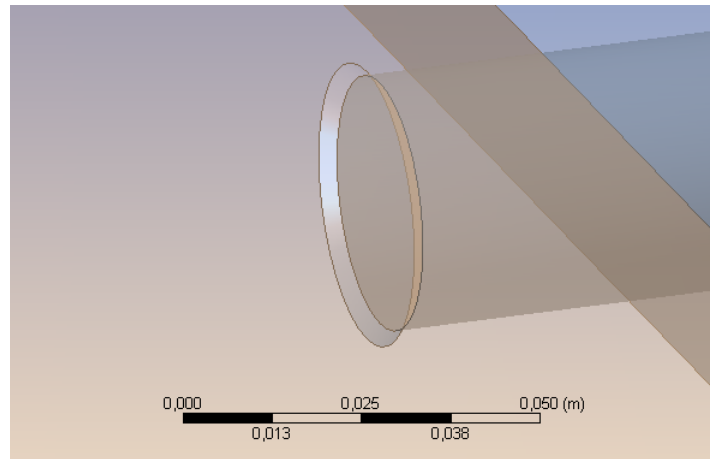


Figure 5.4: 3D simulation geometry.

5.4 Boundary Conditions

Ideal boundary conditions to employ was the respective mass flow rates for oil and water at the inlet and a static pressure boundary condition at the outlet. However, the mass flow rates change over time, and the mass fractions are not known, they are in fact part of the solution. Therefore, alternative approaches were examined to find a suitable alternative.

Much time was spent experimenting and researching on the appropriate boundary conditions for this experiment. Two promising configurations were explored and discussed in depth with Martin Aasved Holst, technical consultant at EDR MEDES0, an expert in the CFX commercial code.

1. The first configuration was using a velocity inlet and a static pressure outlet. In this fashion, the total mass flow rate and mass fractions may vary freely depending on flow phenomenon at the orifice. However, this introduces an added constraint to the problem, namely the volumetric flow rate. The fluids are modeled as incompressible and therefore the volumetric flow rate is fixed at both inlet and outlet for a given velocity at the outlet.
2. The second approach was to set a total pressure boundary condition at the inlet and static pressure with a specified value compared to the domain reference value. More plainly spoken this simulates a fixed static pressure at the outlet, as is the case with a valve in

the experiment. The total pressure boundary at the inlet thus allows for inflow of oil. The upside of this configuration is that the flow rate is not fixed. The downside is however that the correct pressure drop at the orifice, and at the valve is unknown. In order to use this configuration many different static pressure outlet values would need to be tested and compared to experiment data. Hopefully it would behave as the valves in the experiments.

After initial testing of the two approaches the second approach failed for small flow rates, and resulted in back-flow at the outlet. The first approach was more robust and worked for a larger range of flow rates. However, for flow rates smaller than 5-10 liters per minute depending on the chosen oil and annulus gap width, back-flow was present in this solution as well.

The walls in the 2D geometries needed special attention. For the walls in the yz-planes, and the bottom zx-plane, a no-slip boundary condition was imposed, see figure 5.1. Symmetric boundary conditions were assigned to the domain surfaces in the xy-planes to ensure the desired 2D flow domain.

For the 3D geometry all domain surfaces apart from the inlet and outlet surfaces, a no-slip wall boundary was imposed.

5.5 Momentum Source

One drawback of the 2D geometry approach is that there are no annulus walls, only symmetry planes, which implies no shear force generated at these boundaries. Therefore, to improve the 2D model, a momentum source was imposed on the 2D simulations to constitute a friction loss. This source was set to act in every cell, in the opposite direction of the velocity vector. The input to the code was a volume force, $[\text{N}/\text{m}^3]$.

By default all fluid in CFX is treated as a Newtonian fluid. That is appropriate for our simulations as the oils and the water are Newtonian fluids. The Newtonian model of fluid response is based on the following three assumptions [20]:

1. Shear stress is proportional to the rate of shear strain in a fluid particle.
2. Shear stress is zero when the rate of shear strain is zero.
3. The stress to rate-of-strain relation is isotropic—that is, there is no preferred orientation in the fluid.

Generally speaking the shear stress can therefore be modeled as [20]:

$$\tau_{ij} = \mu \frac{D\gamma_{ij}}{Dt} = \mu \left(\frac{\partial v_i}{\partial j} + \frac{\partial v_j}{\partial i} \right) \quad i \neq j \quad (5.1)$$

Hence the shear stress acting on the annular channel walls can be modeled as:

$$\tau_{xy} = \mu \left(\frac{\partial v_x}{\partial y} + \frac{\partial v_y}{\partial x} \right) \quad (5.2)$$

An active shear force results in pressure drop along the flow direction, thus the following force balance is introduced:

$$P\delta A_{cell-face} = \tau_{xy}\delta A_{wall} \quad (5.3)$$

If equation (5.3) is integrated over an arbitrary cell, assuming fully developed flow everywhere in the solution domain then:

$$\tau_{xy}A_{wall} = \Delta PA_{cell-face} \quad (5.4)$$

$$F_v V = \Delta PA_{cell-face} \quad (5.5)$$

Here A_{wall} and $A_{cell-face}$, is the the channel wall and the face connecting one cell to the next, respectively. In equation (5.5) the shear force has been substituted to find the desired volume

force, F_v . Next the pressure drop was defined employing the Darcy friction factor formulation and specifying the appropriate hydraulic diameter as defined in section 2.2 to be twice the gap size.

$$\Delta P = \frac{1}{2} f \frac{L_{cell}}{D_h} \rho u_{ave}^2 \quad (5.6)$$

S is defined as the annulus gap width, which varies depending on the geometry of interest. Combining equation (5.5), and (5.6), and solving for F_v , one arrives at equation (5.7). This equation is as expected similar to equation (2.7). The difference is that equation (2.7) represents the frictional pressure differential for an arbitrary value T , whereas equation (5.7) is the pressure drop over one cell divided by the length of the respective cell.

$$F_v = f \frac{1}{4S} \rho u_{ave}^2 \quad (5.7)$$

Much literature is available on fluid flow between parallel plates. To simplify the case there was assumed to be a fully developed flow in the entire domain when using relations to calculate the Darcy friction factor f . The friction factor for fully developed laminar flow between parallel plates is as given in equation (2.8).

$$f = \frac{96}{Re} \quad (5.8)$$

Equation (5.9) is a friction factor correlation for the case of transitional flow, and equation (5.10) is a friction factor correlation for fully turbulent flows [21]:

$$f = \frac{0.5072}{Re^{0.3}} \quad (5.9)$$

$$f = \frac{0.3472}{Re^{1/4}} \quad (5.10)$$

The assumption of fully-developed laminar flow is a reasonable approximation to employ for these simulations as the flow has a small velocity gradient in most of the simulation domain, as can be seen in figure 5.5, which depicts an example of the velocity contours observed. This is in part due to the fact that the velocity gradients in the flow directions are very small compared to the length scale of the entire domain. In addition, the entrance lengths before the velocity profiles are fully developed is very short compared to the domain size, due to the narrow annulus gap widths.

For channel flow between two parallel plates spaced apart a distance s , one can define the entrance length L_e as the point where the boundary layers from each side meet in the middle. The twin Blasius functions are close enough to the parabolic profile that one can say it is fully-developed at that point. Therefore, the boundary layer equation can be plugged in if the flow is laminar [22]:

$$x = L_e \Rightarrow \frac{s}{2} = \delta = 5\sqrt{\frac{\nu x}{U_\infty}} \quad (5.11)$$

$$L_e = \frac{s^2 U_\infty}{100\nu} \quad (5.12)$$

If Nexbase's fluid property values are plugged in together with the largest simulation gap size of 15 [mm], and an inlet velocity of 0.0148 [m/s], constituting a high flow rate of 40 [l/m], the entrance length is estimated by equation (5.12) to be approximately 0.3 [mm]. This serves to show that the entrance length is indeed negligible.

However, near the orifice the approximation of fully developed laminar flow may not be appropriate as the the velocity gradients are large in this region. The increasing velocities lead to higher local Reynolds numbers, suggesting that the flow may transition into turbulent flow near the orifice. Therefore, this study has tested out using different friction factors depending on the Reynolds number present. The motivation for this is the fact that the laminar friction factor equation (2.8) will grossly underpredict the friction factor for high Reynold number flows

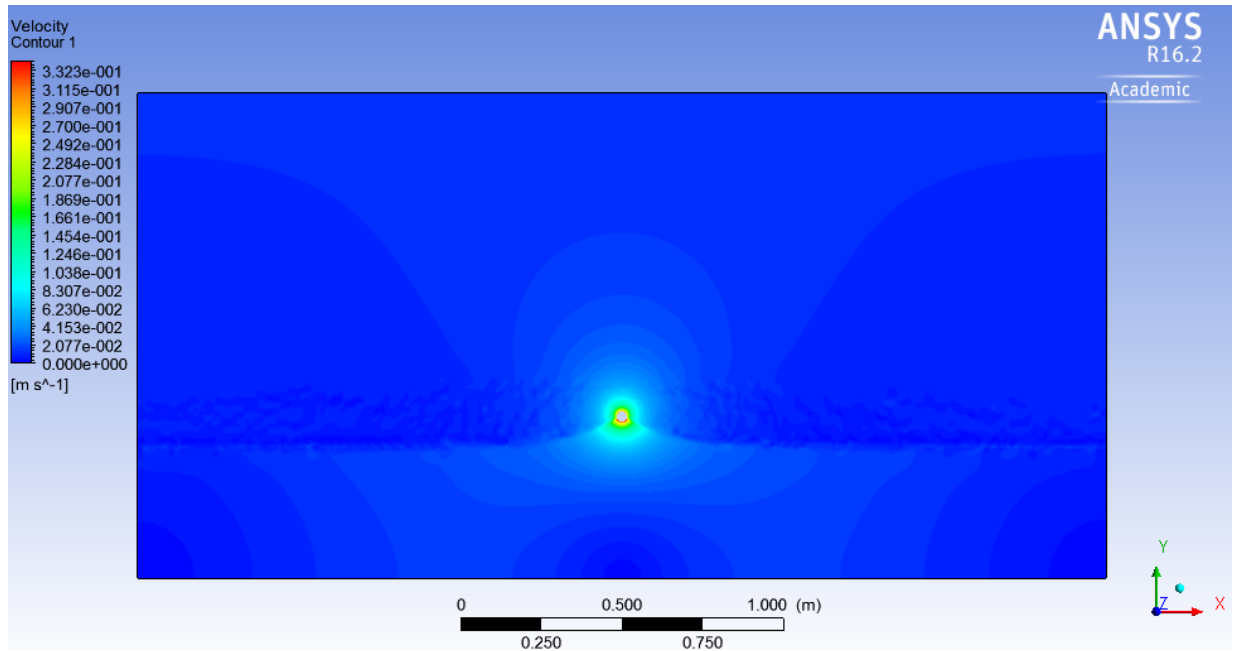


Figure 5.5: Velocity contours plot. Nexbase oil with annulus gap=10 [mm], $Q=20$ [l/m]

as seen in figure 5.6, or figure 5.7 which is plotted by R. R. Rothfus et al. explicitly for parallel plates, [23]. It is to be noted that the plot by R. R. Rothfus et al. utilizes the fanning friction factor, defined as one-fourth the value of the Darcy friction factor.

To quantify the differences in these modeling approaches the following cases were run:

1. Laminar solver utilizing laminar friction factor given in equation (5.8), for the entire simulation domain.
2. Laminar solver utilizing a laminar friction factor given in equation (5.8), for domain regions where $Re < 4000$, a transitional friction factor where the $4000 < Re < 20000$ given in equation (5.9), and a high Reynolds number friction factor when $Re > 20000$, given in equation (5.10).
3. Reynolds Stress Transport (RST) turbulent solver with gamma theta transition modeling, utilizing a laminar friction factor given in equation (5.8), for domain regions where the Reynolds number is < 4000 , a transitional friction factor where the $4000 < Re < 30000$ given in equation (5.9), and a high Reynolds number friction factor when $Re > 20000$, given in equation (5.10).

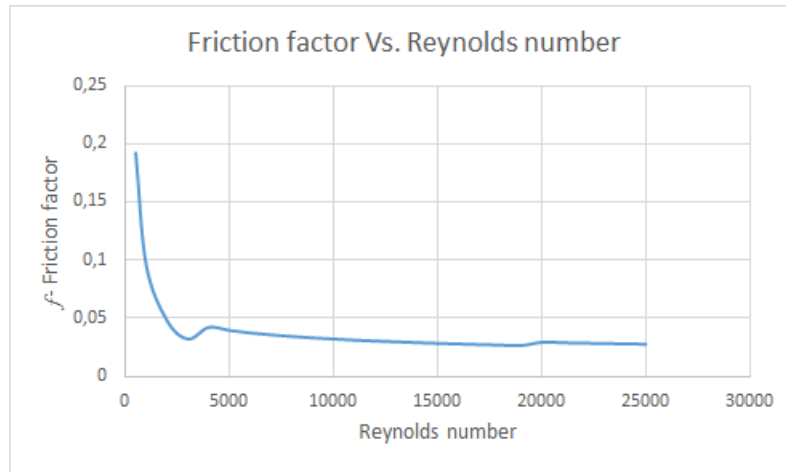


Figure 5.6: Friction factor as a function of Reynolds number, plotted using the the friction factors presented in equation (2.8), (5.9), and (5.10).

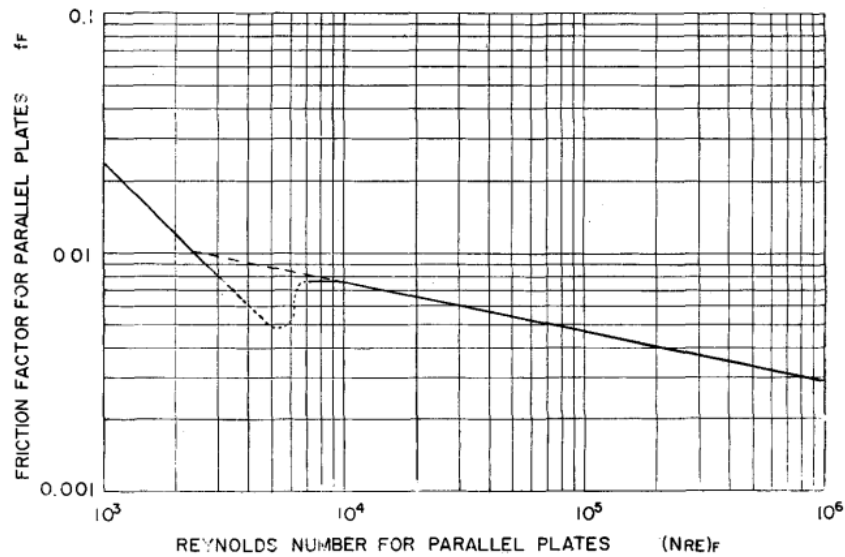


Figure 5.7: Friction factor as a function of Reynolds number, [23, page 208-212]

The friction factors were all implemented using expressions in the CFX-setup module. The complete list of the expressions used in the setup is as seen in figure 5.8. For the composite friction factor modeling, Boolean expressions were created to identify the appropriate correlation for a given computational node. In order to achieve this a series of other supporting expressions needed to be created. These include the cell velocity magnitude, velocity vector decomposition, Reynolds number, and gap size among others.

The latter of the three approaches attempts to take into account that there is a transition from

Expressions	
Reynolds	$(\text{Density} * (\text{cell velocity} + 0.0001[\text{m s}^{-1}])^2 * \text{spacing}) / \text{Dynamic Viscosity}$
cell velocity	$\text{sqrt}((\text{Velocity } u)^2 + (\text{Velocity } v)^2)$
friction factor composite	$\text{if}(\text{Reynolds} < 5000, \text{laminar friction factor}, 0) + \text{if}(\text{Reynolds} > 5000, 1, 0) * \text{if}(\text{Reynolds} < 20000, \text{transition friction factor}, 0) + \text{if}(\text{Reynolds} > 20000, \text{turbulent friction factor}, 0)$
friction force x	$-x\text{vec} * \text{volume force}$
friction force y	$-y\text{vec} * \text{volume force}$
laminar friction factor	$96 / \text{Reynolds}$
mass flow out	$\text{massFlow}() @ \text{outlet}$
oilVF 30	$\text{if}(((y + 0.0805[\text{m}]) / 1[\text{m}]) > 0, 1, 0)$
oilVF 70	$\text{if}(((y + 0.0405[\text{m}]) / 1[\text{m}]) > 0, 1, 0)$
oilVF 50	$\text{if}(((y + 0.0605[\text{m}]) / 1[\text{m}]) > 0, 1, 0)$
oilden	$845[\text{kg m}^{-3}]$
spacing	$0.01[\text{m}]$
transition friction factor	$0.5072 / (\text{Reynolds}^{0.3})$
turbulent friction factor	$0.3472 / (\text{Reynolds}^{0.25})$
volume force	$(\text{friction factor composite} * \text{Density} * (\text{cell velocity})^2) / (4 * \text{spacing})$
water cut	$(\text{areaAve}(\text{Density}) @ \text{outlet} - \text{oilden}) / (\text{waterden} - \text{oilden})$
waterVF 30	$\text{if}(((y + 0.0805[\text{m}]) / 1[\text{m}]) < 0, 1, 0)$
waterVF 50	$\text{if}(((y + 0.0605[\text{m}]) / 1[\text{m}]) < 0, 1, 0)$
waterVF 70	$\text{if}(((y + 0.0405[\text{m}]) / 1[\text{m}]) < 0, 1, 0)$
waterden	$1000[\text{kg m}^{-3}]$
xvec	$\text{Velocity } u / (\text{cell velocity} + 0.0001[\text{m s}^{-1}])$
yvec	$\text{Velocity } v / (\text{cell velocity} + 0.0001[\text{m s}^{-1}])$

Figure 5.8: Expressions implemented in the CFX-setup module.

laminar to turbulent flow in the water phase flow. One method of modelling this is by utilizing a Reynolds Stress Transport (RST) turbulence model together with a transition model. A more detailed description of these models is given in the solver settings section.

5.6 Initial Conditions

As mentioned the initial conditions are quintessential for this simulations and the results produced. Therefore, time was spent on how to correctly define them for the simulation. First off, it was assumed that all flow is stagnant at $t=0$, which represents the experimental case before the valve is opened.

Next, the interface level was set utilizing Boolean statements on the y-coordinates to achieve desired initial water heights. Several of these statements were generated to easily switch between different interface levels.

5.7 Meshing

Meshing is a key element to producing meaningful CFD results. The meshes employed were automatically generated by the CFX algorithms, however modifications were made to tailor fit the mesh. One mesh was made for every geometry created. This section outlines the main methods used in the meshing process.

The geometry domain was split in three regions: oil, water, and interface. The mesh was equally sized in the water and oil sub-domains, and consisted of hexahedral elements. The cells had a specified size growth away from the interface region. In the oil and water regions, large cells can be accepted because the velocities are small, and the gradients of both velocity and pressure are small.

In the interface region however, the sizing is smaller, especially near the orifice. For this region two different approaches were tested. The first was to create a region of densely packed tetrahedral elements near the orifice, as seen in figures 5.9, and 5.10. The second approach was to create a set of inflation layers extending out from the outlet, as seen in figures 5.11, and 5.12. The purpose of the smaller sizing and custom growth sizing from the orifice is due to the expectation that this is where the largest gradients appear. It is important that the resolution of the grid near the orifice is fine enough to capture small-scale flow phenomenon.

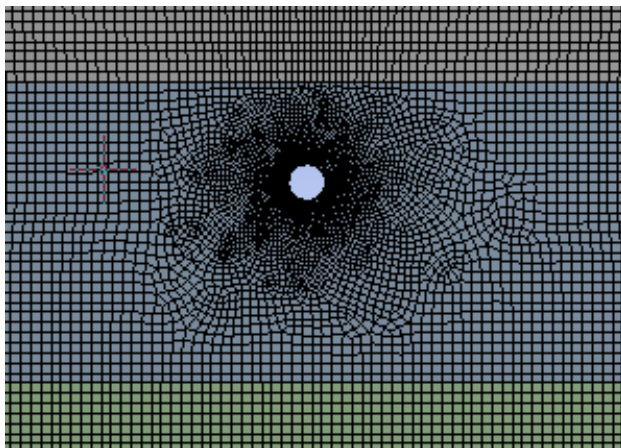


Figure 5.9: 2D Mesh.

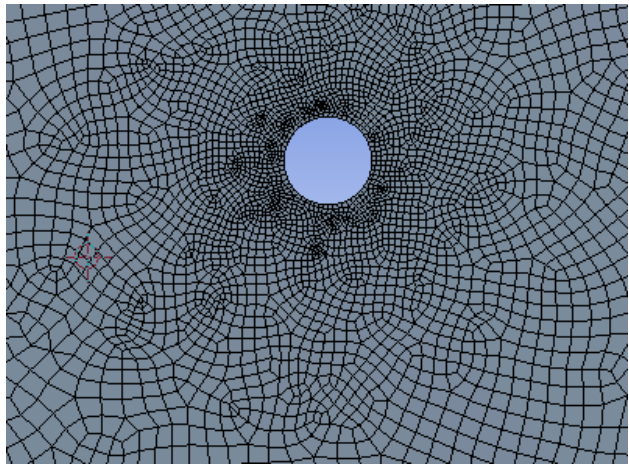


Figure 5.10: 2D Mesh, orifice up-close.

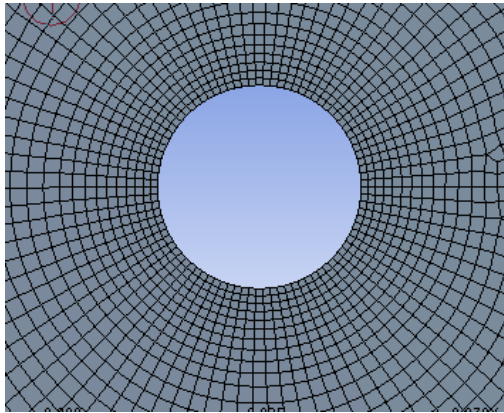


Figure 5.11: 2D Mesh, inflation layers at orifice.

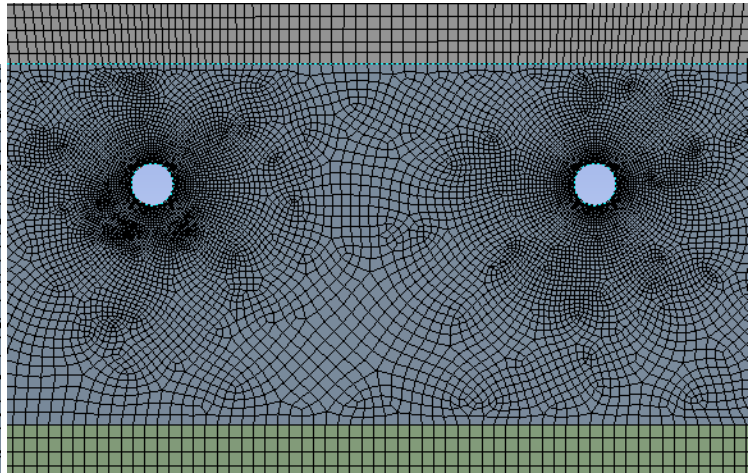


Figure 5.12: 2D Mesh, two outlet orifices with inflation layers.

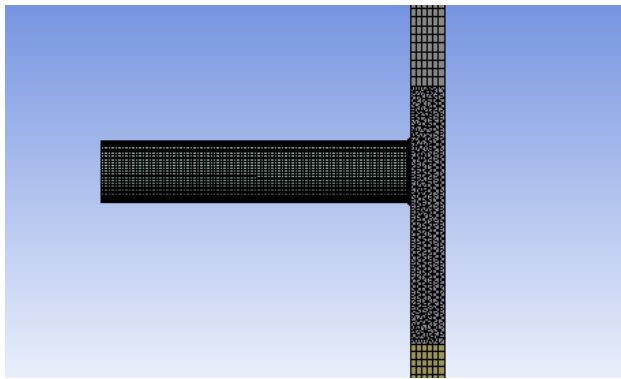


Figure 5.13: 3D Mesh, side view.

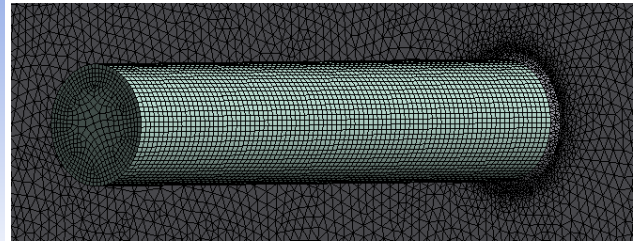


Figure 5.14: 3D Mesh, drainage pipe.

For the drainage pipe in the 3D geometry, a sweep function was employed which divides the length of the tube into equally long sections. The tube was then given several inflation layers to ensure that the velocity profile near the tube wall was accurately captured, as seen 5.14.

In order to obtain the the desired number of cell divisions across the annulus gap the sweep function was again utilized. In this manner 1 cell division was set for the 2D geometry, and 6 cell divisions for the 3D geometry, as seen in figure 5.13.

ANSYS-CFX is a finite volume code with a cell vertex formulation. This means in CFX the volume of control is assembled around the nodes, each cell is divided into sub-volumes. The flux through each face is based on the nodal values of the element. Thus, the number of nodes is of main importance, as it directly influences the computational power needed.

Table 5.1: Mesh Statistics

Geometry	Nodes	Elements
2D Tetrahedral, One outlet	98802	48325
2D Hexahedral inflation, One outlet	81520	40343
2D Hexahedral inflation, Two outlets	91380	45246
3D, One outlet	2587427	8007555

As seen from table 5.1, including the third dimension, and adding a drainage tube results in a large increase of nodes for the simulation domain. Thus the 3D simulations required far longer computational time. Computing on a desktop computer, a 2D simulation required approximately 15 minutes of simulation time, whereas a 3D simulation required in excess of 10 hours.

5.7.1 Mesh sensitivity analysis

A mesh sensitivity analysis was run to quantify how mesh refinement impacts the calculation of the transient simulations. The motivation for this analysis was to find a mesh that is sufficiently fine so that further refinement has little influence on calculation results, yet coarse enough so that the simulation can be run on a desktop computer in a reasonable amount of time.

The most important element of the sensitivity analysis is to refine or coarsen the mesh in a structured manner. The easiest manner to achieve this is often to use a global sizing control which changes all sizing options by a specified factor. However, in ANSYS-CFX this option is not available. Instead, all sizing options were manually changed as presented in table 5.2. In this fashion a structured refinement or coarsening was thus achieved.

As the the simulations in questions are transient, one can not simply use an arbitrary time step for the the respective meshes in a mesh sensitivity analysis. Instead, one must first conduct a time step sensitivity analysis for each of the respective meshes. It is expected that a finer mesh will require a smaller time step, and a that a coarser grid can suffice with a larger time step.

The base case for the simulation was as presented in table 5.3. This case was chosen because it demonstrated a significant amount of coning, and water breakthrough, giving rise to a time-

Table 5.2: Mesh Statistics, for mesh sensitivity analysis.

Tetrahedral Elements at Orifice				
	25% Refinement	Default mesh	25% Coarsening	50% Coarsening
Curvature angle [degrees]	3.2	4	5.3	8
Min element size [m]	0.00075	0.001	0.00125	0.0015
Max face size [m]	0.0075	0.01	0.0125	0.015
Max element size [m]	0.0075	0.01	0.0125	0.015
Nodes	167932	97808	63854	44450

Table 5.3: Base-case configurations for mesh sensitivity analysis.

Base Case			
Oil	Gap size [mm]	Water Level [mm]	Q [l/m]
Marcol	5	70	20

dependent trend to the mass flow at the outlet. Additionally, the residuals were low and the simulations demonstrated a stable behaviour. Several other case configurations could have been chosen for the base case. However, the important aspect is that the base case is representative of the study as a whole, and this was achieved by the case selection in question.

The sensitivity analysis was first run on the mesh consisting of densely packed tetrahedral cells near the outlet orifice. Mass flow at the outlet was chosen as the tracking parameter. Mass flow at the outlet is directly influenced by the coning height, the most important flow phenomenon occurring in the simulations, and therefore chosen as the parameter for comparison. Other parameters such as velocity at a specified Cartesian coordinate showed to be an inferior choice as the mesh refinement may cause the parameter to be interpolated from different nodes depending on element sizes.

As figures 5.15 - 5.18 indicate, a nearly mass flow independent time step was found for each mesh refinement/coarsening. However, when plotting the trends together with each mesh utilizing its respective time step, an unwanted behaviour was observed. It was expected that for a given time in the simulation the value of the mass flow would strictly increase or decrease as the density of the mesh was altered. However, from 5.19 it is evident that this was not the case. The

values of the mass flow increases as the mesh was made coarser, but when the mesh was refined the value of the mass flow was not lower than for the default mesh. It was in fact nearly equal to the case of a 50 % coarsening of the mesh.

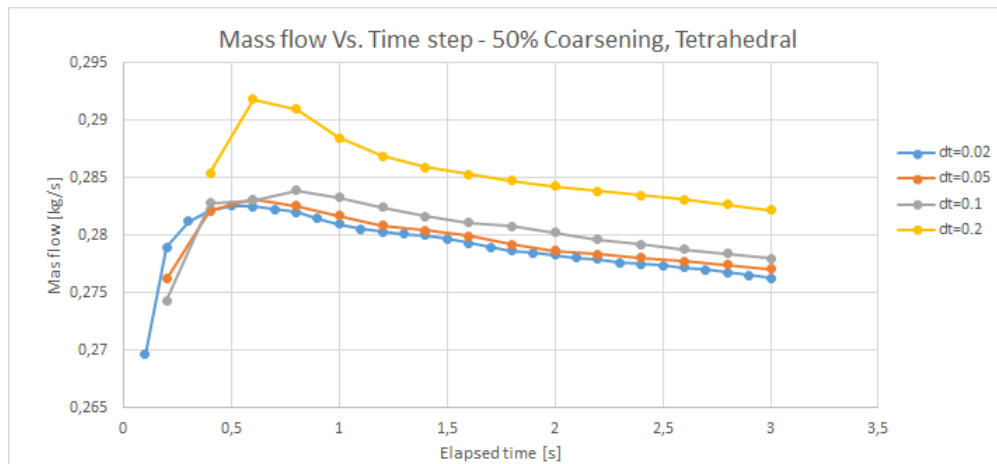


Figure 5.15: Mass flow vs. time step, 50% coarsening of mesh, tetrahedral at orifice.

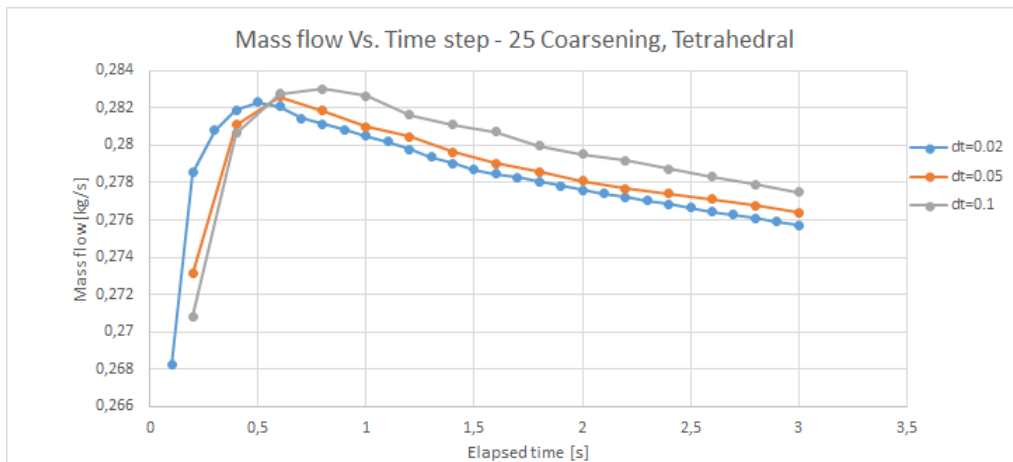


Figure 5.16: Mass flow vs. time step, 25% coarsening of mesh, tetrahedral at orifice.

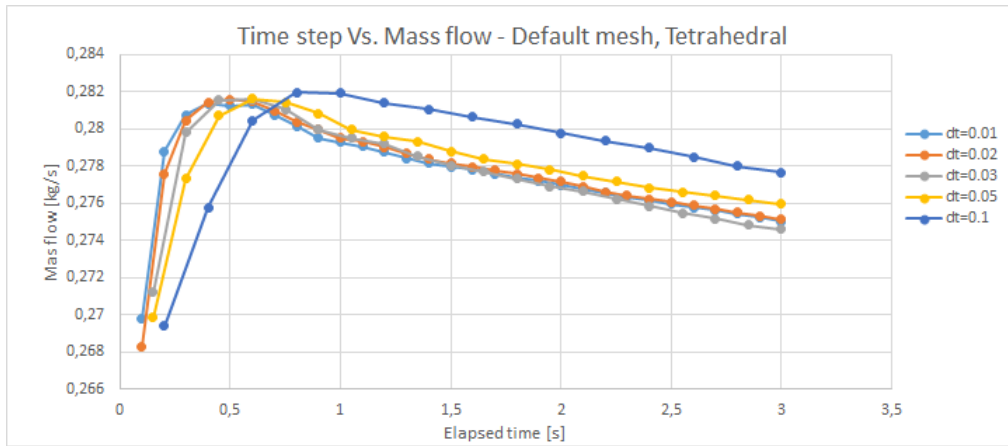


Figure 5.17: Mass flow vs. time step, default mesh, tetrahedral at orifice.

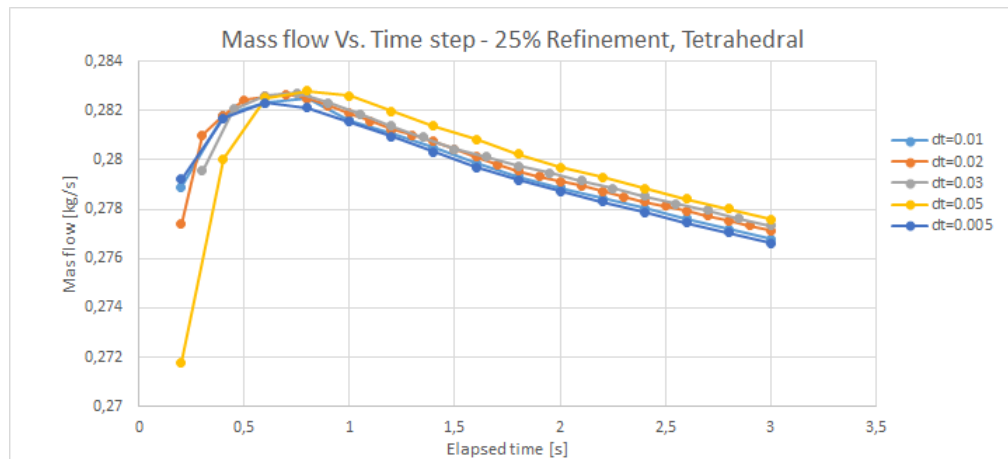


Figure 5.18: Mass flow vs. time step, 25% refinement of mesh, tetrahedral at orifice.

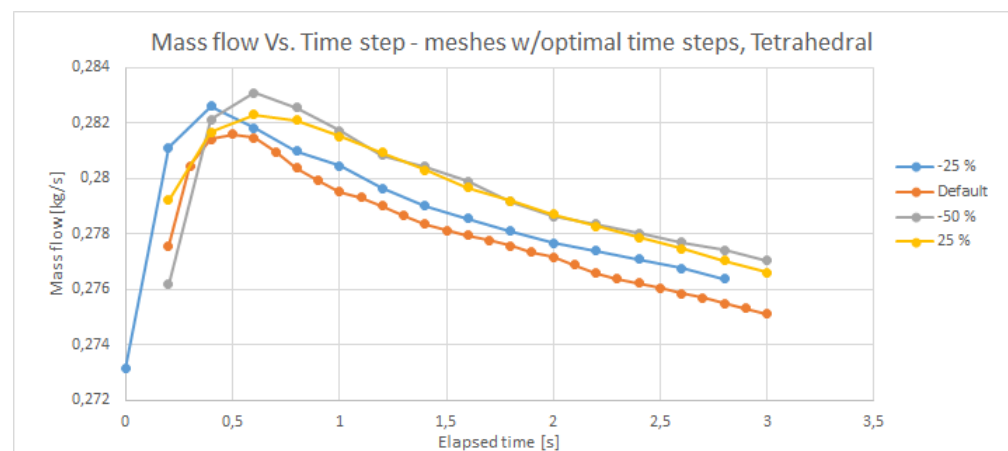


Figure 5.19: Comparison of meshes with respective optimal time steps.

It is more favorable to have a mesh displaying the expected trend as mentioned above. This is due to the fact that the mesh behavior is more predictable when making changes to parameter values. Even though the difference in mass flow was low for all meshes, it was decided to create a mesh that could display the expected trend when refining or coarsening the mesh.

The result was a mesh with 10 hexahedral inflation layers surrounding the outlet orifice as seen in figure 5.11. The same base case was used as with the mesh consisting of tetrahedral elements at the outlet. Moreover, the method of mesh refinement and coarsening was the same as in table 5.2, albeit consisting of fewer computational nodes, seen in figure 5.4, as the inflation method requires fewer elements than the hexahedral mesh.

Table 5.4: Mesh statistics for mesh with inflation Layers.

Mesh With Inflation Layers				
	25% Refinement	Default mesh	25% Coarsening	50% Coarsening
Nodes	131630	84618	57084	41666

As seen in figure 5.20 - 5.23, an appropriate time step was found for each mesh by testing out different values and seeking convergence in the mass flow parameter value as the time step was reduced. Comparison of the meshes with their respective optimal time step, figure 5.24, displayed the behavior of the mesh refinement which was desired. The value of the mass flow increased as the mesh was made coarser. Moreover, the line indicating the 25% refined mesh is only slightly below the line for the default mesh indicating a successful mesh sensitivity analysis. It is therefore evident that refining the mesh beyond the default mesh has little influence on the results, it will however increase the computational time needed. For these reasons the default mesh with hexahedral inflation layers was kept as the standard for all 2D simulations.

A mesh sensitivity analysis was not conducted for the 3D mesh. It was deemed to be very time consuming, and seeing as 3D simulations were not the main focus in this study it was dropped. Instead the result from the 2D mesh sensitivity analysis was used to quantify a suitable mesh resolution and time step. The 3D mesh was as mentioned made by using the 2D mesh with tetrahedral cells near the orifice and creating cell divisions in the z-direction. The results from

the mesh sensitivity analysis indicate that a time step of 0.02 seconds was more than adequate for the the default mesh resolution, thus this time step was chosen for the 3D simulations as well.

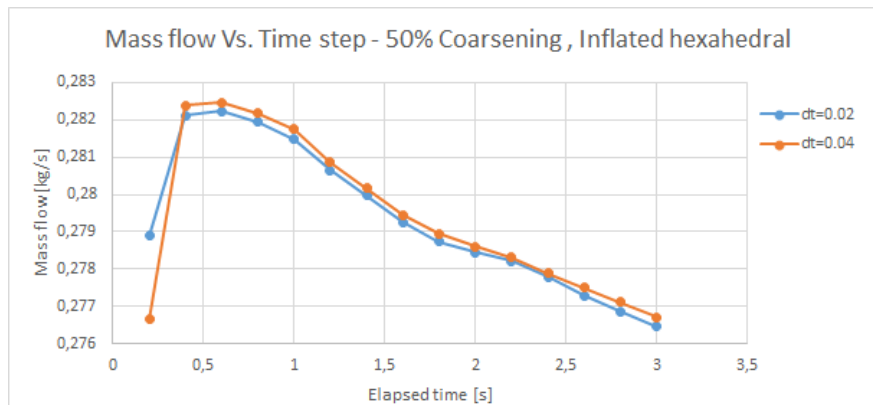


Figure 5.20: Mass flow vs. time step, 50% coarsening of mesh, inflated hexahedral at orifice.

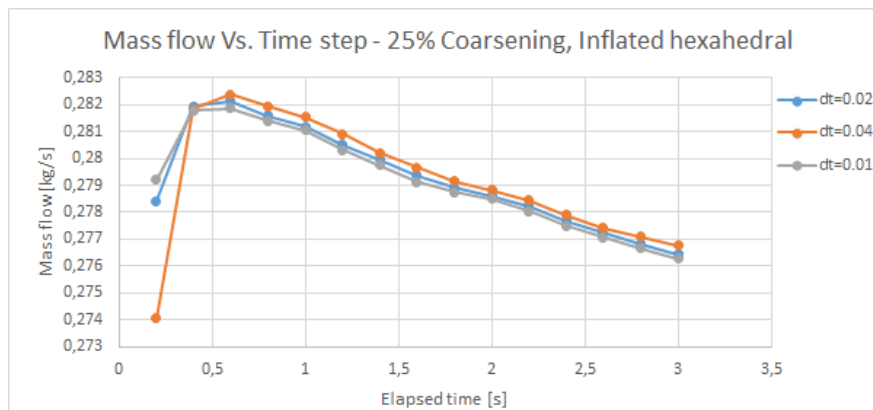


Figure 5.21: Mass flow vs. time step, 25% coarsening of mesh, inflated hexahedral at orifice.

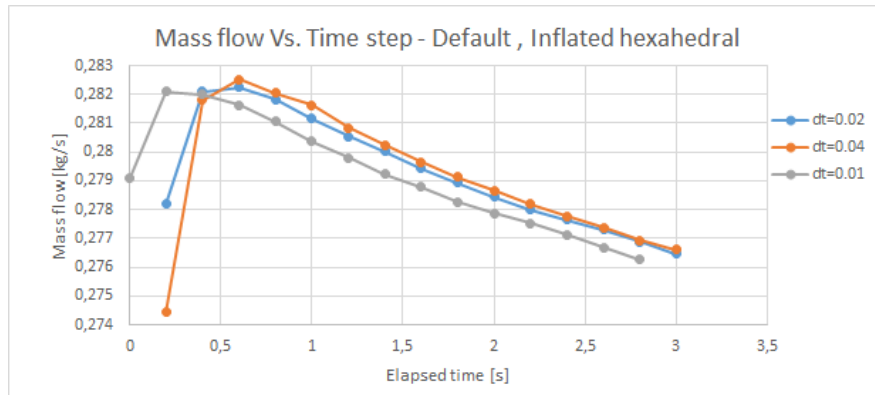


Figure 5.22: Mass flow vs. time step, default mesh, inflated hexahedral at orifice.

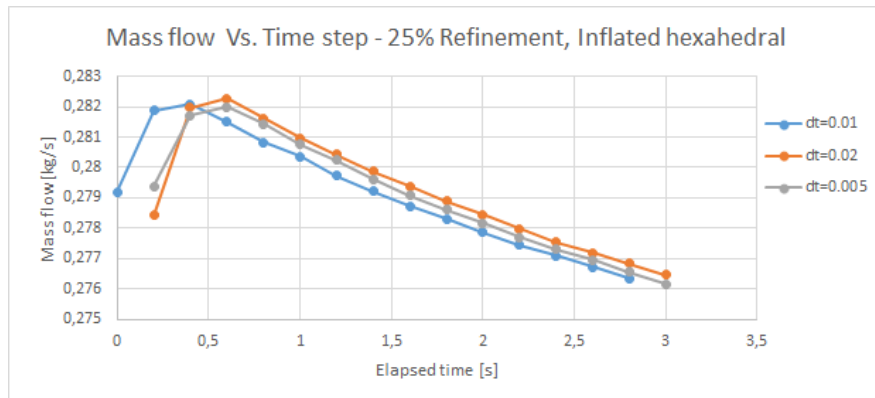


Figure 5.23: Mass flow vs. time step, 25% refinement of mesh, inflated hexahedral at orifice.

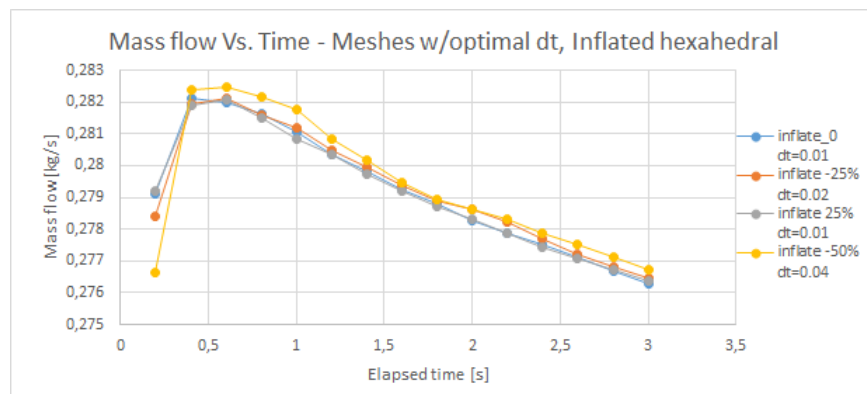


Figure 5.24: Comparison of meshes with respective optimal time steps.

5.8 Solver Settings

ANSYS-CFX presents with it an enormous range of possibilities with respect to solver settings, discretization schemes, and numerical models. In this section the important solver settings utilized are explained.

Multiphase description

A homogenous model was used to model the two fluid model. In a flow under gravity where the phases have completely stratified, for example a free surface flow where the interface is well defined. In such a case the volume fractions of the phases are equal to one or zero everywhere except at the phase boundaries. Thus it makes sense to use a single velocity field [24, section 7.5.2].

The free surface model was activated to capture the interface between the oil and water, with an interface compression level of two, listed as aggressive [24, section 7.18.1].

Interface transfer was set to none, as the intent was to neglect any interface transfer.

The Surface tension model was set to a continuum surface force, adding a surface tension coefficient of 0.04 [N/m]. Thesis supervisor Zhilin Yang suggested this value as it is a representative value for oil-water interfaces. Surface tension is a force that exists at a free interface that acts to minimize the surface area of the interface. It gives rise to effects such as a pressure discontinuity at the interface and capillary effects at adhesive walls [24, section 7.8.1].

Furthermore, a buoyancy model was activated to account for the differences in the densities of the fluids. The reference buoyancy density was set to 1000 [kg/m³], same as for water, and the force set to act in the negative y-direction. In effect this means that oil being the lighter component, has a negative relative density and will therefore feel a buoyancy force acting upward [24, section 1.2.9].

Advection scheme

The advection scheme implemented in ANSYS-CFX can be cast in the form:

$$\phi_{ip} = \phi_{up} + \beta \nabla \phi \Delta \vec{r} \quad (5.13)$$

Here is $\Delta \vec{r}$ the directional vector from the upwind node to the integration point. Particular choices of β yield different advection schemes [24, section 11.1.1.4.5]. For the simulation in this study a so-called high-resolution scheme was chosen, which implies a nonlinear relation for β .

Transient scheme

The default Second Order Backward Euler was kept. It is an implicit time-stepping scheme, and is second order accurate [24, section 15.4.2.8.2.1].

Since the scheme is implicit it allows for Courant numbers larger than 1. The upper Courant number limit is case dependent, however low residual values between inner loops within each time step, suggested that with a time step of $\Delta t = 0.02$ [s], a resulting maximum Courant number of 40 was tolerated.

For the two-dimensional case the Courant number C , is defined as:

$$C = \frac{u_x \Delta t}{\Delta x} + \frac{u_y \Delta t}{\Delta y} \quad (5.14)$$

Turbulence model

The RST-turbulence model was employed for a series of simulations. This approach makes use of experimental correlations. The correlations usually relate the turbulence intensity in the free-

stream to the momentum-thickness Reynolds number, at transition onset. ANSYS has developed a locally formulated transport equation for intermittency, which can be used to trigger transition. The full model is based on two transport equations, one for the intermittency and one for the transition onset criteria in terms of momentum thickness Reynolds number. It is called the ‘Gamma Theta Model’ and is the recommended transition model for general-purpose applications. It uses a new empirical correlation that has been developed to cover standard by-pass transition as well as flows in low free-stream turbulence environments [25]. This built-in correlation has been extensively validated together with the RST turbulence model for a wide range of transitional flows [24, section 4.1.10].

5.9 Monitors and Key Parameters

The most important parameters that were tracked during the simulations are those presented in table 5.5.

Table 5.5: Key Parameters

Parameter	Function of
Mass flow	Inlet velocity, Water cut, Orifice area, Oil
Water cut	Flow rate, Oil, Orifice area
Water jump	Flow rate, Oil, Orifice area

Mass flow was monitored by specifying a user function to integrate the mass flux over the orifice surface, which in the simulation is a band of length πD , and width δ , equal the cell layer width.

The mass flow allows for calculation of a mixture density ρ_m , given in equation (5.15). From this definition the water cut α , given in equation (5.16), can be calculated. To simplify the extraction of these desired quantities from the simulations, a user function was created, defined to monitor the value of α for every time step.

$$\rho_m = \frac{\dot{m}}{Q} \quad (5.15)$$

$$\alpha = \frac{\rho_m - \rho_o}{\rho_w - \rho_o} \quad (5.16)$$

Measuring the water jump from simulations was however more difficult. Creating a user function to automatically extract this value was challenging because the location of the tip of a cone was case dependent, and the interface between oil and water was usually smeared over 2-3 elements. Instead, the the water jump was identified using the CFX post-processing program. Once the time step at which the maximum coning height occurs was identified, a probe was inserted at the middle of the oil-water interface, and specified to extract the location of the max cone height in Cartesian coordinates. As the y-coordinate value for the initial interface level was known, the water jump was thus calculated using simple arithmetic.

For consistency the water jump was defined as the maximum water jump. Similarly, the mass flow rate was defined as the maximum mass flow rate observed from the monitor. Both the maximum water jump and maximum mass flow rate happen at the same point in time. Higher water jump results in higher mass flow rates, due to the higher density of water. In the cases where the water cone never reached the orifice the mass flow rate was equal for all time steps as there was only oil exiting through the orifice and conservation of mass ensures the total volume in the solution domain remained constant.

Chapter 6

CFD Results and Discussions

As stated previously the main goal of the CFD simulations in this study was to analyze to what extent 2D simulations can be used for simulating simplified ICD designs. 3D simulations have also been conducted to assess the hypothesis that 3D simulations can provide more accurate results when compared against experimental data.

The results from all 210 CFD simulations are presented in this chapter where each simulation case is assigned a respective section. Every subsection includes discussions and relevant comparisons of the observed findings.

6.1 Expectations

In the 2D simulations, the flow was not expected to behave identically to what was observed in the experiments. The simulations are unable to capture any three-dimensional effects. Furthermore, the valve inlet in the two-dimensional design was not expected to impose an identical pressure profile, as the two-dimensional outlet was only a pressure boundary.

The annulus gap in the lab experiments was in the range between 5 - 25 [mm], which implies there will be significant pressure losses as the flow moves through the annulus towards the valve

outlet. From equations (2.10), and (2.13) it can be seen that the annular gap width is very important as it appears to the third power in the friction pressure loss term and to the second power in the acceleration pressure loss term.

In the 2D simulations there are no annulus walls, only symmetry planes to ensure a two-dimensional domain, and therefore no annular friction pressure drop. The pressure drop was instead added synthetically as a volume force acting in the direction of the missing wall friction. This implies the friction forces was averaged over the annulus gap and not localized at the walls. This difference may trigger different flow patterns and ultimately deviating results, depending on the specified annulus width.

For the 3D simulations it was expected that the results may be in stronger agreement with the experimental findings as there are fewer modeling simplifications such as the added momentum source. Moreover, the friction force at the walls induces a more realistic parabolic velocity profile.

For narrow annulus widths, surface tension may become a factor of interest. The water will creep up slightly along the walls due to the differences in surface tension, as displayed in figure 6.1.

$$l = \frac{2\sigma \cos\Theta}{(\rho_w - \rho_o)g\delta} \quad (6.1)$$

To assess the theoretical height increase of water due to capillary rise, equation (6.1) may be used. It is applicable for parallel plates [26]. σ is the interfacial tension coefficient between the oil and water, and the water and the wall. The contact angle between the water and the plexiglas is unknown, as it was not quantified. Assuming Nexbase oil with a 5 [mm] annulus gap, and setting $\Theta = 80^\circ$ results in a capillary height l of 2 [mm]. However, assuming Marcol oil with a 15 [mm] annulus gap, and setting $\Theta = 80^\circ$, results in a capillary height l of 0.4 [mm]. These examples indicate that capillary rise, may have an impact on experiments with narrow annuli. As for the simulations, the effect of capillary rise was neglected by setting the contact angle to $\Theta = 90^\circ$. This was done because the 2D simulations do not have the capability to capture a

capillary rise, due to the fact that the gap has no cell divisions. The 3D simulation could however capture this effect, but was still chosen to be neglected as the effect is minor. Moreover, in this manner the two modeling approaches are more easily comparable.

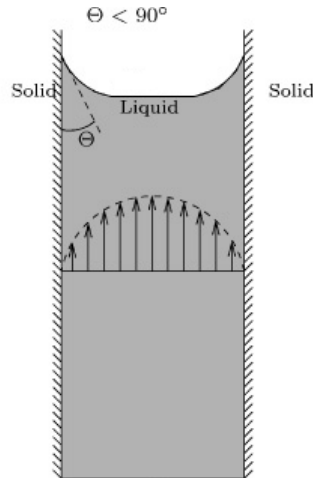


Figure 6.1: Example of capillary rise between parallel plates[27].

As described in section 5.7, a separate mesh was created for each respective annulus gap width. When comparing results from simulations utilizing different meshes one should normally be cautious, and take the necessary measures to make sure that the results are truly comparable. For this study that integrity was ensured by using identical meshing techniques for each annulus gap width, and running mesh integrity tests to ensure appropriate time steps were utilized. Thus, the influence of different meshes on result comparisons was deemed to be negligible.

6.2 2D Simulations - Single Outlet Orifice

For the geometry with one outlet orifice, tables 6.1, 6.2, and 6.3 were the reference for running the simulations. The tables indicate the varying parameter values for each individual simulation. This implies 15 simulations for every gap size. Since two oils were run on all three gap sizes, a total number of 90 simulation configurations were defined for the 2D simulations with one outlet orifice.

Table 6.1: Simulations for 5 [mm] gap

Gap=5[mm]		
Inlet Velocity [m/s]	Q [l/m]	Water Level [mm]
0.0111	10	30,50,70
0.0222	20	30,50,70
0.0333	30	30,50,70
0.0444	40	30,50,70
0.0555	50	30,50,70

Table 6.2: Simulations for 10 [mm] gap

Gap=10[mm]		
Inlet Velocity [m/s]	Q [l/m]	Water Level [mm]
0.00555	10	30,50,70
0.0111	20	30,50,70
0.01667	30	30,50,70
0.0222	40	30,50,70
0.0277	50	30,50,70

Table 6.3: Simulations for 15mm gap

Gap=15[mm]		
Inlet Velocity [m/s]	Q [l/m]	Water Level [mm]
0.0037	10	30,50,70
0.0074	20	30,50,70
0.0111	30	30,50,70
0.0148	40	30,50,70
0.0185	50	30,50,70

6.2.1 Laminar solver with laminar friction

As explained in the first approach of the possible ways to model the friction listed in section 5.5, the first set of simulations were conducted with a laminar solver employing the laminar friction correlation (5.8), to calculate the momentum source for each mesh element. For this approach the entire range of 90 simulation configurations was utilized.

Water jump

The simulations conducted indicate higher water jumps, i.e larger water coning height for increasing flow rates, and that once the water has reached the outlet orifice the jump increase is small if the flow rate is further increased.

Moreover, large differences were observed depending on the respective gap size and oil in question. If figures 6.2, 6.3, and 6.4 are compared, it is evident that the gap has a major impact on the coning height of the water. Smaller gap sizes induce a larger pressure loss and thus a larger water jump. It is also to be noted that the Nexbase oil generally results in a higher coning height when compared with the Marcol oil, due to the lower density difference between Nexbase and water, and the high viscosity of Nexbase. Moreover, the critical rates are observed to be lower for the Nexbase oil. In other words the transition from the a stable stationary cone to water breakthrough occurs at lower flow rates when utilizing the Nexbase oil. The figures also indicate that lower initial water levels gives potential for the largest water jump as we increase the flow rate. However, for low flow rates, the highest water jumps are obtained with high initial water levels. This is most evident from figure 6.4. The mentioned findings from these simulations, regarding water jump, were in agreement with the experimental observations.

The most important governing physics causing the water jump is the friction pressure losses in the annulus. As the flow rate is increased, the pressure gradient surrounding the orifice will increase, and extend further away from the orifice. This is why the simulations indicate a very small water jump for the low initial water levels, yet as the flow rate increases the water jump may surpass that of trials with higher initial water levels. This finding is however not adequately

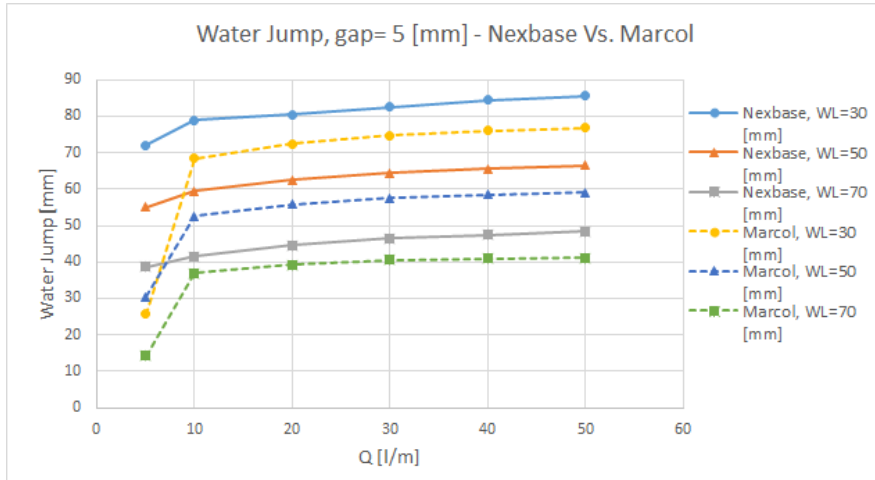


Figure 6.2: Water jump as a function of flowrate, Nexbase oil vs. Marcol oil with $\delta=5$ [mm].

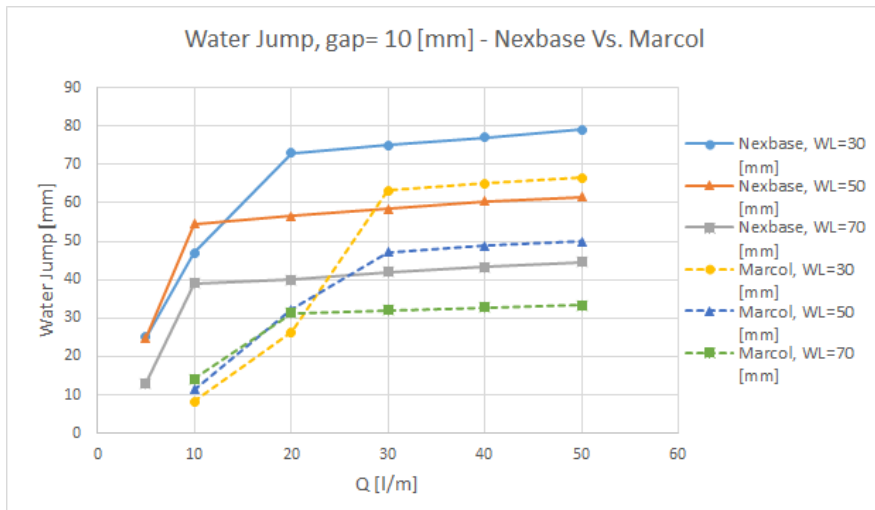


Figure 6.3: Water jump as a function of flowrate, Nexbase oil vs. Marcol oil with $\delta=10$ [mm].

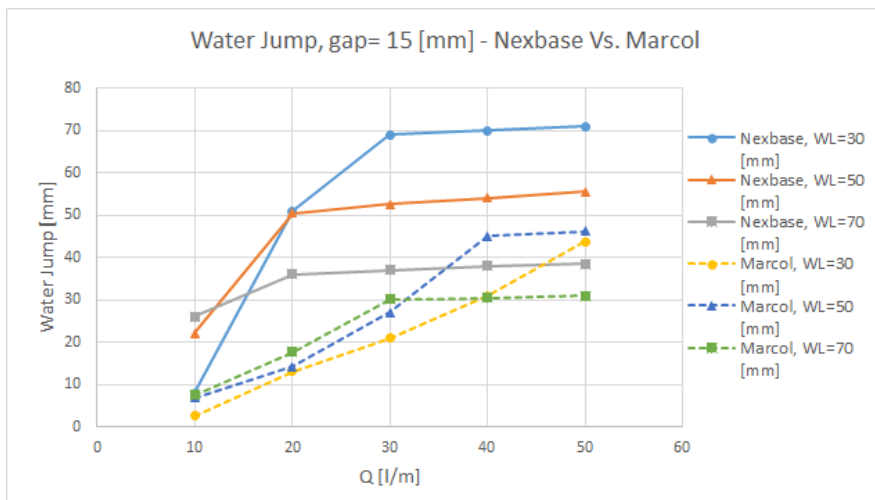


Figure 6.4: Water jump as a function of flowrate, Nexbase oil vs. Marcol oil with $\delta=15$ [mm].

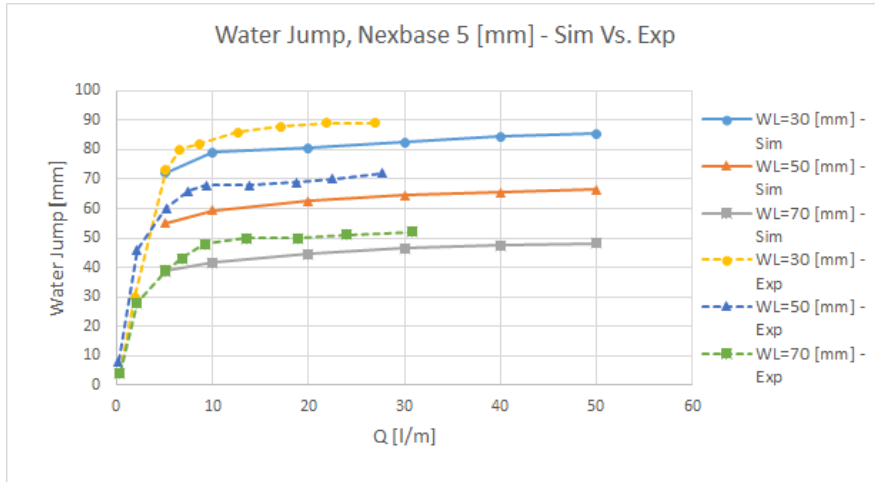


Figure 6.5: Water jump as a function of flowrate. Nexbase oil with $\delta=5$ [mm], simulation vs. experiment.

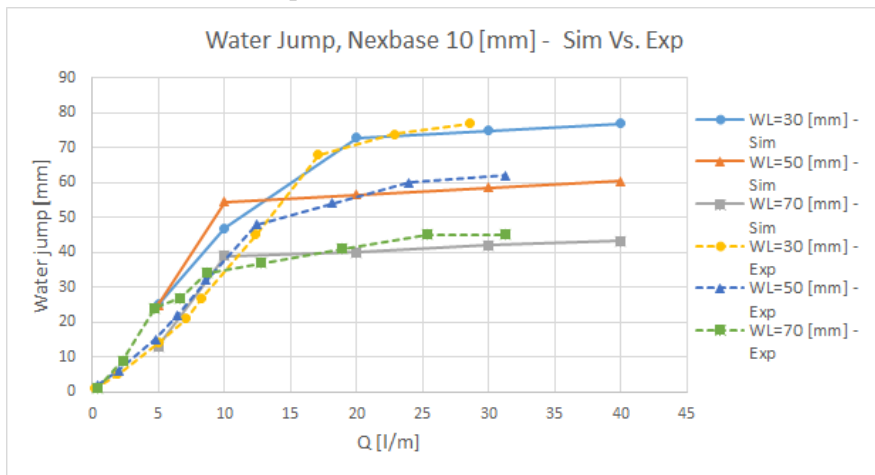


Figure 6.6: Water jump as a function of flowrate. Nexbase oil with $\delta=10$ [mm], simulation vs. experiment.

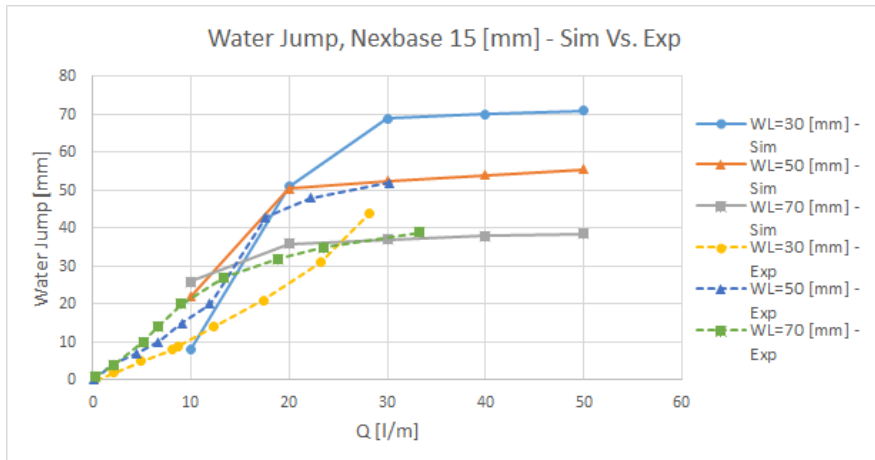


Figure 6.7: Water jump as a function of flowrate. Nexbase oil with $\delta=15$ [mm], simulation vs. experiment.

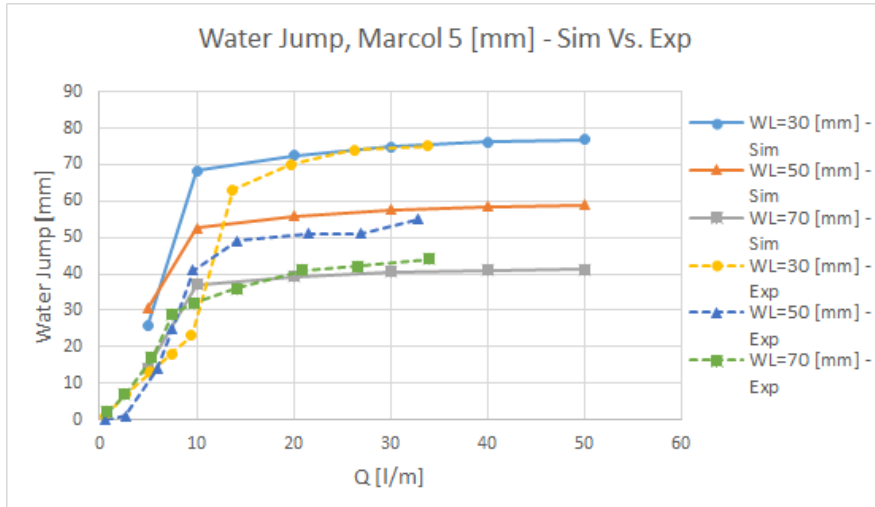


Figure 6.8: Water jump as a function of flowrate. Marcol oil with $\delta=5$ [mm], simulation vs. experiment.

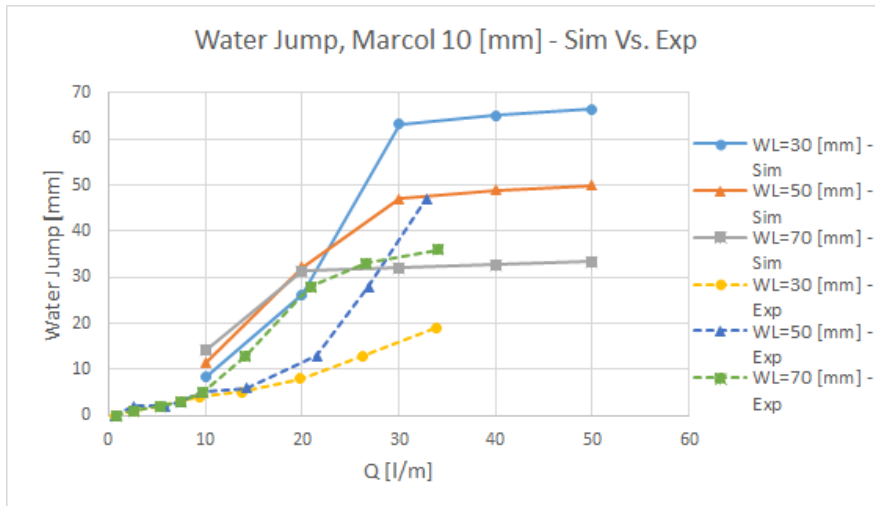


Figure 6.9: Water jump as a function of flowrate. Marcol oil with $\delta=10$ [mm], simulation vs. experiment.

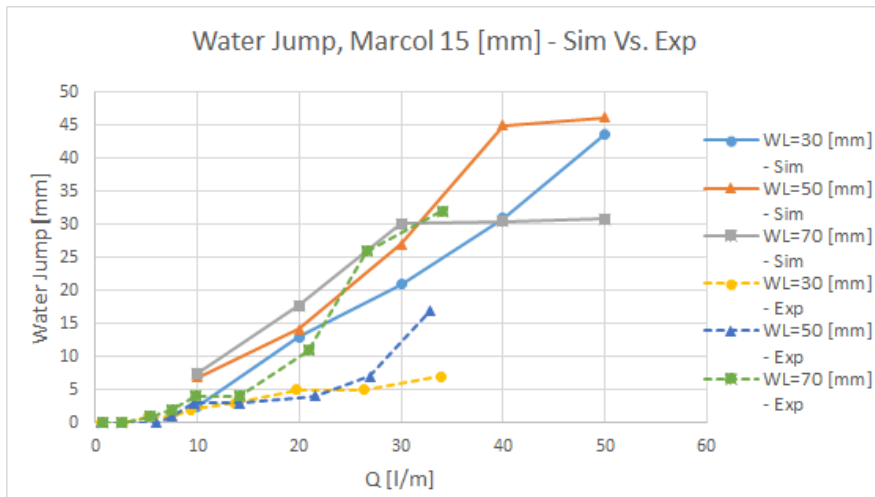


Figure 6.10: Water jump as a function of flowrate. Marcol oil with $\delta=15$ [mm], simulation vs. experiment.

displayed in the results from the simulations utilizing the smallest gaps as this would require runs conducted with a lower flow rate. Due to the difficulties of conducting simulations with low flow rates, as described in section 5.4 where the boundary conditions are discussed, this was not studied.

The outlining trends are in accordance with the experimental findings. However, a detailed comparison reveals several discrepancies. Figures 6.5, 6.6, and 6.7 indicate that the simulations overpredicted the water jump for low flow rates, and underpredicted for higher flow rates. The simulation results suggest that the overprediction was most significant for larger annulus gaps, as visualized in figure 6.7. However, the underprediction was predominantly observed in the cases with a small annulus gap, as visualized in figure 6.5.

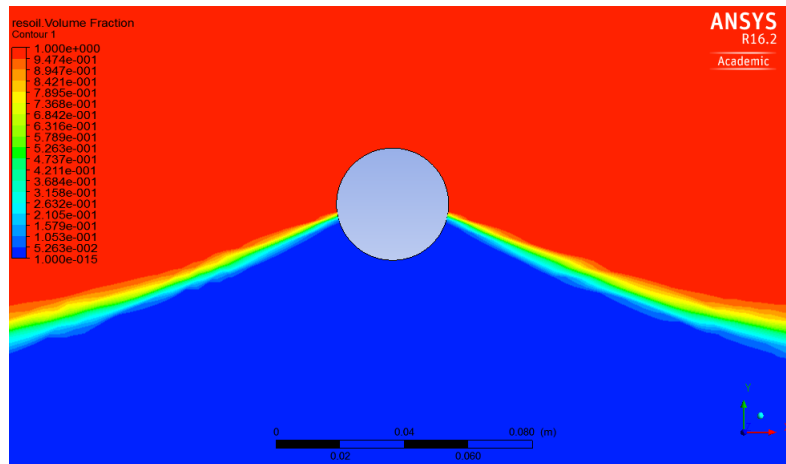


Figure 6.11: Example of water coning. Nexbase oil with $\delta=10$ [mm], $WL=10$ [mm], and $Q=20$ [l/m].

This discrepancy is believed to be due to two main factors. Firstly, the measured values of the water jump are as mentioned in section 5.9, the maximum values observed in the simulation. Videos from lab experiments show that the water cone had a tendency to oscillate in the vertical direction before potentially stabilizing as a stationary cone. This effect was observed to be more pervasive for experiments conducted with a larger gap and, and for less viscous oils. Secondly, the videos from the experiments also indicate that the water cone height maximum was at a location between the housing wall and the outlet orifice, effectively in front of the orifice. This fluid behavior was not achievable in the simulation as this was outside the simulation domain, as demonstrated by figure 6.11, the orifice being void of fluid except at the boundary.

The former factor results in overprediction at low flow rates as the water water jump in the simulations were measured at their peak values. The latter factor results in underprediction, as the two-dimensional simulation can not capture the fluid domain at which the maximum cone height occurs. This factor is for obvious reasons only of importance after water breakthrough.

Water cut

In accordance with the experiments, the simulations indicate that higher water cuts are achieved for higher flow rates. The simulations indicate that the highest water cuts are achieved when utilizing a denser and more viscous oil such as Nexbase, and lower values for the Marcol oil, as seen in figures 6.12, 6.13, and 6.14. Additionally, it was observed that a narrow gap has a greater potential for water cut, and that a higher initial water level results in a higher water cut even for flow rates much higher than that required for water breakthrough.

It is to be noted that the case with Nexbase oil, and annulus gap of 70 [mm], the trend is slightly different. The water cut reaches a maximum value at a flow rate of approximately 20 [l/m], after which it decreases slightly as the flow rate is further increased.

When simulation results are compared to the experimental data, large discrepancies are evident, especially for small annulus gaps, see figure 6.15, and 6.16. Moreover, the declining trend explained for the 5 [mm] gap utilizing Nexbase is more pronounced in the experimental findings. However, when comparing the water when utilizing a 15 [mm] gap, there is a closer match between the simulation and experimental values, as can be seen in figure 6.17.

The reason for this large discrepancy lies in the manner of how the water cut is extracted from the simulations. As explained in chapter 5.9 the water cut is measured as the maximum water cut observed in each respective simulation, in order to maintain a systematic measuring methodology. However, in the laboratory experiments the water cut was a time-averaged value.

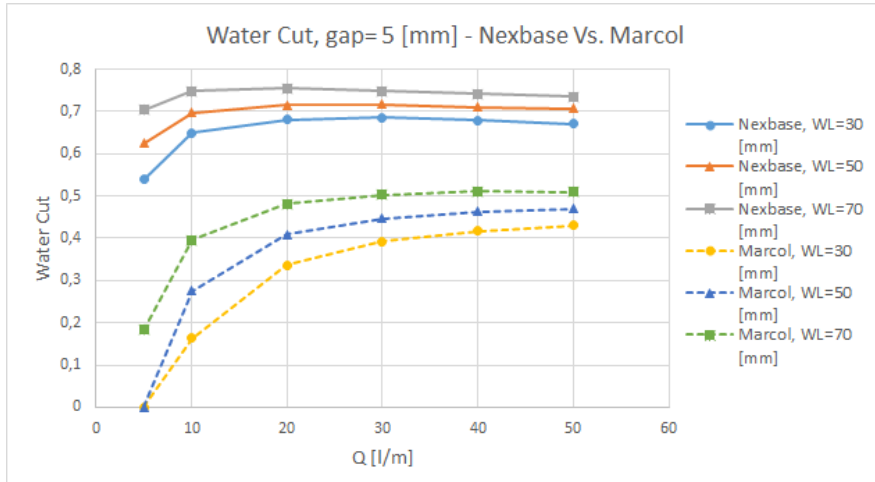


Figure 6.12: Water cut as a function of flowrate, Nexbase oil vs. Marcol oil with $\delta=5$ [mm].

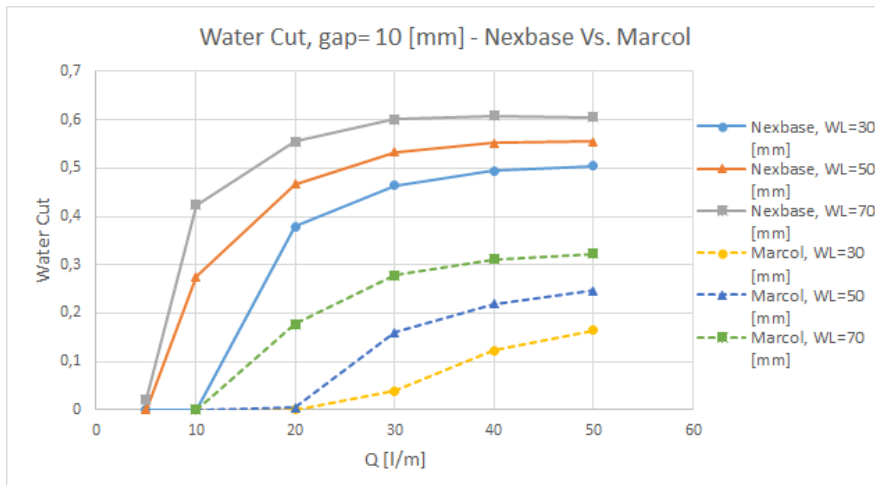


Figure 6.13: Water cut as a function of flowrate, Nexbase oil vs. Marcol oil with $\delta=10$ [mm].

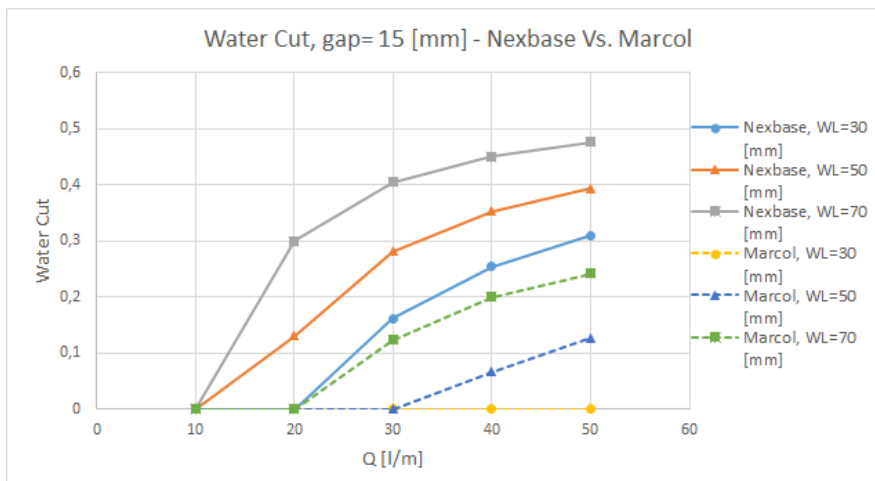


Figure 6.14: Water cut as a function of flowrate, Nexbase oil vs. Marcol oil with $\delta=15$ [mm].

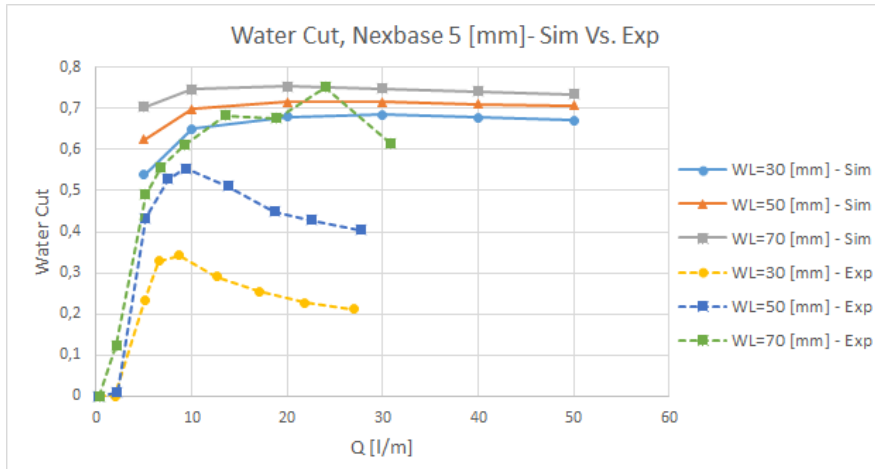


Figure 6.15: Water cut as a function of flowrate. Nexbase oil with $\delta=5$ [mm], simulation vs. experiment.

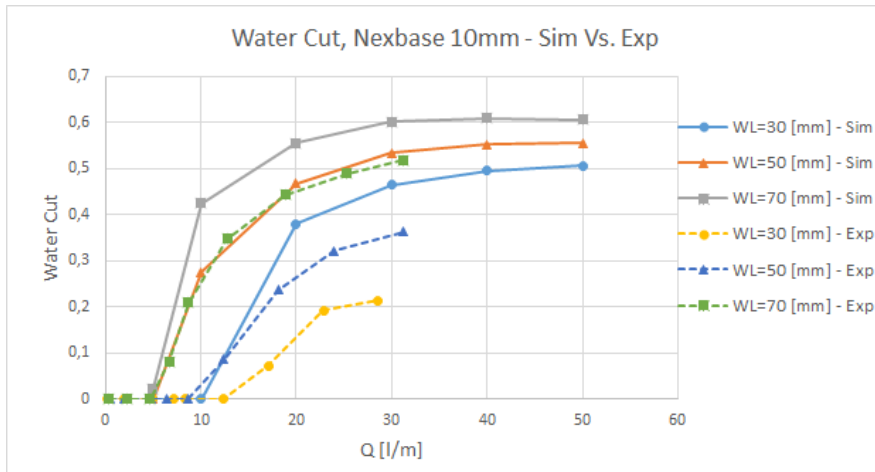


Figure 6.16: Water cut as a function of flowrate. Nexbase oil with $\delta=10$ [mm], simulation vs. experiment.

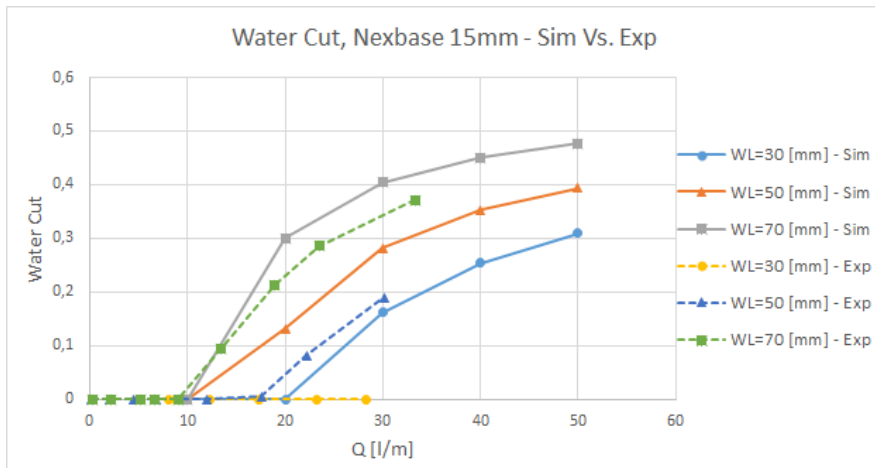


Figure 6.17: Water cut as a function of flowrate. Nexbase oil with $\delta=15$ [mm], simulation vs. experiment.

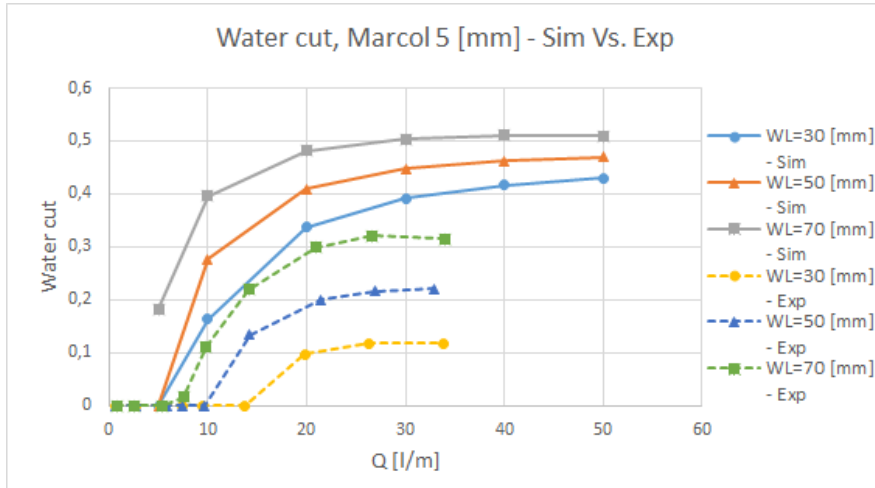


Figure 6.18: Water cut as a function of flowrate. Marcol oil with $\delta=5$ [mm], simulation vs. experiment.

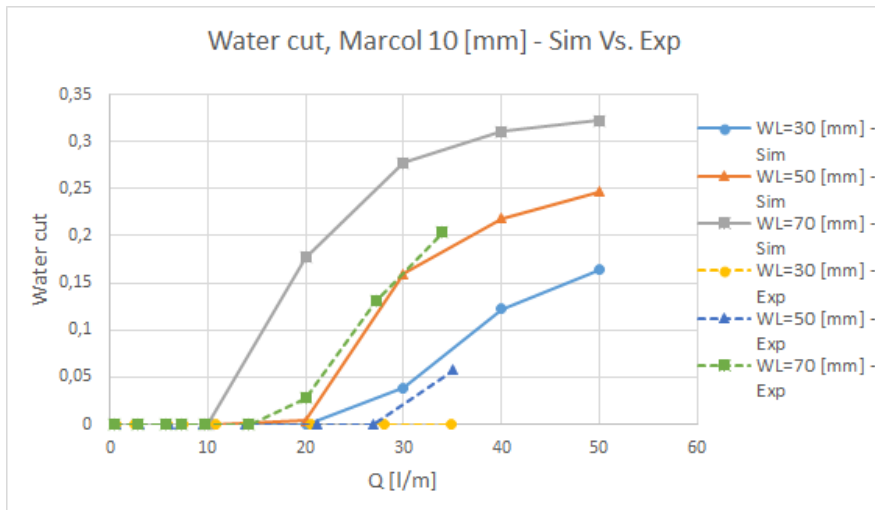


Figure 6.19: Water cut as a function of flowrate. Marcol oil with $\delta=5$ [mm], simulation vs. experiment.

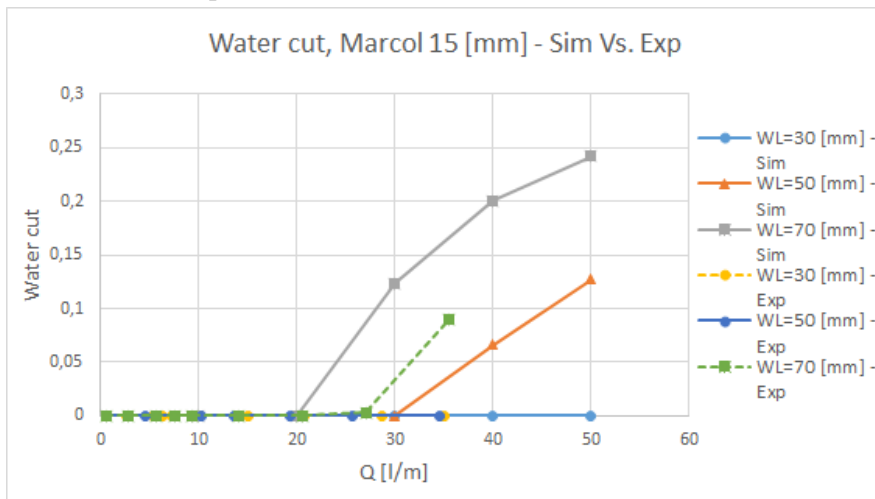


Figure 6.20: Water cut as a function of flowrate. Marcol oil with $\delta=5$ [mm], simulation vs. experiment.

6.2.2 Laminar solver with composite friction

Following the second approach explained in section 5.5, a series of simulations were conducted to see if the turbulent water regime near the orifice has a significant impact on the flow behavior observed. This was achieved by implementing three separate friction factors. The best suited friction factor value was activated by means of a Boolean statement depending on the Reynolds number at each respective computational node.

Water jump

The water jump expressed the same trend as observed when utilizing the laminar friction factor. Moreover most jumps were very similar in value when compared to each equivalent simulation conducted with a laminar friction factor formulation, as seen in figures 6.21, and 6.22.

The mentioned figures clearly show the differences in water jumps measured between the two approaches to be minimal, and arguably negligible for most of the comparisons when taking into account the expected inaccuracy when observing the values of the jumps. As mentioned in section 5.9, the reason for this inaccuracy arises from the fact that the jump was measured using graphical tools to locate a Cartesian coordinate at which the volume fraction of water was approximately 0.5. The margin of error is thus roughly considered to be ± 1 [mm].

There are however two comparisons that do not conform with the behavior of the other simulation comparisons. Figure 6.21 indicates a discrepancy of more than 3 millimeters for the comparison of the case utilizing Nexbase oil with a 15 [mm] gap, and a water level of 30 [mm]. Further, figure 6.22 indicates a discrepancy in excess of 2 millimeters for the case utilizing Marcol oil with a 5 [mm] gap, and a water level of 70 [mm]. Both are case configurations demonstrated by experiments to be near critical conditions, meaning that the water jump is sensitive to what modeling approach is utilized.

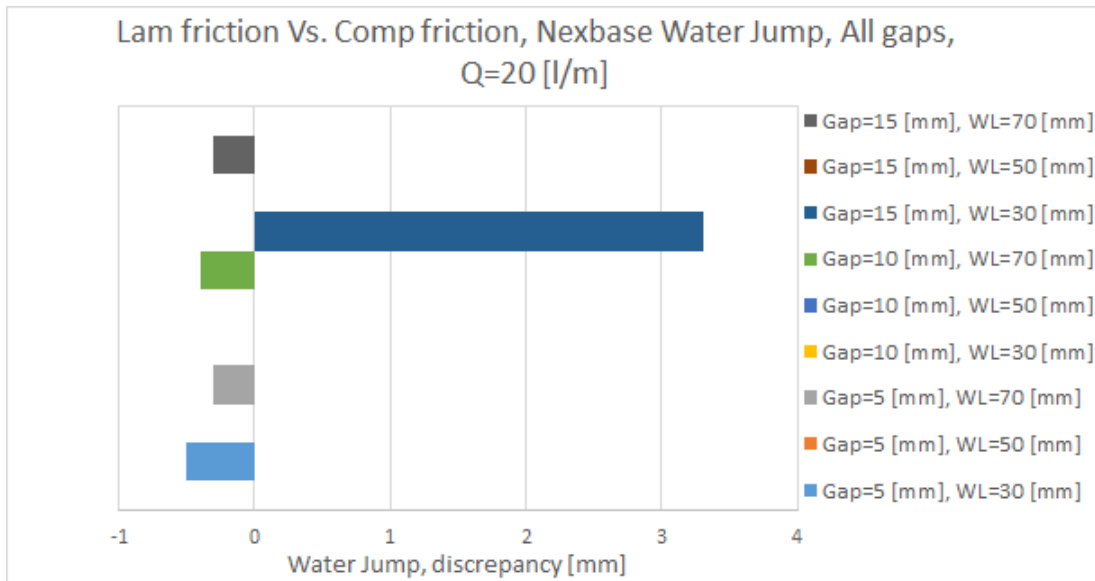


Figure 6.21: Water jump discrepancy, laminar friction vs. composite friction formulation. Nexbase oil, all gaps.

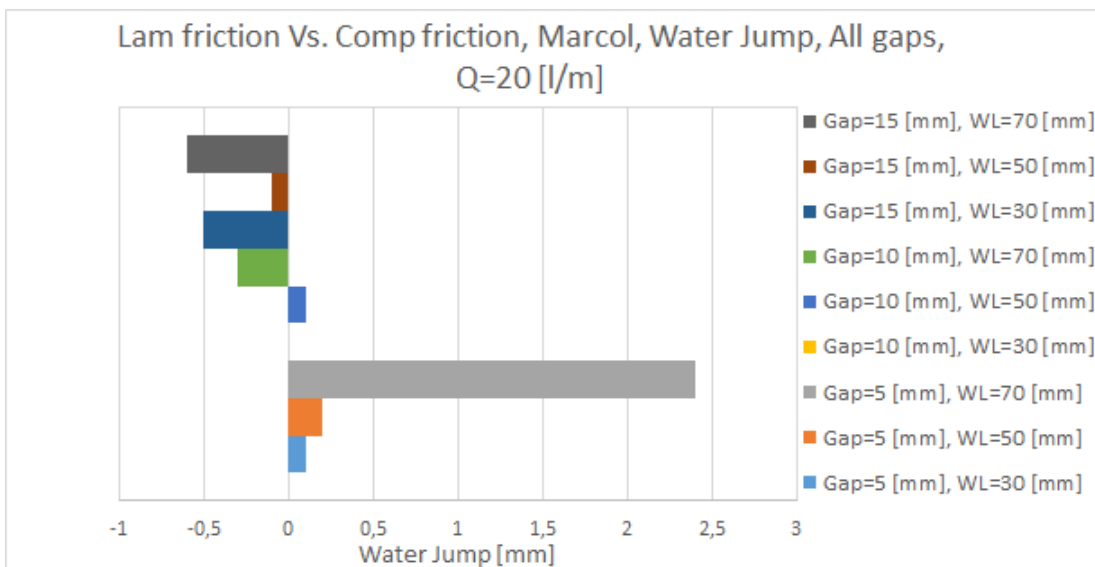


Figure 6.22: Water jump discrepancy, laminar friction vs. composite friction formulation. Marcol oil, all gaps.

Water cut

The discrepancies of the water cuts were in general relatively small, and for most of the case configurations there was no observed discrepancy. The water cut was computed using only the mass flow at the simulation domain outlet as a dependent variable, which was taken from the monitors created in the simulation setup. In other words, any discrepancy due to inaccuracy of measurement is negligible. Plots comparing the water cuts can be found in appendix B, in figures B.1, and B.2.

The previously mentioned figures suggest that the results are quite similar when modeling the friction as either a fully laminar flow or a composite friction taking into account transitional and turbulent flow near the orifice. However it is the authors opinion that more data would be needed to justify defining the discrepancies between these modelling approaches for negligible. The reason for this is the fact that the flow phenomenon of water coning is a stability problem. At small flow increases past a critical rate the water could jump from being a stable cone to protruding the orifice. This implies that if some preset simulation configurations were set sufficiently close to the critical conditions for water breakthrough, the two modelling approaches could produce significantly different results.

6.2.3 Transitional solver with composite friction

Following the third approach listed in section 5.5, the RST-turbulence model with an inbuilt transitional formulation, was employed to determine how a transitional model could predict the flow behavior. Moreover, it was of interest to discover discrepancies between the different modeling approaches.

Water jump

The water jump discrepancies were observed to be small for most simulation comparisons, as is evident from figures 6.23, and 6.24. However, the mean difference is larger than for the previous

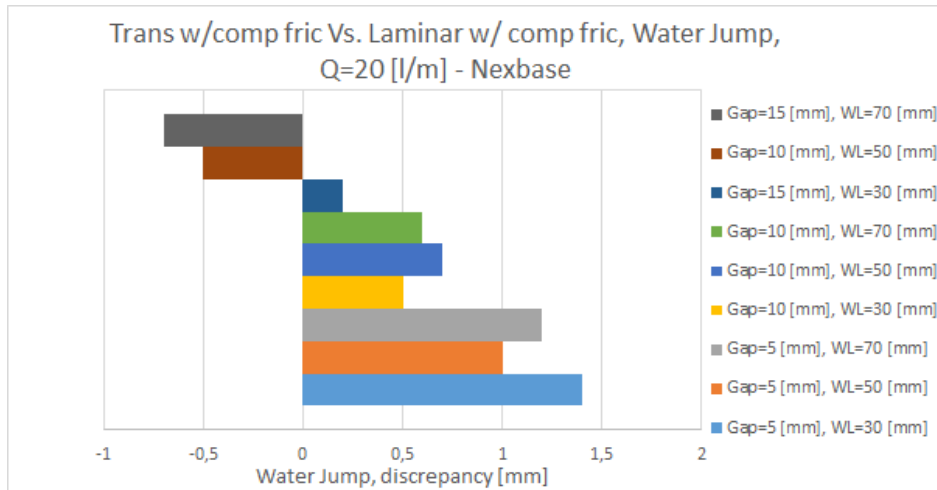


Figure 6.23: Water jump discrepancy. Transitional solver with laminar friction vs. laminar solver with composite friction formulation. Nexbase oil, all gaps.

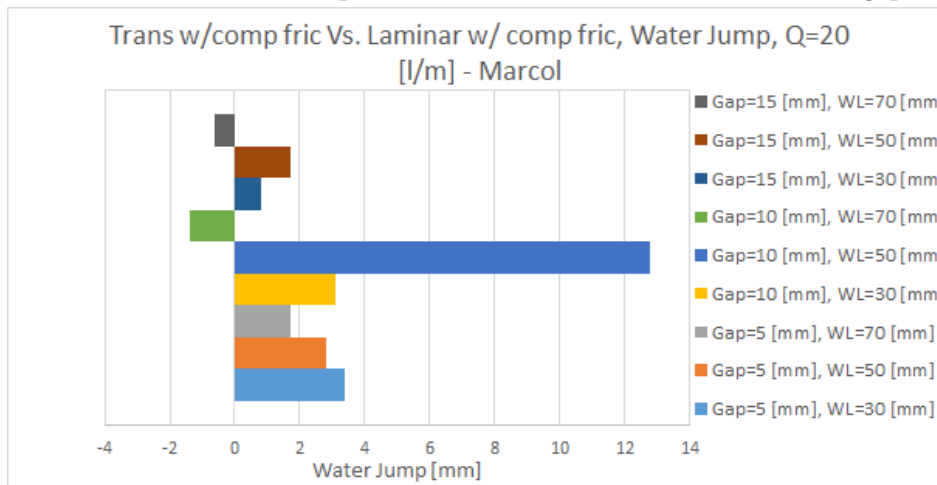


Figure 6.24: Water jump discrepancy. Transitional solver with laminar friction vs. laminar solver with composite friction formulation. Marcol oil, all gaps.

modeling approach, suggesting that the transitional model may produce significant discrepant results for given simulation cases, compared to that of the other modeling approaches. Moreover, figure 6.24, displays a large discrepancy for the simulation case utilizing Marcol oil with a 10 [mm] gap, and an initial water level of 50 [mm].

The case resulting in a large discrepancy had a flow rate close to a critical flow rate, thus small variances in how the transitional solver predicts flow behavior has in a sense pushed the stationary cone over the threshold. However, as can be seen from figure 6.25, this result is not in good agreement with the experimental results. The experimental results indicate that water

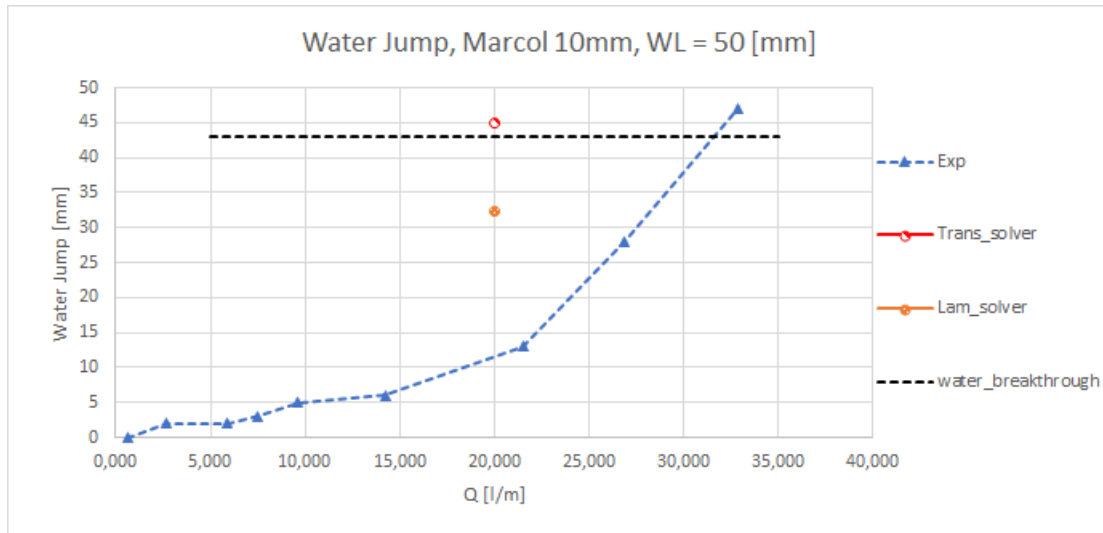


Figure 6.25: Water jump as a function of flowrate for Marcol oil with $\delta=10$ [mm], and $WL=50$ [mm]. Plotted for transitional solver with laminar friction, laminar solver with composite friction formulation, and experiment values.

breakthrough at the orifice only occurs for significantly higher flow rates, as can be read from the bottom axis in figure 6.25. The dashed black line in figure 6.25, constitutes a cone height at which water breakthrough at the orifice occurs.

The mentioned large discrepancy depending on the solver used, is a signal that caution must be taken when predicting water jump values. From figure 6.25 is it clear that the discrepancy was in fact large in this case configuration for both the laminar solver utilizing the composite friction method, and for the transient solver utilizing the composite friction method.

Water cut

Due to the fact that water cut values are computed directly using mass flow values retrieved from the simulation post processing, the discrepancy is generally lower than when compared to the water jump discrepancy. However, again the case for Marcol oil with $\delta=10$ [mm] and $WL=50$ [mm] stands out. The laminar solver with composite friction formulation predicts there to be water breakthrough as seen in figure 6.25, however the transient solver predicts a slight case of water breakthrough.

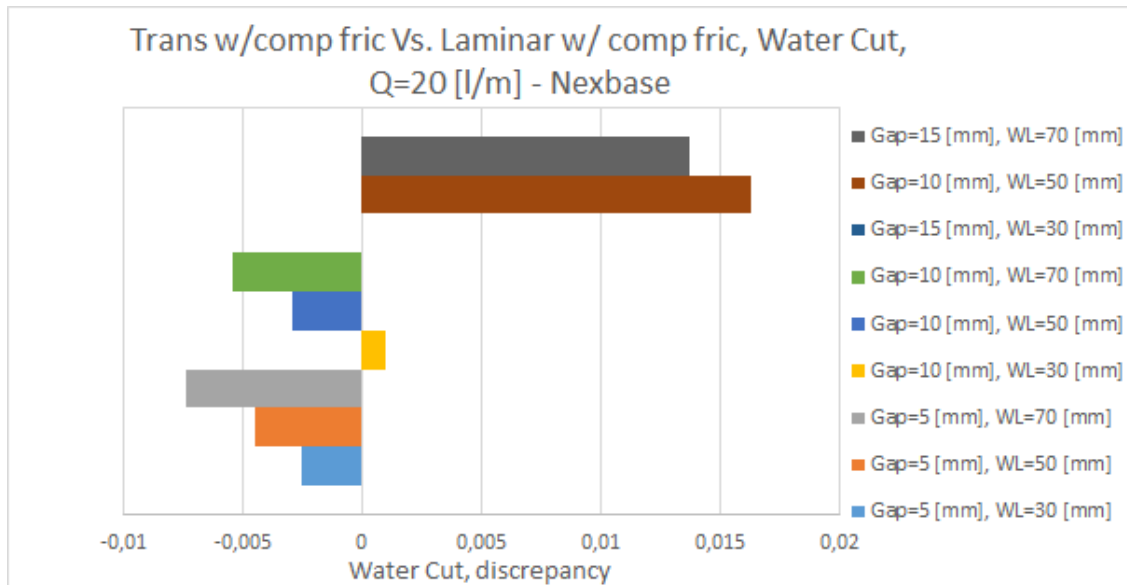


Figure 6.26: Water cut discrepancy. Transitional solver with laminar friction vs. laminar solver with composite friction formulation. Nexbase oil, all gaps.

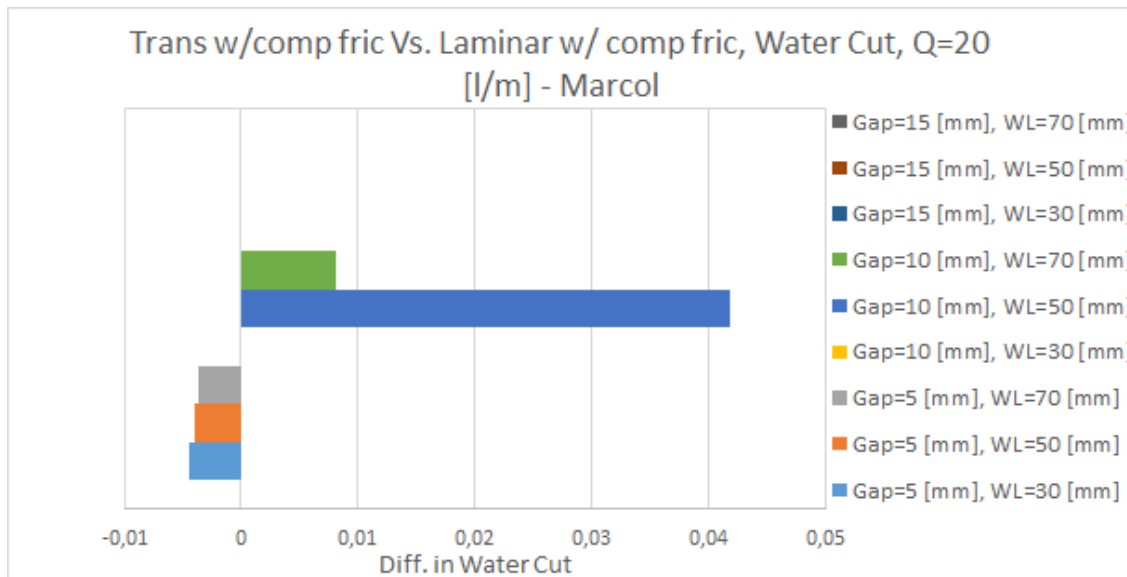


Figure 6.27: Water cut discrepancy. Transitional solver with laminar friction vs. laminar solver with composite friction formulation. Marcol oil, all gaps.

In this subsection clustered bar charts are used to display the discrepancies in the results between the transitional solver approach and the laminar solver approach. For some simulation case configurations the discrepancy was zero, hence there is no observable bar for these cases. The bars are plotted in the same order as their respective legends, seen to the far right in the figures.

6.3 2D Simulations - Multiple Outlet Orifices

A series of simulations with two outlet orifices was conducted for this study. The results from these simulations are presented here, and compared against the experimental data acquired from the laboratory experiments. Table 6.4 lists the experiment cases on which the comparison in this section is based upon.

Table 6.4: Experiments used for comparison with simulations.

Experiments for Comparison			
Oil	Gap[mm]	WL [mm]	Valve position
Nexbase	10, 15	30, 50, 70	All
Marcol	5, 10	30, 50, 70	All

Water jump

The water jump was measured in the same fashion as for all simulations with one outlet orifice; the highest observed water jump in the simulation domain. Because of the inherent symmetry in the geometry with two outlets, water jumps and water cuts were equal for each outlet in the simulations conducted.

As can be seen in figures 6.28 - 6.31, it is evident that the annulus gap has a significant impact on the discrepancies in water jump between the experimental findings and the levels retrieved from the simulations. Moreover, it is clear that the discrepancies were smaller for more narrow annulus gaps.

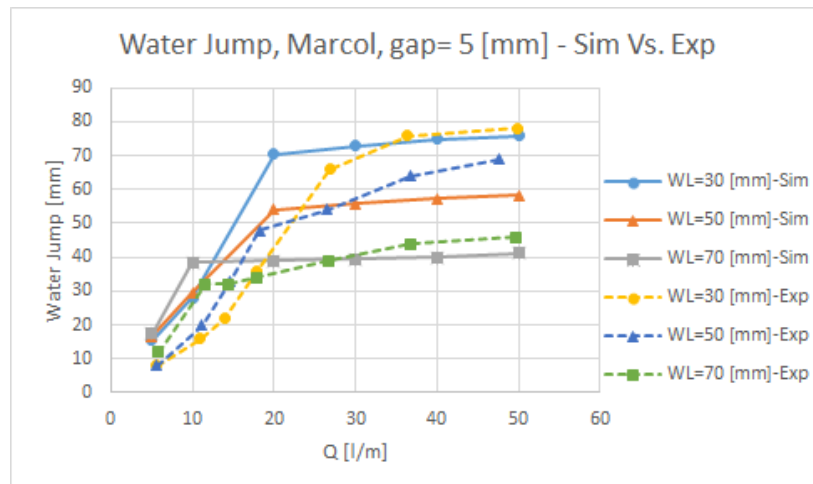


Figure 6.28: Water jump as a function of flowrate. Marcol oil with $\delta=5$ [mm], simulation vs. experiment.

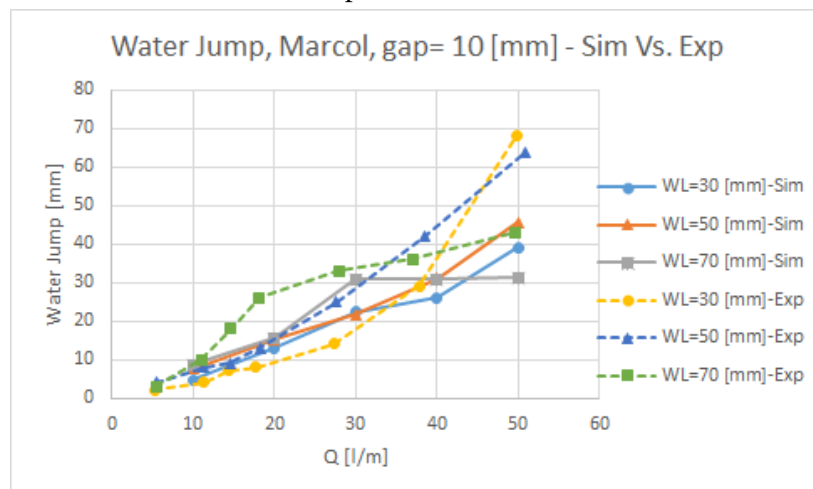


Figure 6.29: Water jump as a function of flowrate. Marcol oil with $\delta=10$ [mm], simulation vs. experiment.

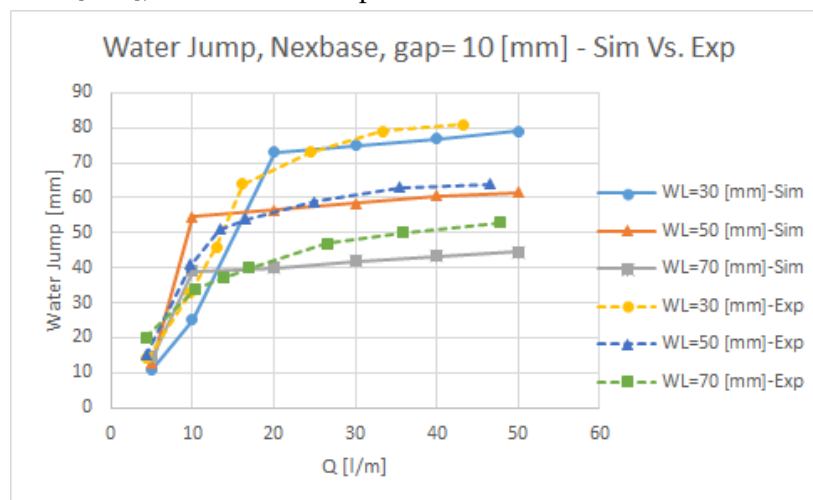


Figure 6.30: Water jump as a function of flowrate. Nexbase oil with $\delta=10$ [mm], simulation vs. experiment.

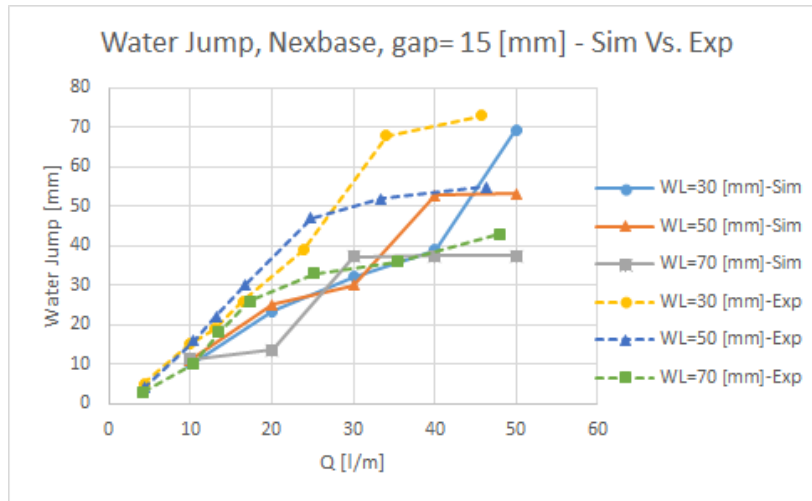


Figure 6.31: Water jump as a function of flowrate. Nexbase oil with $\delta=15$ [mm], simulation vs. experiment.

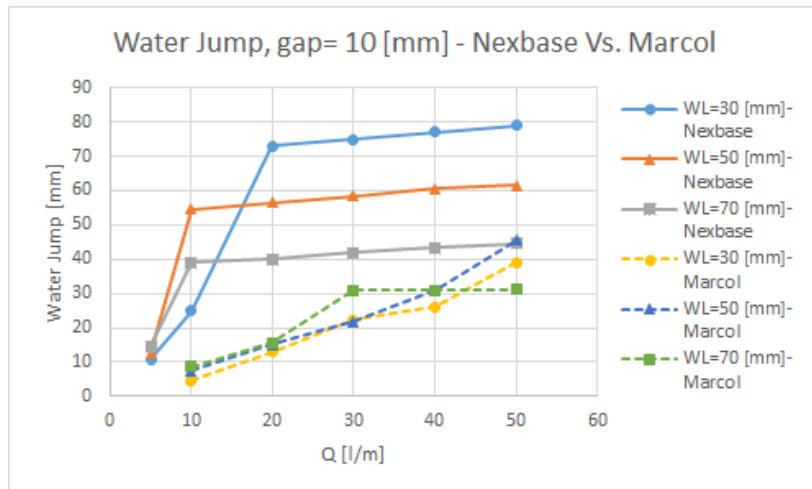


Figure 6.32: Water jump as a function of flowrate, Nexbase vs. Marcol, $\delta=10$ [mm].

It is also to be noted that the simulations underpredict the critical flow rates for for the largest annulus gaps in this comparison study, as seen in figures 6.29, and 6.31. This is implied by observing that the curves for the experimental water jump levels rise sharply at lower flow rates than that of the simulation levels. However, for the smaller annulus gaps this was not the case. Figure 6.28 demonstrates that the critical flow rate was lower in the simulation than in the experiments. In the case of the Nexbase oil with a 10 [mm] gap, the discrepancy was small.

Figure 6.32 shows the difference in behaviour between the Nexbase oil and the Marcol oil. As expected, the denser and the more viscous Nexbase oil generated a higher water cone, and reached

a critical water level far earlier than what was observed in the simulations utilizing Marcol oil.

Water Cut

The water cut for this series of simulations also seems to be significantly dependent on the annulus gap size. Both experiments and simulations demonstrate a decreasing water cut for an increasing gap size, as expected. However, the comparison between the two demonstrates different trends depending on the annulus gap.

When comparing figures 6.33 and 6.34, it is evident that for the case of a smaller gap size the simulations overpredicts the water cut for all initial water levels, and that for the larger gap size the simulations underpredict.

It is also be noted that for the Marcol oil the discrepancy increases for decreasing initial water level in the case of a 5 [mm] gap, and decreases for decreasing initial water level in the case of a 10 [mm] gap. For the cases utilizing Nexbase oil, the discrepancy was observed to increase for decreasing initial water levels for both gap sizes utilized, as seen in figures 6.35 and 6.36.

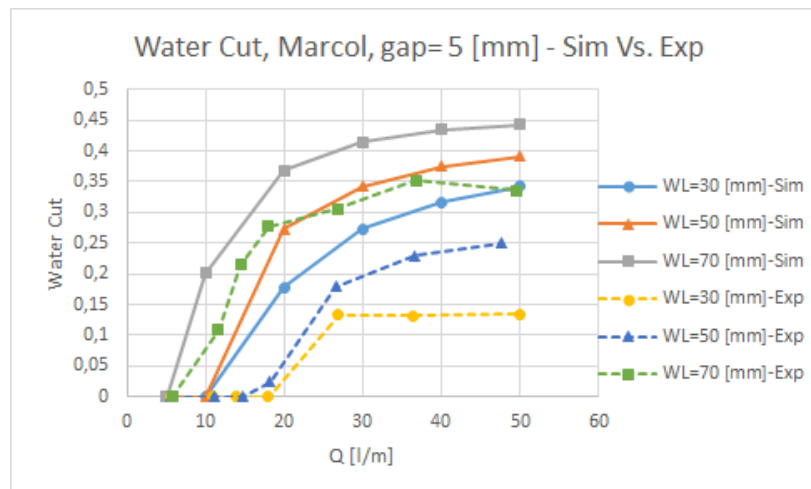


Figure 6.33: Water cut as a function of flowrate. Marcol oil with $\delta=5$ [mm], simulation vs. experiment.

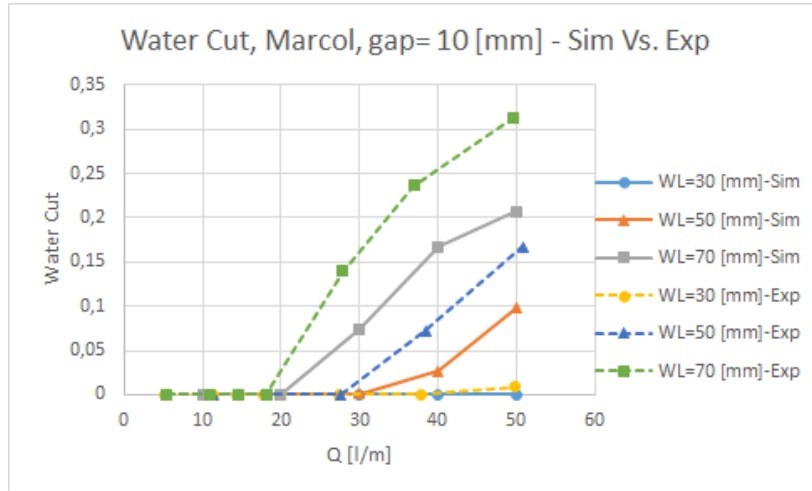


Figure 6.34: Water cut as a function of flowrate. Marcol oil with $\delta=10$ [mm], simulation vs. experiment.

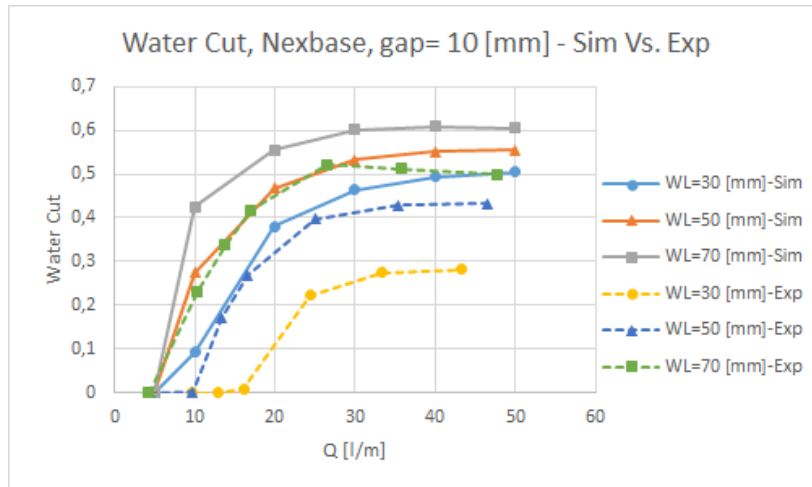


Figure 6.35: Water cut as a function of flowrate. Nexbase oil with $\delta=10$ [mm], simulation vs. experiment.

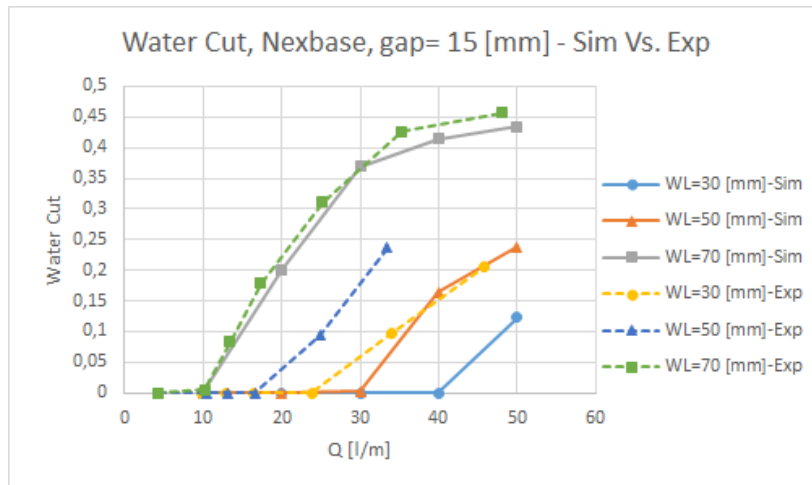


Figure 6.36: Water cut as a function of flowrate. Nexbase oil with $\delta=15$ [mm], simulation vs. experiment.

6.4 3D Simulations - Single Outlet Orifice

As described in the CFD methodology sections, a series of three-dimensional simulations were conducted to assess how results of such a modeling approach would compare to simpler two-dimensional simulations, and perhaps of greater importance how they compare to the experimental observations.

A three-dimensional simulation approach requires far more computational power. Thus, a selection of cases were chosen upon which to base the comparison, and are presented in table 6.5.

Table 6.5: Simulations for 10mm gap

Gap=10[mm]		
Inlet Velocity [m/s]	Q [l/m]	Water Level [mm]
0.002775	5	30, 50, 70
0.00555	10	30, 50, 70
0.0111	20	30, 50, 70
0.01667	30	30, 50, 70

A total of 24 3D simulations were conducted. Each simulation required approximately 40 CPU hours, resulting in a simulation time of 10 hours per simulation for the computer utilized.

Water jump

As opposed to the 2D simulation where there exists only one surface from which water jump values can be extracted, a suitable surface was defined for the 3D simulation cases. Using the ANSYS post-processing software a reference plane was created in the xy-plane with an offset equal to 0.005 [m] in the z-direction. In other words a reference plane was created in the middle of the annulus gap, parallel to the the annulus walls. Thus, water jump values could be observed from graphical representations of the fluid volume fractions, as done for the 2D simulations.

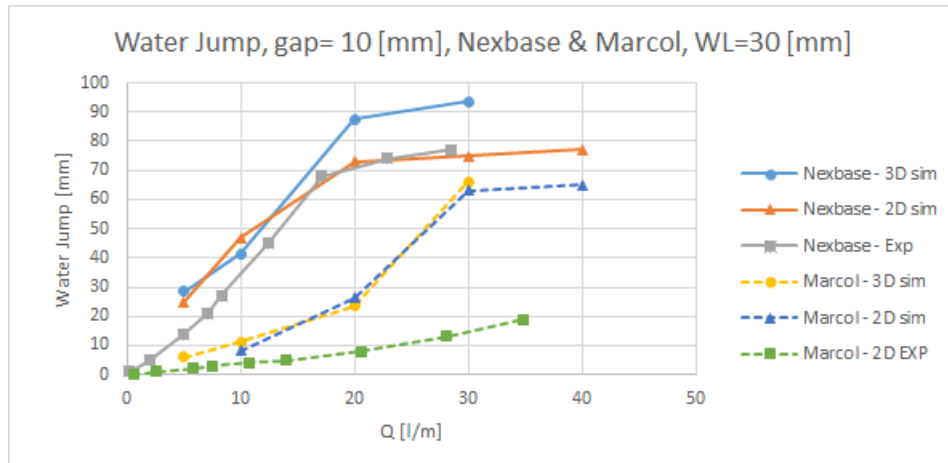


Figure 6.37: Comparison of water jump values observed in 3D simulations, 2D simulation, and experiments for both oils utilizing a $\delta = 10$ [mm], and WL= 30 [mm].

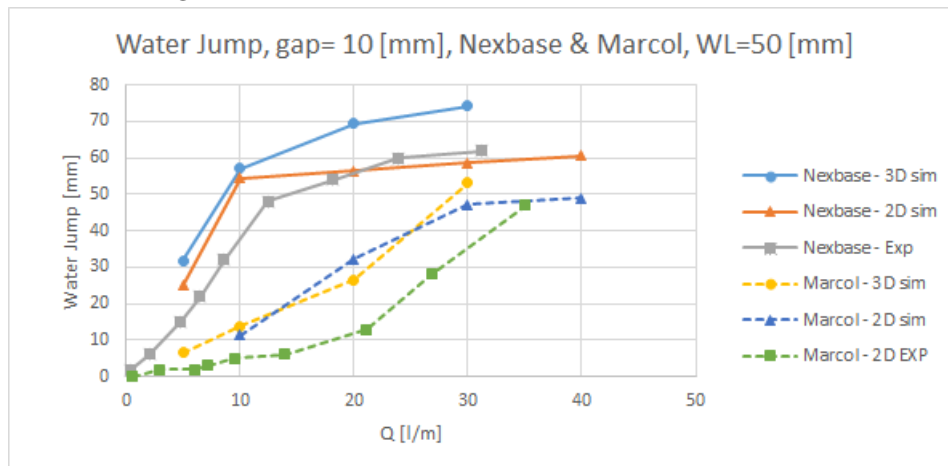


Figure 6.38: Comparison of water jump values observed in 3D simulations, 2D simulation, and experiments for both oils utilizing a $\delta = 10$ [mm], and WL= 50 [mm].

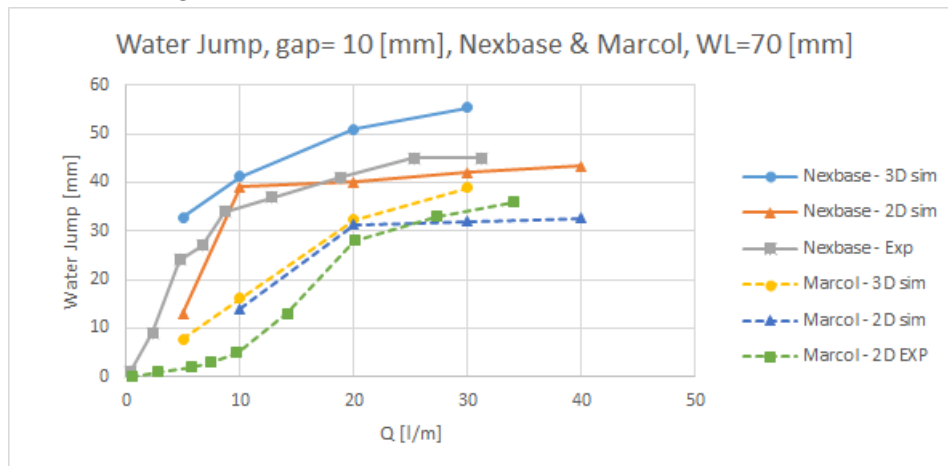


Figure 6.39: Comparison of water jump values observed in 3D simulations, 2D simulation, and experiments for both oils utilizing a $\delta = 10$ [mm], and WL= 70 [mm].

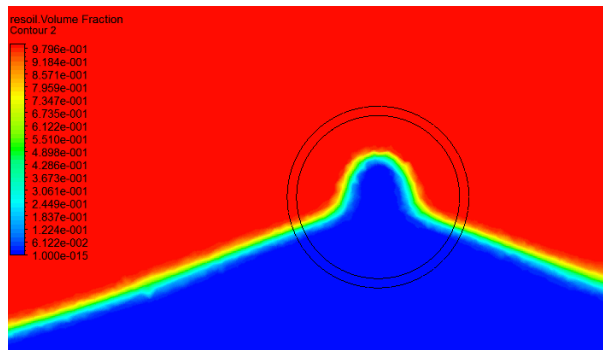


Figure 6.40: Example of oil volume fraction at reference plane.

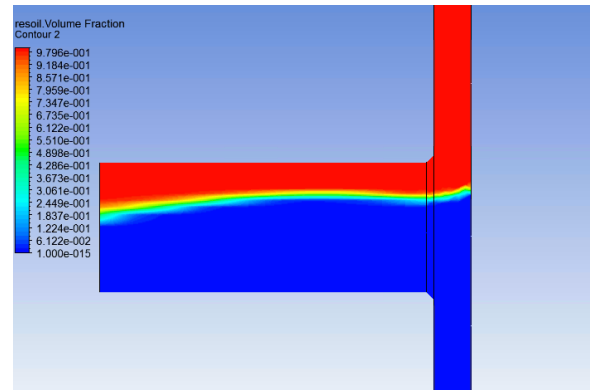


Figure 6.41: Example of oil volume fraction at zy-plane, slicing center of outlet orifice.

From analyzing figures 6.37 - 6.39, it is clear that the 3D simulations overpredict the water jump after water breakthrough. The pictures in figures 6.40, and 6.41, demonstrate the governing reason behind this; the water cone has a spike in front of the outlet orifice. This spiking phenomenon was also observed in the laboratory experiments, albeit less pronounced, thus resulting to the discrepancy in question.

For subcritical flow rates, the 3D simulations are in close agreement with the 2D simulations, however when compared to the experimental values it is not clear whether the 3D simulations provide more accurate water jump predictions before breakthrough. Figures 6.37 - 6.39 seem to indicate that the predictions deviate slightly more on average than those obtained with 2D simulations. However, more 3D simulations are needed before a clear conclusion can be made as to which method provides the most accurate water jump prediction at subcritical conditions when compared to experimental values.

Water cut

To obtain water cut values the mass flow rate at the outlet surface was utilized. This surface is located at the end of the pipe outlet as seen towards the left in figure 5.14. Studying figures 6.42 - 6.44 it is clear that the 2D simulations and the 3D simulations were in close agreement in terms of water cut values. However, this means there was a large discrepancy between the experiments and the 3D simulations, as was the case for 2D simulations conducted.

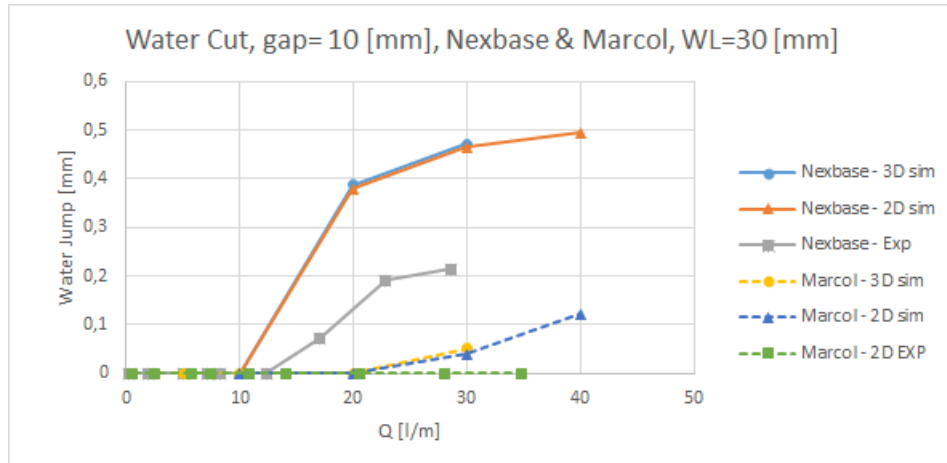


Figure 6.42: Comparison of water cut values calculated from 3D simulations, 2D simulation, and experiments for both oils utilizing a $\delta = 10$ [mm], and WL= 30 [mm].

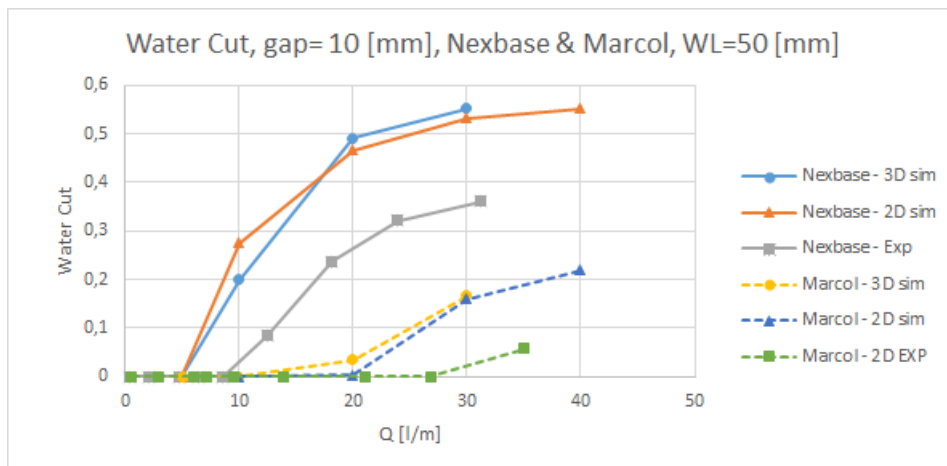


Figure 6.43: Comparison of water cut values calculated from 3D simulations, 2D simulation, and experiments for both oils utilizing a $\delta = 10$ [mm], and WL= 50 [mm].

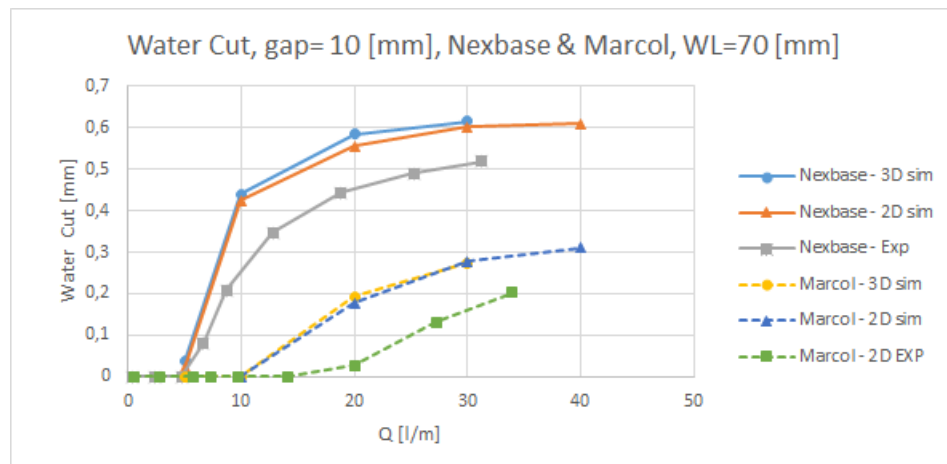


Figure 6.44: Comparison of water cut values calculated from 3D simulations, 2D simulation, and experiments for both oils utilizing a $\delta = 10$ [mm], and WL= 70 [mm].

6.5 Parametric Study

A Parametric study was conducted to analyze how the mass flow rate, water cut, and liquid jumps change as a function of the fluid properties. Such a parametric study can help to understand how the 2D simulation results vary with changes in fluid properties. Moreover, a deeper insight of how fluid properties affect the results, may lead to better ICD designs tailor fit for the reservoir conditions. The results from a parametric study may also be used to calibrate the simulation model to fit experimental data by deviating fluid property values from their true values.

The most important fluid properties governing the physics for these experiments were the fluid viscosities and the fluid densities.

Table 6.6: Base case parameter configuration for parametric study comparison.

Base Case						
Oil	δ [mm]	WL [mm]	Q [l/m]	μ [Pa·s]	ρ_o [kg/m ³]	ρ_w [kg/m ³]
Nexbase	10	50	20	0.09	845	1000

Table 6.7: Parameter variable values utilized for parametric study.

Parameter values	
ρ_o [kg/m ³]	700-1000 - (700,750,800,850,900,950,1000)
ρ_w [kg/m ³]	990-1500 - (990,1000,1010,1020,1030,1040,1050)
μ [Pa·s]	0.025-0.2 - (0.025,0.05,0.075,0.1,0.15,0.2)

For the base case on which to compare the parametric study, the case displayed in the table 6.6 was chosen. The chosen base case demonstrated some water breakthrough when simulated, as seen in figure 6.6. Furthermore, the figure shows that the experiment also has its respective critical flow rate at a value near 10 [l/m]. However, it is to be noted that the closest valve settings resulted in a volumetric flow rate of 8.6 [l/m] or 12.4 [l/m], and that the breakthrough occurs somewhere between these values, see appendix A.1, figure A.6 for further details. Choosing a base case close to critical conditions may be helpful to quantify how changes in parameter values result in a stable water cone without water breakthrough, or induce more severe water breakthrough.

The one-outlet orifice geometry was utilized together with the laminar solver, and the composite friction factor formulation. Table 6.7 displays the 20 parametric variable configurations, resulting in 20 simulations for this parametric study.

Varying oil density

It is evident from figure 6.45 that increased oil density increases the water jump height. This can be seen directly from the pressure balance in equation (2.14), when all other values are held constant. As the ratio of oil density to water density approaches 1, the hydrostatic pressure due to the water cone approaches zero, and the cone height becomes large. This means that for dense oils a higher water jump will occur to counteract the decreased oil density. It can also be seen from figure 6.45 that varying oil density can trigger water breakthrough. For this parametric study, an oil density in the range 750 - 800 [kg/m³] was the threshold value for water breakthrough, when all other case parameters were held constant.

Analyzing figure 6.48, it is clear that increasing the oil density leads to a higher water cut as a result of the increased water jump. The trend appears to be linear for oil density values higher than that of the threshold value. It is to be noted that figure 6.48 gives the incorrect impression that breakthrough occurs at $\rho_o = 750$ [kg/m³]. 750 [kg/m³] is more correctly to be understood as the lowest value of the oil density tested, for which there was no water breakthrough in this parametric study.

Varying water density

Figure 6.46 displays the same trend as observed when varying the oil density. Namely that when the density ratio between water and oil decreases, the water jump increases, and vice versa. It is to be noted that all values of the water density resulted in water breakthrough in this parametric study, thus there is no large jump in the the water jump values as present in figure 6.45. However, a further increase in water density beyond what was tested for will eventually sustain a stable water cone with no water breakthrough.

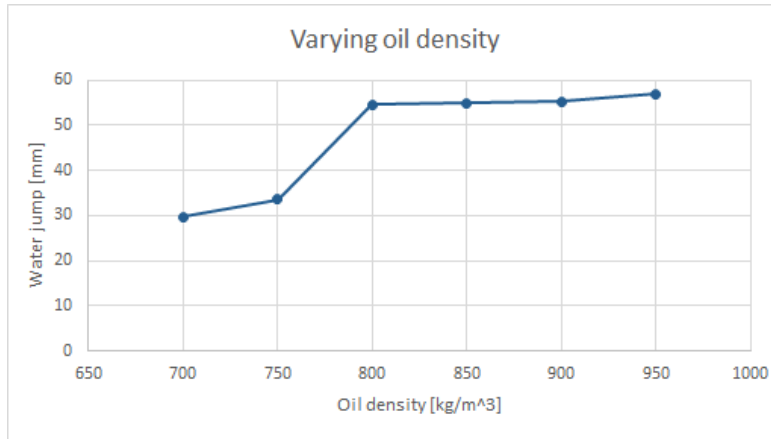


Figure 6.45: Water Jump observed with varying oil density.

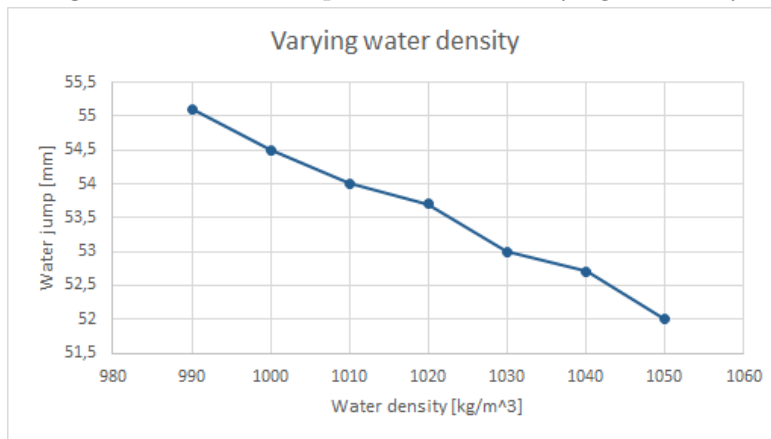


Figure 6.46: Water Jump observed with varying water density.

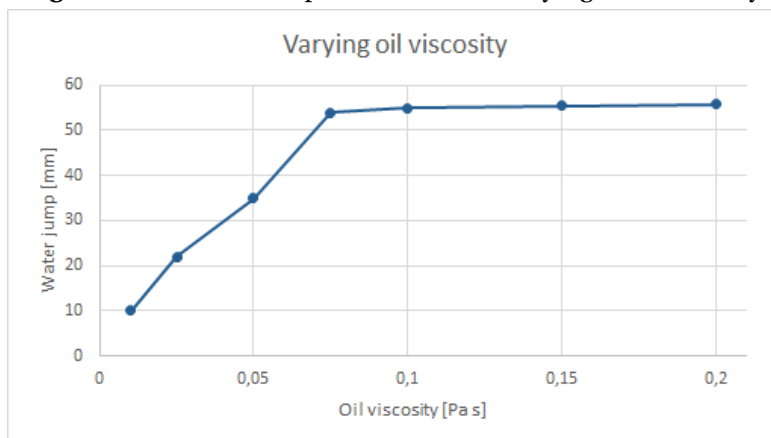


Figure 6.47: Water Jump observed with varying oil viscosity.

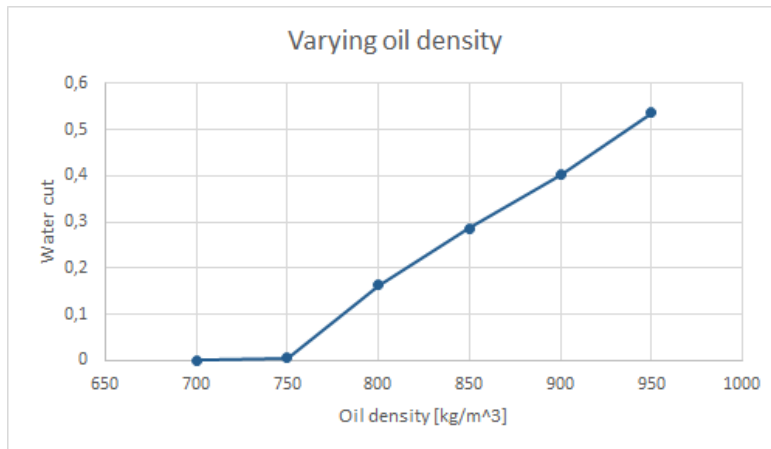


Figure 6.48: Water cut observed with varying oil density.

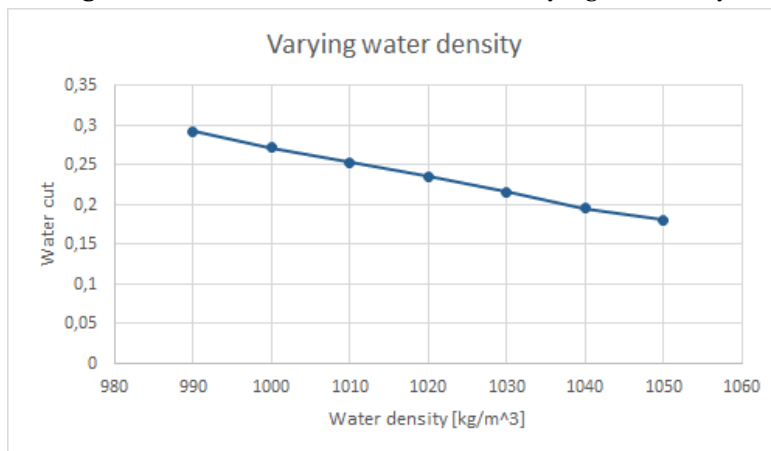


Figure 6.49: Water cut observed with varying water density.

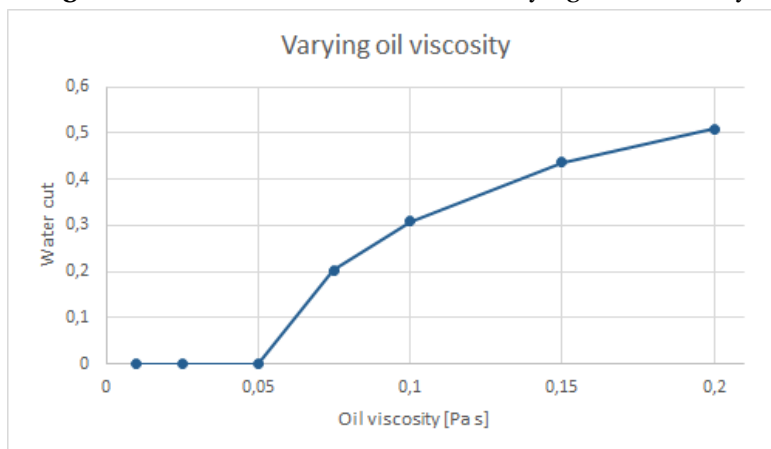


Figure 6.50: Water cut observed with varying oil viscosity.

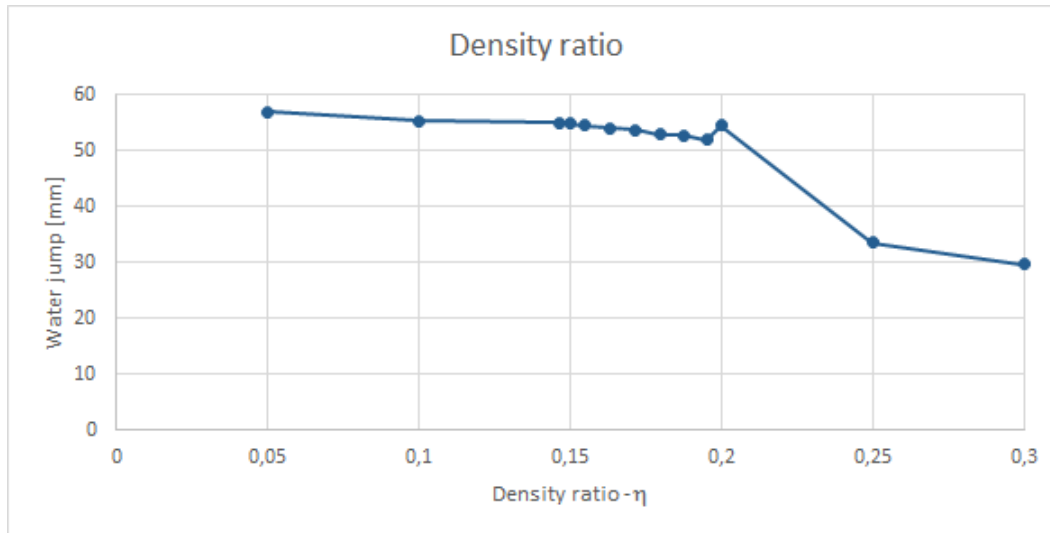


Figure 6.51: Observed water jump for given density ratios- η .

In accordance with the observations of the water jump, the water cut decreases as the water cut increases. Following the argument of further increasing the water density, an increase beyond $1050 \text{ [kg/m}^3\text{]}$ would eventually cause the water cut to drop to zero.

In an oil reservoir, fluid properties change over time in accordance with changing reservoir conditions. Hence it is important to evaluate potential shifts in coning behavior if future property values can be predicted. Changes in reservoir conditions will likely invoke a similar change response of fluid properties in the water and oil phases. For example, reduced pressure will lead to reduced densities of both oil and water. However, depending on the fluids in question the rate of change as a function of shifting reservoir conditions may differ, leading to new values of the density ratio. Thus the density ratio between water and oil is of great importance. For this study the ratio is defined as presented in equation (6.2):

$$\eta = \frac{\rho_w - \rho_o}{\rho_w} \quad (6.2)$$

A plot of the density ratio- η , was created by combining the data from the simulations when varying the water density as well as the data from the simulations when varying the oil density. Each simulation configuration thus constitutes a unique value of η . Studying figure 6.51, the

Table 6.8: Simulation Configurations

Simulation Configurations		
ρ_o [kg/m ³]	ρ_w [kg/m ³]	η
845	1050	0.195
800	1000	0.2

expected trend of decreasing water jump for an increasing value of η was observed. Moreover, the plot also displays that as the density ratio is increased there exists an η -value for which there is no longer water breakthrough, and a stable cone forms instead. This transitions occurred for an η -value somewhere in the range of 0.2 - 0.25.

Note that the kink in the plotted line in figure 6.51 at $\eta \approx 0.2$, is due to the different friction responses that occur when varying the water density as opposed to varying the oil density. Table 6.8 displays the density values for the the simulations in question, and moreover shows they have a nearly identical η value. However the momentum source added is a function of density as can be seen in chapter section 5.5, describing the momentum source. Thus, similar η -values is not sufficient to directly compare water jump values. The distribution of local pressure losses, both frictional and due to acceleration are inherently different as a result of varying fluid properties, and therefor the water jumps may differ.

Varying oil viscosity

It is evident from figure 6.47 that varying the viscosity has a significant impact on the water coning behavior. For values near 0.075 [Pa·s], the simulations experience water breakthrough. Further increase of the viscosity value leads to a small increase in water jump. However, a reduction in viscosity results in a stable water cone and no water breakthrough. This can be seen from the sharp drop in water jump when reducing the viscosity below 0.075 [Pa·s].

Figure 6.50 displays the behavior of the water cut as a function of the oil viscosity. As expected, higher viscosity leads to higher frictional pressure losses and thus a higher water cone, and consequently a higher water cut. It is to be noted that water breakthrough occurred for a viscosity in the range 0.075 - 0.05 [Pa·s]. From figure 6.50 it appears that the water breakthrough first occurs

at a viscosity value of 0.05 [Pa·s], however this is the highest value of the oil viscosity tested for which there was no water breakthrough in the simulations.

Chapter 7

Analytical Methods vs. Experimental Data

For future studies within coning in annular geometries it would be advantageous to obtain quick approximations of the annular coning height using only an analytical model or dimensional analysis, given that fluid properties, piping/ICD geometry, and flow rates are known. To assess this possibility the equations in section, 2.2 were computed using the experiment configurations and respective flow rates. Furthermore a dimensional analysis was carried out, and a critical flow rate correlation was created. The experiments to which the comparisons were made are those presented in table 7.1. Plots and discussions comparing the the methods are found at the end of the chapter.

Table 7.1: Experiments used for comparison with the analytical model.

Experiments for Comparison			
Oil	Gap[mm]	WL [mm]	Valve position
Nexbase	5,10,15	11,29,48,68,87	All
Marcol	5,10,15	11,29,50,67,87	All

7.1 Dimensional Analysis, Pi-Theorem

In order to gain a high-level understanding of how the critical flow rate values vary with changes in fluid properties, geometry, and initial water levels, the Buckingham PI-theorem was em-

ployed to analyze the governing physics.

The theory loosely states that an equation of the the form given in equation (7.1), can be restated as a function of dimensionless groups as seen in equation (7.2) [28].

$$f(q_1, q_2, \dots, q_n) = 0 \quad (7.1)$$

$$F(\pi_1, \pi_2, \dots, \pi_j) = 0 \quad (7.2)$$

$$\pi_j = q_1^{a_1} q_2^{a_2} \dots q_n^{a_n} \quad (7.3)$$

The number of dimensionless groups that can be formed, j , is generally expressed as $j = n - k$. n is the number of variables of interest in expressing the physical phenomenon, and k is the number of independent physical units. Utilizing the theorem resulted in three non-dimensional groups presented in equation (7.4). The full derivation of the non-dimensional groups can be found in appendix C.1.

$$\pi_1 = \frac{Q_c \rho}{\mu \delta} \quad \pi_2 = \frac{h}{\delta} \quad \pi_3 = \frac{\rho^2 g \delta^3}{\mu^2} \quad (7.4)$$

Q_c is the critical flow rate, and h is the height from the initial water level to the entrance of the orifice. Note that π_1 may be interpreted as a modified Reynolds number scaled by the annulus gap δ .

Figure 7.1 displays a clear trend between the respective pi-groups. First off it is clear that π_1 values increases for a given π_2 value when the value of π_3 increases. Furthermore, the relation between π_1 and π_2 appears to be approximately linear. The slope of the relation is steepest for the Marcol oil, and also here the slope is influenced by the value of π_3 . With this analysis it was possible to create a correlation that can predict the critical flow rates without needing to rely on an analytical expression.

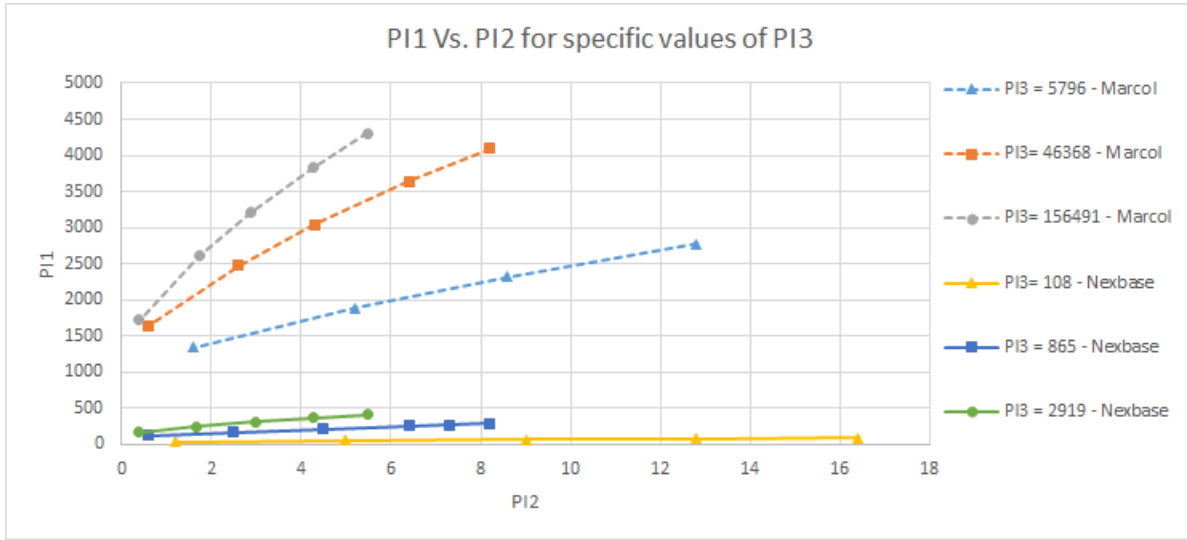


Figure 7.1: Pi-group π_1 plotted as a function of Pi-group π_2 . Each curve for a fixed value of Pi-group π_3 .

Pi group π_1 can be restated as function of the other pi-groups:

$$\pi_1 = \phi(\pi_2, \pi_3) \tag{7.5}$$

The exact relation between the pi groups is unknown. However, employing the knowledge gathered from analyzing figure 7.1, a simplified correlation was made.

$$\pi_1 = \kappa \pi_2 + \epsilon^* \tag{7.6}$$

.
.
.

$$Q_c = \kappa \left(\frac{\mu}{\rho} \right) h + \epsilon \tag{7.7}$$

In the presented correlation, κ can be interpreted as the slope of the curve, and ϵ , the value at the π_1 -axis in figure 7.1 for which h , and thus π_2 , is equal to zero. Utilizing the experimental values for the critical flow rate, the values for κ , and ϵ were defined for every combination of

oil and annulus gap utilized in the experiments. The coefficient values can be seen in table C.1, appendix C.1. The correlations for various combinations of κ , and ϵ are plotted in figures 7.9 - 7.14, along with the other modeling methods presented in this chapter.

7.2 Solving Analytical Models

It is also of interest to predict the stationary coning height for a given water level and flow rate, as well as the critical flow rate using the analytical expression defined in equation (2.14). The former is found by solving the equation directly, bearing in mind that the solution is only valid for subcritical conditions. The latter requires some further approximations to compute. To calculate the critical flow rate a coning height must be provided in order to only have one unknown in equation (2.14), namely the flow rate. As this height is also an unknown, an approximation is made by assuming the coning height is all the way up to the orifice. In this manner the hydrostatic pressure of the water column increases in value. Likewise the friction pressure loss as well as the acceleration pressure loss is set to act from the oil-water interface, and up to the orifice. In this way the pressure losses also increase in absolute value.

The pressure balance equation (2.14) can be written as:

$$g(T_w - T_o) [\rho_w - \rho_o] = \frac{6\mu Q}{\pi\delta^3} \ln\left(\frac{T_o}{T_i}\right) + \frac{\rho_o}{8} \left(\frac{Q}{\pi\delta}\right)^2 \left(\frac{1}{T_i^2} - \frac{1}{T_o^2}\right) \quad (7.8)$$

To solve for the coning height, equation (7.8) is solved for T_o , using the flow rate, Q , as the dependent variable. For simplicity, equation (7.8) is rewritten as follows:

$$a(T_w - T_o) - bQ \ln\left(\frac{T_o}{T_i}\right) - cQ^2 \left(\frac{1}{T_i^2} - \frac{1}{T_o^2}\right) = 0 \quad (7.9)$$

where a , b , and c are defined as:

$$a = g [\rho_w - \rho_o]$$

$$b = \frac{6\mu}{\pi\delta^3}$$

$$c = \frac{\rho_o}{8} \left(\frac{1}{\pi\delta} \right)^2$$

A very simplified analytical model was defined by neglecting the acceleration term. The reason for this is that equation (7.9) now becomes an equation that can easily be solved implicitly. This allows the possibility to compute the coning height without computer assistance.

$$T_o = T_i \exp \left\{ \frac{a}{bQ} (T_w - T_o) \right\} \quad (7.10)$$

From figures 7.2, and 7.3, it is evident that the discrepancy between the stationary coning height observed in the experiments and that predicted by equation (7.10). The general trend is that equation (7.10), underpredicts the height of the stationary cone for all initial water levels, and moreover for all flow rates. However, it is to be noted that the analytical models are not valid after the water jumps past the maximum cone height, and up into the orifice. Additionally, the model is restricted to jumps no further than to the edge of the orifice. This restriction gives rise to especially large percent-wise discrepancies for high initial water levels, as can be seen for WL = 87 [mm] in figure 7.2

The figures also indicate large differences between Marcol oil and Nexbase oil, with respect to frictional pressure loss. Nexbase displays a lower discrepancy from the experimental coning height than compared to that of the Marcol oil. This is due to the fact that the Nexbase is much more viscous and therefore the frictional pressure loss dominates over the acceleration pressure loss. The opposite is true for the Marcol oil.

A Matlab script was created to solve equation (7.9) including the acceleration term, for the values of the coning heights. The inputs for the script were the fluid property values, the gap size, the water level, and the flow rates of interest. The inbuilt *fzero* function was utilized as the equation solver, supplemented with reasonable initial guesses for the coning height to initiate the calculation. The scripts written can be found in appendix C.2.

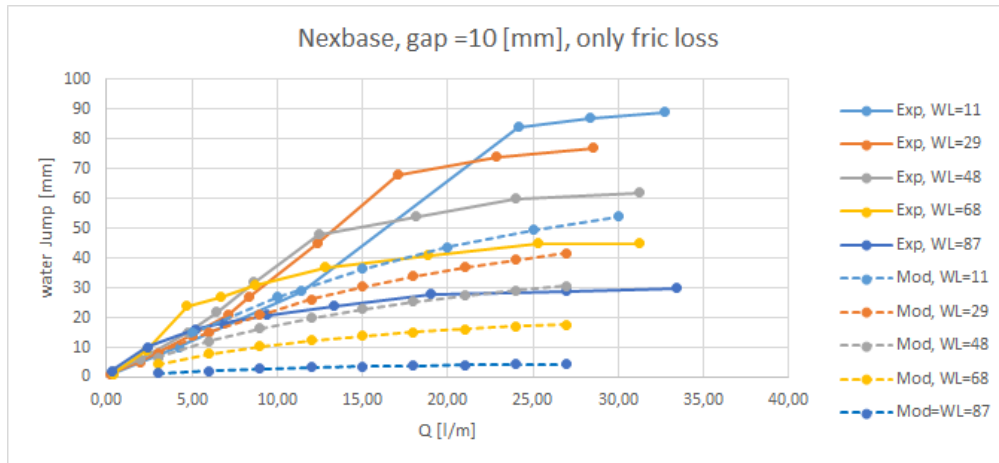


Figure 7.2: Water jump values predicted by equation (7.10) vs. experimental values, utilizing Nexbase oil and $\delta=10$ [mm].

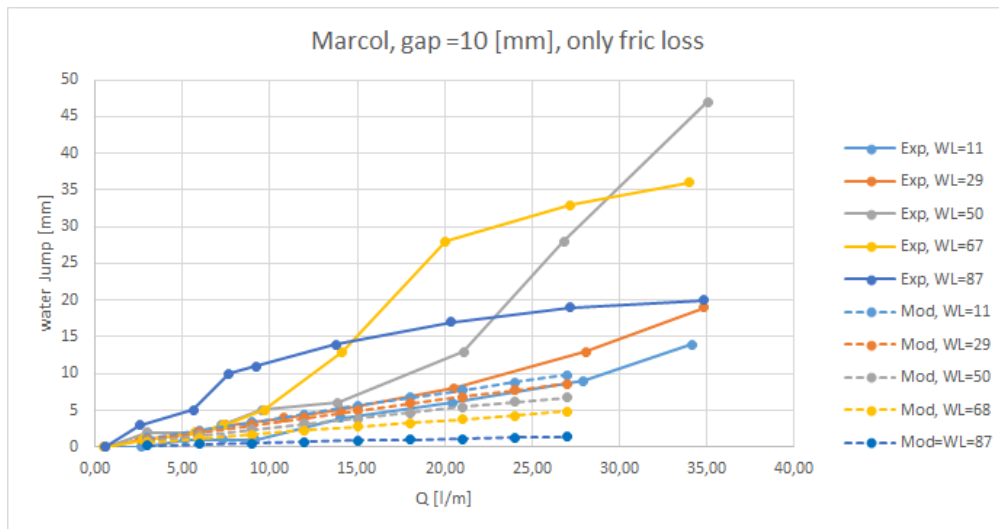


Figure 7.3: Water jump values predicted by equation (7.10) vs. experimental values, utilizing Marcol oil and $\delta=10$ [mm].

Studying figure 7.4, it is evident that the model predictions are improved for the Nexbase oil when the acceleration pressure loss term is included. However, as displayed in figure 7.5, the predictions when utilizing Marcol oil become exceedingly different from what was observed without the acceleration term, as seen in figure 7.3. Figure 7.5 demonstrates overpredictions of the stationary cone height for initial water levels 50 [mm], 29 [mm] and 11 [mm]. Plots were also created for both Nexbase and Marcol oils, when utilizing gap sizes $\delta = 5$ [mm] and $\delta = 15$ [mm]. These figures are located in appendix C.3.

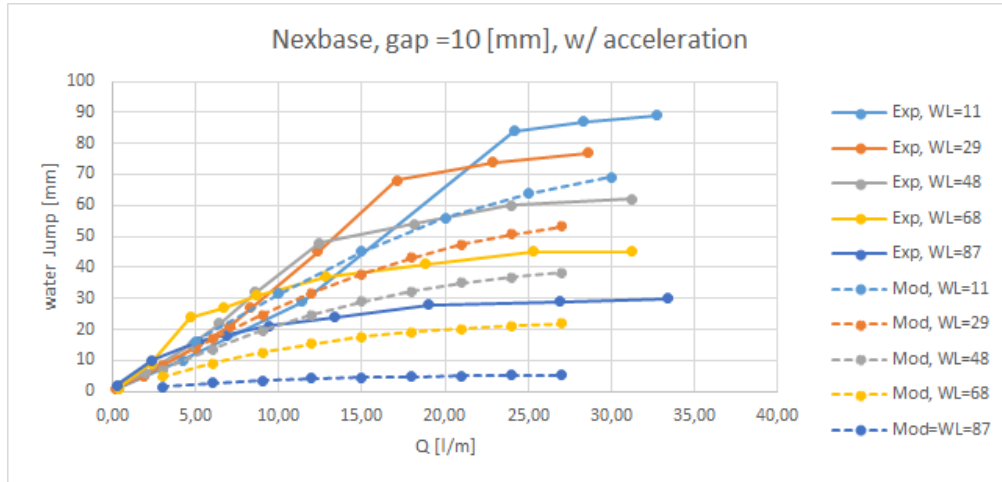


Figure 7.4: Water jump values predicted by equation (7.8) vs. experimental values, utilizing Nexbase oil and $\delta=10$ [mm].

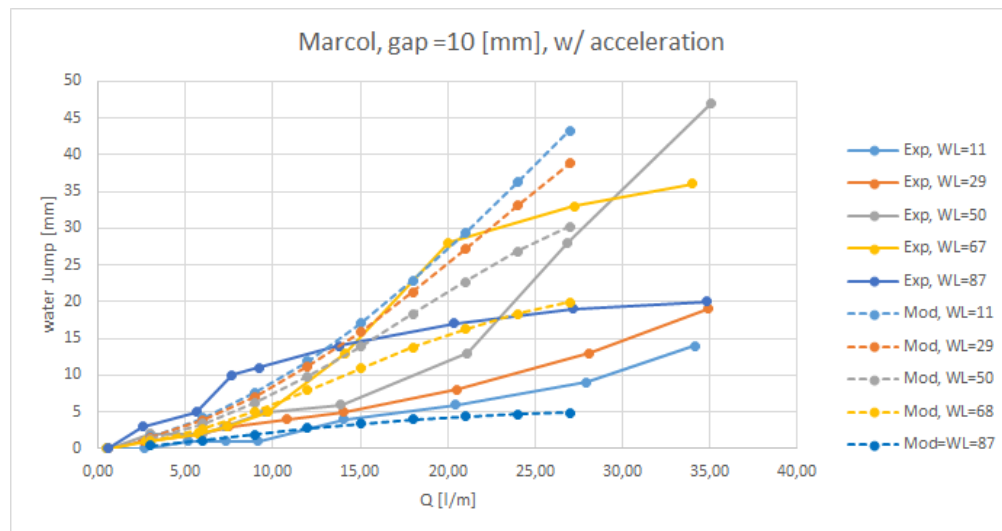


Figure 7.5: Water jump values predicted by equation (7.8) vs. experimental values, utilizing Marcol oil and $\delta=10$ [mm].

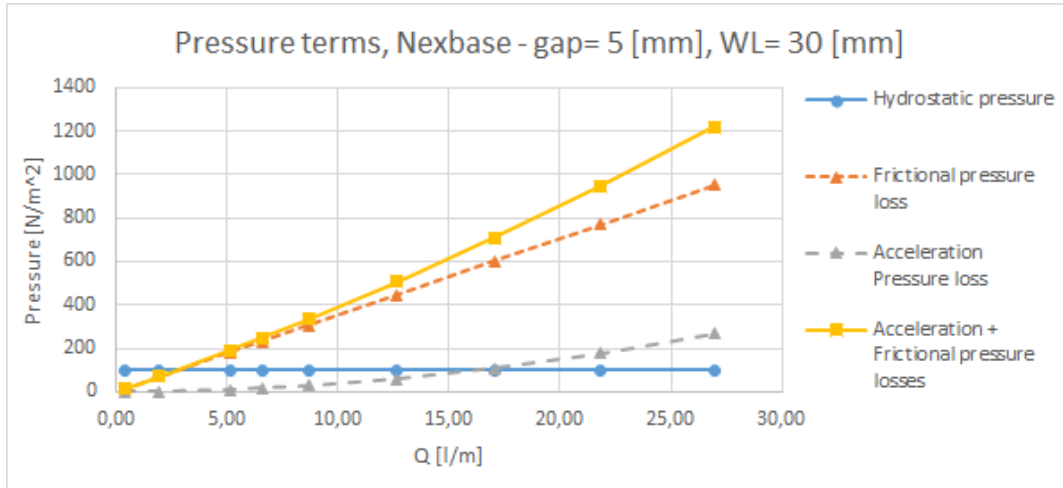


Figure 7.6: Pressure losses as a function of flow rate, for Nexbase oil with $\delta = 5$ [mm], and WL=30 [mm]. Computed from equation (7.8).

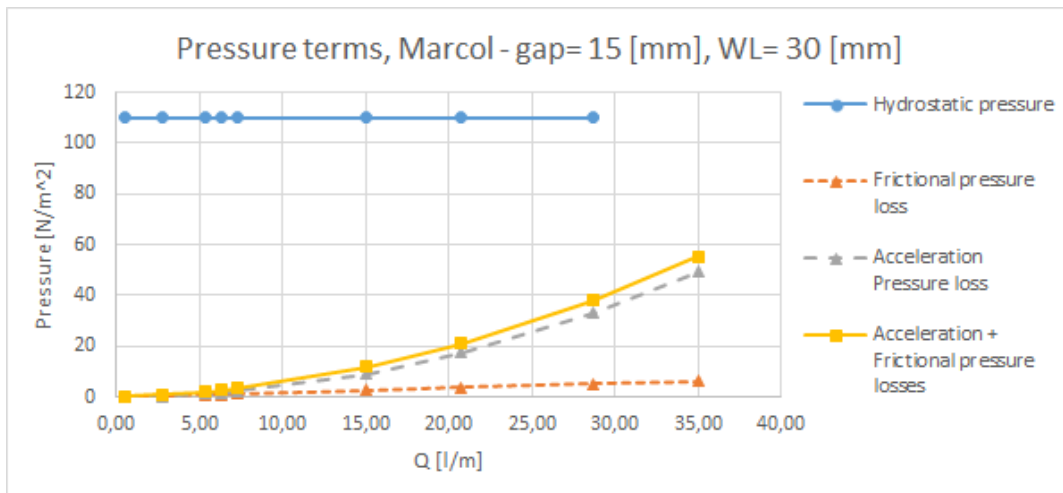


Figure 7.7: Pressure losses as a function of flow rate, for Marcol oil with $\delta = 15$ [mm], and WL=30 [mm]. Computed from equation (7.8).

Figure 7.6 and 7.7 indicate that for Nexbase oil and in particular for the smallest gap sizes, the frictional pressure losses dominate, whilst accelerational pressure losses dominate for Marcol oil, especially for larger gap sizes. The figures indicate why a model neglecting friction is only accurate for Nexbase utilizing small annulus gaps. Furthermore, figure 7.7 indicates that the accelerational pressure drop is important for cases with Marcol oil for all annulus gaps.

Matlab was also used to calculate the critical flow rates by computing equation(7.9). The scripts written can be found in appendix C.2.

7.3 Tuning The Analytical Models

As evident from the previous section, there are relatively large discrepancies between the analytical model presented in equation (7.8), and the experimental values regarding stationary coning heights and critical flow rates. In an attempt to overcome this, equation (7.8) was modified using the findings from the experiments. As a first approach a model of the following form was sought after:

$$g(T_w - T_o) [\rho_w - \rho_o] = f(\mu, \rho_o, Q...) \frac{6\mu Q}{\pi\delta^3} \ln\left(\frac{T_o}{T_i}\right) + f(\mu, \rho_o, Q...) \frac{\rho_o}{8} \left(\frac{Q}{\pi\delta}\right)^2 \left(\frac{1}{T_i^2} - \frac{1}{T_o^2}\right) \quad (7.11)$$

Here $f(\mu, \rho_o, Q...)$ signifies a function dependent on case properties. It was not desirable to multiply the terms in equation (7.8) with simple empirical constants as this only resulted in vertical shifts of the analytical predictions, and not acting towards higher overall prediction accuracy.

Figures 7.6, and 7.7 indicate why the task of creating a function f that would be sensible for both oils proved a challenging task. The oils have significantly different responses regarding friction pressure losses and accelerational pressure losses. Instead, a function was formulated for each oil and set to act only on the the dominating friction loss contributor as displayed in equations (7.12), valid for Nexbase oil, and (7.13) valid for Marcol oil.

$$g(T_w - T_o) [\rho_w - \rho_o] = \left(\frac{\alpha}{Q}\right) \frac{6\mu Q}{\pi\delta^3} \ln\left(\frac{T_o}{T_i}\right) + \frac{\rho_o}{8} \left(\frac{Q}{\pi\delta}\right)^2 \left(\frac{1}{T_i^2} - \frac{1}{T_o^2}\right) \quad (7.12)$$

$$g(T_w - T_o) [\rho_w - \rho_o] = \frac{6\mu Q}{\pi\delta^3} \ln\left(\frac{T_o}{T_i}\right) + \left(\frac{\alpha}{Q}\right) \frac{\rho_o}{8} \left(\frac{Q}{\pi\delta}\right)^2 \left(\frac{1}{T_i^2} - \frac{1}{T_o^2}\right) \quad (7.13)$$

Utilizing matlab, both equations (7.12) and (7.13) were solved for the critical flow rate for all experiment case configurations. The results are plotted in figures 7.9 - 7.14 where it is compared to the other modeling methods described in this section.

7.4 Tuning The Analytical Data

As is evident from the findings presented in the previous sections, equation (7.9) can contribute a rough prediction of the critical flow rates for given initial water levels. An effort was made to tune the analytical predictions to more closely match the experimental observations.

By identifying a suitable pivotal point on each analytical plot, the curve can essentially be rotated to better fit the experimental curve. An example is shown in figure 7.8. The red arrows indicate the direction of rotation and the red marker displays the pivotal point.

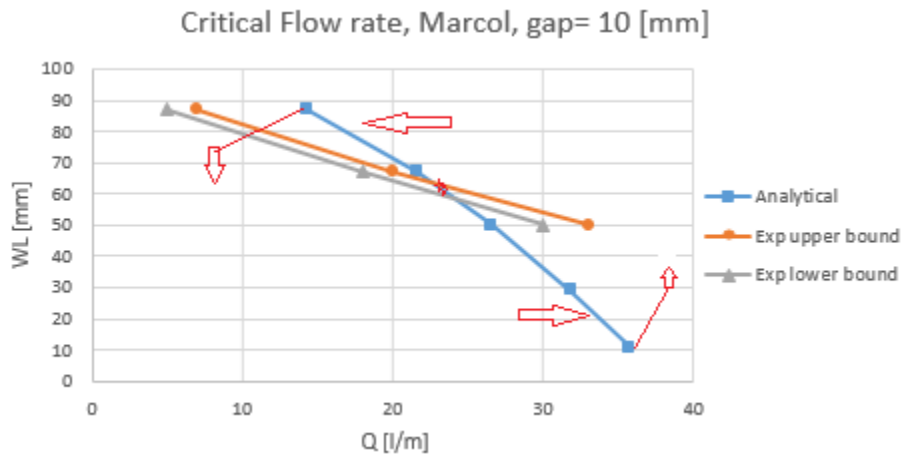


Figure 7.8: Illustration of how the plot of the analytical model can be tuned to fit the experimental findings.

Table 7.2: Tuning parameter values

Nexbase oil			Marcol oil		
δ [mm]	ω [l/m]	WL_{pivot} [mm]	δ [mm]	ω [l/m]	WL_{pivot} [mm]
5	0.15	60	5	0.2	50
10	1.667	22	10	2.5	57
15	2.85	11	15	3	27

A function was created that takes the analytical prediction and transforms it in order to achieve the desired rotation.

$$Q' = Q - \frac{\omega}{\delta} [WL - WL_{pivot}] \quad (7.14)$$

The constant ω is created as a purely empirical constant, tweaked to obtain the desired degree of rotation. The expression within the parenthesis defines the pivotal point on the curve. δ is the annulus gap width. Table 7.2 lists the pivot point values and ω -values utilized. As can be seen in figures 7.9 - 7.14, the tuned fit curve is in better agreement with the experimental data. Unfortunately there is no guarantee that this approach will yield similar results for other oils, gaps or orifice diameters. Although this approach relies on experimental data, the tuning parameter trends provide insight into what can be expected for other oils and gap sizes. From table 7.2 it is evident that the less viscous oil Marcol results in a higher ω -value, a more narrow range of WL_{pivot} -values, and an overall lower average for WL_{pivot} -value. Utilizing an analysis of this kind it may be possible to infer reasonable approximations for ω and WL_{pivot} , for scenarios employing other oils or other gap sizes.

7.5 Comparison of The Analytical Methods

Plotted in figures 7.9 - 7.14 are the different analytical methods discussed in this chapter and the experimental values for the critical flow rates. In theory the critical flow rate has a fixed value for a given set of case parameters. However, the experimental values can not be pinpointed due to the fact that the valve position in the experimental rig was a discrete variable. From studying the experimental data however, it is possible to define a narrow range of flow rates for which

the flow becomes critical, and water jumps up to the orifice. The ranges for every configuration consisting of an oil, a specific gap and a specific initial water level thus have an upper bound and a lower bound value. The upper bound value is plotted as orange circles, and the lower bound as grey triangles.

The legend "*Analytical*", refers to the critical flow rates obtained when solving equation (7.9). From figures 7.9 -7.14 it is evident that there is a significant discrepancy between what the equation predicts and the range of critical flow rates for each respective initial water level.

The legend "*Tuned Model*", refers to the attempt at tuning equation (7.9) by multiplying the friction loss terms with functions of case properties. This proved very challenging, as this approach is not based upon a physical or dimensional analysis, more a mere trial and error, and use of intuition. The result was as described previously in this chapter two separate tuned models, one for each oil. Figures 7.9 -7.14 show that this approach worked best for the least viscous oil, Marcol 52, with small discrepancies with respect to the experimental values. However, from the figures displaying the cases utilizing Nexbase oil it is evident the tuned model was only better in the case for a large annulus gap. In fact, Nexbase resulted in a larger discrepancy for the narrow annulus gaps when compared to the analytical expression from which the tuned model was based upon.

The legend "*Tuned fit*", refers to the method of tuning the output from the analytical expression in equation (7.9) to match the experimental values. This method does not directly help towards creating a model that can predict critical flow rates as it relies on tuning data from an already supplied analytical expression. However, it was a helpful tool to understand how the values obtained from the analytical expression in equation (7.9) deviated from the experimental values, and provided clues as to how one can tune the analytical expression itself.

The legend "*PI*" refers to the method of dimensional analysis using the Buckingham Pi-theorem. The figures show that tuning a simplified expression created using dimensional analysis has significant potential. The discrepancies are low for all combination of oil and gap sizes when compared to experimental values. This suggest that the dimensional analysis approach may be advantageous in the study of the coning phenomenon, due to the generality of the demon-

strated applicability. Moreover, the full potential of this method was not tested. In the derivation the focus was placed on the relation between pi-group π_1 and pi-group π_2 . Pi-group π_1 is also a function of pi-group π_3 , however in this study that relation has instead been handled by adding the constant ϵ to the expression describing the relation between π_1 , and π_2 , as seen in equation (7.7). By fully analyzing the the relation between between each pi-group and creating a more comprehensive correlation based on the findings, it may be possible to create a more general purpose correlation.

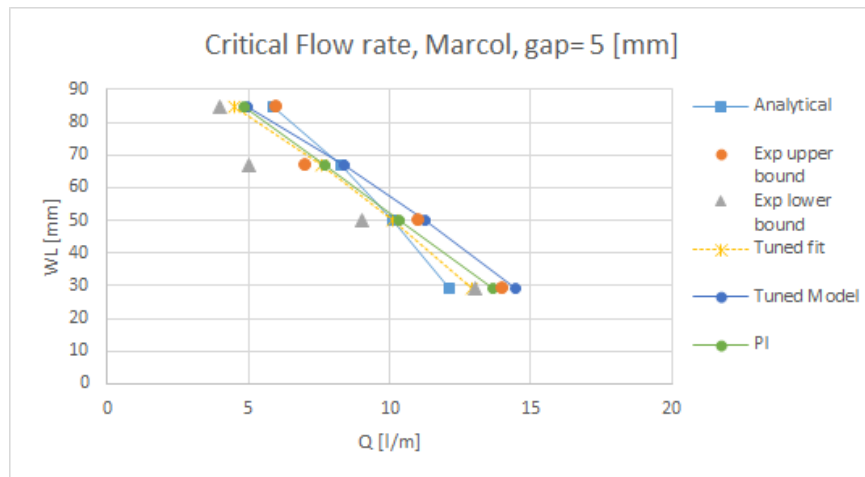


Figure 7.9: Comparison of critical flow rates, the analytical methods vs. experimental values for Marcol oil, $\delta=5$ [mm].

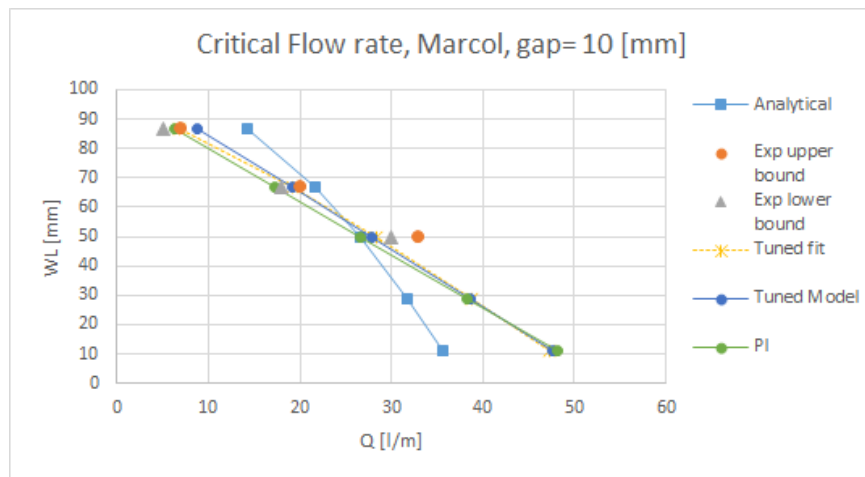


Figure 7.10: Comparison of critical flow rates, the analytical methods vs. experimental values for Marcol oil, $\delta=10$ [mm].

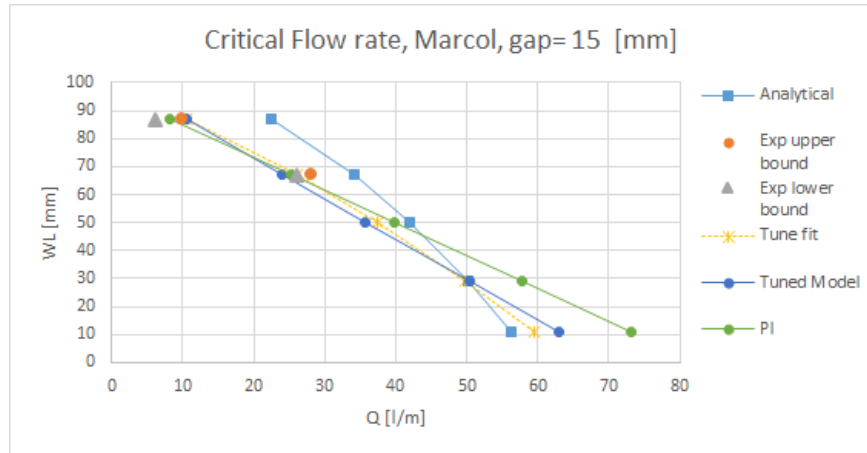


Figure 7.11: Comparison of critical flow rates, the analytical methods vs. experimental values for Marcol oil, $\delta=15$ [mm].

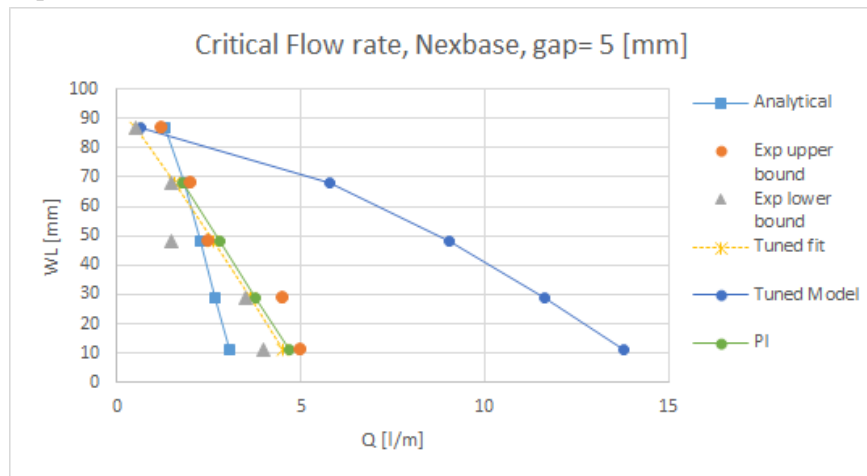


Figure 7.12: Comparison of critical flow rates, the analytical methods vs. experimental values for Nexbase oil, $\delta=5$ [mm].

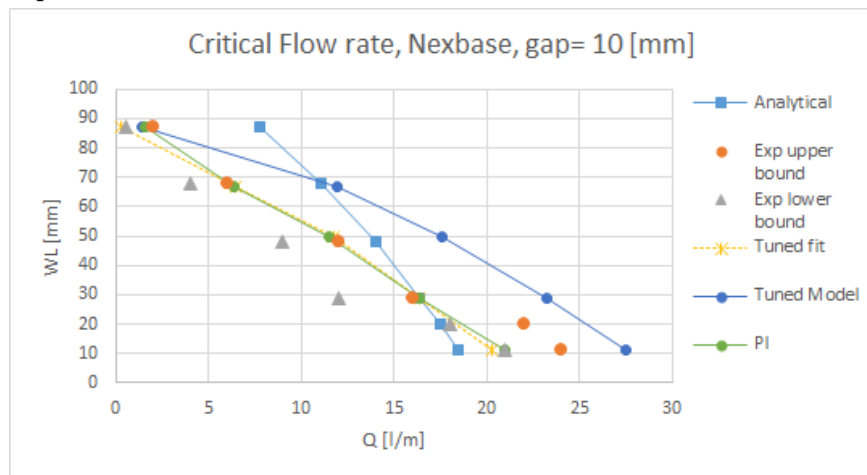


Figure 7.13: Comparison of critical flow rates, the analytical methods vs. experimental values for Nexbase oil, $\delta=10$ [mm].

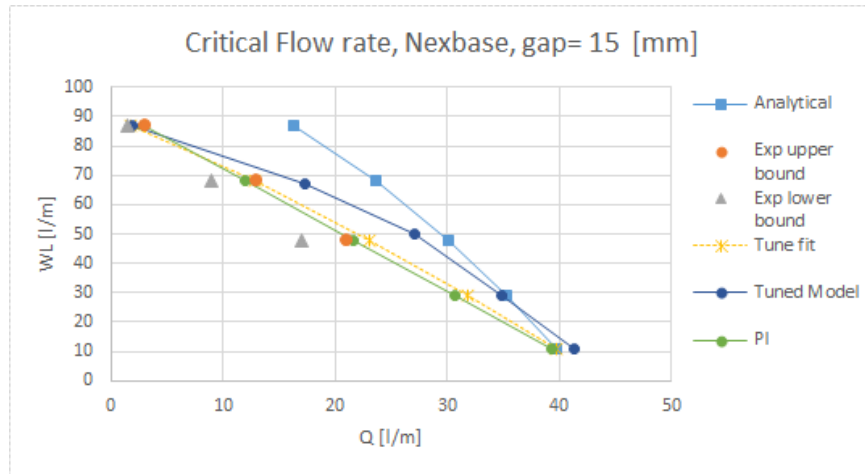


Figure 7.14: Comparison of critical flow rates, the analytical methods vs. experimental values for Nexbase oil, $\delta=15$ [mm].

Chapter 8

Conclusions and Further Work

8.1 Conclusions

In the laboratory the phenomenon of water coning as function of the annulus gap, water levels, viscosity, plate geometry and flow rate has been studied. The same simulations have been done utilizing ANSYS-CFX commercial CFD package in both 2D and 3D. All the results have been extensively analyzed. The following conclusions can be made:

- For the highly viscous Nexbase 3080 the total flow rate increases when water breaks into the production, due to the relatively low viscosity of water. The Marcol oil however, has a much lower viscosity, thus the increase in flow rate was negligible.
- Both the water cut and the water jump were highly dependent on the annulus gap and the flow rate. For a narrow gap of $\delta = 5$ [mm], water coning was observed for all initial water levels and all values of flow rates tested. For the gap of $\delta = 25$ [mm] water cones were faint, and the coning heights were in general small for all initial water levels and respective flow rates. An increase in flow rate gives a higher water jump and water cut. The flow rates for which water breakthrough occurs, referred to as the critical flow rate, increases with low initial water levels and large annulus gaps.

- Nexbase 3080 has a larger tendency to induce water cones than Marcol 52. This is shown by higher values of both water jump and water cut. The experiments as well as the parametric study indicate that this is caused by the contrast in viscosity between the oils and the water.
- With regards to water coning, the two-sided inflow is considered to be more efficient than the one-sided inflow due to better inflow conditions for the oil phase. The results also show that the plate with a single orifice gave lower water cones than plates with two orifices, both when orifices were located at the same height and when located at different heights.
- The lack of annulus walls in the 2D simulations implies that the pressure drop due to viscous fluid will be missing. This hurdle was overcome by modeling the friction as a momentum source term in every cell. Two different momentum source approaches were tested. Comparison of the simulations conducted utilizing the momentum source approaches were in generally good agreement with the experiments conducted regarding the water jump, but large discrepancies were observed with respect to the water cut. Furthermore the two momentum source approaches yielded nearly identical results.
- The Reynolds Stress (RST) turbulence model with a gamma-theta transition model utilizing the composite friction approach, was tested for a series of simulations to assess how a transitional modeling approach could predict water jumps and water cuts. Comparisons of the results to that of the simulations utilizing a laminar solver displayed close agreement for most simulation cases. However, for case configurations demonstrated by experiments to be at subcritical conditions, yet close to becoming critical, a small discrepancy was sufficient to produce critical conditions and water breakthrough at the orifice. Thus, this approach may not be well suited for the study of water coning in annular geometry.
- The water cut values were in close agreement for all flow rate values when comparing the 2D simulations to the 3D simulations. The water jump values also demonstrated close agreement with the values observed in the 2D simulations, however only for subcritical flow rates. For supercritical flow rates the water cone displayed a spike at the top of the

cone, in front of the outlet orifice, thus the water jump values exceed that of the experimental values.

- The series of simulations conducted with a geometry consisting of two outlet orifices demonstrated the same underlying trends seen in the experiments, with respect to water jump and water cut. However, the discrepancies were larger than those observed in the one-hole comparison. It is clear that the increased complexity in the geometry leads to larger discrepancies.
- The results from a simplified dimensional analysis produced a general-use correlation for the critical flow rate, dependent on the case geometry and fluid properties. The correlation relies on case-specific coefficients that can be determined from experimental data. With the determined coefficients, the critical flow rates values were in sound agreement with the experimental findings. Tuning the analytical model expressing the pressure balance to obtain a revised general model proved to be challenging, however a tuned model was created for each respective oil.

8.2 Further Work

Although this thesis sheds some light on the study of water coning in annular geometry, there is a great deal of work that can be done to further investigate, and provide a deeper understanding of the topic.

- For further studies in the laboratory a new experimental rig should be developed. The rig used for this study has two major weaknesses. One is due to its size and varying liquid levels during the experimental runs. This creates extra uncertainties in the results. The second issue is due to the continuous valve. One improvement would be to change the flow control valves with another control device for the flow rate.
- To gain a deeper understanding of how multiple orifices influence one another, more experiments utilizing a range of orifice-to-orifice distances need to be conducted.

- The discrepancies between experimental values and those obtained from simulations, both 2D and 3D, are in some cases relatively large. Using the results from the parametric study, it may be possible to tune the simulation model to better match experimental values by deviating fluid properties from their true values.
- The pressure-pressure boundary configuration was not tested on the 3D simulations. This testing would require simulation configurations consisting of a wide range of annulus gap widths, flow rates, and initial water levels, and thus very time consuming. It is possible that if such a boundary condition configuration displayed stable behavior in 3D simulations, the spike observed on the water cone observed for higher than critical flow rates may reduce and align with observations from experiments.
- A more detailed investigation of the dimensional analysis could prove useful. The correlation developed for critical flow rates is dependent on determining coefficient values from experiments. Further work on developing correlations could lead to the coefficient being expressed in a more general nature, making it applicable to a wide range of oils and annulus gap widths.

Appendix A

Laboratory data

A.1 Spreadsheet with every single experimental run

BEFORE			DURING						AFTER							
Liquid level, mm			Valve	Liquid level (max Δ), mm					Amount, ml			WC, %	Time, s	Flowrate, l/min		
wL	oL	ΔL		wL'	oL'	ΔL'	wJ	oJ	wV	oV	totV			wQ	oQ	totQ
11	210	81	1	12	210	80	1	0	0	650	650	0,0	150,50	0,00	0,26	0,26
11	210	81	1,5	37	210	55	26	0	0	1020	1020	0,0	29,70	0,00	2,06	2,06
11	210	81	2	99	210	-7	88	0	450	4350	4800	9,4	59,50	0,45	4,39	4,84
11	210	81	2,5	103	210	-11	92	0	360	4035	4395	8,2	30,30	0,71	7,99	8,70
11	210	81	3	104	210	-12	93	0	275	4300	4575	6,0	23,50	0,70	10,98	11,68
11	210	81	3,5	107	210	-15	96	0	330	5865	6195	5,3	22,80	0,87	15,43	16,30
11	210	81	4	108	210	-16	97	0	225	4200	4425	5,1	13,50	1,00	18,67	19,67
11	210	81	4,5	112	210	-20	101	0	220	4390	4610	4,8	12,00	1,10	21,95	23,05
29	210	63	1	33	210	59	4	0	0	850	850	0,0	150,50	0,00	0,34	0,34
29	210	63	1,5	59	210	33	30	0	0	960	960	0,0	29,70	0,00	1,94	1,94
29	210	63	2	102	210	-10	73	0	1050	3450	4500	23,3	53,00	1,19	3,91	5,09
29	210	63	2,25	109	210	-17	80	0	1550	3150	4700	33,0	43,00	2,16	4,40	6,56
29	210	63	2,5	111	210	-19	82	0	1470	2820	4290	34,3	29,70	2,97	5,70	8,67
29	210	63	3	115	210	-23	86	0	1290	3135	4425	29,2	21,00	3,69	8,96	12,64
29	210	63	3,5	117	210	-25	88	0	1365	4005	5370	25,4	18,90	4,33	12,71	17,05
29	210	63	4	118	210	-26	89	0	1140	3860	5000	22,8	13,75	4,97	16,84	21,82
29	210	63	4,5	118	210	-26	89	0	1010	3750	4760	21,2	10,60	5,72	21,23	26,94
48	210	44	1	56	210	36	8	0	0	500	500	0,0	150,50	0,00	0,20	0,20
48	210	44	1,5	94	210	-2	46	0	10	1070	1080	0,9	30,00	0,02	2,14	2,16
48	210	44	2	108	210	-16	60	0	2100	2750	4850	43,3	56,50	2,23	2,92	5,15
48	210	44	2,25	114	210	-22	66	0	2600	2325	4925	52,8	39,50	3,95	3,53	7,48
48	210	44	2,5	116	210	-24	68	0	2175	1755	3930	55,3	25,20	5,18	4,18	9,36
48	210	44	3	116	210	-24	68	0	1965	1885	3850	51,0	16,75	7,04	6,75	13,79
48	210	44	3,5	117	210	-25	69	0	2100	2575	4675	44,9	15,00	8,40	10,30	18,70
48	210	44	4	118	210	-26	70	0	1800	2400	4200	42,9	11,20	9,64	12,86	22,50
48	210	44	4,5	120	210	-28	72	0	950	1400	2350	40,4	5,10	11,18	16,47	27,65
68	210	24	1	72	210	20	4	0	0	775	775	0,0	151,00	0,00	0,31	0,31
68	210	24	1,5	96	210	-4	28	0	135	945	1080	12,5	30,60	0,26	1,85	2,12
68	210	24	2	107	210	-15	39	0	2450	2550	5000	49,0	58,55	2,51	2,61	5,12
68	210	24	2,25	111	210	-19	43	0	2750	2175	4925	55,8	43,50	3,79	3,00	6,79
68	210	24	2,5	116	210	-24	48	0	2985	1905	4890	61,0	31,80	5,63	3,59	9,23
68	210	24	3	118	210	-26	50	0	3075	1425	4500	68,3	20,00	9,23	4,28	13,50
68	210	24	3,5	118	210	-26	50	0	3190	1525	4715	67,7	15,00	12,76	6,10	18,86
68	210	24	4	119	210	-27	51	0	3900	1290	5190	75,1	13,00	18,00	5,95	23,95
68	210	24	4,5	120	210	-28	52	0	3100	1940	5040	61,5	9,80	18,98	11,88	30,86
87	210	5	1	95	210	-3	8	0	50	1650	1700	2,9	82,00	0,04	1,21	1,24
87	210	5	1,5	107	210	-15	20	0	660	330	990	66,7	22,90	1,73	0,86	2,59
87	210	5	2	115	210	-23	28	0	3700	1200	4900	75,5	53,50	4,15	1,35	5,50
87	210	5	2,25	119	210	-27	32	0	3875	950	4825	80,3	40,00	5,81	1,43	7,24
87	210	5	2,5	119	210	-27	32	0	3450	1185	4635	74,4	30,60	6,76	2,32	9,09
87	210	5	3	119	210	-27	32	0	3190	925	4115	77,5	18,25	10,49	3,04	13,53
87	210	5	3,5	119	210	-27	32	0	4000	1225	5225	76,6	16,75	14,33	4,39	18,72
87	210	5	4	119	210	-27	32	0	4090	1560	5650	72,4	13,75	17,85	6,81	24,65
87	210	5	4,5	120	210	-28	33	0	3750	1660	5410	69,3	10,40	21,63	9,58	31,21
105	210	-13	1	107	210	-15	2	0	555	0	555	100,0	61,10	0,55	0,00	0,55
105	210	-13	1,5	114	210	-22	9	0	930	0	930	100,0	21,00	2,66	0,00	2,66
105	210	-13	2	117	210	-25	12	0	4350	600	4950	87,9	54,50	4,79	0,66	5,45
105	210	-13	2,25	118	210	-26	13	0	4150	550	4700	88,3	44,00	5,66	0,75	6,41
105	210	-13	2,5	119	210	-27	14	0	4395	555	4950	88,8	32,40	8,14	1,03	9,17
105	210	-13	3	121	210	-29	16	0	4200	615	4815	87,2	21,00	12,00	1,76	13,76
105	210	-13	3,5	121	210	-29	16	0	4540	700	5240	86,6	16,60	16,41	2,53	18,94
105	210	-13	4	121	210	-29	16	0	4975	950	5925	84,0	14,25	20,95	4,00	24,95
105	210	-13	4,5	123	210	-31	18	0	4540	1190	5730	79,2	10,40	26,19	6,87	33,06

Figure A.1: Spreadsheet for Nexbase 3080, $\delta = 5$ [mm], single orifice.

BEFORE			DURING						AFTER								
Liquid level, mm			Valve	Liquid level (max Δ), mm						Amount, ml			WC, %	Time, s	Flowrate, l/min		
wL	oL	ΔL		wL'	oL'	ΔL'	wJ	oJ	wV	oV	totV	wQ			oQ	totQ	
11	210	81	1	12	210	80	1	0	0	700	700	0,0	133,00	0,00	0,32	0,32	
11	210	81	2	21	210	71	10	0	0	3250	3250	0,0	46,00	0,00	4,24	4,24	
11	210	81	3	40	210	52	29	0	0	4475	4475	0,0	23,50	0,00	11,43	11,43	
11	210	81	4	95	210	-3	84	0	260	5210	5470	4,8	13,60	1,15	22,99	24,13	
11	210	81	4,5	98	210	-6	87	0	270	4335	4605	5,9	9,75	1,66	26,68	28,34	
11	210	81	5	100	210	-8	89	0	295	4775	5070	5,8	9,30	1,90	30,81	32,71	
20	210	72	1	21	210	71	1	0	0	550	550	0,0	151,50	0,00	0,22	0,22	
20	210	72	1,5	24	210	68	4	0	0	985	985	0,0	29,85	0,00	1,98	1,98	
20	210	72	2	32	210	60	12	0	0	5500	5500	0,0	60,00	0,00	5,50	5,50	
20	210	72	2,25	36	210	56	16	0	0	4700	4700	0,0	41,00	0,00	6,88	6,88	
20	210	72	2,5	39	210	53	19	0	0	4080	4080	0,0	29,40	0,00	8,33	8,33	
20	210	72	3	53	210	39	33	0	0	4240	4240	0,0	20,75	0,00	12,26	12,26	
20	210	72	3,5	79	210	13	59	0	0	5100	5100	0,0	16,75	0,00	18,27	18,27	
20	210	72	4	97	210	-5	77	0	41,5	4875	5290	7,8	14,00	1,78	20,89	22,67	
20	210	72	4,5	101	210	-9	81	0	71,0	4650	5360	13,2	11,40	3,74	24,47	28,21	
29	210	63	1	30	210	62	1	0	0	550	550	0,0	170,50	0,00	0,19	0,19	
29	210	63	1,5	34	210	58	5	0	0	1000	1000	0,0	30,90	0,00	1,94	1,94	
29	210	63	2	43	210	49	14	0	0	4700	4700	0,0	56,50	0,00	4,99	4,99	
29	210	63	2,25	50	210	42	21	0	0	6150	6150	0,0	52,00	0,00	7,10	7,10	
29	210	63	2,5	56	210	36	27	0	0	3945	3945	0,0	28,50	0,00	8,31	8,31	
29	210	63	3	74	210	18	45	0	0	4375	4375	0,0	21,25	0,00	12,35	12,35	
29	210	63	3,5	97	210	-5	68	0	350	4490	4840	7,2	17,00	1,24	15,85	17,08	
29	210	63	4	103	210	-11	74	0	965	4085	5050	19,1	13,25	4,37	18,50	22,87	
29	210	63	4,5	106	210	-14	77	0	1180	4340	5520	21,4	11,60	6,10	22,45	28,55	
48	210	44	1	50	210	42	2	0	0	1050	1050	0,0	150,50	0,00	0,42	0,42	
48	210	44	1,5	54	210	38	6	0	0	990	990	0,0	29,70	0,00	2,00	2,00	
48	210	44	2	63	210	29	15	0	0	4925	4925	0,0	61,50	0,00	4,80	4,80	
48	210	44	2,25	70	210	22	22	0	0	5000	5000	0,0	46,50	0,00	6,45	6,45	
48	210	44	2,5	80	210	12	32	0	0	4350	4350	0,0	30,30	0,00	8,61	8,61	
48	210	44	3	96	210	-4	48	0	365	3935	4300	8,5	20,75	1,06	11,38	12,43	
48	210	44	3,5	102	210	-10	54	0	1200	3865	5065	23,7	16,75	4,30	13,84	18,14	
48	210	44	4	108	210	-16	60	0	1765	3725	5490	32,1	13,75	7,70	16,25	23,96	
48	210	44	4,5	110	210	-18	62	0	1960	3460	5420	36,2	10,40	11,31	19,96	31,27	
68	210	24	1	69	210	23	1	0	0	950	950	0,0	150,50	0,00	0,38	0,38	
68	210	24	1,5	77	210	15	9	0	0	1000	1000	0,0	25,61	0,00	2,34	2,34	
68	210	24	2	92	210	0	24	0	0	4950	4950	0,0	63,00	0,00	4,71	4,71	
68	210	24	2,25	95	210	-3	27	0	400	4550	4950	8,1	44,50	0,54	6,13	6,67	
68	210	24	2,5	99	210	-7	31	0	930	3540	4470	20,8	30,90	1,81	6,87	8,68	
68	210	24	3	105	210	-13	37	0	1240	2335	3575	34,7	16,75	4,44	8,36	12,81	
68	210	24	3,5	109	210	-17	41	0	2365	2975	5340	44,3	17,00	8,35	10,50	18,85	
68	210	24	4	113	210	-21	45	0	2525	2640	5165	48,9	12,25	12,37	12,93	25,30	
68	210	24	4,5	113	210	-21	45	0	2590	2410	5000	51,8	9,60	16,19	15,06	31,25	
87	210	5	1	89	210	3	2	0	0	560	560	0,0	126,20	0,00	0,27	0,27	
87	210	5	1,5	97	210	-5	10	0	195	1230	1425	13,7	35,70	0,33	2,07	2,39	
87	210	5	2	103	210	-11	16	0	1800	3000	4800	37,5	55,00	1,96	3,27	5,24	
87	210	5	2,25	105	210	-13	18	0	2175	2725	4900	44,4	43,00	3,03	3,80	6,84	
87	210	5	2,5	108	210	-16	21	0	2415	2445	4860	49,7	30,90	4,69	4,75	9,44	
87	210	5	3	111	210	-19	24	0	2950	2215	5165	57,1	23,25	7,61	5,72	13,33	
87	210	5	3,5	115	210	-23	28	0	3365	2100	5465	61,6	17,25	11,70	7,30	19,01	
87	210	5	4	116	210	-24	29	0	3090	1670	4760	64,9	10,60	17,49	9,45	26,94	
87	210	5	4,5	117	210	-25	30	0	3150	2310	5460	57,7	9,80	19,29	14,14	33,43	
105	210	-13	1	105	210	-13	0	0	1040	0	1040	100,0	115,60	0,54	0,00	0,54	
105	210	-13	1,5	107	210	-15	2	0	875	105	980	89,3	24,70	2,13	0,26	2,38	
105	210	-13	2	110	210	-18	5	0	3400	1250	4650	73,1	56,00	3,64	1,34	4,98	
105	210	-13	2,25	113	210	-21	8	0	3475	1275	4750	73,2	41,00	5,09	1,87	6,95	
105	210	-13	2,5	114	210	-22	9	0	3975	1275	5250	75,7	31,10	7,67	2,46	10,13	
105	210	-13	3	116	210	-24	11	0	3425	1190	4615	74,2	21,00	9,79	3,40	13,19	
105	210	-13	3,5	118	210	-26	13	0	4015	1225	5240	76,6	16,25	14,82	4,52	19,35	
105	210	-13	4	119	210	-27	14	0	4200	1250	5450	77,1	13,00	19,38	5,77	25,15	
105	210	-13	4,5	119	210	-27	14	0	4510	1290	5800	77,8	10,00	27,06	7,74	34,80	

Figure A.2: Spreadsheet for Nexbase 3080, $\delta = 10$ [mm], single orifice.

BEFORE			DURING						AFTER								
Liquid level, mm			Valve	Liquid level (max Δ), mm					Amount, ml			WC, %	Time, s	Flowrate, l/min			
wL	oL	ΔL		wL'	oL'	ΔL'	wJ	oJ	wV	oV	totV			wQ	oQ	totQ	
11	210	81	1	11	210	81	0	0	0	925	925	0,0	149,50	0,00	0,37	0,37	
11	210	81	1,5	12	210	80	1	0	0	1000	1000	0,0	30,00	0,00	2,00	2,00	
11	210	81	2	13	210	79	2	0	0	4775	4775	0,0	61,50	0,00	4,66	4,66	
11	210	81	2,5	17	210	75	6	0	0	5120	5120	0,0	34,00	0,00	9,04	9,04	
11	210	81	3	20	210	72	9	0	0	4890	4890	0,0	24,30	0,00	12,07	12,07	
11	210	81	3,5	27	210	65	16	0	0	5140	5140	0,0	17,25	0,00	17,88	17,88	
11	210	81	4	32	210	60	21	0	0	5030	5030	0,0	12,80	0,00	23,58	23,58	
11	210	81	4,5	38	210	54	27	0	0	5390	5390	0,0	11,60	0,00	27,88	27,88	
29	210	63	1	29	210	63	0	0	0	700	700	0,0	153,00	0,00	0,27	0,27	
29	210	63	1,5	31	210	61	2	0	0	1110	1110	0,0	30,30	0,00	2,20	2,20	
29	210	63	2	34	210	58	5	0	0	4975	4975	0,0	60,00	0,00	4,98	4,98	
29	210	63	2,25	37	210	55	8	0	0	5500	5500	0,0	41,00	0,00	8,05	8,05	
29	210	63	2,5	38	210	54	9	0	0	4825	4825	0,0	33,00	0,00	8,77	8,77	
29	210	63	3	43	210	49	14	0	0	4315	4315	0,0	21,00	0,00	12,33	12,33	
29	210	63	3,5	50	210	42	21	0	0	5065	5065	0,0	17,50	0,00	17,37	17,37	
29	210	63	4	60	210	32	31	0	0	5415	5415	0,0	14,00	0,00	23,21	23,21	
29	210	63	4,5	73	210	19	44	0	0	4990	4990	0,0	10,60	0,00	28,25	28,25	
48	210	44	1	48	210	44	0	0	0	525	525	0,0	168,50	0,00	0,19	0,19	
48	210	44	1,5	52	210	40	4	0	0	1005	1005	0,0	30,30	0,00	1,99	1,99	
48	210	44	2	55	210	37	7	0	0	4775	4775	0,0	63,50	0,00	4,51	4,51	
48	210	44	2,25	58	210	34	10	0	0	4650	4650	0,0	41,50	0,00	6,72	6,72	
48	210	44	2,5	63	210	29	15	0	0	4590	4590	0,0	30,30	0,00	9,09	9,09	
48	210	44	3	68	210	24	20	0	0	4075	4075	0,0	20,50	0,00	11,93	11,93	
48	210	44	3,5	91	210	1	43	0	25	4815	4840	0,5	16,50	0,09	17,51	17,60	
48	210	44	4	96	210	-4	48	0	440	5010	5450	8,1	14,75	1,79	20,38	22,17	
48	210	44	4,5	100	210	-8	52	0	1100	4730	5830	18,9	11,60	5,69	24,47	30,16	
68	210	24	1	69	210	23	1	0	0	825	825	0,0	180,50	0,00	0,27	0,27	
68	210	24	1,5	72	210	20	4	0	0	955	955	0,0	26,00	0,00	2,20	2,20	
68	210	24	2	78	210	14	10	0	0	4900	4900	0,0	57,00	0,00	5,16	5,16	
68	210	24	2,25	82	210	10	14	0	0	4975	4975	0,0	45,00	0,00	6,63	6,63	
68	210	24	2,5	88	210	4	20	0	0	4800	4800	0,0	31,80	0,00	9,06	9,06	
68	210	24	3	95	210	-3	27	0	500	4865	5365	9,3	24,00	1,25	12,16	13,41	
68	210	24	3,5	100	210	-8	32	0	1090	4035	5125	21,3	16,25	4,02	14,90	18,92	
68	210	24	4	103	210	-11	35	0	1565	3925	5490	28,5	14,00	6,71	16,82	23,53	
68	210	24	4,5	107	210	-15	39	0	2100	3560	5660	37,1	10,20	12,35	20,94	33,29	
87	210	5	1	87	210	5	0	0	0	600	600	0,0	173,50	0,00	0,21	0,21	
87	210	5	1,5	93	210	-1	6	0	0	1395	1395	0,0	35,85	0,00	2,33	2,33	
87	210	5	2	97	210	-5	10	0	650	4850	5500	11,8	59,00	0,66	4,93	5,59	
87	210	5	2,25	98	210	-6	11	0	1025	3975	5000	20,5	44,50	1,38	5,36	6,74	
87	210	5	2,5	101	210	-9	14	0	1290	3390	4680	27,6	31,20	2,48	6,52	9,00	
87	210	5	3	105	210	-13	18	0	1700	2765	4465	38,1	20,00	5,10	8,30	13,40	
87	210	5	3,5	108	210	-16	21	0	2450	2940	5390	45,5	17,00	8,65	10,38	19,02	
87	210	5	4	110	210	-18	23	0	3100	3065	6165	50,3	14,00	13,29	13,14	26,42	
87	210	5	4,5	112	210	-20	25	0	2940	2590	5530	53,2	9,80	18,00	15,86	33,86	
105	210	-13	1	105	210	-13	0	0	915	0	915	100,0	89,85	0,61	0,00	0,61	
105	210	-13	1,5	105	210	-13	0	0	855	115	970	88,1	23,20	2,21	0,30	2,51	
105	210	-13	2	108	210	-16	3	0	3150	1850	5000	63,0	54,00	3,50	2,06	5,56	
105	210	-13	2,25	110	210	-18	5	0	3025	1775	4800	63,0	39,00	4,65	2,73	7,38	
105	210	-13	2,5	110	210	-18	5	0	3060	1800	4860	63,0	30,60	6,00	3,53	9,53	
105	210	-13	3	112	210	-20	7	0	3425	1950	5375	63,7	22,25	9,24	5,26	14,49	
105	210	-13	3,5	113	210	-21	8	0	3450	1850	5300	65,1	16,50	12,55	6,73	19,27	
105	210	-13	4	115	210	-23	10	0	3210	1470	4680	68,6	10,80	17,83	8,17	26,00	
105	210	-13	4,5	116	210	-24	11	0	3930	1710	5640	69,7	10,00	23,58	10,26	33,84	

Figure A.3: Spreadsheet for Nexbase 3080, $\delta = 15$ [mm], single orifice.

BEFORE			DURING						AFTER							
Liquid level, mm			Valve	Liquid level (max Δ), mm					Amount, ml			WC, %	Time, s	Flowrate, l/min		
wL	oL	ΔL		wL'	oL'	ΔL'	wJ	oJ	wV	oV	totV			wQ	oQ	totQ
11	210	81	1	11	210	81	0	0	0	500	500	0,0	151,50	0,00	0,20	0,20
11	210	81	1,5	11	210	81	0	0	0	955	955	0,0	23,80	0,00	2,41	2,41
11	210	81	2	12	210	80	1	0	0	4425	4425	0,0	57,50	0,00	4,62	4,62
11	210	81	2,5	13	210	79	2	0	0	4740	4740	0,0	32,10	0,00	8,86	8,86
11	210	81	3	14	210	78	3	0	0	4215	4215	0,0	20,50	0,00	12,34	12,34
11	210	81	3,5	15	210	77	4	0	0	4575	4575	0,0	15,75	0,00	17,43	17,43
11	210	81	4	17	210	75	6	0	0	5520	5520	0,0	13,80	0,00	24,00	24,00
11	210	81	4,5	19	210	73	8	0	0	4990	4990	0,0	10,60	0,00	28,25	28,25
29	210	63	1	29	210	63	0	0	0	850	850	0,0	148,50	0,00	0,34	0,34
29	210	63	1,5	30	210	62	1	0	0	975	975	0,0	28,95	0,00	2,02	2,02
29	210	63	2	31	210	61	2	0	0	4825	4825	0,0	58,00	0,00	4,99	4,99
29	210	63	2,25	32	210	60	3	0	0	4850	4850	0,0	43,00	0,00	6,77	6,77
29	210	63	2,5	33	210	59	4	0	0	4710	4710	0,0	32,10	0,00	8,80	8,80
29	210	63	3	34	210	58	5	0	0	4625	4625	0,0	21,75	0,00	12,76	12,76
29	210	63	3,5	35	210	57	6	0	0	4775	4775	0,0	16,75	0,00	17,10	17,10
29	210	63	4	37	210	55	8	0	0	4690	4690	0,0	12,20	0,00	23,07	23,07
29	210	63	4,5	40	210	52	11	0	0	5050	5050	0,0	11,00	0,00	27,55	27,55
48	210	44	1	48	210	44	0	0	0	500	500	0,0	164,50	0,00	0,18	0,18
48	210	44	1,5	48	210	44	0	0	0	1065	1065	0,0	30,30	0,00	2,11	2,11
48	210	44	2	49	210	43	1	0	0	4900	4900	0,0	58,50	0,00	5,03	5,03
48	210	44	2,25	51	210	41	3	0	0	4900	4900	0,0	46,00	0,00	6,39	6,39
48	210	44	2,5	53	210	39	5	0	0	4410	4410	0,0	30,90	0,00	8,56	8,56
48	210	44	3	55	210	37	7	0	0	4590	4590	0,0	21,25	0,00	12,96	12,96
48	210	44	3,5	57	210	35	9	0	0	5140	5140	0,0	17,75	0,00	17,37	17,37
48	210	44	4	62	210	30	14	0	0	4410	4410	0,0	11,60	0,00	22,81	22,81
48	210	44	4,5	63	210	29	15	0	0	4960	4960	0,0	11,20	0,00	26,57	26,57
68	210	24	1	68	210	24	0	0	0	525	525	0,0	164,00	0,00	0,19	0,19
68	210	24	1,5	69	210	23	1	0	0	1035	1035	0,0	29,85	0,00	2,08	2,08
68	210	24	2	71	210	21	3	0	0	4775	4775	0,0	60,00	0,00	4,78	4,78
68	210	24	2,25	72	210	20	4	0	0	4700	4700	0,0	44,50	0,00	6,34	6,34
68	210	24	2,5	74	210	18	6	0	0	4425	4425	0,0	31,20	0,00	8,51	8,51
68	210	24	3	76	210	16	8	0	0	3790	3790	0,0	18,75	0,00	12,13	12,13
68	210	24	3,5	79	210	13	11	0	0	4715	4715	0,0	16,00	0,00	17,68	17,68
68	210	24	4	85	210	7	17	0	90	4570	4660	1,9	11,80	0,46	23,24	23,69
68	210	24	4,5	91	210	1	23	0	380	4830	5210	7,3	10,60	2,15	27,34	29,49
87	210	5	1	88	210	4	1	0	0	800	800	0,0	168,00	0,00	0,29	0,29
87	210	5	1,5	89	210	3	2	0	0	950	950	0,0	23,40	0,00	2,44	2,44
87	210	5	2	90	210	2	3	0	25	4750	4775	0,5	59,00	0,03	4,83	4,86
87	210	5	2,25	91	210	1	4	0	200	4700	4900	4,1	40,50	0,30	6,96	7,26
87	210	5	2,5	92	210	0	5	0	285	4200	4485	6,4	32,40	0,53	7,78	8,31
87	210	5	3	96	210	-4	9	0	565	3950	4515	12,5	20,25	1,67	11,70	13,38
87	210	5	3,5	97	210	-5	10	0	1020	3490	4510	22,6	14,80	4,14	14,15	18,28
87	210	5	4	99	210	-7	12	0	1280	3190	4470	28,6	11,20	6,86	17,09	23,95
87	210	5	4,5	101	210	-9	14	0	1850	3950	5800	31,9	10,40	10,67	22,79	33,46
105	210	-13	1	105	210	-13	0	0	1050	0	1050	100,0	89,25	0,71	0,00	0,71
105	210	-13	1,5	105	210	-13	0	0	830	90	920	90,2	19,60	2,54	0,28	2,82
105	210	-13	2	105	210	-13	0	0	2725	2100	4825	56,5	54,00	3,03	2,33	5,36
105	210	-13	2,25	105	210	-13	0	0	2575	2250	4825	53,4	38,00	4,07	3,55	7,62
105	210	-13	2,5	105	210	-13	0	0	2445	2220	4665	52,4	29,40	4,99	4,53	9,52
105	210	-13	3	106	210	-14	1	0	2445	2235	4680	52,2	19,50	7,52	6,88	14,40
105	210	-13	3,5	108	210	-16	3	0	3000	2440	5440	55,1	16,75	10,75	8,74	19,49
105	210	-13	4	109	210	-17	4	0	2820	2220	5040	56,0	11,20	15,11	11,89	27,00
105	210	-13	4,5	109	210	-17	4	0	3250	2520	5770	56,3	10,20	19,12	14,82	33,94

Figure A.4: Spreadsheet for Nexbase 3080, $\delta = 25$ [mm], single orifice.

BEFORE			DURING					AFTER								
Liquid level, mm			Valve	Liquid level (max Δ), mm					Amount, ml			WC, %	Time, s	Flowrate, l/min		
wl	oL	ΔL		wl'	oL'	ΔL'	wj	oJ	wV	oV	totV			wQ	oQ	totQ
11	210	81	1		210	92	-11	0	0	1000	1000	0,0	106,50	0,00	0,56	0,56
11	210	81	1,5		210	92	-11	0	0	880	880	0,0	20,20	0,00	2,61	2,61
11	210	81	2		210	92	-11	0	0	2980	2980	0,0	31,10	0,00	5,75	5,75
11	210	81	2,25		210	92	-11	0	0	3105	3105	0,0	25,03	0,00	7,44	7,44
11	210	81	2,5		210	92	-11	0	0	3640	3640	0,0	22,50	0,00	9,71	9,71
11	210	81	3		210	92	-11	0	0	4000	4000	0,0	16,80	0,00	14,29	14,29
11	210	81	3,5		210	92	-11	0	0	5010	5010	0,0	15,40	0,00	19,52	19,52
11	210	81	4		210	92	-11	0	110	4340	4450	2,5	9,70	0,68	26,85	27,53
11	210	81	4,5		210	92	-11	0	120	3285	3405	3,5	5,80	1,24	33,98	35,22
29	210	63	1	30	210	62	1	0	0	995	995	0,0	97,70	0,00	0,61	0,61
29	210	63	1,5	36	210	56	7	0	0	960	960	0,0	21,50	0,00	2,68	2,68
29	210	63	2	42	210	50	13	0	0	5260	5260	0,0	60,30	0,00	5,23	5,23
29	210	63	2,25	47	210	45	18	0	0	4930	4930	0,0	40,00	0,00	7,40	7,40
29	210	63	2,5	52	210	40	23	0	0	4510	4510	0,0	28,70	0,00	9,43	9,43
29	210	63	3	92	210	0	63	0	0	4720	4720	0,0	20,60	0,00	13,75	13,75
29	210	63	3,5	99	210	-7	70	0	520	4820	5340	9,7	16,20	1,93	17,85	19,78
29	210	63	4	103	210	-11	74	0	615	4645	5260	11,7	12,00	3,08	23,23	26,30
29	210	63	4,5	104	210	-12	75	0	565	4270	4835	11,7	8,56	3,96	29,93	33,89
50	210	42	1	50	210	42	0	0	0	985	985	0,0	95,00	0,00	0,62	0,62
50	210	42	1,5	51	210	41	1	0	0	960	960	0,0	21,84	0,00	2,64	2,64
50	210	42	2	64	210	28	14	0	0	5730	5730	0,0	58,20	0,00	5,91	5,91
50	210	42	2,25	75	210	17	25	0	0	5230	5230	0,0	41,86	0,00	7,50	7,50
50	210	42	2,5	91	210	1	41	0	0	5110	5110	0,0	31,80	0,00	9,64	9,64
50	210	42	3	99	210	-7	49	0	650	4210	4860	13,4	20,50	1,90	12,32	14,22
50	210	42	3,5	101	210	-9	51	0	1100	4380	5480	20,1	15,30	4,31	17,18	21,49
50	210	42	4	101	210	-9	51	0	1090	3965	5055	21,6	11,28	5,80	21,09	26,89
50	210	42	4,5	105	210	-13	55	0	885	3115	4000	22,1	7,31	7,26	25,57	32,83
67	210	25	1	69	210	23	2	0	0	1000	1000	0,0	78,00	0,00	0,77	0,77
67	210	25	1,5	74	210	18	7	0	0	980	980	0,0	22,90	0,00	2,57	2,57
67	210	25	2	84	210	8	17	0	0	5300	5300	0,0	59,10	0,00	5,38	5,38
67	210	25	2,25	96	210	-4	29	0	90	5400	5490	1,6	43,70	0,12	7,41	7,54
67	210	25	2,5	99	210	-7	32	0	580	4640	5220	11,1	32,00	1,09	8,70	9,79
67	210	25	3	103	210	-11	36	0	1120	3990	5110	21,9	21,70	3,10	11,03	14,13
67	210	25	3,5	108	210	-16	41	0	1700	3980	5680	29,9	16,30	6,26	14,65	20,91
67	210	25	4	109	210	-17	42	0	1650	3500	5150	32,0	11,60	8,53	18,10	26,64
67	210	25	4,5	111	210	-19	44	0	1285	2795	4080	31,5	7,20	10,71	23,29	34,00
85	210	7	1	85	210	7	0	0	0	970	970	0,0	107,20	0,00	0,54	0,54
85	210	7	1,5	85	210	7	0	0	0	970	970	0,0	23,00	0,00	2,53	2,53
85	210	7	2	95	210	-3	10	0	1120	4220	5340	21,0	56,20	1,20	4,51	5,70
85	210	7	2,25	102	210	-10	17	0	1400	3980	5380	26,0	43,10	1,95	5,54	7,49
85	210	7	2,5	105	210	-13	20	0	2220	4050	6270	35,4	40,00	3,33	6,08	9,41
85	210	7	3	107	210	-15	22	0	2180	3030	5210	41,8	22,20	5,89	8,19	14,08
85	210	7	3,5	111	210	-19	26	0	2460	3040	5500	44,7	16,60	8,89	10,99	19,88
85	210	7	4	115	210	-23	30	0	2190	2710	4900	44,7	11,30	11,63	14,39	26,02
85	210	7	4,5	115	210	-23	30	0	2040	2530	4570	44,6	8,40	14,57	18,07	32,64
106	210	-14	1	106	210	-14	0	0	0	0	0	100,0	#DIV/0!	#DIV/0!	#DIV/0!	#DIV/0!
106	210	-14	1,5	106	210	-14	0	0	0	0	0	100,0	#DIV/0!	#DIV/0!	#DIV/0!	#DIV/0!
106	210	-14	2	112	210	-20	6	0	3340	1840	5180	64,5	57,60	3,48	1,92	5,40
106	210	-14	2,25	115	210	-23	9	0	3250	2060	5310	61,2	43,20	4,51	2,86	7,38
106	210	-14	2,5	117	210	-25	11	0	3240	1980	5220	62,1	32,60	5,96	3,64	9,61
106	210	-14	3	118	210	-26	12	0	2920	1870	4790	61,0	21,50	8,15	5,22	13,37
106	210	-14	3,5	118	210	-26	12	0	2900	1900	4800	60,4	15,10	11,52	7,55	19,07
106	210	-14	4	118	210	-26	12	0	2780	1875	4655	59,7	10,60	15,74	10,61	26,35
106	210	-14	4,5	119	210	-27	13	0	2435	1740	4175	58,3	7,80	18,73	13,38	32,12

Figure A.5: Spreadsheet for Marcol 52, $\delta = 5$ [mm], single orifice.

BEFORE			DURING						AFTER							
Liquid level, mm			Valve	Liquid level (max Δ), mm					Amount, ml			WC, %	Time, s	Flowrate, l/min		
wL	oL	ΔL		wL'	oL'	ΔL'	wJ	oJ	wV	oV	totV			wQ	oQ	totQ
11	210	81	1	11	210	81	0	0	0	980	980	0,0	110,30	0,00	0,53	0,53
11	210	81	1,5	11	210	81	0	0	0	950	950	0,0	21,30	0,00	2,68	2,68
11	210	81	2	12	210	80	1	0	0	2545	2545	0,0	29,80	0,00	5,12	5,12
11	210	81	2,25	12	210	80	1	0	0	3050	3050	0,0	25,10	0,00	7,29	7,29
11	210	81	2,5	12	210	80	1	0	0	3195	3195	0,0	20,90	0,00	9,17	9,17
11	210	81	3	15	210	77	4	0	0	3660	3660	0,0	15,60	0,00	14,08	14,08
11	210	81	3,5	17	210	75	6	0	0	4505	4505	0,0	13,20	0,00	20,48	20,48
11	210	81	4	20	210	72	9	0	0	2700	2700	0,0	5,80	0,00	27,93	27,93
11	210	81	4,5	25	210	67	14	0	0	3130	3130	0,0	5,50	0,00	34,15	34,15
29	210	63	1	29	210	63	0	0	0	980	980	0,0	102,80	0,00	0,57	0,57
29	210	63	1,5	30	210	62	1	0	0	970	970	0,0	22,90	0,00	2,54	2,54
29	210	63	2	31	210	61	2	0	0	5790	5790	0,0	59,80	0,00	5,81	5,81
29	210	63	2,25	32	210	60	3	0	0	5130	5130	0,0	41,10	0,00	7,49	7,49
29	210	63	2,5	33	210	59	4	0	0	5460	5460	0,0	30,40	0,00	10,78	10,78
29	210	63	3	34	210	58	5	0	0	4770	4770	0,0	20,40	0,00	14,03	14,03
29	210	63	3,5	37	210	55	8	0	0	5000	5000	0,0	14,60	0,00	20,55	20,55
29	210	63	4	42	210	50	13	0	0	5150	5150	0,0	11,00	0,00	28,09	28,09
29	210	63	4,5	48	210	44	19	0	0	5055	5055	0,0	8,70	0,00	34,86	34,86
50	210	42	1	50	210	42	0	0	0	955	955	0,0	97,90	0,00	0,59	0,59
50	210	42	1,5	52	210	40	2	0	0	1045	1045	0,0	21,10	0,00	2,97	2,97
50	210	42	2	52	210	40	2	0	0	5830	5830	0,0	58,60	0,00	5,97	5,97
50	210	42	2,25	53	210	39	3	0	0	4960	4960	0,0	41,40	0,00	7,19	7,19
50	210	42	2,5	55	210	37	5	0	0	4850	4850	0,0	30,60	0,00	9,51	9,51
50	210	42	3	56	210	36	6	0	0	4840	4840	0,0	20,90	0,00	13,89	13,89
50	210	42	3,5	63	210	29	13	0	0	5170	5170	0,0	14,70	0,00	21,10	21,10
50	210	42	4	78	210	14	28	0	0	4920	4920	0,0	11,00	0,00	26,84	26,84
50	210	42	4,5	97	210	-5	47	0	250	4075	4325	5,8	7,40	2,03	33,04	35,07
67	210	25	1	67	210	25	0	0	0	930	930	0,0	110,70	0,00	0,50	0,50
67	210	25	1,5	68	210	24	1	0	0	955	955	0,0	20,70	0,00	2,77	2,77
67	210	25	2	69	210	23	2	0	0	5260	5260	0,0	55,30	0,00	5,71	5,71
67	210	25	2,25	70	210	22	3	0	0	5390	5390	0,0	43,90	0,00	7,37	7,37
67	210	25	2,5	72	210	20	5	0	0	5140	5140	0,0	31,80	0,00	9,70	9,70
67	210	25	3	80	210	12	13	0	0	5380	5380	0,0	22,80	0,00	14,16	14,16
67	210	25	3,5	95	210	-3	28	0	150	5230	5380	2,8	16,10	0,56	19,49	20,05
67	210	25	4	100	210	-8	33	0	660	4375	5035	13,1	11,10	3,57	23,65	27,22
67	210	25	4,5	103	210	-11	36	0	945	3700	4645	20,3	8,20	6,91	27,07	33,99
87	210	5	1	87	210	5	0	0	0	940	940	0,0	102,40	0,00	0,55	0,55
87	210	5	1,5	90	210	2	3	0	0	950	950	0,0	22,30	0,00	2,56	2,56
87	210	5	2	92	210	0	5	0	50	5370	5420	0,9	57,80	0,05	5,57	5,63
87	210	5	2,25	97	210	-5	10	0	280	5220	5500	5,1	43,00	0,39	7,28	7,67
87	210	5	2,5	98	210	-6	11	0	450	4520	4970	9,1	32,40	0,83	8,37	9,20
87	210	5	3	101	210	-9	14	0	990	4130	5120	19,3	22,30	2,66	11,11	13,78
87	210	5	3,5	104	210	-12	17	0	1610	4030	5640	28,5	16,60	5,82	14,57	20,39
87	210	5	4	106	210	-14	19	0	1770	3570	5340	33,1	11,80	9,00	18,15	27,15
87	210	5	4,5	107	210	-15	20	0	1720	2865	4585	37,5	7,90	13,06	21,76	34,82
106	210	-14	1	106	210	-14	0	0	950	0	950	100,0	88,00	0,65	0,00	0,65
106	210	-14	1,5	106	210	-14	0	0	935	0	935	100,0	22,70	2,47	0,00	2,47
106	210	-14	2	107	210	-15	1	0	2920	2150	5070	57,6	57,10	3,07	2,26	5,33
106	210	-14	2,25	107	210	-15	1	0	2960	2200	5160	57,4	42,70	4,16	3,09	7,25
106	210	-14	2,5	109	210	-17	3	0	2480	2430	4910	50,5	31,90	4,66	4,57	9,24
106	210	-14	3	110	210	-18	4	0	2460	2240	4700	52,3	21,10	7,00	6,37	13,36
106	210	-14	3,5	111	210	-19	5	0	2880	2500	5380	53,5	15,80	10,94	9,49	20,43
106	210	-14	4	111	210	-19	5	0	2675	2260	4935	54,2	11,30	14,20	12,00	26,20
106	210	-14	4,5	112	210	-20	6	0	2505	2040	4545	55,1	8,20	18,33	14,93	33,26

Figure A.6: Spreadsheet for Marcol 52, $\delta = 10$ [mm], single orifice.

BEFORE			DURING						AFTER								
Liquid level, mm			Valve	Liquid level (max Δ), mm						Amount, ml			WC, %	Time, s	Flowrate, l/min		
wl	ol	ΔL		wl'	ol'	ΔL'	wl	ol	wV	oV	totV	wQ			oQ	totQ	
11	210	81	1	11	210	81	0	0	0	960	960	0,0	92,80	0,00	0,62	0,62	
11	210	81	1,5	11	210	81	0	0	0	1000	1000	0,0	23,90	0,00	2,51	2,51	
11	210	81	2	12	210	80	1	0	0	2720	2720	0,0	30,90	0,00	5,28	5,28	
11	210	81	2,25	13	210	79	2	0	0	2460	2460	0,0	20,60	0,00	7,17	7,17	
11	210	81	2,5	14	210	78	3	0	0	2960	2960	0,0	18,00	0,00	9,87	9,87	
11	210	81	3	14	210	78	3	0	0	2475	2475	0,0	10,70	0,00	13,88	13,88	
11	210	81	3,5	16	210	76	5	0	0	4525	4525	0,0	13,50	0,00	20,11	20,11	
11	210	81	4	17	210	75	6	0	0	4760	4760	0,0	10,40	0,00	27,46	27,46	
11	210	81	4,5	18	210	74	7	0	0	4480	4480	0,0	7,70	0,00	34,91	34,91	
29	210	63	1	29	210	63	0	0	0	980	980	0,0	102,50	0,00	0,57	0,57	
29	210	63	1,5	29	210	63	0	0	0	960	960	0,0	21,10	0,00	2,73	2,73	
29	210	63	2	30	210	62	1	0	0	5320	5320	0,0	59,10	0,00	5,40	5,40	
29	210	63	2,25	30	210	62	1	0	0	5060	5060	0,0	41,50	0,00	7,32	7,32	
29	210	63	2,5	31	210	61	2	0	0	5200	5200	0,0	30,20	0,00	10,33	10,33	
29	210	63	3	32	210	60	3	0	0	5750	5750	0,0	22,90	0,00	15,07	15,07	
29	210	63	3,5	34	210	58	5	0	0	5580	5580	0,0	16,12	0,00	20,77	20,77	
29	210	63	4	34	210	58	5	0	0	5165	5165	0,0	10,81	0,00	28,67	28,67	
29	210	63	4,5	36	210	56	7	0	0	5245	5245	0,0	9,00	0,00	34,97	34,97	
50	210	42	1	50	210	42	0	0	0	1000	1000	0,0	90,90	0,00	0,66	0,66	
50	210	42	1,5	50	210	42	0	0	0	955	955	0,0	20,80	0,00	2,75	2,75	
50	210	42	2	50	210	42	0	0	0	5660	5660	0,0	59,70	0,00	5,69	5,69	
50	210	42	2,25	51	210	41	1	0	0	5080	5080	0,0	41,10	0,00	7,42	7,42	
50	210	42	2,5	53	210	39	3	0	0	5540	5540	0,0	32,20	0,00	10,32	10,32	
50	210	42	3	53	210	39	3	0	0	4720	4720	0,0	20,70	0,00	13,68	13,68	
50	210	42	3,5	54	210	38	4	0	0	5030	5030	0,0	15,62	0,00	19,32	19,32	
50	210	42	4	57	210	35	7	0	0	4710	4710	0,0	11,00	0,00	25,69	25,69	
50	210	42	4,5	67	210	25	17	0	0	4885	4885	0,0	8,50	0,00	34,48	34,48	
67	210	25	1	67	210	25	0	0	0	960	960	0,0	104,90	0,00	0,55	0,55	
67	210	25	1,5	67	210	25	0	0	0	990	990	0,0	21,20	0,00	2,80	2,80	
67	210	25	2	68	210	24	1	0	0	5290	5290	0,0	55,40	0,00	5,73	5,73	
67	210	25	2,25	69	210	23	2	0	0	5430	5430	0,0	42,60	0,00	7,65	7,65	
67	210	25	2,5	71	210	21	4	0	0	5140	5140	0,0	33,00	0,00	9,35	9,35	
67	210	25	3	71	210	21	4	0	0	5590	5590	0,0	23,70	0,00	14,15	14,15	
67	210	25	3,5	78	210	14	11	0	0	6650	6650	0,0	19,40	0,00	20,57	20,57	
67	210	25	4	93	210	-1	26	0	15	4715	4730	0,3	10,50	0,09	26,94	27,03	
67	210	25	4,5	99	210	-7	32	0	410	4155	4565	9,0	7,70	3,19	32,38	35,57	
87	210	5	1	87	210	5	0	0	0	970	970	0,0	94,20	0,00	0,62	0,62	
87	210	5	1,5	89	210	3	2	0	0	990	990	0,0	23,30	0,00	2,55	2,55	
87	210	5	2	91	210	1	4	0	0	5400	5400	0,0	58,60	0,00	5,53	5,53	
87	210	5	2,25	93	210	-1	6	0	40	5570	5610	0,7	44,20	0,05	7,56	7,62	
87	210	5	2,5	93	210	-1	6	0	250	6330	6580	3,8	41,70	0,36	9,11	9,47	
87	210	5	3	100	210	-8	13	0	550	4850	5400	10,2	22,70	1,45	12,82	14,27	
87	210	5	3,5	101	210	-9	14	0	980	4360	5340	18,4	15,40	3,82	16,99	20,81	
87	210	5	4	103	210	-11	16	0	1145	3545	4690	24,4	10,30	6,67	20,65	27,32	
87	210	5	4,5	105	210	-13	18	0	1410	3380	4790	29,4	8,30	10,19	24,43	34,63	
106	210	-14	1	106	210	-14	0	0	970	0	970	100,0	74,30	0,78	0,00	0,78	
106	210	-14	1,5	106	210	-14	0	0	960	0	960	100,0	21,00	2,74	0,00	2,74	
106	210	-14	2	106	210	-14	0	0	2520	2910	5430	46,4	58,60	2,58	2,98	5,56	
106	210	-14	2,25	106	210	-14	0	0	2580	2740	5320	48,5	42,90	3,61	3,83	7,44	
106	210	-14	2,5	107	210	-15	1	0	2340	2630	4970	47,1	32,90	4,27	4,80	9,06	
106	210	-14	3	107	210	-15	1	0	2430	2640	5070	47,9	22,20	6,57	7,14	13,70	
106	210	-14	3,5	108	210	-16	2	0	2590	2710	5300	48,9	16,30	9,53	9,98	19,51	
106	210	-14	4	109	210	-17	3	0	2370	2400	4770	49,7	10,50	13,54	13,71	27,26	
106	210	-14	4,5	111	210	-19	5	0	2420	2355	4775	50,7	8,70	16,69	16,24	32,93	

Figure A.7: Spreadsheet for Marcol 52, $\delta = 15$ [mm], single orifice.

BEFORE			DURING	Liquid level (max Δ), mm					AFTER			WC, %	Time, s	Flowrate, l/min			
wL	oL	ΔL		Valve	wL'	oL'	ΔL'	wJ	oJ	wV	oV			totV	wQ	oQ	totQ
11	210	81	10	1	11	210	81	0	0	0	970	970	0,0	103,50	0,00	0,56	0,56
11	210	81		1,5	11	210	81	0	0	0	960	960	0,0	21,50	0,00	2,68	2,68
11	210	81		2	11	210	81	0	0	0	5400	5400	0,0	59,60	0,00	5,44	5,44
11	210	81		2,25	11	210	81	0	0	0	5010	5010	0,0	41,00	0,00	7,33	7,33
11	210	81		2,5	11	210	81	0	0	0	5000	5000	0,0	30,10	0,00	9,97	9,97
11	210	81		3	11	210	81	0	0	0	4750	4750	0,0	20,50	0,00	13,90	13,90
11	210	81		3,5	13	210	79	2	0	0	4480	4480	0,0	13,50	0,00	19,91	19,91
11	210	81		4	13	210	79	2	0	0	4350	4350	0,0	9,60	0,00	27,19	27,19
11	210	81		4,5	14	210	78	3	0	0	4605	4605	0,0	8,00	0,00	34,54	34,54
29	210	63	30	1	29	210	63	0	0	0	980	980	0,0	102,50	0,00	0,57	0,57
29	210	63		1,5	29	210	63	0	0	0	960	960	0,0	21,10	0,00	2,73	2,73
29	210	63		2	29	210	63	0	0	0	5330	5330	0,0	59,00	0,00	5,42	5,42
29	210	63		2,25	29	210	63	0	0	0	5040	5040	0,0	41,20	0,00	7,34	7,34
29	210	63		2,5	29	210	63	0	0	0	5010	5010	0,0	30,30	0,00	9,92	9,92
29	210	63		3	30	210	62	1	0	0	4760	4760	0,0	20,70	0,00	13,80	13,80
29	210	63		3,5	30	210	62	1	0	0	5560	5560	0,0	16,00	0,00	20,85	20,85
29	210	63		4	31	210	61	2	0	0	4915	4915	0,0	11,09	0,00	26,59	26,59
29	210	63		4,5	33	210	59	4	0	0	4990	4990	0,0	8,56	0,00	34,98	34,98
50	210	42	50	1	50	210	42	0	0	0	945	945	0,0	93,10	0,00	0,61	0,61
50	210	42		1,5	50	210	42	0	0	0	1010	1010	0,0	21,30	0,00	2,85	2,85
50	210	42		2	50	210	42	0	0	0	5560	5560	0,0	59,40	0,00	5,62	5,62
50	210	42		2,25	50	210	42	0	0	0	5180	5180	0,0	41,80	0,00	7,44	7,44
50	210	42		2,5	50	210	42	0	0	0	5080	5080	0,0	32,20	0,00	9,47	9,47
50	210	42		3	51	210	41	1	0	0	5340	5340	0,0	21,70	0,00	14,76	14,76
50	210	42		3,5	51	210	41	1	0	0	5230	5230	0,0	14,90	0,00	21,06	21,06
50	210	42		4	52	210	40	2	0	0	4850	4850	0,0	11,00	0,00	26,45	26,45
50	210	42		4,5	54	210	38	4	0	0	4715	4715	0,0	7,90	0,00	35,81	35,81
67	210	25	70	1	67	210	25	0	0	0	975	975	0,0	90,20	0,00	0,65	0,65
67	210	25		1,5	67	210	25	0	0	0	970	970	0,0	21,40	0,00	2,72	2,72
67	210	25		2	67	210	25	0	0	0	5260	5260	0,0	55,70	0,00	5,67	5,67
67	210	25		2,25	67	210	25	0	0	0	4970	4970	0,0	40,60	0,00	7,34	7,34
67	210	25		2,5	67	210	25	0	0	0	4710	4710	0,0	30,20	0,00	9,36	9,36
67	210	25		3	68	210	24	1	0	0	4620	4620	0,0	19,90	0,00	13,93	13,93
67	210	25		3,5	69	210	23	2	0	0	5330	5330	0,0	16,40	0,00	19,50	19,50
67	210	25		4	71	210	21	4	0	0	4910	4910	0,0	11,00	0,00	26,78	26,78
67	210	25		4,5	76	210	16	9	0	0	4715	4715	0,0	8,20	0,00	34,50	34,50
87	210	5	90	1	87	210	5	0	0	0	940	940	0,0	110,20	0,00	0,51	0,51
87	210	5		1,5	87	210	5	0	0	0	930	930	0,0	20,40	0,00	2,74	2,74
87	210	5		2	88	210	4	1	0	0	5330	5330	0,0	58,60	0,00	5,46	5,46
87	210	5		2,25	91	210	1	4	0	0	5420	5420	0,0	43,10	0,00	7,55	7,55
87	210	5		2,5	92	210	0	5	0	0	4830	4830	0,0	30,90	0,00	9,38	9,38
87	210	5		3	94	210	-2	7	0	260	4750	5010	5,2	20,90	0,75	13,64	14,38
87	210	5		3,5	99	210	-7	12	0	520	4920	5440	9,6	16,10	1,94	18,34	20,27
87	210	5		4	102	210	-10	15	0	765	4400	5165	14,8	11,30	4,06	23,36	27,42
87	210	5		4,5	103	210	-11	16	0	795	3355	4150	19,2	7,30	6,53	27,58	34,11
106	210	-14	110	1	106	210	-14	0	0	960	0	960	100,0	87,70	0,66	0,00	0,66
106	210	-14		1,5	106	210	-14	0	0	900	0	900	100,0	21,70	2,49	0,00	2,49
106	210	-14		2	106	210	-14	0	0	2980	2400	5380	55,4	59,90	2,98	2,40	5,39
106	210	-14		2,25	106	210	-14	0	0	2480	2610	5090	48,7	44,40	3,35	3,53	6,88
106	210	-14		2,5	106	210	-14	0	0	2220	2730	4950	44,8	32,60	4,09	5,02	9,11
106	210	-14		3	106	210	-14	0	0	2470	2920	5390	45,8	23,00	6,44	7,62	14,06
106	210	-14		3,5	106	210	-14	0	0	2610	2870	5480	47,6	16,60	9,43	10,37	19,81
106	210	-14		4	106	210	-14	0	0	2340	2565	4905	47,7	10,90	12,88	14,12	27,00
106	210	-14		4,5	107	210	-15	1	0	2215	2390	4605	48,1	8,30	16,01	17,28	33,29

Figure A.8: Spreadsheet for Marcol 52, $\delta = 25$ [mm], single orifice.

BEFORE										DURING										AFTER									
Liquid level, mm					Liquid level (max Δ), mm					Amount, ml Valve 1					Amount, ml Valve 2					Flowrate, l/min Valve 1					Flowrate, l/min Valve 2				
wL	oL	AL	Valve	wL	oL	AL	wL	oV	totV	WC, %	wV	oV	totV	WC, %	wV	oV	totV	WC, %	Time, s	wQ	oQ	totQ	wQ	oQ	totQ				
10	210	82	1.5	24	23	210	68	14	860	860	0.0	0	860	915	0	915	915	0.0	25.53	0.00	2.02	2.02	0.00	2.15	2.15				
10	210	82	2	44	43	210	48	34	2035	2035	0.0	0	2035	2035	0.0	2235	2235	0.0	25.87	0.00	4.72	4.72	0.00	5.18	5.18				
10	210	82	2.25	58	53	210	34	48	1945	1945	0.0	0	1945	1945	0.0	1990	1990	0.0	18.87	0.00	6.18	6.18	0.00	6.33	6.33				
10	210	82	2.5	76	70	210	16	66	1515	1515	0.0	0	1515	1635	0.0	1635	1635	0.0	11.40	0.00	7.97	7.97	0.00	8.61	8.61				
10	210	82	3	98	95	210	-6	88	150	1490	1640	9.1	30	1645	1675	1.8	8.43	1.07	10.60	11.67	0.21	11.71	11.92	11.92					
10	210	82	3.5	101	96	210	-9	91	170	1505	1675	10.1	20	1650	1670	1.2	6.34	1.61	14.24	15.85	0.19	15.62	15.80	15.80					
10	210	82	4	104	98	210	-12	94	200	2060	2260	8.8	20	2145	2165	0.9	6.28	1.91	19.68	21.59	0.19	20.49	20.68	20.68					
29	210	63	1.5	43	42	210	49	14	910	910	0.0	0	910	970	0.0	970	970	0.0	25.56	0.00	2.14	2.14	0.00	2.28	2.28				
29	210	63	2	62	58	210	30	33	1830	1830	0.0	0	1830	1925	0.0	1925	1925	0.0	23.15	0.00	4.74	4.74	0.00	4.99	4.99				
29	210	63	2.25	75	68	210	17	46	1950	1950	0.0	0	1950	2020	0.0	2020	2020	0.0	18.37	0.00	6.37	6.37	0.00	6.60	6.60				
29	210	63	2.5	93	81	210	-1	64	1750	1765	0.8	0	1765	1765	0.0	1765	1765	0.0	13.15	0.07	7.98	8.05	0.00	8.05	8.05				
29	210	63	3	102	97	210	-10	73	385	1350	1735	22.2	210	1540	1750	12.0	8.56	2.70	9.46	12.16	1.47	10.79	12.27	12.27					
29	210	63	3.5	108	103	210	-16	79	490	1295	1785	27.5	210	1475	1685	12.5	6.25	4.70	12.43	17.14	2.02	14.16	16.18	16.18					
29	210	63	4	110	103	210	-18	81	585	1495	2080	28.1	190	1740	1930	9.8	5.56	6.31	16.13	22.45	2.05	18.78	20.83	20.83					
49	210	43	1.5	64	64	210	28	15	900	900	0.0	0	900	900	0.0	915	915	0.0	25.18	0.00	2.14	2.14	0.00	2.18	2.18				
49	210	43	2	90	85	210	2	41	5	2000	2005	0.2	0	2100	2100	0.0	25.34	0.00	4.74	4.75	0.00	4.97	4.97						
49	210	43	2.25	100	96	210	-8	51	340	1640	1980	17.2	95	1785	1880	5.1	17.31	1.18	5.68	6.86	0.33	6.19	6.52	6.52					
49	210	43	2.5	103	101	210	-11	54	480	1300	1780	27.0	250	1510	1760	14.2	12.81	2.25	6.09	8.34	1.17	7.07	8.24	8.24					
49	210	43	3	108	104	210	-16	59	650	990	1640	39.6	475	1110	1585	30.0	7.75	5.03	7.66	12.70	3.68	8.59	12.27	12.27					
49	210	43	3.5	112	111	210	-20	63	715	955	1670	42.8	490	1110	1600	30.6	5.53	7.76	10.36	18.12	5.32	12.04	17.36	17.36					
49	210	43	4	113	119	210	-21	64	910	1195	2105	43.2	520	1495	2015	25.8	5.31	10.28	13.50	23.79	5.88	16.89	22.77	22.77					
67	210	25	1.5	87	88	210	5	20	870	870	0.0	0	870	950	0.0	950	950	0.0	25.34	0.00	2.06	2.06	0.00	2.25	2.25				
67	210	25	2	101	100	210	-9	34	580	1385	1965	29.5	455	1515	1970	23.1	22.81	1.53	3.64	5.17	1.20	3.99	5.18	5.18					
67	210	25	2.25	104	105	210	-12	37	815	1245	2060	39.6	670	1315	1985	33.8	17.59	2.78	4.25	7.03	2.29	4.49	6.77	6.77					
67	210	25	2.5	107	107	210	-15	40	785	955	1740	45.1	750	1045	1795	41.8	12.50	3.77	4.58	8.35	3.60	5.02	8.62	8.62					
67	210	25	3	114	116	210	-22	47	840	740	1580	53.2	865	795	1660	52.1	7.34	6.87	6.05	12.92	7.07	6.50	13.57	13.57					
67	210	25	3.5	117	119	210	-25	50	900	695	1595	56.4	795	755	1550	51.3	5.28	10.23	7.90	18.13	9.03	8.58	17.61	17.61					
67	210	25	4	120	121	210	-28	53	970	935	1905	50.9	935	935	1870	50.0	4.75	12.25	11.81	24.06	11.81	11.81	23.62	23.62					
88	210	4	1.5	102	103	210	-10	14	460	440	900	51.1	430	380	1010	42.6	24.37	1.13	1.08	2.22	1.06	1.43	2.49	2.49					
88	210	4	2	106	109	210	-14	18	1120	750	1870	59.9	1065	750	1815	58.7	20.46	3.28	2.20	5.48	3.12	2.20	5.32	5.32					
88	210	4	2.25	110	111	210	-18	22	1170	660	1830	63.9	1100	695	1795	61.3	15.65	4.49	2.53	7.02	4.22	2.66	6.88	6.88					
88	210	4	2.5	111	113	210	-19	23	1085	585	1670	65.0	1090	570	1660	65.7	11.37	5.73	3.09	8.81	5.75	3.01	8.76	8.76					
88	210	4	3	117	120	210	-25	29	1140	525	1665	68.5	1130	510	1660	69.3	7.59	9.01	4.15	13.16	9.09	4.03	13.12	13.12					
88	210	4	3.5	119	126	210	-27	31	1135	535	1670	68.0	1085	520	1605	67.6	5.50	12.38	5.84	18.22	11.84	5.67	17.51	17.51					
88	210	4	4	126	139	210	-34	38	1240	665	1905	65.1	1155	795	1950	59.2	4.71	15.80	8.47	24.27	14.71	10.13	24.84	24.84					

Figure A.9: Spreadsheet for Nexbase 3080, δ = 10 [mm], two orifices at same height.

BEFORE												DURING												AFTER											
Liquid level, mm		Valve		Liquid level (max Δ), mm						Amount, ml Valve 1						Amount, ml Valve 2						Time, s		Flowrate, l/min Valve 1		Flowrate, l/min Valve 2									
wL	ΔL	wL'v1	ΔL'	wL'v2	ΔL'	wL'v1	ΔL'	wL'v2	ΔL'	wV	ΔV	totV	WC, %	wV	ΔV	totV	WC, %	wV	ΔV	totV	WC, %	Time, s	wQ	totQ	wQ	totQ	wQ	totQ	wQ	totQ					
10	210	82	1.5	15	16	210	77	5	5	0	920	920	0.0	0	900	900	0.0	0	900	900	0.0	25.03	0.00	2.21	0.00	0.00	2.21	0.00	2.16						
10	210	82	2	23	24	210	69	13	13	0	1850	1850	0.0	0	1910	1910	0.0	0	1910	1910	0.0	23.12	0.00	4.80	0.00	4.80	0.00	4.96							
10	210	82	2.25	27	28	210	65	17	17	0	1820	1820	0.0	0	1910	1910	0.0	0	1910	1910	0.0	17.34	0.00	6.30	0.00	6.30	0.00	6.61							
10	210	82	2.5	32	31	210	60	22	22	0	1640	1640	0.0	0	1735	1735	0.0	0	1735	1735	0.0	12.31	0.00	7.99	0.00	7.99	0.00	8.46							
10	210	82	3	44	42	210	48	34	34	0	1730	1730	0.0	0	1820	1820	0.0	0	1820	1820	0.0	8.78	0.00	11.82	0.00	11.82	0.00	12.44							
10	210	82	3.5	60	55	210	32	50	50	0	1620	1620	0.0	0	1655	1655	0.0	0	1655	1655	0.0	5.93	0.00	16.39	0.00	16.75	0.00	16.75							
10	210	82	4	96	86	210	-4	86	86	30	2105	2135	1.4	0	2070	2070	0.0	0	2070	2070	0.0	5.84	0.31	21.63	21.93	0.00	21.27	21.27	21.27						
29	210	63	1.5	34	35	210	58	5	5	0	895	895	0.0	0	910	910	0.0	0	910	910	0.0	25.43	0.00	2.11	2.11	0.00	2.15	2.15	2.15						
29	210	63	2	44	43	210	48	15	15	0	1835	1835	0.0	0	1840	1840	0.0	0	1840	1840	0.0	22.31	0.00	4.94	4.94	0.00	4.95	4.95	4.95						
29	210	63	2.25	48	48	210	44	19	19	0	1900	1900	0.0	0	1900	1900	0.0	0	1900	1900	0.0	17.68	0.00	6.45	6.45	0.00	6.45	6.45	6.45						
29	210	63	2.5	55	53	210	37	26	26	0	1755	1755	0.0	0	1745	1745	0.0	0	1745	1745	0.0	12.81	0.00	8.22	8.22	0.00	8.17	8.17	8.17						
29	210	63	3	68	66	210	24	39	39	0	1610	1610	0.0	0	1710	1710	0.0	0	1710	1710	0.0	8.37	0.00	11.54	11.54	0.00	12.26	12.26	12.26						
29	210	63	3.5	97	93	210	-5	68	68	15	1565	1580	0.9	15	1565	1580	0.9	15	1565	1580	0.9	5.65	1.70	15.61	17.31	0.16	16.62	16.78	16.78						
29	210	63	4	102	100	210	-10	73	73	440	1705	2145	20.5	240	1875	2115	11.3	5.39	4.72	18.30	23.02	2.58	4.72	18.30	23.02	2.58	20.13	22.70	22.70						
49	210	43	1.5	53	54	210	39	4	4	0	900	900	0.0	0	910	910	0.0	0	910	910	0.0	25.09	0.00	2.15	2.15	0.00	2.18	2.18	2.18						
49	210	43	2	65	67	210	27	16	16	0	1935	1935	0.0	0	1910	1910	0.0	0	1910	1910	0.0	22.15	0.00	5.24	5.24	0.00	5.17	5.17	5.17						
49	210	43	2.25	71	71	210	21	22	22	0	1970	1970	0.0	0	1880	1880	0.0	0	1880	1880	0.0	17.56	0.00	6.73	6.73	0.00	6.42	6.42	6.42						
49	210	43	2.5	79	80	210	13	30	30	0	1730	1730	0.0	0	1760	1760	0.0	0	1760	1760	0.0	12.59	0.00	8.24	8.24	0.00	8.39	8.39	8.39						
49	210	43	3	96	97	210	-4	47	47	150	1455	1605	9.3	100	1485	1585	6.3	7.71	1.17	11.32	12.49	0.78	11.32	12.49	0.78	11.56	12.33	12.33							
49	210	43	3.5	101	101	210	-9	52	52	400	1290	1690	23.7	335	1280	1615	20.7	5.93	4.05	13.05	17.10	3.39	4.05	13.05	17.10	3.39	12.95	16.34	16.34						
49	210	43	4	104	104	210	-12	55	55	650	1360	2010	32.3	580	1385	1965	29.5	5.15	7.57	15.84	23.42	6.76	7.57	15.84	23.42	6.76	16.14	22.89	22.89						
67	210	25	1.5	77	78	210	15	10	10	0	880	880	0.0	0	900	900	0.0	0	900	900	0.0	25.21	0.00	2.09	2.09	0.00	2.14	2.14	2.14						
67	210	25	2	90	91	210	2	23	23	10	1885	1895	0.5	0	1795	1795	0.0	0	1795	1795	0.0	21.65	0.03	5.22	5.22	0.00	4.97	4.97	4.97						
67	210	25	2.25	94	94	210	-2	27	27	165	1830	1995	8.3	80	1820	1900	4.2	17.43	0.57	6.30	6.87	0.28	17.43	6.30	6.87	0.28	6.54	6.54	6.54						
67	210	25	2.5	98	98	210	-6	31	31	320	1470	1790	17.9	290	1500	1790	16.2	12.43	1.54	7.10	8.64	1.40	12.43	7.10	8.64	1.40	7.24	8.64	8.64						
67	210	25	3	102	105	210	-10	35	35	475	1050	1525	31.1	480	1055	1535	31.3	7.28	3.91	8.65	12.57	3.96	7.28	8.65	12.57	3.96	8.70	12.65	12.65						
67	210	25	3.5	106	107	210	-14	39	39	745	1005	1750	42.6	660	995	1655	39.9	5.78	7.73	10.43	18.17	6.85	5.78	7.73	10.43	6.85	10.33	17.18	17.18						
67	210	25	4	111	111	210	-19	44	44	910	1080	1990	45.7	930	1050	1980	47.0	4.96	11.01	13.06	24.07	11.25	4.96	11.01	13.06	11.25	12.70	23.95	23.95						
88	210	4	1.5	97	97	210	-5	9	9	135	855	990	13.6	125	840	965	13.0	24.78	0.33	2.07	2.40	0.30	24.78	2.07	2.40	0.30	2.34	2.34	2.34						
88	210	4	2	103	104	210	-11	15	15	780	1255	2035	38.3	700	1305	2005	34.9	22.93	2.04	3.28	5.32	1.83	22.93	3.28	5.32	1.83	3.41	5.25	5.25						
88	210	4	2.25	104	106	210	-12	16	16	810	995	1805	44.9	750	1010	1760	42.6	15.28	3.18	3.91	7.09	2.95	15.28	3.91	7.09	2.95	3.97	6.91	6.91						
88	210	4	2.5	106	108	210	-14	18	18	920	855	1775	51.8	870	990	1860	46.8	12.81	4.31	4.00	8.31	4.07	12.81	4.31	4.00	8.31	4.07	4.64	8.71	8.71					
88	210	4	3	109	111	210	-17	21	21	890	735	1625	54.8	915	735	1650	55.5	7.53	7.09	5.86	12.95	7.29	7.53	7.09	5.86	12.95	7.29	5.86	13.15	13.15					
88	210	4	3.5	114	115	210	-22	26	26	955	567	1685	56.7	950	650	1600	59.4	5.46	10.49	8.02	18.52	10.44	5.46	10.49	8.02	18.52	10.44	7.14	17.58	17.58					
88	210	4	4	116	117	210	-24	28	28	1245	825	2070	60.1	1275	765	2040	62.5	4.96	15.06	9.98	25.04	15.42	4.96	15.06	9.98	25.04	15.42	9.25	24.68	24.68					

Figure A.10: Spreadsheet for Nexbase 3080, δ = 15 [mm], two orifices at same height.

BEFORE												AFTER																																			
Liquid level, mm						Liquid level (max Δ), mm						Amount, ml Valve 1						Amount, ml Valve 2						WC, %						Time, s						Flowrate, l/min, Valve 1						Flowrate, l/min Valve 2					
wL	oL	AL	Valve	wL/v1	wL/v2	oL	AL	w/v1	w/v2	w/v1	o/v	totV	WC, %	w/v	o/v	totV	WC, %	w/v	o/v	totV	WC, %	Time, s	wQ	oQ	totQ	wQ	oQ	totQ	wQ	oQ	totQ	wQ	oQ	totQ													
10	210	82	1.5	15	14	210	77	5	5	0	1350	1350	0.0	0	1740	1740	0.0	0	1740	1740	0.0	30.25	0.00	2.68	2.68	0.00	2.44	2.44	0.00	2.68	2.68	0.00	2.44	2.44													
10	210	82	2	22	23	210	70	12	12	0	1795	1795	0.0	0	1345	1345	0.0	0	1345	1345	0.0	19.50	0.00	5.52	5.52	0.00	5.35	5.35	0.00	5.52	5.52	0.00	5.35	5.35													
10	210	82	2.25	35	31	210	57	25	25	0	1780	1780	0.0	0	1830	1830	0.0	0	1830	1830	0.0	11.25	0.00	7.17	7.17	0.00	6.99	6.99	0.00	7.17	7.17	0.00	6.99	6.99													
10	210	82	2.5	36	34	210	56	26	26	0	1780	1780	0.0	0	1835	1835	0.0	0	1835	1835	0.0	13.59	0.00	7.86	7.86	0.00	8.08	8.08	0.00	7.86	7.86	0.00	8.08	8.08													
10	210	82	3	67	61	210	25	57	57	15	1840	1855	0.8	15	1860	1860	0.0	0	1860	1860	0.0	6.06	0.15	18.22	18.37	0.00	18.42	18.42	0.00	18.22	18.37	0.00	18.42	18.42													
10	210	82	3.5	104	93	210	-12	94	94	135	2315	2450	5.5	0	2530	2530	0.0	0	2530	2530	0.0	6.18	1.31	22.48	23.79	0.00	24.56	24.56	0.00	22.48	23.79	0.00	24.56	24.56													
30	210	62	1.5	38	39	210	54	8	8	0	1200	1200	0.0	0	1805	1805	0.0	0	1805	1805	0.0	25.34	0.00	2.84	2.84	0.00	2.79	2.79	0.00	2.84	2.84	0.00	2.79	2.79													
30	210	62	2	46	49	210	46	16	16	0	1805	1805	0.0	0	1750	1750	0.0	0	1750	1750	0.0	20.09	0.00	5.39	5.39	0.00	5.51	5.51	0.00	5.39	5.39	0.00	5.51	5.51													
30	210	62	2.25	52	56	210	40	22	22	0	1820	1820	0.0	0	1885	1885	0.0	0	1885	1885	0.0	15.34	0.00	7.12	7.12	0.00	6.84	6.84	0.00	7.12	7.12	0.00	6.84	6.84													
30	210	62	2.5	66	74	210	26	36	36	0	2335	2335	0.0	0	2350	2350	0.0	0	2350	2350	0.0	15.65	0.00	8.95	8.95	0.00	9.01	9.01	0.00	8.95	8.95	0.00	9.01	9.01													
30	210	62	3	96	101	210	-4	66	66	85	1825	1910	4.5	265	1720	1985	13.4	8.71	0.59	12.57	13.16	8.71	2.32	16.41	18.73	2.32	15.34	17.66	2.32	15.34	17.66	2.32	15.34	17.66													
30	210	62	3.5	106	105	210	-14	76	76	260	1835	2095	12.4	260	1715	1975	13.2	6.71	2.32	16.41	18.73	6.71	2.32	16.41	18.73	2.32	15.34	17.66	2.32	15.34	17.66	2.32	15.34	17.66													
30	210	62	4	108	106	210	-16	78	78	290	2145	2435	11.9	320	2050	2370	13.5	5.78	3.01	22.27	25.28	5.78	2.81	22.27	25.28	3.32	21.28	24.60	3.32	21.28	24.60	3.32	21.28	24.60													
49	210	43	1.5	57	56	210	35	8	8	0	960	960	0.0	0	960	960	0.0	0	960	960	0.0	20.50	0.00	2.81	2.81	0.00	2.81	2.81	0.00	2.81	2.81	0.00	2.81	2.81													
49	210	43	2	69	68	210	23	20	20	0	1945	1945	0.0	0	1915	1915	0.0	0	1915	1915	0.0	20.71	0.00	5.63	5.63	0.00	5.55	5.55	0.00	5.63	5.63	0.00	5.55	5.55													
49	210	43	2.25	82	82	210	10	33	33	0	1860	1860	0.0	0	1885	1885	0.0	0	1885	1885	0.0	15.34	0.00	7.28	7.28	0.00	7.37	7.37	0.00	7.28	7.28	0.00	7.37	7.37													
49	210	43	2.5	97	98	210	-5	48	48	45	1835	1880	2.4	50	1895	1945	2.6	12.62	0.21	8.72	8.94	12.62	0.21	8.72	8.94	0.24	9.01	9.25	0.24	9.01	9.25	0.24	9.01	9.25													
49	210	43	3	103	104	210	-11	54	54	405	1860	2265	17.9	400	1920	2320	17.2	10.37	2.34	10.76	13.11	10.37	2.34	10.76	13.11	2.31	11.11	13.42	2.31	11.11	13.42	2.31	11.11	13.42													
49	210	43	3.5	113	112	210	-21	64	64	390	1310	1700	22.9	355	1305	1660	21.4	5.50	4.25	14.29	18.55	5.50	4.25	14.29	18.55	3.87	14.24	18.11	3.87	14.24	18.11	3.87	14.24	18.11													
49	210	43	4	118	116	210	-26	69	69	480	1435	1915	25.1	385	1535	1920	20.1	4.84	5.95	17.79	23.74	4.84	5.95	17.79	23.74	4.77	19.03	23.80	4.77	19.03	23.80	4.77	19.03	23.80													
69	210	23	1.5	81	81	210	11	12	12	0	935	935	0.0	0	1005	1005	0.0	0	1005	1005	0.0	20.15	0.00	2.78	2.78	0.00	2.99	2.99	0.00	2.78	2.78	0.00	2.99	2.99													
69	210	23	2	101	100	210	-9	32	32	220	1800	2020	10.9	155	1805	1960	7.9	20.71	0.64	5.21	5.85	20.71	0.64	5.21	5.85	0.45	5.23	5.68	0.45	5.23	5.68	0.45	5.23	5.68													
69	210	23	2.25	101	103	210	-9	32	32	400	1465	1865	21.4	300	1540	1840	16.3	15.40	1.56	5.71	7.27	15.40	1.56	5.71	7.27	1.17	6.00	7.17	1.17	6.00	7.17	1.17	6.00	7.17													
69	210	23	2.5	103	103	210	-11	34	34	570	1485	2055	27.7	475	1545	2020	23.5	13.65	2.51	6.53	9.03	13.65	2.51	6.53	9.03	2.09	6.79	8.88	2.09	6.79	8.88	2.09	6.79	8.88													
69	210	23	3	108	110	210	-16	39	39	670	1520	2190	30.6	750	1530	2280	32.9	10.03	4.01	9.09	13.10	10.03	4.01	9.09	13.10	4.49	9.15	13.64	4.49	9.15	13.64	4.49	9.15	13.64													
69	210	23	3.5	113	113	210	-21	44	44	580	1070	1650	35.2	540	1100	1640	32.9	5.37	6.48	11.96	18.44	5.37	6.48	11.96	18.44	6.03	12.29	18.32	6.03	12.29	18.32	6.03	12.29	18.32													
69	210	23	4	115	118	210	-23	46	46	610	1210	1820	33.5	570	1275	1845	30.9	4.43	8.26	16.39	24.65	4.43	8.26	16.39	24.65	7.72	17.27	24.99	7.72	17.27	24.99	7.72	17.27	24.99													
88	210	4	1.5	100	100	210	-8	12	12	170	725	895	19.0	120	815	935	12.8	20.12	0.51	2.16	2.67	20.12	0.51	2.16	2.67	0.36	2.43	2.79	0.36	2.43	2.79	0.36	2.43	2.79													
88	210	4	2	106	105	210	-14	18	18	690	1130	1820	37.9	540	1235	1775	30.4	19.96	2.07	3.40	5.47	19.96	2.07	3.40	5.47	1.62	3.71	5.34	1.62	3.71	5.34	1.62	3.71	5.34													
88	210	4	2.25	108	105	210	-16	20	20	750	1000	1750	42.9	600	1085	1685	35.6	14.40	3.13	4.17	7.29	14.40	3.13	4.17	7.29	2.50	4.52	7.02	2.50	4.52	7.02	2.50	4.52	7.02													
88	210	4	2.5	111	106	210	-19	23	23	620	750	1370	45.3	535	870	1405	38.1	9.40	3.96	4.79	8.74	9.40	3.96	4.79	8.74	3.41	5.55	8.97	3.41	5.55	8.97	3.41	5.55	8.97													
88	210	4	3	116	109	210	-24	28	28	810	780	1590	50.9	695	935	1630	42.6	7.25	6.70	6.46	13.16	7.25	6.70	6.46	13.16	5.75	7.74	13.49	5.75	7.74	13.49	5.75	7.74	13.49													
88	210	4	3.5	121	116	210	-29	33	33	905	810	1715	52.8	670	975	1645	40.7	5.56	9.77	8.74	18.51	5.56	9.77	8.74	18.51	7.23	10.52	17.75	7.23	10.52	17.75	7.23	10.52	17.75													
88	210	4	4	122	118	210	-30	34	34	1040	880	1920	54.2	715	1225	1940	36.9	4.68	13.33	11.28	24.62	4.68	13.33	11.28	24.62	9.17	15.71	24.87	9.17	15.71	24.87	9.17	15.71	24.87													

Figure A.11: Spreadsheet for Marcol 52, $\delta = 10$ [mm], two orifices at same height.

BEFORE										DURING										AFTER									
wL	oL	ΔL	Valve	Liquid level (max Δ), mm						Amount, ml Valve 1		WC, %		Amount, ml Valve 2		WC, %		Time, s	Flowrate, l/min, Valve 1		Flowrate, l/min Valve 2								
				wL/v1	wL/v2	oL/v1	oL/v2	w/v1	w/v2	oV	totV	WC, %	oV	totV	WC, %	wQ	oQ		totQ	wQ	oQ	totQ							
10	210	82	1.5	11	210	81	1	1	0	675	675	0.0	615	615	0.0	15.46	0.00	2.62	2.62	0.00	2.39	2.39							
10	210	82	2	13	210	79	3	3	0	985	985	0.0	965	965	0.0	10.75	0.00	5.50	5.50	0.00	5.39	5.39							
10	210	82	2.25	14	210	78	4	4	0	1415	1415	0.0	1375	1375	0.0	11.15	0.00	7.61	7.61	0.00	7.40	7.40							
10	210	82	2.5	19	210	73	9	9	0	1595	1595	0.0	1535	1535	0.0	10.34	0.00	9.26	9.26	0.00	8.91	8.91							
10	210	82	3	27	210	65	17	17	0	1650	1650	0.0	1600	1600	0.0	7.50	0.00	13.20	13.20	0.00	13.60	13.60							
10	210	82	3.5	35	210	57	25	25	0	1850	1850	0.0	1850	1850	0.0	5.81	0.00	18.81	18.81	0.00	18.81	18.81							
10	210	82	4	57	210	35	47	47	0	2445	2445	0.0	2445	2445	0.0	5.81	0.00	25.25	25.25	0.00	25.25	25.25							
30	210	62	1.5	32	210	60	2	2	0	885	885	0.0	920	920	0.0	20.68	0.00	2.57	2.57	0.00	2.67	2.67							
30	210	62	2	34	210	58	4	4	0	1905	1905	0.0	1965	1965	0.0	20.43	0.00	5.59	5.59	0.00	5.77	5.77							
30	210	62	2.25	37	210	55	7	7	0	1850	1850	0.0	1870	1870	0.0	15.65	0.00	7.09	7.09	0.00	7.17	7.17							
30	210	62	2.5	38	210	54	8	8	0	2265	2265	0.0	2295	2295	0.0	15.43	0.00	8.81	8.81	0.00	8.92	8.92							
30	210	62	3	44	210	48	14	14	0	2265	2265	0.0	2340	2340	0.0	10.12	0.00	13.43	13.43	0.00	13.87	13.87							
30	210	62	3.5	59	210	33	29	29	0	2045	2045	0.0	2010	2010	0.0	6.43	0.00	19.08	19.08	0.00	18.76	18.76							
30	210	62	4	98	210	-6	68	68	35	2260	2295	1.5	20	2350	2370	0.8	5.62	0.37	24.13	24.50	0.21	25.09	25.30						
49	210	43	1.5	53	210	39	4	4	0	900	900	0.0	905	905	0.0	20.06	0.00	2.69	2.69	0.00	2.71	2.71							
49	210	43	2	57	210	35	8	8	0	1895	1895	0.0	1850	1850	0.0	19.90	0.00	5.71	5.71	0.00	5.58	5.58							
49	210	43	2.25	58	210	34	9	9	0	1805	1805	0.0	1880	1880	0.0	15.28	0.00	7.09	7.09	0.00	7.38	7.38							
49	210	43	2.5	62	210	30	13	13	0	1865	1865	0.0	1840	1840	0.0	12.21	0.00	9.16	9.16	0.00	9.04	9.04							
49	210	43	3	74	210	18	25	25	0	2020	2020	0.0	2060	2060	0.0	8.87	0.00	13.66	13.66	0.00	13.93	13.93							
49	210	43	3.5	91	210	1	42	42	150	1920	2070	7.2	100	1930	2030	4.9	6.40	1.41	18.00	19.41	0.94	18.09	19.03						
49	210	43	4	113	210	-21	64	64	320	1600	1920	16.7	300	1645	1945	15.4	4.56	4.21	21.05	25.26	3.95	21.64	25.59						
69	210	23	1.5	72	210	20	3	3	0	935	935	0.0	890	890	0.0	20.12	0.00	2.79	2.79	0.00	2.65	2.65							
69	210	23	2	79	210	13	10	10	0	1840	1840	0.0	1820	1820	0.0	20.03	0.00	5.51	5.51	0.00	5.45	5.45							
69	210	23	2.25	87	210	5	18	18	0	1735	1735	0.0	1750	1750	0.0	14.31	0.00	7.27	7.27	0.00	7.34	7.34							
69	210	23	2.5	95	210	-3	26	26	30	1700	1730	1.7	0	1710	1710	0.0	11.40	0.16	8.95	9.11	0.00	9.00	9.00						
69	210	23	3	102	103	210	-10	33	360	1875	2235	16.1	310	1915	2225	13.9	9.59	2.25	11.73	13.98	1.94	11.98	13.92						
69	210	23	3.5	105	106	210	-13	36	400	1200	1600	25.0	380	1230	1610	23.6	5.21	4.61	13.82	18.43	4.38	14.17	18.54						
69	210	23	4	112	115	210	-20	43	570	1315	1885	30.2	605	1330	1935	31.3	4.62	7.40	17.08	24.48	7.86	17.27	25.13						
88	210	4	1.5	94	95	210	-2	6	6	870	870	0.0	900	900	0.0	20.43	0.00	2.56	2.56	0.00	2.64	2.64							
88	210	4	2	100	99	210	-8	12	265	1635	1900	13.9	245	1600	1845	13.3	20.18	0.79	4.86	5.65	0.73	4.76	5.49						
88	210	4	2.25	102	102	210	-10	14	490	1850	2340	20.9	430	1885	2315	18.6	19.46	1.51	5.70	7.21	1.33	5.81	7.14						
88	210	4	2.5	102	103	210	-10	14	460	1265	1725	26.7	415	1275	1690	24.6	11.46	2.41	6.62	9.03	2.17	6.68	8.85						
88	210	4	3	104	107	210	-12	16	535	1065	1600	33.4	575	1080	1655	34.7	7.34	4.37	8.71	13.08	4.70	8.83	13.53						
88	210	4	3.5	108	110	210	-16	20	675	990	1665	40.5	670	980	1650	40.6	5.37	7.54	11.06	18.60	7.49	10.95	18.44						
88	210	4	4	111	112	210	-19	23	840	1050	1890	44.4	860	1115	1975	43.5	4.68	10.77	13.46	24.23	11.03	14.29	25.32						

Figure A.12: Spreadsheet for Marcol 52, $\delta = 5$ [mm], two orifices at same height.

BEFORE				DURING				AFTER				Flowrate, Jmin Valve 1		Flowrate, Jmin Valve 2															
Liquid level, mm	Valve	Liquid level (max Δ), mm	Amount, ml Valve 1	WC, %	Amount, ml Valve 2	WC, %	Time, s	wQ	totQ	wQ	totQ	wQ	totQ	wQ	totQ														
wL	ΔL	wL	ΔL	wL	ΔL	wL	ΔL	wV	totV	wV	totV	wV	totV	wV	totV														
10	210	82	1.5	19	210	73	9	0	940	940	0.0	0	940	940	0.0	25.31	2.23	2.23	0.00	2.23	0.00	2.23	0.00	2.23	0.00	2.23	0.00	2.23	
10	210	82	2	33	210	59	23	0	1870	1870	0.0	0	1890	1890	0.0	22.43	5.00	5.00	0.00	5.00	0.00	5.00	0.00	5.06	0.00	5.06	0.00	5.06	
10	210	82	2.25	41	210	51	31	0	1790	1790	0.0	150	1790	1940	7.7	16.87	6.37	6.37	0.00	6.37	0.00	6.37	0.00	6.37	0.00	6.37	0.00	6.90	
10	210	82	2.5	45	210	47	35	0	1750	1750	0.0	220	1705	1925	11.4	12.90	8.14	8.14	0.00	8.14	0.00	8.14	0.00	7.93	0.00	7.93	0.00	8.95	
10	210	82	3	46	210	46	36	0	1465	1465	0.0	160	1420	1580	10.1	7.50	11.72	11.72	0.00	11.72	0.00	11.72	0.00	11.36	0.00	11.36	0.00	12.64	
10	210	82	3.5	47	210	45	37	0	1550	1550	0.0	175	1420	1595	11.0	5.68	16.37	16.37	0.00	16.37	0.00	16.37	0.00	15.00	0.00	15.00	0.00	16.85	
10	210	82	4	84	210	8	74	0	1725	1725	0.0	180	1585	1765	10.2	4.93	20.99	20.99	0.00	20.99	0.00	20.99	0.00	19.29	0.00	19.29	0.00	21.48	
29	210	63	1.5	40	210	52	11	0	940	940	0.0	30	865	895	3.4	24.68	2.29	2.29	0.00	2.29	0.00	2.29	0.00	2.10	0.00	2.10	0.00	2.18	
29	210	63	2	55	210	37	26	0	1765	1765	0.0	835	1090	1925	43.4	21.43	4.94	4.94	0.00	4.94	0.00	4.94	0.00	3.05	0.00	3.05	0.00	5.39	
29	210	63	2.25	64	210	28	35	0	1675	1675	0.0	885	870	1755	50.4	15.40	6.53	6.53	0.00	6.53	0.00	6.53	0.00	3.45	0.00	3.45	0.00	6.84	
29	210	63	2.5	76	210	16	47	0	1715	1715	0.0	920	955	1875	49.1	12.40	8.30	8.30	0.00	8.30	0.00	8.30	0.00	4.45	0.00	4.45	0.00	9.07	
29	210	63	3	85	210	7	56	0	1630	1630	0.0	870	950	1820	47.8	8.56	11.43	11.43	0.00	11.43	0.00	11.43	0.00	6.10	0.00	6.10	0.00	12.76	
29	210	63	3.5	97	210	-5	68	75	1475	1550	4.8	600	975	1575	38.1	5.59	15.83	15.83	0.00	15.83	0.00	15.83	0.00	6.44	0.00	6.44	0.00	16.91	
29	210	63	4	103	210	-11	74	125	1630	1755	7.1	585	1280	1865	31.4	4.93	19.84	19.84	0.00	19.84	0.00	19.84	0.00	7.12	0.00	7.12	0.00	22.70	
49	210	43	1.5	59	210	33	10	0	865	865	0.0	760	270	1030	73.8	24.30	2.12	2.12	0.00	2.12	0.00	2.12	0.00	1.86	0.00	1.86	0.00	2.52	
49	210	43	2	77	210	15	28	0	1310	1310	0.0	1150	350	1500	76.7	16.06	4.89	4.89	0.00	4.89	0.00	4.89	0.00	4.30	0.00	4.30	0.00	5.60	
49	210	43	2.25	90	210	2	41	0	1720	1720	0.0	1490	325	1815	82.1	15.78	6.54	6.54	0.00	6.54	0.00	6.54	0.00	5.67	0.00	5.67	0.00	6.90	
49	210	43	2.5	96	210	-4	47	20	1675	1695	1.2	1460	300	1760	83.0	12.34	8.14	8.14	0.00	8.14	0.00	8.14	0.00	7.10	0.00	7.10	0.00	8.56	
49	210	43	3	102	210	-10	53	270	1240	1510	17.9	1180	405	1585	74.4	7.31	12.39	12.39	0.00	12.39	0.00	12.39	0.00	9.69	0.00	9.69	0.00	13.01	
49	210	43	3.5	103	210	-11	54	315	1285	1600	19.7	1040	600	1640	63.4	5.53	13.94	13.94	0.00	13.94	0.00	13.94	0.00	11.28	0.00	11.28	0.00	17.79	
49	210	43	4	112	210	-20	63	420	1295	1715	24.5	1030	870	1900	54.2	4.63	16.78	16.78	0.00	16.78	0.00	16.78	0.00	13.35	0.00	13.35	0.00	24.62	
67	210	25	1.5	84	210	8	17	0	980	980	0.0	1030	0	1030	100.0	24.68	2.38	2.38	0.00	2.38	0.00	2.38	0.00	2.50	0.00	2.50	0.00	2.50	
67	210	25	2	97	210	-5	30	290	1710	2000	14.5	2020	0	2020	100.0	23.21	0.75	0.75	0.00	0.75	0.00	0.75	0.00	5.22	0.00	5.22	0.00	5.22	
67	210	25	2.25	104	210	-12	37	470	1325	1795	26.2	1825	0	1825	100.0	15.31	1.84	1.84	0.00	1.84	0.00	1.84	0.00	7.15	0.00	7.15	0.00	7.15	
67	210	25	2.5	107	210	-15	40	525	1180	1705	30.8	1815	110	1925	94.3	12.53	2.51	2.51	0.00	2.51	0.00	2.51	0.00	5.65	0.00	5.65	0.00	9.22	
67	210	25	3	113	210	-21	46	570	935	1505	37.9	1405	160	1565	89.8	7.28	4.70	4.70	0.00	4.70	0.00	4.70	0.00	4.11	0.00	4.11	0.00	12.90	
67	210	25	3.5	120	210	-28	53	690	1055	1745	39.5	1290	400	1690	76.3	5.84	7.09	7.09	0.00	7.09	0.00	7.09	0.00	13.25	0.00	13.25	0.00	17.36	
67	210	25	4	124	210	-32	57	660	1175	1835	36.0	1265	425	1690	74.9	4.75	8.34	8.34	0.00	8.34	0.00	8.34	0.00	15.98	0.00	15.98	0.00	21.35	
88	210	4	1.5	101	210	-9	13	300	720	1020	29.4	1060	0	1060	100.0	25.46	0.71	0.71	0.00	0.71	0.00	0.71	0.00	2.50	0.00	2.50	0.00	2.50	
88	210	4	2	106	210	-14	18	760	975	1735	43.8	1815	0	1815	100.0	20.43	2.23	2.23	0.00	2.23	0.00	2.23	0.00	5.33	0.00	5.33	0.00	5.33	
88	210	4	2.25	110	210	-18	22	920	795	1715	53.6	1780	0	1780	100.0	15.37	3.59	3.10	0.00	3.10	0.00	3.10	0.00	6.95	0.00	6.95	0.00	6.95	
88	210	4	2.5	113	210	-21	25	990	770	1760	56.3	1795	0	1795	100.0	12.25	4.85	3.77	0.00	3.77	0.00	3.77	0.00	8.79	0.00	8.79	0.00	8.79	
88	210	4	3	116	210	-24	28	950	710	1660	57.2	1705	0	1705	100.0	7.53	7.57	5.66	5.66	0.00	5.66	0.00	5.66	0.00	13.59	0.00	13.59	0.00	13.59
88	210	4	3.5	125	210	-33	37	870	765	1635	53.2	1555	80	1635	95.1	5.43	9.61	8.45	8.45	0.00	8.45	0.00	8.45	0.00	17.18	0.00	17.18	0.00	18.07
88	210	4	4	136	210	-44	48	905	865	1770	51.1	1550	340	1890	82.0	4.46	12.17	11.64	11.64	0.00	11.64	0.00	11.64	0.00	20.85	0.00	20.85	0.00	25.43

Figure A.13: Spreadsheet for Nexbase 3080, δ = 10 [mm], two orifices at different height.

BEFORE										DURING										AFTER											
Liquid level, mm		Liquid level (max Δ), mm		Amount, ml Valve 1		Amount, ml Valve 2		WC, %		Time, s		Flowrate, l/min Valve 1		Flowrate, l/min Valve 2		Liquid level, mm		Liquid level (max Δ), mm		Amount, ml Valve 1		Amount, ml Valve 2		WC, %		Time, s		Flowrate, l/min Valve 1		Flowrate, l/min Valve 2	
wL	oL	ΔL	wL	oL	ΔL	wV	oV	totV	wC	oC	totC	wV	oV	totV	wC	oC	totC	Time	wQ	oQ	totQ	wQ	oQ	totQ	wC	oC	totC	Time	wQ	oQ	totQ
10	210	82	11	210	81	1	0	900	0.0	0.0	900	0	960	960	0.0	0.0	22.46	0.0	0.00	0.00	2.12	0.00	2.26	0.00	0.00	2.26	0.00	0.00	2.26		
10	210	82	2	210	72	10	0	1730	0.0	0.0	1730	0	1735	1735	0.0	0.0	16.37	0.0	0.00	0.00	4.71	0.00	4.72	0.00	0.00	4.72	0.00	0.00	4.72		
10	210	82	2.5	210	67	15	0	1795	0.0	0.0	1795	0	1865	1865	0.0	0.0	16.37	0.0	0.00	0.00	6.58	0.00	6.84	0.00	0.00	6.84	0.00	0.00	6.84		
10	210	82	2.5	210	65	17	0	1700	0.0	0.0	1700	0	1775	1845	3.8	0.0	12.84	0.0	0.00	0.00	7.94	0.33	8.29	0.00	0.00	8.29	0.00	0.00	8.29		
10	210	82	3	210	61	21	0	1560	0.0	0.0	1560	0	1600	1660	0.0	0.0	7.84	0.00	0.00	0.00	11.94	1.22	12.70	0.00	0.00	12.70	0.00	0.00	12.70		
10	210	82	3.5	210	64	18	0	1475	0.0	0.0	1475	0	1385	1520	8.9	0.0	5.50	0.00	0.00	0.00	16.09	1.47	16.58	0.00	0.00	16.58	0.00	0.00	16.58		
10	210	82	4	210	66	16	0	1785	0.0	0.0	1785	0	150	1820	8.2	0.0	5.03	0.00	0.00	0.00	21.29	1.79	19.92	0.00	0.00	19.92	0.00	0.00	19.92		
29	210	63	1.5	210	60	3	0	940	0.0	0.0	940	0	990	990	0.0	0.0	25.12	0.00	0.00	0.00	2.25	0.00	2.36	0.00	0.00	2.36	0.00	0.00	2.36		
29	210	63	2	210	53	10	0	1810	0.0	0.0	1810	0	425	1490	1915	22.2	22.00	0.00	0.00	4.94	4.94	4.06	1.16	4.06	5.22	5.22	5.22	5.22	5.22		
29	210	63	2.25	210	48	15	0	1665	0.0	0.0	1665	0	540	1150	1690	32.0	14.96	0.00	0.00	6.68	6.68	2.17	4.61	6.78	6.78	6.78	6.78	6.78	6.78		
29	210	63	2.5	210	45	18	0	1575	0.0	0.0	1575	0	620	1010	1630	38.0	11.56	0.00	0.00	8.17	8.17	3.22	5.24	8.46	8.46	8.46	8.46	8.46	8.46		
29	210	63	3	210	34	29	0	1515	0.0	0.0	1515	0	765	930	1695	45.1	7.65	0.00	0.00	11.88	11.88	6.00	7.29	13.29	13.29	13.29	13.29	13.29	13.29	13.29	
29	210	63	3.5	210	30	33	0	1530	0.0	0.0	1530	0	660	870	1530	43.1	5.46	0.00	0.00	16.81	16.81	7.25	9.56	16.81	16.81	16.81	16.81	16.81	16.81	16.81	
29	210	63	4	210	37	26	0	1615	0.0	0.0	1615	0	690	1090	1780	38.8	4.75	0.00	0.00	20.40	20.40	8.72	13.77	22.48	22.48	22.48	22.48	22.48	22.48	22.48	
49	210	43	1.5	210	39	4	0	945	0.0	0.0	945	0	755	320	1075	70.2	25.03	0.00	0.00	2.27	2.27	1.81	0.77	2.58	2.58	2.58	2.58	2.58	2.58	2.58	
49	210	43	2	210	30	13	0	1750	0.0	0.0	1750	0	1440	470	1910	75.4	21.37	0.00	0.00	4.91	4.91	4.04	1.32	5.36	5.36	5.36	5.36	5.36	5.36	5.36	
49	210	43	2.25	210	26	17	0	1780	0.0	0.0	1780	0	1365	460	1825	74.8	16.12	0.00	0.00	6.63	6.63	5.08	1.71	6.79	6.79	6.79	6.79	6.79	6.79	6.79	
49	210	43	2.5	210	23	20	0	1720	0.0	0.0	1720	0	1315	425	1740	75.6	12.43	0.00	0.00	8.30	8.30	6.35	2.05	8.40	8.40	8.40	8.40	8.40	8.40	8.40	
49	210	43	3	210	8	35	0	1555	0.0	0.0	1555	0	1260	440	1700	74.1	7.81	0.00	0.00	11.95	11.95	9.68	3.38	13.06	13.06	13.06	13.06	13.06	13.06	13.06	13.06
49	210	43	3.5	210	-1	44	95	1510	0.0	0.0	1605	5.9	1185	450	1635	72.5	5.65	1.01	16.04	17.04	12.58	4.78	17.36	17.36	17.36	17.36	17.36	17.36	17.36	17.36	
49	210	43	4	210	-6	49	95	1680	0.0	0.0	1775	5.4	1185	755	1940	61.1	4.87	1.17	20.70	21.87	14.60	9.30	23.90	23.90	23.90	23.90	23.90	23.90	23.90	23.90	
67	210	25	1.5	210	18	7	0	935	0.0	0.0	935	0	1085	0	1085	100.0	25.25	0.00	0.00	2.22	2.22	2.58	0.00	2.58	2.58	2.58	2.58	2.58	2.58	2.58	
67	210	25	2	210	9	16	0	1730	0.0	0.0	1730	0	1880	0	1880	100.0	20.90	0.00	0.00	4.97	4.97	5.40	0.00	5.40	5.40	5.40	5.40	5.40	5.40	5.40	
67	210	25	2.25	210	4	21	0	1670	0.0	0.0	1670	0	1880	0	1880	100.0	15.71	0.00	0.00	6.38	6.38	7.18	0.00	7.18	7.18	7.18	7.18	7.18	7.18	7.18	
67	210	25	2.5	210	0	25	50	1635	0.0	0.0	1685	3.0	1785	0	1785	100.0	12.25	0.24	8.01	8.25	8.74	0.00	8.74	8.74	8.74	8.74	8.74	8.74	8.74	8.74	
67	210	25	3	210	-6	31	225	1335	0.0	0.0	1360	14.4	1600	120	1720	93.0	7.62	1.77	10.51	12.28	12.60	0.94	13.54	13.54	13.54	13.54	13.54	13.54	13.54	13.54	
67	210	25	3.5	210	-15	40	410	1205	0.0	0.0	1615	25.4	1375	200	1575	87.3	5.34	4.61	13.54	18.15	15.45	2.25	17.70	17.70	17.70	17.70	17.70	17.70	17.70	17.70	
67	210	25	4	210	-21	46	470	1385	0.0	0.0	1855	25.3	1550	380	1930	80.3	4.78	5.90	17.38	23.28	19.46	4.77	24.23	24.23	24.23	24.23	24.23	24.23	24.23	24.23	
88	210	4	1.5	210	0	4	10	885	0.0	0.0	895	1.1	1040	0	1040	100.0	23.34	0.03	2.28	2.30	2.67	0.00	2.67	2.67	2.67	2.67	2.67	2.67	2.67	2.67	
88	210	4	2	210	-6	10	360	1450	0.0	0.0	1450	19.9	1930	0	1930	100.0	21.09	1.02	4.13	5.15	5.49	0.00	5.49	5.49	5.49	5.49	5.49	5.49	5.49	5.49	
88	210	4	2.25	210	-9	13	450	1270	0.0	0.0	1720	26.2	1895	0	1895	100.0	15.56	1.74	4.90	6.63	7.31	0.00	7.31	7.31	7.31	7.31	7.31	7.31	7.31	7.31	
88	210	4	2.5	210	-11	15	590	1225	0.0	0.0	1815	32.5	1840	0	1840	100.0	12.43	2.85	5.91	8.76	8.88	0.00	8.88	8.88	8.88	8.88	8.88	8.88	8.88	8.88	
88	210	4	3	210	-15	19	630	950	0.0	0.0	1580	39.9	1690	0	1690	100.0	7.43	5.09	7.67	12.76	13.65	0.00	13.65	13.65	13.65	13.65	13.65	13.65	13.65	13.65	
88	210	4	3.5	210	-22	26	710	950	0.0	0.0	1660	42.8	1750	0	1750	100.0	5.59	7.62	10.20	17.82	18.78	0.00	18.78	18.78	18.78	18.78	18.78	18.78	18.78	18.78	
88	210	4	4	210	-27	31	710	1155	0.0	0.0	1865	38.1	2010	100	2110	95.3	4.84	8.80	14.32	23.12	24.92	0.00	24.92	24.92	24.92	24.92	24.92	24.92	24.92	24.92	

Figure A.14: Spreadsheet for Nexbase 3080, δ = 15 [mm], two orifices at different height.

BEFORE										DURING										AFTER									
Liquid level, mm		Valve		Liquid level (max Δ), mm						Amount, ml Valve 1		WC, %		Amount, ml Valve 2		WC, %		Time, s		Flowrate, l/min, Valve 1		Flowrate, l/min Valve 2							
wL	oL	AL	VL	wL v1	wL v2	oL	AL	wL v1	wL v2	wV	oV	totV	WC, %	wV	oV	totV	WC, %	Time, s	wQ	oQ	totQ	wQ	oQ	totQ					
10	210	82	1.5	14	210	77	5	5	0	1350	1350	0.0	0.0	0	1740	1740	0.0	30.25	0.00	2.68	2.68	0.00	2.44	2.44					
10	210	82	2.25	23	210	70	12	12	0	1795	1795	0.0	0.0	0	1730	1730	0.0	19.50	0.00	5.52	5.52	0.00	5.35	5.35					
10	210	82	2.25	31	210	57	25	25	0	1345	1345	0.0	0.0	0	1810	1810	0.0	11.25	0.00	7.17	7.17	0.00	6.99	6.99					
10	210	82	2.5	36	210	56	26	26	0	1780	1780	0.0	0.0	0	1830	1830	0.0	13.59	0.00	7.86	7.86	0.00	8.08	8.08					
10	210	82	3	67	210	25	57	57	0	1925	1925	0.0	0.0	0	1835	1835	0.0	8.62	0.00	13.40	13.40	0.00	12.77	12.77					
10	210	82	3.5	104	93	210	-12	94	94	15	1840	1855	0.8	0	1860	1860	0.0	6.06	0.15	18.22	18.37	0.00	18.42	18.42					
10	210	82	4	104	99	210	-12	94	94	135	2315	2450	5.5	0	2530	2530	0.0	6.18	1.31	22.48	23.79	0.00	24.56	24.56					
30	210	62	1.5	38	210	54	8	8	0	1200	1200	0.0	0.0	0	1180	1180	0.0	25.34	0.00	2.84	2.84	0.00	2.79	2.79					
30	210	62	2	46	210	46	16	16	0	1805	1805	0.0	0.0	0	1845	1845	0.0	20.09	0.00	5.39	5.39	0.00	5.51	5.51					
30	210	62	2.25	52	210	40	22	22	0	1820	1820	0.0	0.0	0	1750	1750	0.0	15.34	0.00	7.12	7.12	0.00	6.84	6.84					
30	210	62	2.5	66	210	26	36	36	0	2335	2335	0.0	0.0	0	2350	2350	0.0	15.65	0.00	8.95	8.95	0.00	9.01	9.01					
30	210	62	3	96	101	210	-4	66	66	85	1825	1910	4.5	265	1720	1985	13.4	8.71	0.59	12.57	13.16	1.83	11.85	13.67					
30	210	62	3.5	106	105	210	-14	76	76	260	1835	2095	12.4	260	1715	1975	13.2	6.71	2.32	16.41	18.73	2.32	15.34	17.66					
30	210	62	4	108	106	210	-16	78	78	290	2145	2435	11.9	320	2050	2370	13.5	5.78	3.01	22.27	25.28	3.32	21.28	24.60					
49	210	43	1.5	57	210	35	8	8	0	960	960	0.0	0.0	0	960	960	0.0	20.50	0.00	2.81	2.81	0.00	2.81	2.81					
49	210	43	2	69	210	23	20	20	0	1945	1945	0.0	0.0	0	1915	1915	0.0	20.71	0.00	5.63	5.63	0.00	5.55	5.55					
49	210	43	2.25	82	210	10	33	33	0	1860	1860	0.0	0.0	0	1885	1885	0.0	15.34	0.00	7.28	7.28	0.00	7.37	7.37					
49	210	43	2.5	97	210	-5	48	48	45	1835	1880	2.4	50	1895	1945	2.6	12.62	0.21	8.72	8.94	0.24	9.01	9.25						
49	210	43	3	103	104	210	-11	54	54	405	1860	2265	17.9	400	1920	2320	17.2	10.37	2.34	10.76	13.11	2.31	11.11	13.42					
49	210	43	3.5	113	112	210	-21	64	64	390	1310	1700	22.9	355	1305	1660	21.4	5.50	4.25	14.29	18.55	3.87	14.24	18.11					
49	210	43	4	118	116	210	-26	69	69	480	1435	1915	25.1	385	1535	1920	20.1	4.84	5.95	17.79	23.74	4.77	19.03	23.80					
69	210	23	1.5	81	210	11	12	12	0	935	935	0.0	0.0	0	1005	1005	0.0	20.15	0.00	2.78	2.78	0.00	2.99	2.99					
69	210	23	2	101	100	210	-9	32	32	220	1800	2020	10.9	155	1805	1960	7.9	20.71	0.64	5.21	5.85	0.45	5.23	5.68					
69	210	23	2.25	101	103	210	-9	32	32	400	1465	1865	21.4	300	1540	1840	16.3	15.40	1.56	5.71	7.27	1.17	6.00	7.17					
69	210	23	2.5	103	103	210	-11	34	34	570	1485	2055	27.7	475	1545	2020	23.5	13.65	2.51	6.53	9.03	2.09	6.79	8.88					
69	210	23	3	108	110	210	-16	39	39	670	1520	2190	30.6	750	1530	2280	32.9	10.03	4.01	9.09	13.10	4.49	9.15	13.64					
69	210	23	3.5	113	113	210	-21	44	44	580	1070	1650	35.2	540	1100	1640	32.9	5.37	6.48	11.96	18.44	6.03	12.29	18.32					
69	210	23	4	115	118	210	-23	46	46	610	1210	1820	33.5	570	1275	1845	30.9	4.43	8.26	16.39	24.65	7.72	17.27	24.99					
88	210	4	1.5	100	100	210	-8	12	12	170	725	895	19.0	120	815	935	12.8	20.12	0.51	2.16	2.67	0.36	2.43	2.79					
88	210	4	2	106	105	210	-14	18	18	690	1130	1820	37.9	540	1235	1775	30.4	19.96	2.07	3.40	5.47	1.62	3.71	5.34					
88	210	4	2.25	108	105	210	-16	20	20	750	1000	1750	42.9	600	1085	1685	35.6	14.40	3.13	4.17	7.29	2.50	4.52	7.02					
88	210	4	2.5	111	106	210	-19	23	23	620	750	1370	45.3	535	870	1405	38.1	9.40	3.96	4.79	8.74	3.41	5.55	8.97					
88	210	4	3	116	109	210	-24	28	28	810	780	1590	50.9	695	935	1630	42.6	7.25	6.70	6.46	13.16	5.75	7.74	13.49					
88	210	4	3.5	121	116	210	-29	33	33	905	810	1715	52.8	670	975	1645	40.7	5.56	9.77	8.74	18.51	7.23	10.52	17.75					
88	210	4	4	122	118	210	-30	34	34	1040	880	1920	54.2	715	1225	1940	36.9	4.68	13.33	11.28	24.62	9.17	15.71	24.87					

Figure A.15: Spreadsheet for Marcol 52, $\delta = 5$ [mm], two orifices at different height.

BEFORE										DURING										AFTER									
Liquid level, mm		Valve		Liquid level (max Δ), mm						Amount, ml Valve 1		WC, %		Amount, ml Valve 2		WC, %		Time, s		Flowrate, l/min, Valve 1		Flowrate, l/min Valve 2							
wL	oL	ΔL	Valve	wL'v1	wL'v2	oL'	wL'v1	wL'v2	oL'v2	wV	oV	totV	WC, %	wV	oV	totV	WC, %	Time, s	wQ	oQ	totQ	wQ	oQ	totQ					
10	210	82	1.5	11	210	81	1	1	0	675	675	0.0	0.0	0	615	615	0.0	15.46	0.00	2.62	2.62	0.00	2.39	2.39					
10	210	82	2	13	210	79	3	3	0	985	985	0.0	0.0	0	965	965	0.0	10.75	0.00	5.50	5.50	0.00	5.39	5.39					
10	210	82	2.25	14	210	78	4	4	0	1415	1415	0.0	0.0	0	1375	1375	0.0	11.15	0.00	7.61	7.61	0.00	7.40	7.40					
10	210	82	2.5	19	210	73	9	9	0	1595	1595	0.0	0.0	0	1535	1535	0.0	10.34	0.00	9.26	9.26	0.00	8.91	8.91					
10	210	82	3	27	210	65	17	17	0	1650	1650	0.0	0.0	0	1700	1700	0.0	7.50	0.00	13.20	13.20	0.00	13.60	13.60					
10	210	82	3.5	35	210	57	25	25	0	1850	1850	0.0	0.0	0	1850	1850	0.0	5.81	0.00	18.81	18.81	0.00	18.81	18.81					
10	210	82	4	57	210	35	47	47	0	2445	2445	0.0	0.0	0	2445	2445	0.0	25.25	0.00	25.25	25.25	0.00	25.25	25.25					
30	210	62	1.5	32	210	60	2	2	0	885	885	0.0	0.0	0	920	920	0.0	20.68	0.00	2.57	2.57	0.00	2.67	2.67					
30	210	62	2	34	210	58	4	4	0	1905	1905	0.0	0.0	0	1965	1965	0.0	20.43	0.00	5.59	5.59	0.00	5.77	5.77					
30	210	62	2.25	37	210	55	7	7	0	1850	1850	0.0	0.0	0	1870	1870	0.0	15.65	0.00	7.09	7.09	0.00	7.17	7.17					
30	210	62	2.5	38	210	54	8	8	0	2265	2265	0.0	0.0	0	2295	2295	0.0	15.43	0.00	8.81	8.81	0.00	8.92	8.92					
30	210	62	3	44	210	48	14	14	0	2265	2265	0.0	0.0	0	2340	2340	0.0	10.12	0.00	13.43	13.43	0.00	13.87	13.87					
30	210	62	3.5	59	210	33	29	29	0	2045	2045	0.0	0.0	0	2010	2010	0.0	6.43	0.00	19.08	19.08	0.00	18.76	18.76					
30	210	62	4	98	210	-6	68	68	35	2260	2295	1.5	20	2350	2370	0.8	5.62	0.37	24.13	24.50	0.21	25.09	25.30						
49	210	43	1.5	53	210	39	4	4	0	900	900	0.0	0.0	0	905	905	0.0	20.06	0.00	2.69	2.69	0.00	2.71	2.71					
49	210	43	2	57	210	35	8	8	0	1895	1895	0.0	0.0	0	1850	1850	0.0	19.90	0.00	5.71	5.71	0.00	5.58	5.58					
49	210	43	2.25	58	210	34	9	9	0	1805	1805	0.0	0.0	0	1880	1880	0.0	15.28	0.00	7.09	7.09	0.00	7.38	7.38					
49	210	43	2.5	62	210	30	13	13	0	1865	1865	0.0	0.0	0	1840	1840	0.0	12.21	0.00	9.16	9.16	0.00	9.04	9.04					
49	210	43	3	74	210	18	25	25	0	2020	2020	0.0	0.0	0	2060	2060	0.0	8.87	0.00	13.66	13.66	0.00	13.93	13.93					
49	210	43	3.5	91	210	1	42	42	150	1920	2070	7.2	100	1930	2030	4.9	6.40	1.41	18.00	19.41	0.94	18.09	19.03						
49	210	43	4	113	210	-21	64	64	320	1600	1920	16.7	300	1645	1945	15.4	4.56	4.21	21.05	25.26	3.95	21.64	25.59						
69	210	23	1.5	72	210	20	3	3	0	935	935	0.0	0.0	0	890	890	0.0	20.12	0.00	2.79	2.79	0.00	2.65	2.65					
69	210	23	2	79	210	13	10	10	0	1840	1840	0.0	0.0	0	1820	1820	0.0	20.03	0.00	5.51	5.51	0.00	5.45	5.45					
69	210	23	2.25	87	210	5	18	18	0	1735	1735	0.0	0.0	0	1750	1750	0.0	14.31	0.00	7.27	7.27	0.00	7.34	7.34					
69	210	23	2.5	95	210	-3	26	26	30	1700	1730	1.7	0	1710	1710	0.0	11.40	0.16	8.95	9.11	0.00	9.00	9.00						
69	210	23	3	102	103	210	-10	33	360	1875	2235	16.1	310	1915	2225	13.9	9.59	2.25	11.73	13.98	1.94	11.98	13.92						
69	210	23	3.5	105	106	210	-13	36	400	1200	1600	25.0	380	1230	1610	23.6	5.21	4.61	13.82	18.43	4.38	14.17	18.54						
69	210	23	4	112	115	210	-20	43	570	1315	1885	30.2	605	1330	1935	31.3	4.62	7.40	17.08	24.48	7.86	17.27	25.13						
88	210	4	1.5	94	95	210	-2	6	6	870	870	0.0	0.0	0	900	900	0.0	20.43	0.00	2.56	2.56	0.00	2.64	2.64					
88	210	4	2	100	99	210	-8	12	265	1635	1900	13.9	245	1600	1845	13.3	20.18	0.79	4.86	5.65	0.73	4.76	5.49						
88	210	4	2.25	102	102	210	-10	14	490	1850	2340	20.9	430	1885	2315	18.6	19.46	1.51	5.70	7.21	1.33	5.81	7.14						
88	210	4	2.5	102	103	210	-10	14	460	1265	1725	26.7	415	1275	1690	24.6	11.46	2.41	6.62	9.03	2.17	6.68	8.85						
88	210	4	3	104	107	210	-12	16	535	1065	1600	33.4	575	1080	1655	34.7	7.34	4.37	8.71	13.08	4.70	8.83	13.53						
88	210	4	3.5	108	110	210	-16	20	675	990	1665	40.5	670	980	1650	40.6	5.37	7.54	11.06	18.60	7.49	10.95	18.44						
88	210	4	4	111	112	210	-19	23	840	1050	1890	44.4	860	1115	1975	43.5	4.68	10.77	13.46	24.23	11.03	14.29	25.32						

Figure A.16: Spreadsheet for Marcol 52, δ = 10 [mm], two orifices at different height.

A.2 Water jump vs. flow rate for each gap

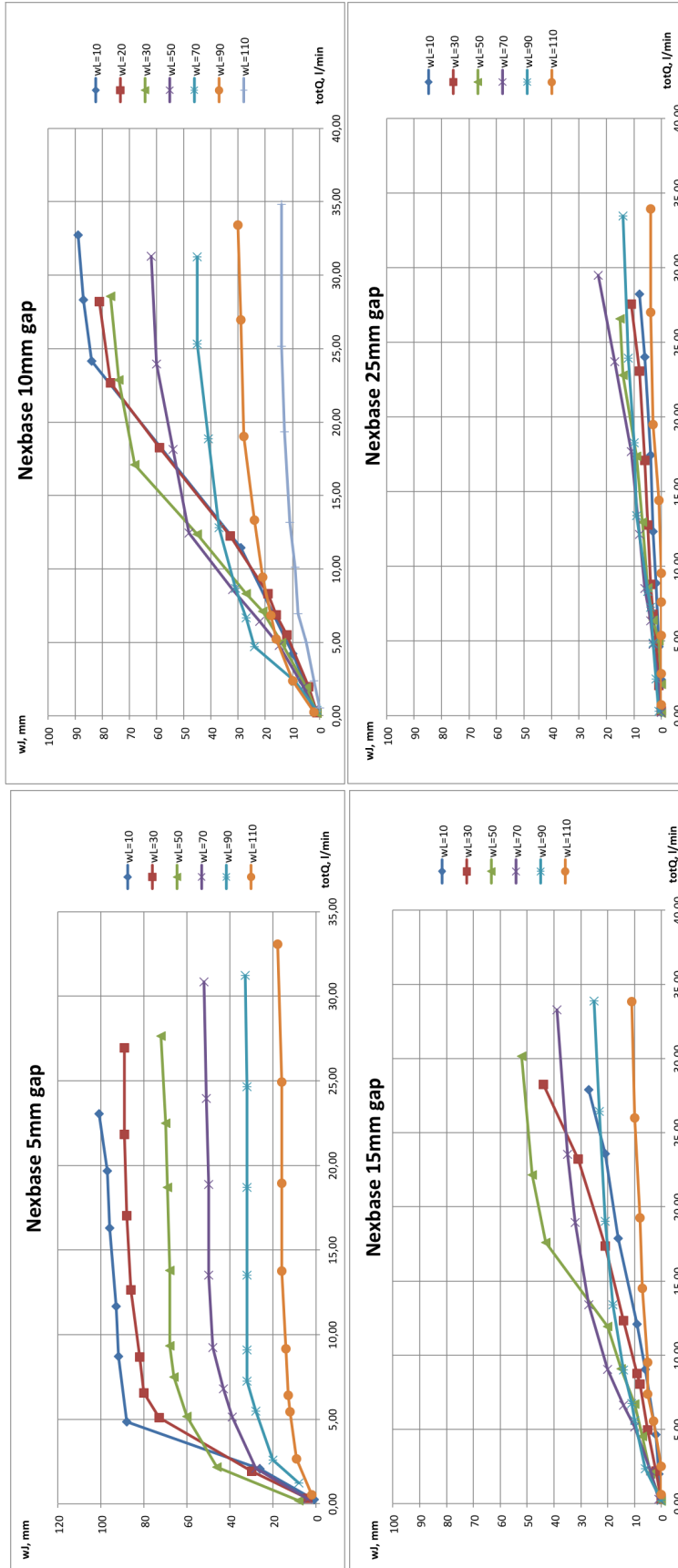


Figure A.17: Water jump as function of the flow rate for each annulus gap for Nexbase 3080.

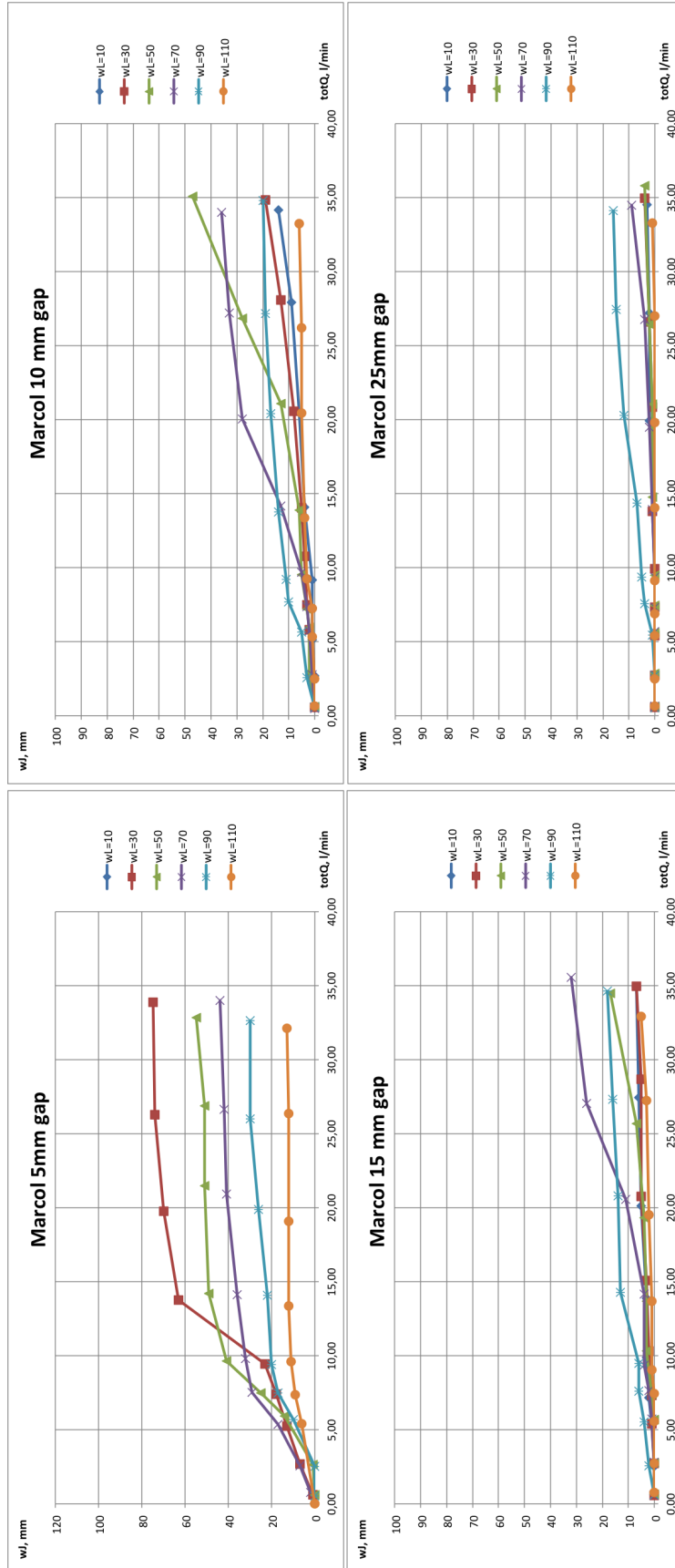


Figure A.18: Water jump as function of the flow rate for each annulus gap for Marcol 52.

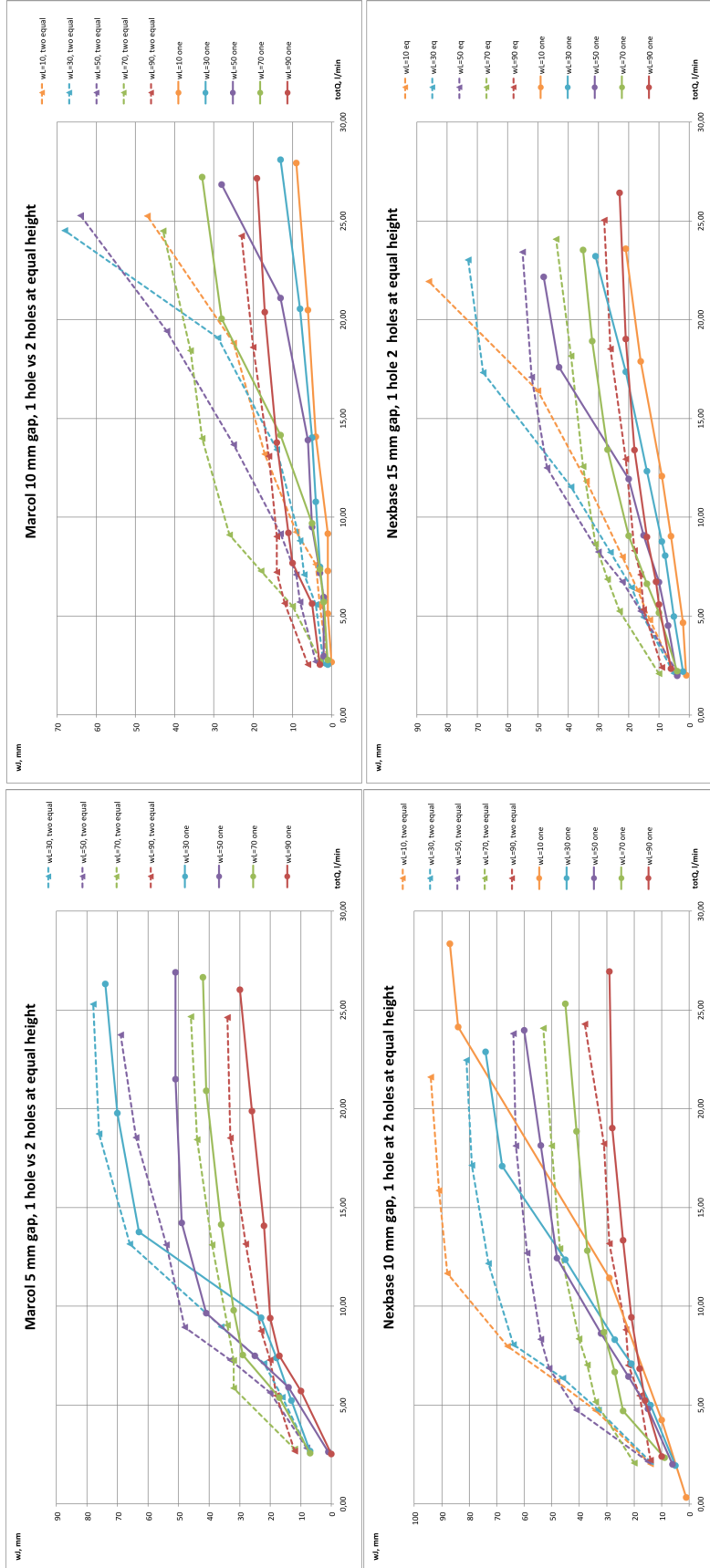


Figure A.19: Comparison of water jump as function of flow rate for Marcol and Nexbase, between one single outlet and two outlets at the same height.

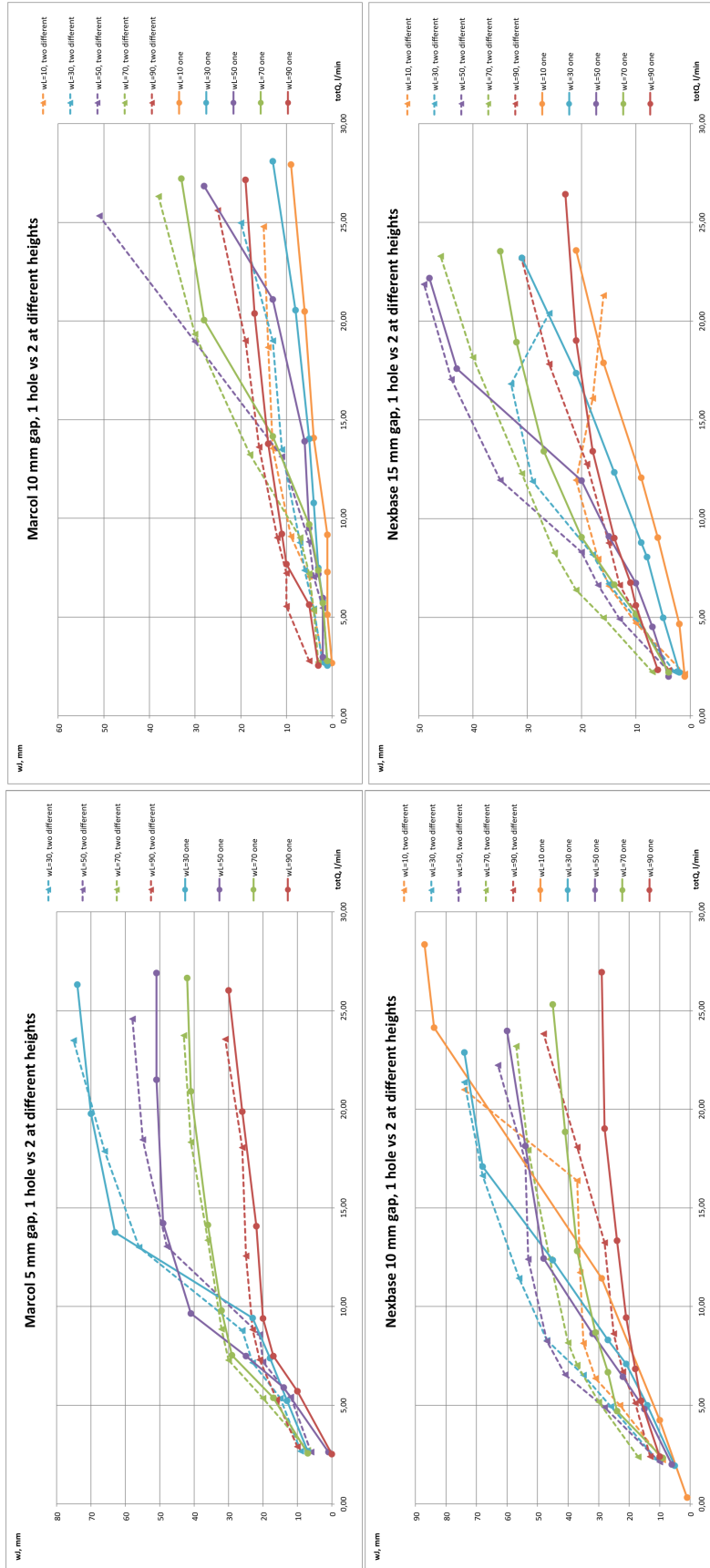


Figure A.20: Comparison of water jump as function of flow rate for Marcol and Nexbase, between one single outlet and two outlets at different heights.

A.3 Water cut vs. flow rate for each gap

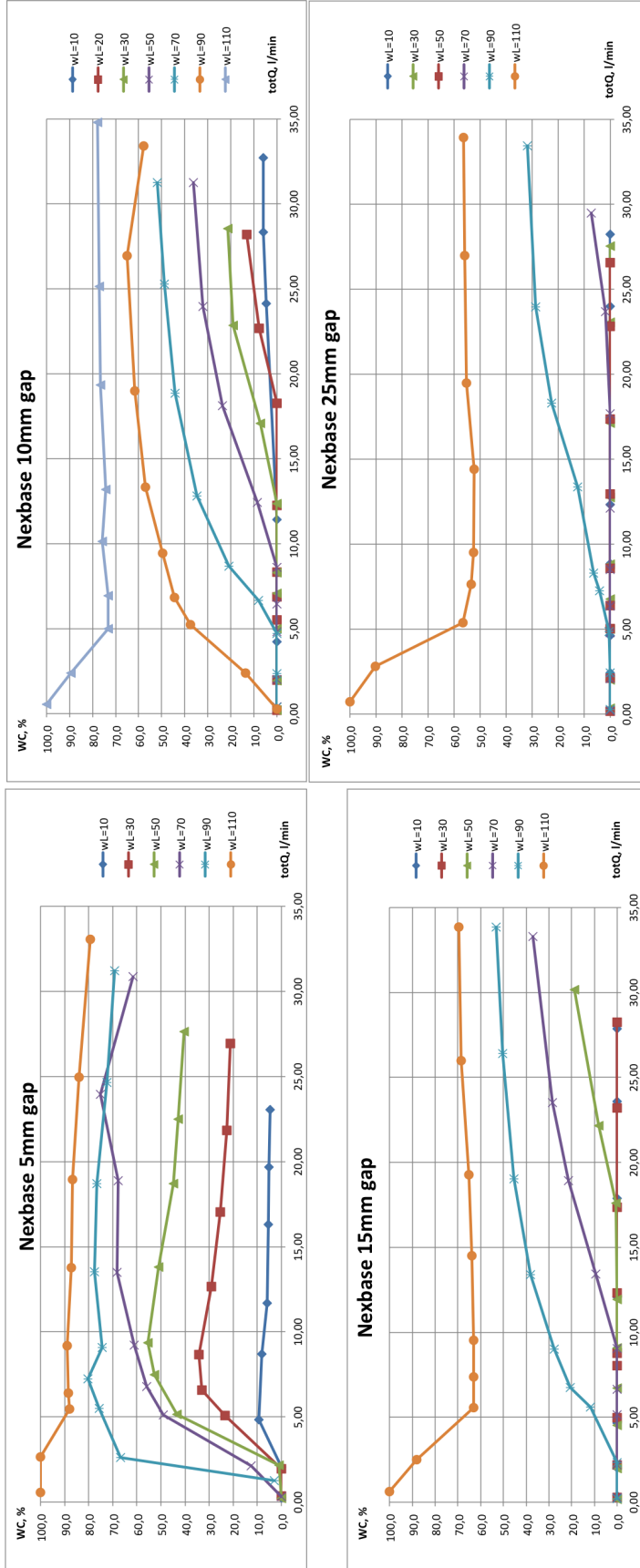


Figure A.21: Water cut as function of flow rate for each annulus gap for Nexbase 3080.

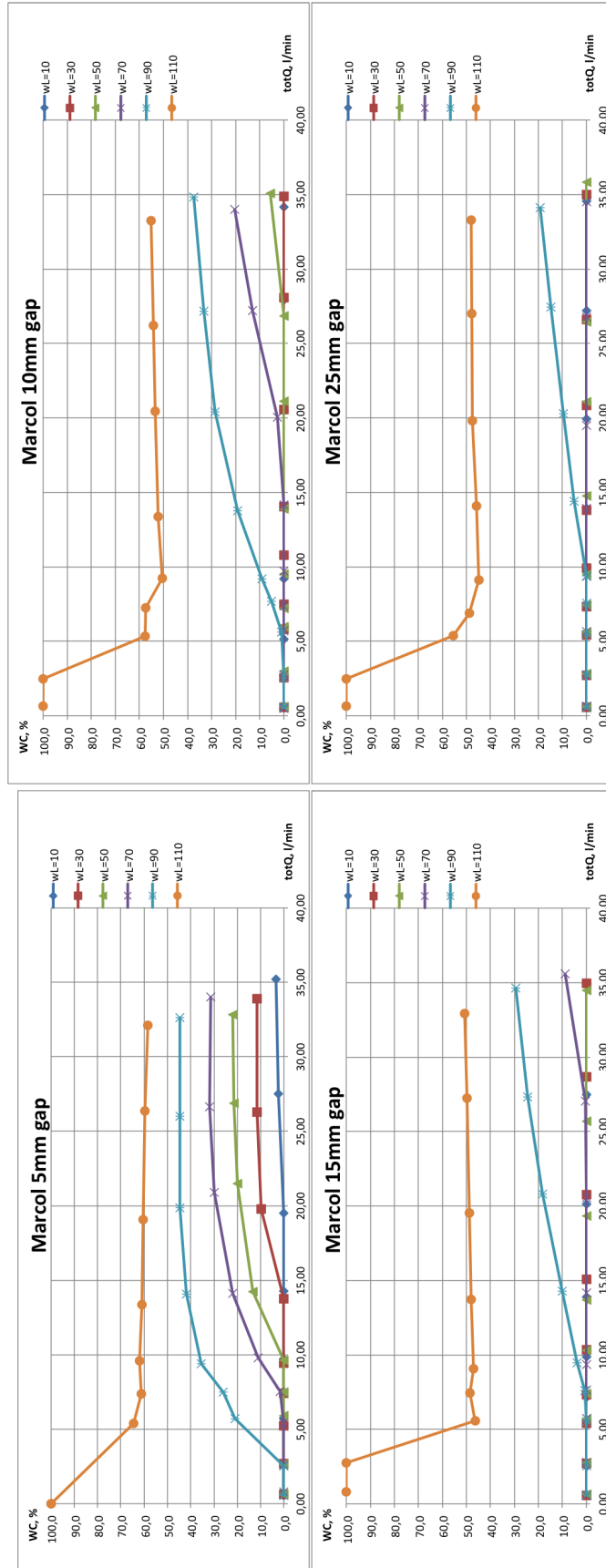


Figure A.22: Water cut as function of flow rate for each annulus gap for Marcol 52.

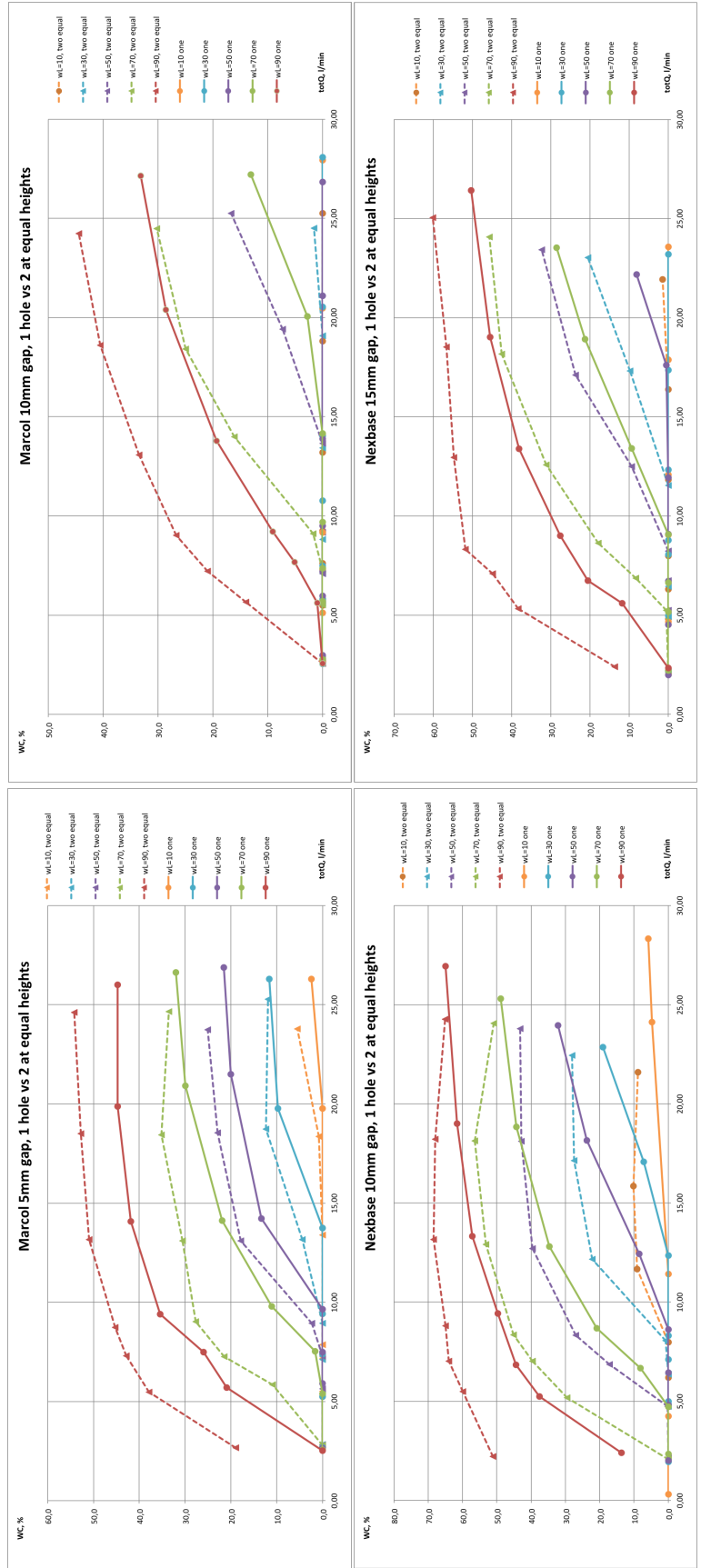


Figure A.23: Comparison of the water cut as function of flow rate for Marcol and Nexbase, between one single outlet and two outlets at the same height.

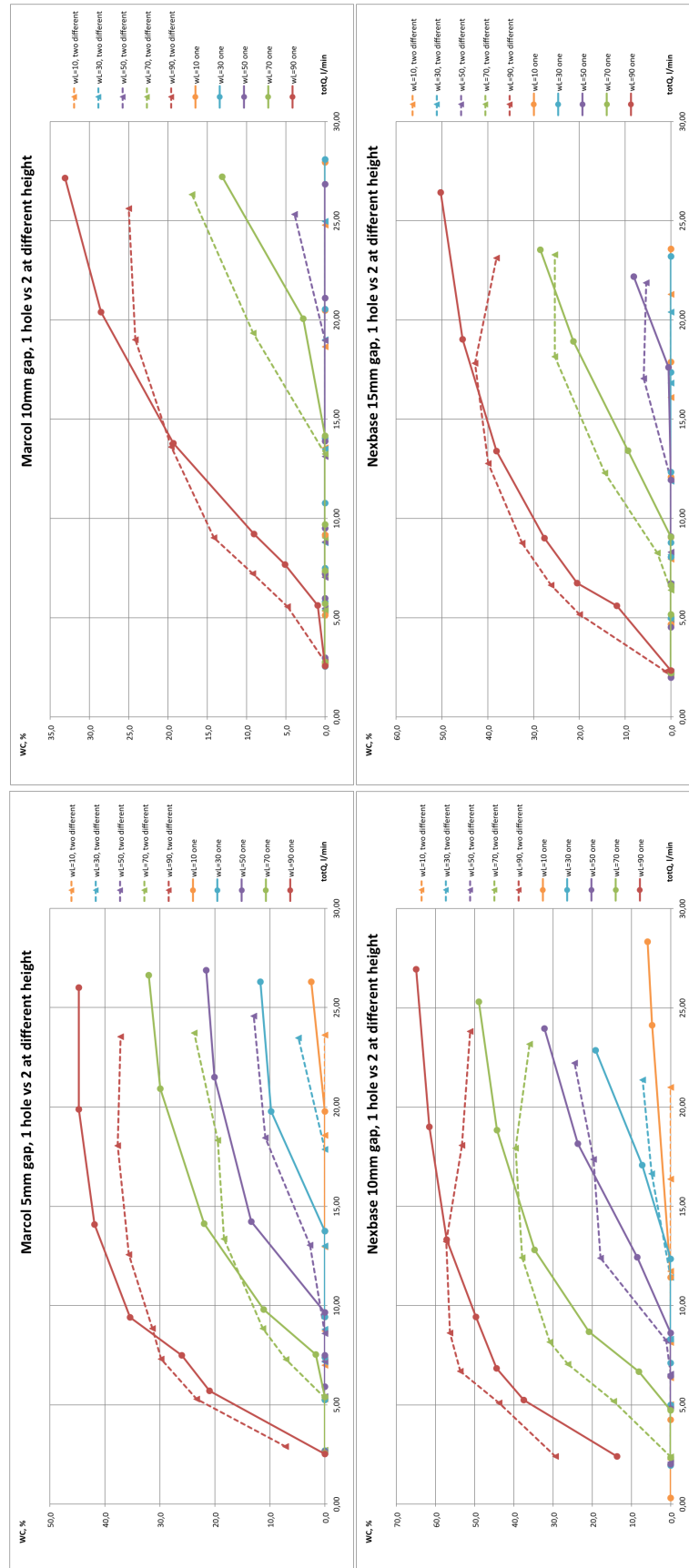


Figure A.24: Comparison of the water cut as function of flow rate for Marcol and Nexbase, between one single outlet and two outlets at different heights.

A.4 Flow rate correlations for each gap

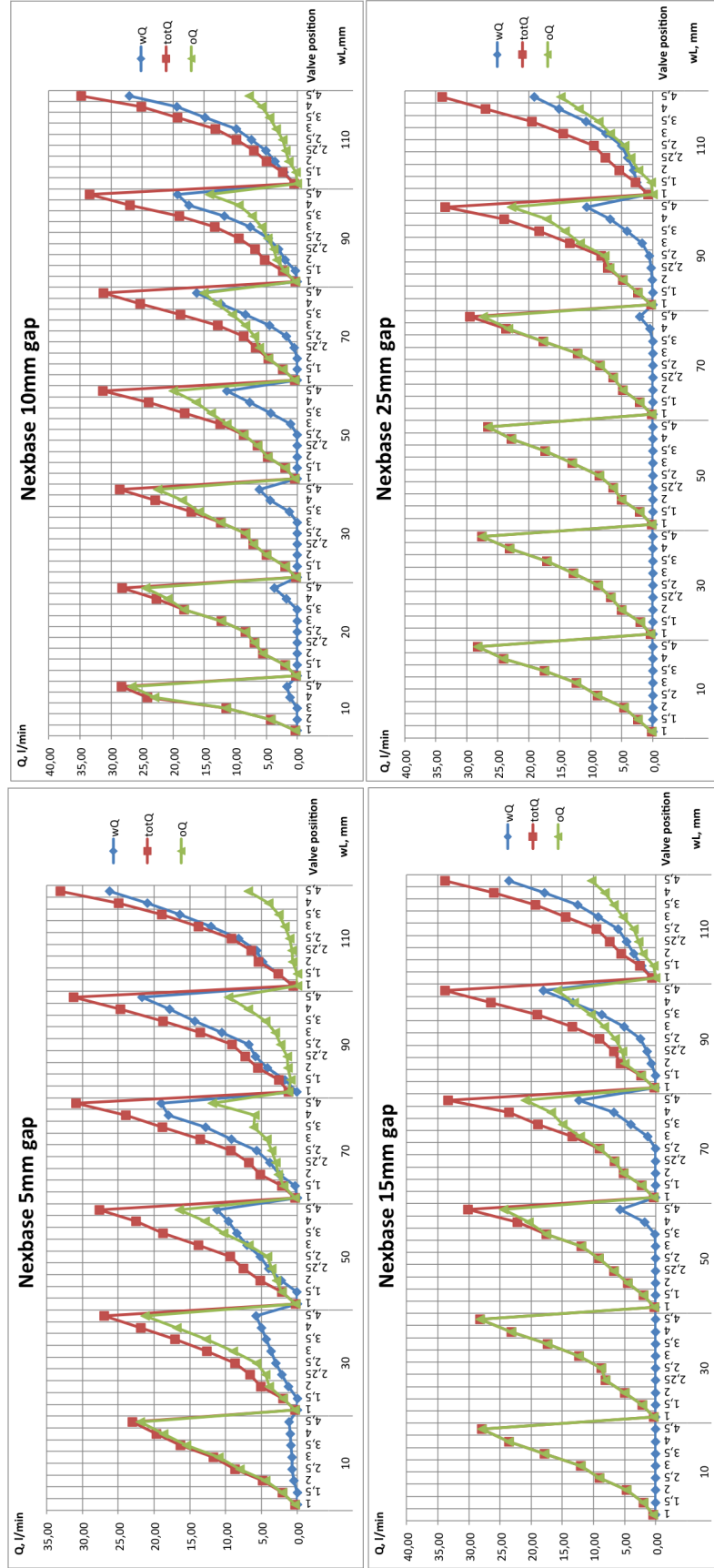


Figure A.25: The flow rate of oil, water and the total flow rate for Nexbase 3080 $\delta = 10$ mm. Moving from left to right the different sequences are: $wL = 10$ mm, ($wL = 20$ mm only for $\delta = 10$ mm), $wL = 30$ mm, $wL = 50$ mm, $wL = 70$ mm, $wL = 90$ mm and $wL = 110$ mm.

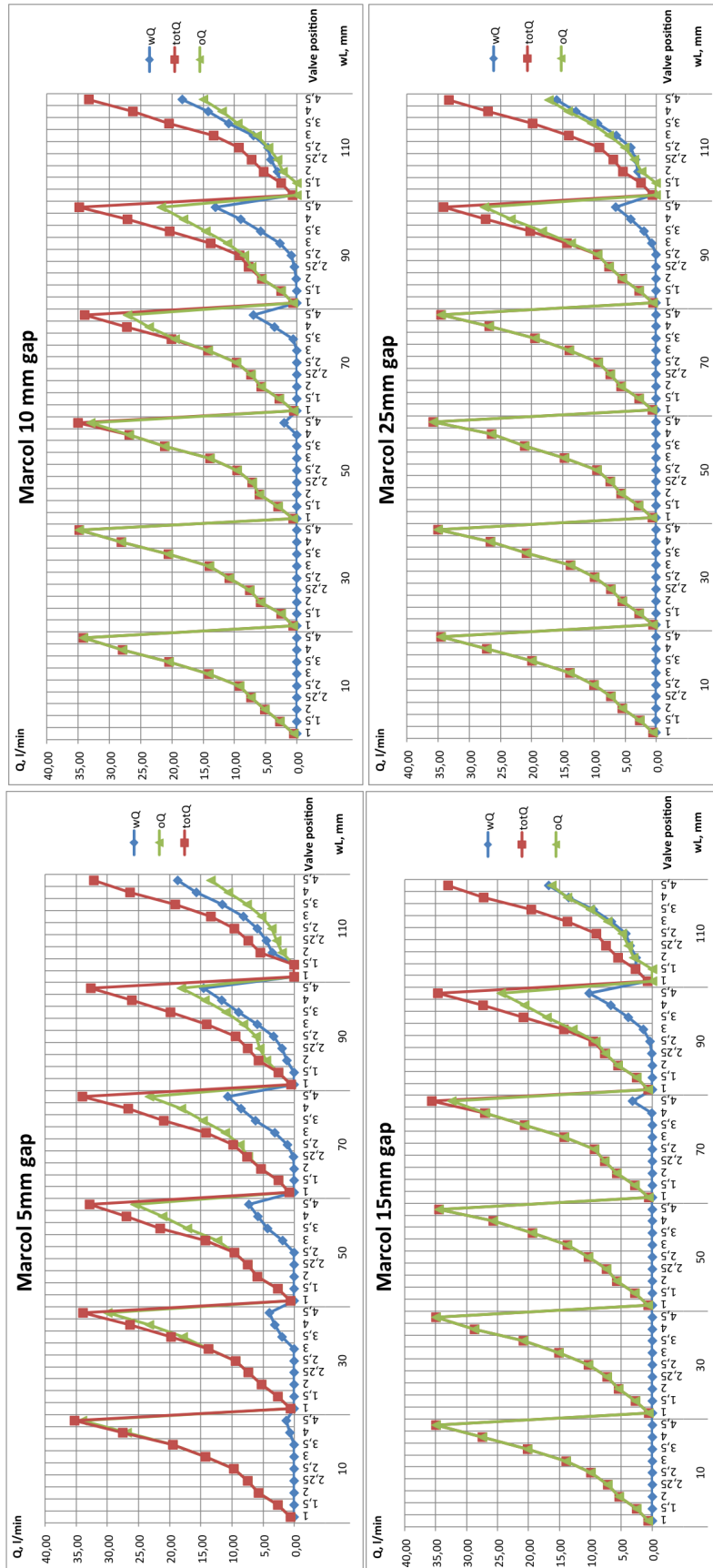


Figure A.26: The flow rate of oil, water and the total flow rate for Marcol 52 $\delta = 10$ mm. Moving from left to right the different sequences are: $wL = 10$ mm, $wL = 30$ mm, $wL = 50$ mm, $wL = 70$ mm, $wL = 90$ mm, $wL = 110$ mm.

Appendix B

CFD Simulations & Results

B.1 Laminar Solver with Composite Friction, Plots

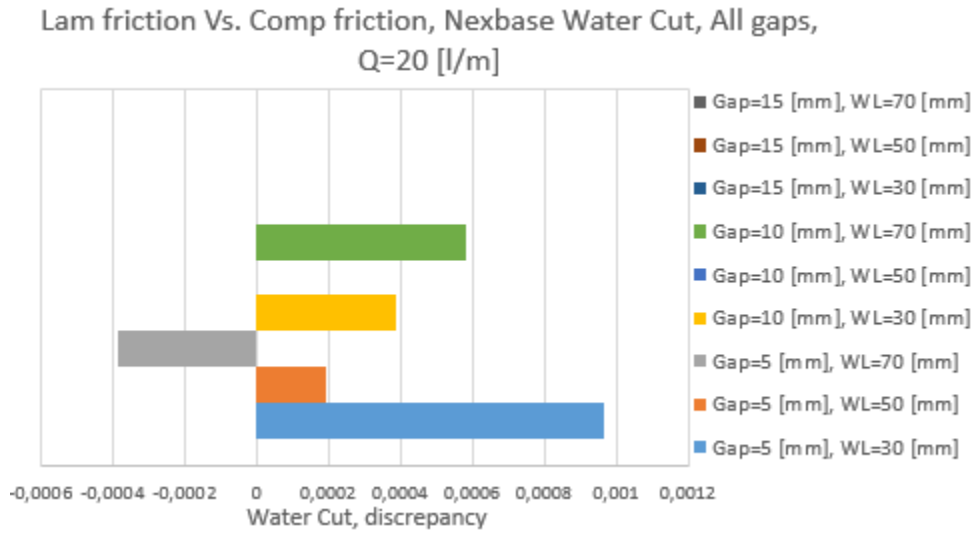


Figure B.1: Water cut discrepancy, laminar friction vs. composite friction formulation. Nexbase oil, all gaps.

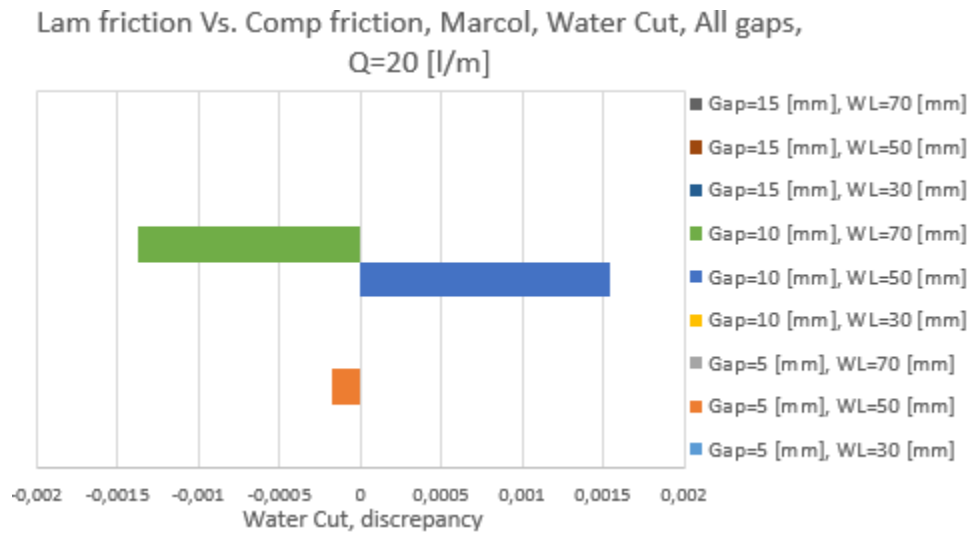


Figure B.2: Water cut discrepancy, laminar friction vs. composite friction formulation. Marcol oil, all gaps.

Appendix C

Analytical Methods

C.1 Dimensional Analysis

Variables of interest: $\mu, \rho, \delta, h, g, Q$

Chosen repeating variables: μ, ρ, δ

Expect $j = n - k$, $\rightarrow j = 3$ non-dimensional groups

$$\pi_1 = \pi_1(\mu, \rho, \delta, Q)$$

$$(MT^{-1}L^{-1})^a (ML^{-3})^b (L)^c (L^3T^{-1})$$

$$L: -a - 3b + c + 3 = 0$$

$$M: a + b = 0$$

$$T: -a - 1 = 0$$

Solving this set of equations gives, $a = -1, b = 1, c = -1$. Thus π_1 can be defined as:

$$\pi_1 = \frac{Q\rho}{\mu\delta}$$

$$\pi_2 = \pi_2(\mu, \rho, \delta, h)$$

$$(MT^{-1}L^{-1})^a (ML^{-3})^b (L)^c (L)$$

$$L: -a - 3b + c + 1 = 0$$

$$M: a + b = 0$$

$$T: -a = 0$$

Solving this set of equations gives, $a = 0, b = 0, c = -1$. Thus π_2 can be defined as:

$$\pi_2 = \frac{h}{\delta}$$

$$\pi_3 = \pi_3(\mu, \rho, \delta, g)$$

$$(MT^{-1}L^{-1})^a (ML^{-3})^b (L)^c (LT^{-2})$$

$$L: -a - 3b + c + 1 = 0$$

$$M: a + b = 0$$

$$T: -a - 2 = 0$$

Solving this set of equations gives, $a = -2, b = 2, c = 3$. Thus π_3 can be defined as:

$$\pi_3 = \frac{\rho^2 g \delta^3}{\mu}$$

Table C.1: Table representing the coefficient values κ , and ϵ used in equation 7.7, for each respective configuration of oil and annulus gap width δ .

Equation 7.7 Coefficient Values				
Oil	δ [mm]	WL [mm]	κ [-]	ϵ [l/m]
Marcol	5	29,50,67,85	180	3.42
Marcol	10	11,29,50,67,87	630	0
Marcol	15	11,29,50,67,87	980	0
Nexbase	5	11,29,50,67,87	8	0.5
Nexbase	10	11,29,50,67,87	40	0
Nexbase	15	11,29,50,67,87	75	0

C.2 Matlab Scripts

Listing C.1: Matlab script for solving equation 7.9 for the critical flow rate.

```

1 h=0.1105; %Constant used to calculate coning height
2 g=9.81; %Gravitational constant
3 wl=0.067; %Initial water level of interest
4 gap=0.005; %Annulus gap of interest
5 rho_o=825; %Density of oil of interest
6 rho_w=1000; %Density of water
7 r_i=0.0175; %Radius of outlet orifice
8 c_h=h-wl-r_i; %Coning height
9 crit_flow=0; %Initializing output variable
10 q_0=0.0009; %Initial guess
11
12 b=((6*0.012)/(pi*(gap)^3))*log((c_h+r_i)/r_i); % Calculating variables as
13 a=g*c_h*(rho_w-rho_o); % defined in equation 6.11
14 c=((rho_o/8)*(1/(pi*gap))^2)*((1/(c_h+r_i))^2)-((1/r_i)^2);
15 crit_flow=fzero(@(q) a-(b*q)+(c*q^2),q_0) % Solving for critical flow rate
16
17 root_pos=(sqrt((b^2)-4*c*a)+b)/(2*c) % Check to see that correct root is
18 root_neg=(-sqrt((b^2)-4*a*c)+b)/(2*c) % extracted

```

Listing C.2: Matlab script for solving equation 7.9 for the stationary coning height.

```

1
2 h=0.1105; %Constant used to calculate coning height
3 wl=0.087; % Water level of interest
4 Q=[3 6 9 12 15 18 21 24 27]; %Flow rates of interest [l/m]
5 q=Q/60000; %flow rates of interest [m^3/s]
6 r_0=0.02; %Initial guess of coning height
7 gap=0.005; %Annulus gap of interest
8 rho=845; %Density of oil of interest
9 r_i=0.0175; %Radius of outlet orifice
10 r_w=h-wl; %Height from interface to center of orifice
11 vec=zeros(1,length(q)); %Output vector
12
13 for i=1:length(q)
14     a=(6*0.09*q(i))/(pi*(gap)^3);
15     b=(1000-845)*9.81;
16     c=((rho/8)*(q(i)/(pi*gap))^2);
17     vec(i)=fzero(@(r) b*(r_w-r)-a*log(r/r_i)+c*((1/r^2)-(1/r_i^2)),r_0);
18 end % Solving equation 6.10 for the stationary coning height

```

Listing C.3: Matlab script for solving equation 7.13 for the critical flow rate.

```

1 h=0.1105; %Constant used to calculate coning height
2 g=9.81; %Gravitational constant
3 wl=0.011; %Water level of interestFlyvninger
4 gap=0.015; %Annulus gap of interest
5 rho_o=825; %Oil density of interest
6 rho_w=1000; %Water density
7 r_i=0.0175; %Radius of outlet orifice
8 c_h=h-wl-r_i; %Coning height
9 alpha=50/60000; %Coefficient used for model tuning [m^3/s]
10
11 b=((6*0.012)/(pi*(gap)^3))*log((c_h+r_i)/r_i);
12 a=g*c_h*(rho_w-rho_o);
13 c=((alpha*rho_o/8)*(1/(pi*gap))^2)*(((1/(c_h+r_i))^2)-((1/r_i)^2));
14     % Solving equation 6.15 for the critical flow rate

```

```
15 Q=- (a/ (c-b));  
16 Q_liter_per_min=Q*60000;
```

Listing C.4: Matlab script for solving equation 7.12 for the critical flow rate.

```
1 h=0.1105; %constant used to calculate coning height  
2 g=9.81; %Gravitational constant  
3 wl=[0.011 0.029 0.048 0.068 0.087]; %Water levels of interest  
4 gap=0.01; %Annulus gap of interest  
5 rho_o=845; %Oil density of interest  
6 rho_w=1000; %Water density  
7 r_i=0.0175; %Radius of outlet orifice  
8 alpha=10.7/60000; %Tuning parameter  
9 q_sol=[]; %Output vector  
10  
11 for i=1:length(wl)  
12  
13     wl_i=wl(i);  
14     c_h=h-wl_i-r_i; % Coning height  
15     b=((6*0.09)/(pi*(gap)^3))*log((c_h+r_i)/r_i);  
16     a=g*c_h*(rho_w-rho_o);  
17     c=((rho_o/8)*(1/(pi*gap))^2)*(((1/(c_h+r_i))^2)-((1/r_i)^2));  
18     %Solving equation 6.14 for the critical flow rate  
19     Q=sqrt(((b*alpha)-a)/(c));  
20     Q_liter_per_min=Q*60000;  
21     q_sol(i)=Q_liter_per_min;  
22 end
```

Listing C.5: Matlab script for computing the critical flow rates utilizing equation 7.7.

```
1 rho=825; %Density of oil in question
2 gap=0.015; %Annulus gap width in question
3 kappa=980; %Value of kappa coefficient
4 epsilon=0.00005; %Value of epsilon coefficient
5 ri=0.0175; %Radius of outlet orifice
6 wl=[0.011 0.029 0.050 0.067 0.087]; %Water levels used in experiments
7 q=[]; % Vector to store critical flow rates calculated
8 mu=0.012;
9
10 for i=1:length(wl) % Loops through all initial water levels
11 h=0.1105-ri-wl(i); % Calculate the height from interface to orifice
12 q(i)=((gap*mu*kappa)/rho)*(h/gap)+epsilon)*60000;
13 end %Utilizes correlation to calculate critical flow rate
```

C.3 Solving Analytical Models, Plots

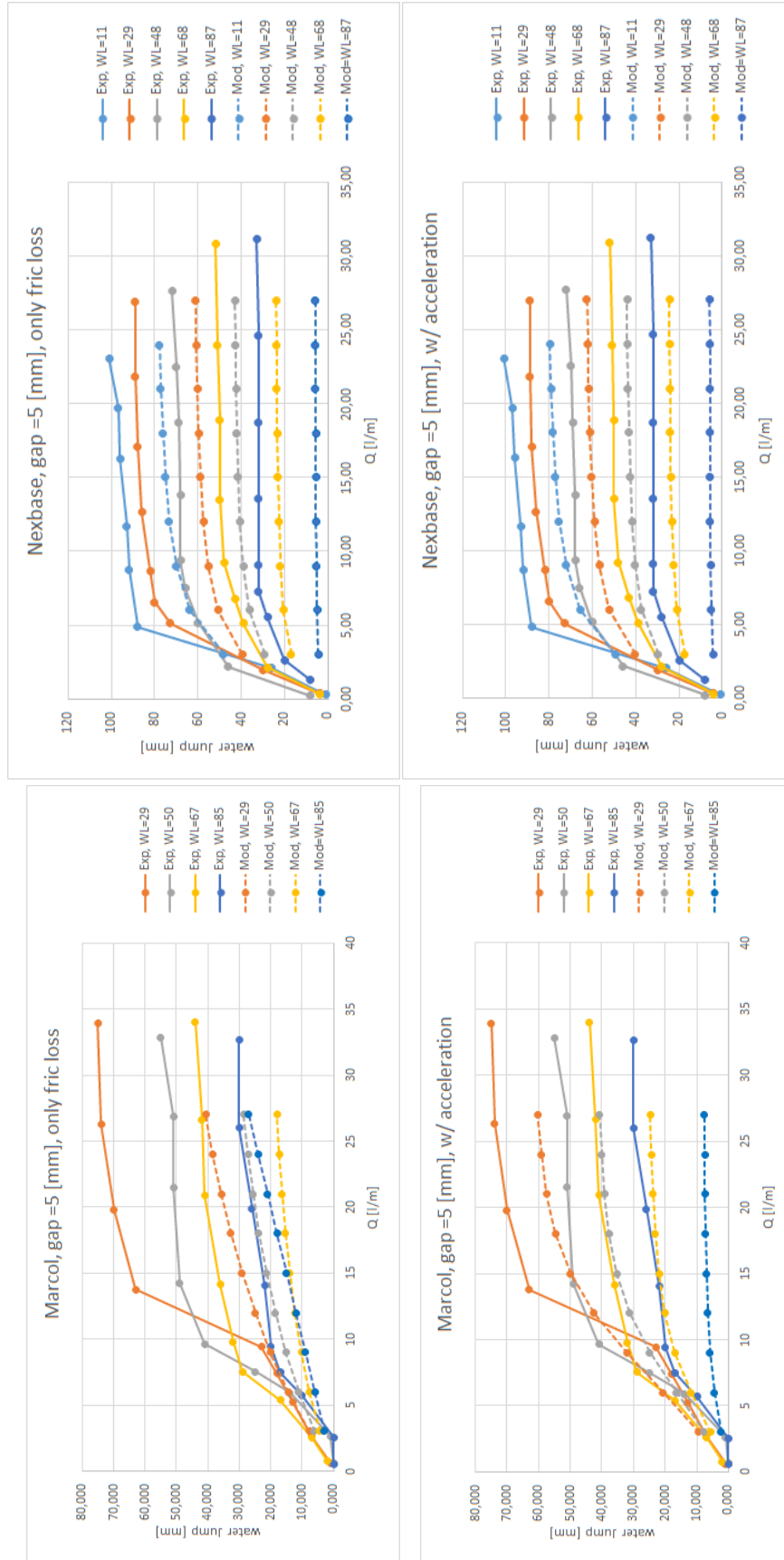


Figure C.1: Predicted stable water cone height with and with accelerational pressure loss. For Marcol and Nexbase, $\delta=5$ [mm].

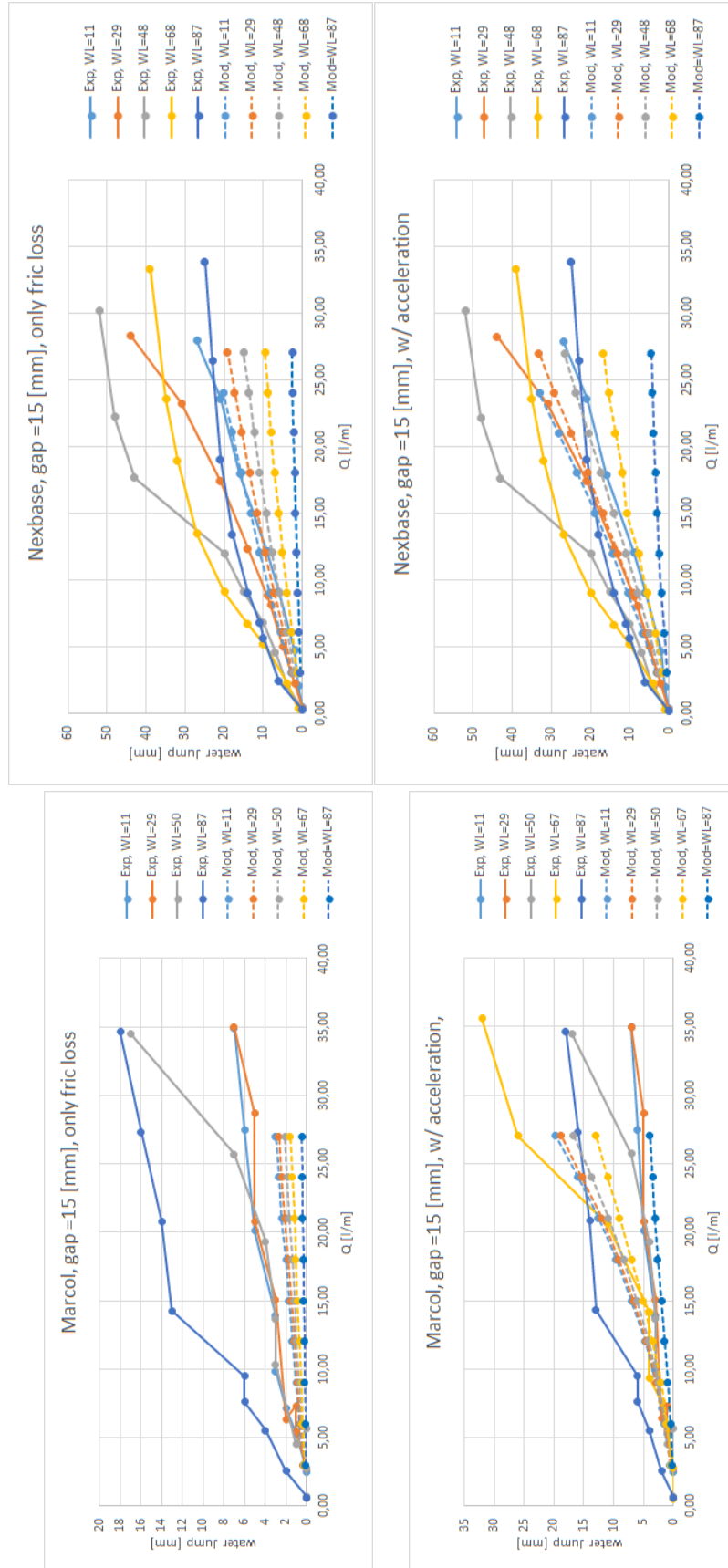


Figure C.2: Predicted stable water cone height with and with accelerational pressure loss. For Marcol and Nexbase, $\delta=15$ [mm].

Appendix D

Miscellaneous

List of Figures

2.1	Coning in a vertical well[3].	7
2.2	Cresting in a horizontal well[3].	7
2.3	Cresting in horizontal well [5].	7
2.4	Cresting at the heel in a horizontal well [5].	8
2.5	Heterogenous reservoir with AICV completion including plot of pressure drops [8].	8
2.6	Stationary water cone in a vertical well[7, page 144].	9
2.7	Prediction of dimensionless critical rate for high fractional well penetration ratios[11].	10
2.8	Pressure gradient in oil zone vs. water zone [7].	11
2.9	ICD designs[5, page 31].	12
2.10	Flow schematic in nozzle-type ICD [12].	12
2.11	AICV design cut open [8].	14
2.12	Laminar-and turbulent restrictor in series vs. pressure drop [8].	15
2.13	The stratified pattern of the fluid mixture with valves arbitrarily oriented along the pipe[15, page 7].	15

2.14	Cross-sectional geometry of production piping at valve position[15, page 11]. . . .	16
2.15	Lower completion design for a horizontal well[15, page 14]	19
2.16	Geometry of housing design 1[15, page 5]	20
2.17	Geometry of housing design 2[15, page 5]	20
3.1	The total rig used for the experiments.	23
3.2	The 2D-principle[17, page 22].	24
3.3	A top-side view of the tank with the key components.	25
3.4	Custom-made metal pieces at the top of the tank which are attached with magnets to the plate.	25
3.5	Custom-made metal pieces at the bottom of the tank.	25
3.6	The bended transparent wall.	26
3.7	The total solution of keeping the wall distance constant with a roof to avoid air coning.	26
3.8	Geometry of improved single orifice housing plate.	26
3.9	Geometry of housing plate with two holes at equal height.	27
3.10	Geometry of housing plate with two holes at different height.	27
3.11	Draining valve (left) and downstream flow valve (right).	27
3.12	Flow rate as a function of the liquid height in the tank.	30

3.13 Water cut with and without metal pieces at the bottom of the annulus for water level of 10 [mm] and Nexbase 3080.	31
3.14 Metalpieces blocking the inflow of water.	31
3.15 Test with roof at $\delta = 5$ [mm], WL = 10 [mm] and valve position 4.	32
3.16 Test without roof at $\delta = 5$ [mm], WL = 10 [mm] and valve position 4.	32
3.17 Figure (a) and (b) shows the rig in standby mode while (c) and (d) shows the rig in operational mode.	36
3.18 The two bucket system.	37
4.1 Screen shots of different experimental runs illustrating the water coning phenomenon.	41
4.2 The flow rate of oil, water and the total flow rate for Nexbase 3080, $\delta = 5$ mm. Moving from left to right the different sequences are: WL = 10 [mm], WL = 30 [mm], WL = 50 [mm], WL = 70 [mm], WL = 90 [mm] and WL = 110 [mm].	42
4.3 The flow rate of oil, water and the total flow rate for Nexbase 3080, $\delta = 25$ mm. Moving from left to right the different sequences are: WL = 10 [mm], WL = 30 [mm], WL = 50 [mm], WL = 70 [mm], WL = 90 [mm] and WL = 110 [mm].	43
4.4 The flow rate of oil, water and the total flow rate for Marcol 52, $\delta = 5$ [mm]. Moving from left to right the different sequences are: WL = 10 [mm], WL = 30 [mm], WL = 50 [mm], WL = 70 [mm], WL = 90 [mm] and WL = 110 [mm].	43
4.5 Water jump as function of flow rate, $\delta = 10$ [mm], Nexbase 3080.	44
4.6 Water jump as function of flow rate, $\delta = 15$ [mm], Nexbase 3080.	45
4.7 Water jump as function of flow rate, $\delta = 10$ [mm], Marcol.	45

4.8	Water jump as function of valve position for different annulus gaps for Nexbase 3080. Moving from left to right the different sequences are: WL = 10 [mm], WL = 30 [mm], WL = 50 [mm], WL = 70 [mm], WL = 90 [mm] and WL = 110 [mm].	47
4.9	Water jump as function of valve position for different annulus gaps for Marcol 52. Moving from left to right the different sequences are: WL = 30 [mm], WL = 50 [mm], WL = 70 [mm], WL = 90 [mm] and WL = 110 [mm].	48
4.10	Comparison of water jump as function of flow rate for Nexbase 3080 and Marcol 52 for $\delta = 10$ [mm].	48
4.11	Comparison of water jump as function of flow rate for Nexbase 3080 and Marcol 52 for $\delta = 15$ [mm].	49
4.12	Water jump as function of flow rate compared with Egor's for the same system, $\delta = 10$ [mm].	50
4.13	Steady state pictures of the water jump for high flow rates and small annulus gaps. Here (a) shows the situation for symmetric inflow, while (b) [17, page 41] shows one-sided inflow.	50
4.14	Snapshots from the experiments with two orifices at the same height, where (a) is done with Nexbase 3080 and (b) is done with Marcol 52.	51
4.15	Comparison of water jump as function of flow rate for Marcol 52 for $\delta = 5$ [mm] between one single outlet and two outlets at the same height.	52
4.16	Comparison of water jump as function of flow rate for Marcol 52 for $\delta = 10$ [mm] between one single outlet and two outlets at the same height.	52
4.17	Comparison of water jump as function of flow rate for Nexbase for $\delta = 10$ [mm] between one single outlet and two outlets at the same height.	53
4.18	Snapshots from the experiments with two orifices at different height. Both done with Nexbase 3080 with high flow rates between 20 and 30 [l/min].	54

4.19	Snapshots from the experiments with two orifices at different height. Both done with Nexbase 3080 with high flow rates between 6 and 7 [l/min].	55
4.20	Comparison of water jump as function of flow rate for Marcol for $\delta = 10$ [mm] between one single outlet and two outlets at different heights.	55
4.21	Comparison of water jump as function of flow rate for Marcol for $\delta = 5$ [mm] between one single outlet and two outlets at different heights.	56
4.22	Water cut as function of flow rate for Nexbase 3080, $\delta = 15$ [mm].	57
4.23	Water cut as function of flow rate for Marcol 52, $\delta = 5$ [mm].	57
4.24	Illustration of why the water cut for WL = 110 [mm] is wrong for some flow rates.	58
4.25	Comparison of water cut as function of flow rate for Nexbase 3080 and Marcol 52 for $\delta = 10$ [mm].	59
4.26	Water cut as function of flow rate for Nexbase, $\delta = 5$ [mm].	59
4.27	Steady state pictures of the flow transition. Figure (a) has valve position= 2.25, (b) = 2.5 and (c) = 3.	60
4.28	Water cut as function of flow rate compared with Egor's for the same system, $\delta = 10$ [mm].	61
4.29	Comparison of water cut as function of flow rate for Marcol 52 for $\delta = 10$ [mm] between one single outlet and two outlets at the same height.	62
4.30	Comparison of water cut as function of flow rate for Nexbase for $\delta = 10$ [mm] between one single outlet and two outlets at the same height.	62
4.31	Comparison of water cut as function of flow rate for Nexbase for $\delta = 10$ [mm] between one single outlet and two outlets at different height.	63

4.32 Comparison of water cut as function of flow rate for Marcol 52 for $\delta = 5$ [mm] between one single outlet and two outlets at different height.	63
5.1 2D simulation geometry, with one outlet orifice.	67
5.2 2D simulation geometry, with two outlet orifices.	68
5.3 3D simulation geometry, side view.	68
5.4 3D simulation geometry.	69
5.5 Velocity contours plot. Nexbase oil with annulus gap=10 [mm], Q=20 [l/m]	74
5.6 Friction factor as a function of Reynolds number, plotted using the the friction factors presented in equation (2.8), (5.9), and (5.10).	75
5.7 Friction factor as a function of Reynolds number, [23, page 208-212]	75
5.8 Expressions implemented in the CFX-setup module.	76
5.9 2D Mesh.	77
5.10 2D Mesh, orifice up-close.	77
5.11 2D Mesh, inflation layers at orifice.	78
5.12 2D Mesh, two outlet orifices with inflation layers.	78
5.13 3D Mesh, side view.	78
5.14 3D Mesh, drainage pipe.	78
5.15 Mass flow vs. time step, 50% coarsening of mesh, tetrahedral at orifice.	81
5.16 Mass flow vs. time step, 25% coarsening of mesh, tetrahedral at orifice.	81

5.17 Mass flow vs. time step, default mesh, tetrahedral at orifice.	82
5.18 Mass flow vs. time step, 25% refinement of mesh, tetrahedral at orifice.	82
5.19 Comparison of meshes with respective optimal time steps.	82
5.20 Mass flow vs. time step, 50% coarsening of mesh, inflated hexahedral at orifice. . .	84
5.21 Mass flow vs. time step, 25% coarsening of mesh, inflated hexahedral at orifice. . .	84
5.22 Mass flow vs. time step, default mesh, inflated hexahedral at orifice.	85
5.23 Mass flow vs. time step, 25% refinement of mesh, inflated hexahedral at orifice. . .	85
5.24 Comparison of meshes with respective optimal time steps.	85
6.1 Example of capillary rise between parallel plates[27].	92
6.2 Water jump as a function of flowrate, Nexbase oil vs. Marcol oil with $\delta=5$ [mm]. . .	95
6.3 Water jump as a function of flowrate, Nexbase oil vs. Marcol oil with $\delta=10$ [mm]. . .	95
6.4 Water jump as a function of flowrate, Nexbase oil vs. Marcol oil with $\delta=15$ [mm]. . .	95
6.5 Water jump as a function of flowrate. Nexbase oil with $\delta=5$ [mm], simulation vs. experiment.	96
6.6 Water jump as a function of flowrate. Nexbase oil with $\delta=10$ [mm], simulation vs. experiment.	96
6.7 Water jump as a function of flowrate. Nexbase oil with $\delta=15$ [mm], simulation vs. experiment.	96
6.8 Water jump as a function of flowrate. Marcol oil with $\delta=5$ [mm], simulation vs. experiment.	97

6.9 Water jump as a function of flowrate. Marcol oil with $\delta=10$ [mm], simulation vs. experiment.	97
6.10 Water jump as a function of flowrate. Marcol oil with $\delta=15$ [mm], simulation vs. experiment.	97
6.11 Example of water coning. Nexbase oil with $\delta=10$ [mm], WL=10 [mm], and Q=20[l/m].	98
6.12 Water cut as a function of flowrate, Nexbase oil vs. Marcol oil with $\delta=5$ [mm]. . . .	100
6.13 Water cut as a function of flowrate, Nexbase oil vs. Marcol oil with $\delta=10$ [mm]. . . .	100
6.14 Water cut as a function of flowrate, Nexbase oil vs. Marcol oil with $\delta=15$ [mm]. . . .	100
6.15 Water cut as a function of flowrate. Nexbase oil with $\delta=5$ [mm], simulation vs. experiment.	101
6.16 Water cut as a function of flowrate. Nexbase oil with $\delta=10$ [mm], simulation vs. experiment.	101
6.17 Water cut as a function of flowrate. Nexbase oil with $\delta=15$ [mm], simulation vs. experiment.	101
6.18 Water cut as a function of flowrate. Marcol oil with $\delta=5$ [mm], simulation vs. experiment.	102
6.19 Water cut as a function of flowrate. Marcol oil with $\delta=5$ [mm], simulation vs. experiment.	102
6.20 Water cut as a function of flowrate. Marcol oil with $\delta=5$ [mm], simulation vs. experiment.	102
6.21 Water jump discrepancy, laminar friction vs. composite friction formulation. Nexbase oil, all gaps.	104

6.22 Water jump discrepancy, laminar friction vs. composite friction formulation. Marcol oil, all gaps.	104
6.23 Water jump discrepancy. Transitional solver with laminar friction vs. laminar solver with composite friction formulation. Nexbase oil, all gaps.	106
6.24 Water jump discrepancy. Transitional solver with laminar friction vs. laminar solver with composite friction formulation. Marcol oil, all gaps.	106
6.25 Water jump as a function of flowrate for Marcol oil with $\delta=10$ [mm], and WL=50 [mm]. Plotted for transitional solver with laminar friction, laminar solver with composite friction formulation, and experiment values.	107
6.26 Water cut discrepancy. Transitional solver with laminar friction vs. laminar solver with composite friction formulation. Nexbase oil, all gaps.	108
6.27 Water cut discrepancy. Transitional solver with laminar friction vs. laminar solver with composite friction formulation. Marcol oil, all gaps.	108
6.28 Water jump as a function of flowrate. Marcol oil with $\delta=5$ [mm], simulation vs. experiment.	110
6.29 Water jump as a function of flowrate. Marcol oil with $\delta=10$ [mm], simulation vs. experiment.	110
6.30 Water jump as a function of flowrate. Nexbase oil with $\delta=10$ [mm], simulation vs. experiment.	110
6.31 Water jump as a function of flowrate. Nexbase oil with $\delta=15$ [mm], simulation vs. experiment.	111
6.32 Water jump as a function of flowrate, Nexbase vs. Marcol, $\delta=10$ [mm].	111
6.33 Water cut as a function of flowrate. Marcol oil with $\delta=5$ [mm], simulation vs. experiment.	112

6.34 Water cut as a function of flowrate. Marcol oil with $\delta=10$ [mm], simulation vs. experiment.	113
6.35 Water cut as a function of flowrate. Nexsbase oil with $\delta=10$ [mm], simulation vs. experiment.	113
6.36 Water cut as a function of flowrate. Nexsbase oil with $\delta=15$ [mm], simulation vs. experiment.	113
6.37 Comparion of water jump values observed in 3D simulations, 2D simulation, and experiments for both oils utilizing a $\delta =10$ [mm], and WL= 30 [mm].	115
6.38 Comparion of water jump values observed in 3D simulations, 2D simulation, and experiments for both oils utilizing a $\delta =10$ [mm], and WL= 50 [mm].	115
6.39 Comparion of water jump values observed in 3D simulations, 2D simulation, and experiments for both oils utilizing a $\delta =10$ [mm], and WL= 70 [mm].	115
6.40 Example of oil volume fraction at reference plane.	116
6.41 Example of oil volume fraction at zy-plane, slicing center of outlet orifice.	116
6.42 Comparion of water cut values calculated from 3D simulations, 2D simulation, and experiments for both oils utilizing a $\delta =10$ [mm], and WL= 30 [mm].	117
6.43 Comparion of water cut values calculated from 3D simulations, 2D simulation, and experiments for both oils utilizing a $\delta =10$ [mm], and WL= 50 [mm].	117
6.44 Comparion of water cut values calculated from 3D simulations, 2D simulation, and experiments for both oils utilizing a $\delta =10$ [mm], and WL= 70 [mm].	117
6.45 Water Jump observed with varying oil density.	120
6.46 Water Jump observed with varying water density.	120
6.47 Water Jump observed with varying oil viscosity.	120

6.48	Water cut observed with varying oil density.	121
6.49	Water cut observed with varying water density.	121
6.50	Water cut observed with varying oil viscosity.	121
6.51	Observed water jump for given density ratios- η	122
7.1	Pi-group π_1 plotted as a function of Pi-group π_2 . Each curve for a fixed value of Pi-group π_3	127
7.2	Water jump values predicted by equation (7.10) vs. experimental values, utilizing Nexbase oil and $\delta=10$ [mm].	130
7.3	Water jump values predicted by equation (7.10) vs. experimental values, utilizing Marcol oil and $\delta=10$ [mm].	130
7.4	Water jump values predicted by equation (7.8) vs. experimental values, utilizing Nexbase oil and $\delta=10$ [mm].	131
7.5	Water jump values predicted by equation (7.8) vs. experimental values, utilizing Marcol oil and $\delta=10$ [mm].	131
7.6	Pressure losses as a function of flow rate, for Nexbase oil with $\delta = 5$ [mm], and WL=30 [mm]. Computed from equation (7.8).	132
7.7	Pressure losses as a function of flow rate, for Marcol oil with $\delta = 15$ [mm], and WL=30 [mm]. Computed from equation (7.8).	132
7.8	Illustration of how the plot of the analytical model can be tuned to fit the experi- mental findings.	134
7.9	Comparison of critical flow rates, the analytical methods vs. experimental values for Marcol oil, $\delta=5$ [mm].	137

7.10 Comparison of critical flow rates, the analytical methods vs. experimental values for Marcol oil, $\delta=10$ [mm].	137
7.11 Comparison of critical flow rates, the analytical methods vs. experimental values for Marcol oil, $\delta=15$ [mm].	138
7.12 Comparison of critical flow rates, the analytical methods vs. experimental values for Nexbase oil, $\delta=5$ [mm].	138
7.13 Comparison of critical flow rates, the analytical methods vs. experimental values for Nexbase oil, $\delta=10$ [mm].	138
7.14 Comparison of critical flow rates, the analytical methods vs. experimental values for Nexbase oil, $\delta=15$ [mm].	139
A.1 Spreadsheet for Nexbase 3080, $\delta = 5$ [mm], single orifice.	145
A.2 Spreadsheet for Nexbase 3080, $\delta = 10$ [mm], single orifice.	146
A.3 Spreadsheet for Nexbase 3080, $\delta = 15$ [mm], single orifice.	147
A.4 Spreadsheet for Nexbase 3080, $\delta = 25$ [mm], single orifice.	148
A.5 Spreadsheet for Marcol 52, $\delta = 5$ [mm], single orifice.	149
A.6 Spreadsheet for Marcol 52, $\delta = 10$ [mm], single orifice.	150
A.7 Spreadsheet for Marcol 52, $\delta = 15$ [mm], single orifice.	151
A.8 Spreadsheet for Marcol 52, $\delta = 25$ [mm], single orifice.	152
A.9 Spreadsheet for Nexbase 3080, $\delta = 10$ [mm], two orifices at same height.	153
A.10 Spreadsheet for Nexbase 3080, $\delta = 15$ [mm], two orifices at same height.	154
A.11 Spreadsheet for Marcol 52, $\delta = 10$ [mm], two orifices at same height.	155

A.12 Spreadsheet for Marcol 52, $\delta = 5$ [mm], two orifices at same height.	156
A.13 Spreadsheet for Nexbase 3080, $\delta = 10$ [mm], two orifices at different height.	157
A.14 Spreadsheet for Nexbase 3080, $\delta = 15$ [mm], two orifices at different height.	158
A.15 Spreadsheet for Marcol 52, $\delta = 5$ [mm], two orifices at different height.	159
A.16 Spreadsheet for Marcol 52, $\delta = 10$ [mm], two orifices at different height.	160
A.17 Water jump as function of the flow rate for each annulus gap for Nexbase 3080.	161
A.18 Water jump as function of the flow rate for each annulus gap for Marcol 52.	162
A.19 Comparison of water jump as function of flow rate for Marcol and Nexbase, between one single outlet and two outlets at the same height.	163
A.20 Comparison of water jump as function of flow rate for Marcol and Nexbase, between one single outlet and two outlets at different heights.	164
A.21 Water cut as function of flow rate for each annulus gap for Nexbase 3080.	165
A.22 Water cut as function of flow rate for each annulus gap for Marcol 52.	166
A.23 Comparison of the water cut as function of flow rate for Marcol and Nexbase, between one single outlet and two outlets at the same height.	167
A.24 Comparison of the water cut as function of flow rate for Marcol and Nexbase, between one single outlet and two outlets at different heights.	168
A.25 The flow rate of oil, water and the total flow rate for Nexbase 3080 $\delta = 10$ mm. Moving from left to right the different sequences are: $wL = 10$ mm, ($wL = 20$ mm only for $\delta = 10$ mm), $wL = 30$ mm, $wL = 50$ mm, $wL = 70$ mm, $wL = 90$ mm and $wL = 110$ mm.	169

A.26 The flow rate of oil, water and the total flow rate for Marcol 52 $\delta = 10$ mm. Moving from left to right the different sequences are: $wL = 10$ mm, $wL = 30$ mm, $wL = 50$ mm, $wL = 70$ mm, $wL = 90$ mm and $wL = 110$ mm. 170

B.1 Water cut discrepancy, laminar friction vs. composite friction formulation. Nexbase oil, all gaps. 172

B.2 Water cut discrepancy, laminar friction vs. composite friction formulation. Marcol oil, all gaps. 172

C.1 Predicted stable water cone height with and with accelerational pressure loss. For Marcol and Nexbase, $\delta=5$ [mm]. 179

C.2 Predicted stable water cone height with and with accelerational pressure loss. For Marcol and Nexbase, $\delta=15$ [mm]. 180

List of Tables

3.1	Data of the oils used during the experiments.	28
3.2	Flow rate versus valve position for Nexbase 3080 and Marcol 52.	29
3.3	Approximate running time for each valve position for one orifice	33
3.4	Approximate running time for each valve position for two orifices	34
3.5	Operational variables.	34
3.6	Key observables during the experiments.	35
5.1	Mesh Statistics	79
5.2	Mesh Statistics, for mesh sensitivity analysis.	80
5.3	Base-case configurations for mesh sensitivity analysis.	80
5.4	Mesh statistics for mesh with inflation Layers.	83
5.5	Key Parameters	88
6.1	Simulations for 5 [mm] gap	93
6.2	Simulations for 10 [mm] gap	93

6.3	Simulations for 15mm gap	93
6.4	Experiments used for comparison with simulations.	109
6.5	Simulations for 10mm gap	114
6.6	Base case parameter configuration for parametric study comparison.	118
6.7	Parameter variable values utilized for parametric study.	118
6.8	Simulation Configurations	123
7.1	Experiments used for comparison with the analytical model.	125
7.2	Tuning parameter values	135
C.1	Table representing the coefficient values κ , and ϵ used in equation 7.7, for each respective configuration of oil and annulus gap width δ	175

Bibliography

- [1] "Horizontal wells," 2001. Available from http://petrowiki.org/Horizontal_wells, accessed May 2016.
- [2] R. F. King, "Drilling sideways - a review of horizontal well technology and its domestic application.," *Energy Information Administration Office of Oil and Gas U.S Department of Energy*, 1993.
- [3] PetroWiki, "Water and gas coning." Available from http://petrowiki.org/Water_and_gas_coning#Basis_of_terminology, downloaded Desember 9. 2015.
- [4] J. McCarthy, "Gas and water cresting towards horizontal wells.," *Australian Mathematical Society*, 1993.
- [5] T. Ellis *et al.*, "Inflow control device - raising profiles.," *Oilfield Review Journal*, 2009/2010.
- [6] Schlumberger, "Glossary - cresting," <http://www.glossary.oilfield.slb.com/en/Terms/c/cresting.aspx>, Accessed February 2016.
- [7] M. Muskat and R. D. Wyckoff, "An approximate theory of water-coning in oil production.," *Society of Petroleum Engineers*, 1934.
- [8] H. Aakre, B. Halvorsen, *et al.*, "Autonomus inflow control valve for heavy and extra-heavy oil.," *Society of Petroleum Engineers*, 2014.
- [9] S. O. Inkori, "Numerical study of water coning with downhole water sink (dws) well completions in vertical and horizontal wells.," 2002. A Dissertation submitted to the Graduate Faculty of the Louisiana State University and Agricultural and Mechanical

- College in partial fulfillment of the requirements for the degree of Doctor of Philosophy. Available from http://etd.lsu.edu/docs/available/etd-0610102-080619/unrestricted/Inikori_dis.pdf,.
- [10] L. A. Høyland, P. Papatzacos, and S. M. Skjaeveland, “Critical rate for water coning: Correlation and analytical solution,” *Society of Petroleum Engineers*, November 1989. Available from <https://www.onepetro.org/download/journal-paper/SPE-15855-PA?id=journal-paper%2FSPE-15855-PA>, downloaded December 10. 2015.
- [11] A. Bahadori and A. Nouri, “Prediction of critical oil rate for bottom water coning in anisotropic and homogeneous formations,” *Journal of Petroleum Science and Engineering*, February 2012. Available from <http://www.nioclibrary.ir/latin-articles/120953.pdf>, downloaded December 10. 2015.
- [12] “Resflow icd’s in horizontal open-hole wells optimize production in thin oil-rim reservoir,” 2010. Available from http://www.slb.com/~media/Files/sand_control/case_studies/resflow_malaysia_cs.pdf,.
- [13] F. Porturas, I. Vela, J. Pazos, and O. Humbert, “Lifting more dry oil by reducing water production with inflow control devices in wells drilled and completed in consolidated reservoirs, bloque 15, ecuador,” *AAPGER Newsletter*, June 2009. Available from <https://www2.aapg.org/europe/newsletters/2009/06jun/06jun09europe.pdf>, downloaded December 9. 2015.
- [14] B. S. Aadnoy, “Autonomous flow control valve or “intelligent” icd,” 2008. Available from http://www.hansenenergy.biz/HANSEN_Energy_Solutions/InflowControl2008B.pdf, downloaded December 9. 2015.
- [15] A. Valle, “Oil-water flow patterns upstream and downstream icd/aicd,” *Statoil document*, August 2012. Document received from Statoil.
- [16] F. White, *Fluid Mechanics*. McGraw Hill, 1991.
- [17] E. Shevchenko, “Experimental study of water coning phenomenon in perforated pipes geometry,” Master’s thesis, NTNU, Trondheim, Norway, 2013.

- [18] Y. A. Cengel and J. M. Cimbala, *Fluid Mechanics, Fundamentals and Applications*. McGraw Hill, 2010.
- [19] A. Techet, “2.016 hydrodynamics,” september 2005. Available from <http://web.mit.edu/2.016/www/handouts/2005Reading4.pdf>, downloaded Desember 6. 2015.
- [20] A. A. Sonin, “Equation of motion for viscous fluids,” 2001. Available from http://web.mit.edu/2.25/www/pdf/viscous_flow_eqn.pdf, accessed March 2016.
- [21] S. Kakaç *et al.*, *Handbook of Single phase Convective Heat Transfer*. Wiley, 1987.
- [22] A. Powell, “Fluid dynamics,” January 2003. Available from <http://ocw.mit.edu/courses/materials-science-and-engineering/3-185-transport-phenomena-in-materials-engineering-fall-2003/lecture-notes/chap4.pdf>, downloaded April 2016.
- [23] R. R. Rothfus *et al.*, “Simplified flow calculations for tubes and parallel plates,” *A.I.Ch.E. Journal*, 1957. Available from <http://onlinelibrary.wiley.com/doi/10.1002/aic.690030215/pdf>, downloaded February 2016.
- [24] ANSYS, “Ansys reference manual,” 2016. Version 15.0 available online <http://148.204.81.206/Ansys/readme.html>,.
- [25] Langtry and Menter, “A correlation-based transition model using local variables—part i: Model formulation,” 2006. Available from https://www.researchgate.net/publication/228628272_A_Correlation-Based_Transition_Model_Using_Local_Variables-Part_I_Model_Formulation,.
- [26] I. V. Kalmikov, “Capillary action,” 2016. Available from <http://www.thermopedia.com/content/31/>, Accessed January 2016.
- [27] K. Nielsen *et al.*, “Selective filling of photonic crystal fibres,” *Journal of Optics: Pure and Applied Optics*, 2005. Available from <http://iopscience.iop.org/article/10.1088/1464-4258/7/8/L02/pdf>, downloaded February 2016.

- [28] G. W. Bluman, "Symmetries and differential equations," 1989. Available from <https://www.math.ucdavis.edu/~temple/MAT119A/DimensionalAnalysisBlumanKumei.pdf>, downloaded May 2016.